Radiative Heating and Cooling in Circumstellar Envelopes

von

Dipl.-Phys. Peter Woitke

aus Berlin

Vom Fachbereich 04 (Physik)
der Technischen Universität Berlin
zur Erlangung des akademischen Grades

Doktor der Naturwissenschaften (Dr. rer. nat.)

genehmigte Dissertation

Berlin 1997

D 83

Promotionsausschuß

Vorsitzender: Prof. Dr. D. Zimmermann
Berichter: Prof. Dr. E. Sedlmayr
Priv. Doz. Dr. J. P. Kaufmann

Tag der mündlichen Prüfung: 18.06.1997

*Weiß man, wo man innehalten muß, entsteht geistige Festigkeit.
Gibt es geistige Festigkeit, dann entsteht innere Ruhe.
Hat man innere Ruhe, dann entsteht Gelassenheit.
Hat man Gelassenheit, dann entsteht besonnenes Nachdenken.
Gibt es besonnenes Nachdenken, so kommt das Gelingen.*

(Konfuzius, Buch der Riten)

Zusammenfassung

Kleine Festkörperpartikel von einer Größe bis zu etwa 1 μm bilden auf den ersten Blick eine unbedeutende, eher störende Komponente der Materie in unserem Kosmos. Genauer betrachtet kommt diesen „Staubteilchen“ jedoch eine grundsätzliche Bedeutung zu. Aufgrund ihrer großen Wirkungsquerschnitte für die Wechselwirkung mit Licht prägen sie in ganz entscheidender Weise das Erscheinungsbild des heutigen Universums. Sie beeinflussen wesentlich die dynamischen, thermischen und chemischen Eigenschaften des Gases in der Interstellaren Materie und sind ohne Zweifel mitverantwortlich für den kosmischen Kreislauf und die chemische Evolution der Materie. Man kann ohne Übertreibung sagen, daß es ohne die Existenz der Staubteilchen weder die Erde, noch den Menschen, ja vielleicht nicht einmal die Sonne geben würde.

Die Bildung dieser Staubteilchen aus der Gasphase erfordert relativ spezifische thermodynamische Bedingungen. Neben hohen Dichten sind insbesondere niedrige, aber nicht zu niedrige Temperaturen unterhalb der Sublimationstemperatur des betrachteten Festkörpermaterials erforderlich. Diese Voraussetzung ist absolut zwingend.

Fragt man nach der Existenz solcher Bedingungen in astrophysikalischen Objekten, so liegen diese vor allem in den zirkumstellaren Hüllen von kühlen Riesensternen vor; demzufolge gelten die massiven Winde dieser Objekte als Hauptproduktionsstätten des Staubes im Universum. Bei Riesensternen mit Effektivtemperaturen unterhalb von etwa 3000 K ist der Mechanismus der Staubbildung und des Massenverlustes — nicht zuletzt durch die Arbeiten der Berliner Arbeitsgruppe von Prof. Dr. Sedlmayr — hinreichend verstanden: Bei genügend großen radialen Abständen vom Stern erreicht das Gas Temperaturen, die niedrig genug sind, um den Phasenübergang vom Molekül zum Festkörper zu ermöglichen. Die entstehenden Staubteilchen nehmen durch Absorptions– und Streuprozesse den Impuls des Strahlungsfeldes teilweise auf und geben diesen durch Stöße an das Gas weiter. Dieser Impulseintrag treibt den stellaren Wind.

Neben diesen Sternen gibt es eine Reihe von weiteren staubbildenden Objekten. Insbesondere existiert eine zahlenmäßig eher unbedeutende Klasse von R Coronae Borealis (RCB) Sternen, die sich nicht recht in das obige Bild einordnen lassen. Bei diesen Objekten kommt es in unvorhersagbaren zeitlichen Abständen immer wieder zur Bildung von riesigen Staubwolken, die den gesamten Stern vorübergehend verdecken können, so daß dieser für das bloße Auge für Monate oder Jahre vom Himmel zu verschwinden scheint[1]. Beobachtungen legen nahe, daß der Staubbildungsprozeß

[1] Ähnliche, wenn auch nicht derart spektakuläre Beobachtungen liegen für Wolf–Rayet–Sterne und Novae–Explosionen vor.

bei diesen Sternen in einer Entfernung von nur einigen wenigen Sternradien stattfinden muß, obwohl die RCB–Sterne Effektivtemperaturen von etwa 7000 K besitzen, die also heißer und viel leuchtkräftiger als die Sonne sind. Die vorliegende Arbeit nimmt diese Beobachtungsergebnisse ernst.

Gängige Methoden zur Temperaturbestimmung ergeben in so geringen radialen Entfernungen vom Stern sehr hohe Temperaturen, so daß die Staubbildungstheorien durch die RCB–Sterne auf eine harte Probe gestellt werden: Läßt sich die Staubbildung in der Nähe dieser Sterne mit den üblichen Theorien erklären? Setzt man die Gültigkeit der Theorien voraus, so müssen entweder die Beobachtungen falsch sein, oder es müssen in der Nähe dieser Sterne — zumindest zeitweilig — viel niedrigere Temperaturen als erwartet herrschen.

Kann es in der Nähe von heißen Sternen zu thermodynamischen Bedingungen kommen, die Staubbildungsprozesse zulassen? Angeregt durch diese Fragestellung untersucht die vorliegende Arbeit *den thermischen Zustand dünner Gase unter dem Einfluß von stellaren Strahlungsfeldern*. Es handelt sich hierbei zunächst um allgemeine (nicht RCB–spezifische), grundlegende Studien. Eine Methode zur zeitabhängigen Temperaturbestimmung von Gasen in zirkumstellaren Hüllen wird entwickelt, die von vornherein so konzipiert ist, daß sie als elementarer Bestandteil von komplexeren Modellrechnungen in zukünftigen Arbeiten verwendet werden kann.

Das thermodynamische Konzept dieser Methode beruht auf einer non–LTE Beschreibung des Gases, in der jedoch eine Geschichtsabhängigkeit der Konzentrationen der Moleküle und der Besetzungsdichten vernachlässigt wird. Stattdessen wird ein kinetisches Gleichgewicht ("steady state") vorausgesetzt. Es wird gezeigt, daß diese Annahme eine gewöhnliche thermodynamische Beschreibung des Gases zuläßt.

Die folgenden radiative Prozesse werden in dieser Arbeit berücksichtigt: Linienübergänge von Atomen und einfach geladenen Ionen, Vibrations– und Rotationsübergänge von polaren diatomischen bzw. linearen Molekülen, Quadrupol–Übergänge von H_2, gebunden–frei–Übergänge von Atomen aus dem Grundzustand und (im Falle von Wasserstoff) aus angeregten elektronischen Niveaus, ferner Photodissoziationsprozesse und frei–frei–Übergänge. Diese Prozesse ergeben in der Summe die radiativen Heiz– und Kühlraten, d. h. die Wärmemengen, die das Gas durch Absorptionsprozesse pro Zeit aufnimmt bzw. durch Emissionsprozesse verliert. Die radiativen Heiz– und Kühlraten bilden somit die Grundlage zur thermodynamischen Modellierung des Gases.

Drei Anwendungen der entwickelten Methode werden vorgestellt:

Zunächst werden die stabilen Gleichgewichtszustände des Gases in den zirkumstellaren Hüllen von RCB–Sternen bestimmt. Diese Zustände zeichnen sich dadurch aus, daß sich die radiativen Heiz– und Kühlraten ausgleichen (Strahlungsgleichgewicht). Es wird jedoch festgestellt, daß das Strahlungsgleichgewicht eine zwar notwendige, aber nicht hinreichende Bedingung zur Berechnung des thermischen Zustand des Gases darstellt. Unter gegebenen Druck– und Strahlungsfeldbedingungen können mehrere Lösungen existieren, d. h. eine räumliche Koexistenz von heißen, atomaren

Phasen neben kalten, molekularen Phasen erscheint prinzipiell möglich („thermische Bifurkationen").

Der Relaxationsprozeß des Gases zum Strahlungsgleichgewicht wird in den zirkumstellaren Hüllen von C–Sternen untersucht. Hierbei wird insbesondere das Verhalten des Gases hinter Stoßwellen diskutiert, die durch eine Pulsation des zentralen Sterns verursacht werden. Es ergibt sich, daß nach der Passage einer solchen Stoßwelle nur ein hinreichend dichtes Gas in der Lage ist, den Strahlungsgleichgewichtszustand nach einiger Zeit wieder zu erreichen. Bei Teilchendichten $\lesssim 10^{8}\,\mathrm{cm}^{-3}$ verhält sich das Gas zunehmend adiabatisch, so daß schließlich die Bedingung des Strahlungsgleichgewichtes ihre bestimmende Bedeutung für die Temperaturstruktur dieser Sternhüllen verliert.

Schließlich wird das zeitabhängige thermische Verhalten des Gases in den zirkumstellaren Hüllen von pulsierenden RCB–Sternen genauer untersucht. Es wird eine periodische Situation studiert, in der das Gas in der Nähe des Sterns fortlaufend durch Stoßwellen erhitzt und komprimiert wird, und in der Zwischenzeit reexpandiert. In einem bestimmten Dichtebereich kann dabei das Gas durch einen 2–Stufen–Prozeß, bestehend aus radiativer Kühlung gefolgt von adiabatischer Expansion, Temperaturen erreichen, die weit unterhalb der Strahlungsgleichgewichtstemperatur liegen. Schon bei radialen Abständen von etwa $1.5-3\,R_*$ treten hierbei zeitweilig Temperaturen unterhalb von 1500 K auf, abhängig von der Stoßwellengeschwindigkeit. Diese Arbeit stellt daher die Hypothese auf, daß die Kondensation von Rußteilchen in der Nähe der RCB–Sterne durch Stoßwellen verursacht wird, wodurch die spektakulären Verdunklungsereignisse dieser Objekte auslöst werden könnten.

Die vorliegende Arbeit enthält somit grundlegende Erkenntnisse über das thermodynamische Verhalten der Gase in zirkumstellaren Hüllen. Neue, alternative Wege zur Staubbildung werden aufgezeigt.

Abstract

This thesis investigates the thermal state of diluted gases being exposed to stellar radiation fields. On the basis of a steady–state non–LTE description, the radiative heating and cooling rates of the gas are determined, considering the typical densities present in circumstellar envelopes.

The following radiative processes are examined: line transitions of neutral and singly ionized atoms, vibrational and rotational transitions of polar diatomic and linear molecules, respectively, quadrupole transitions of H_2, bound–free transitions from the electronic ground states and (in case of hydrogen) from excited electronic levels, photodissociation and free–free transitions.

A thermodynamic description of the gas is developed which allows for a time–dependent determination of the temperature structure in the circumstellar envelopes of cool and warm stars and can be included into more complex, e. g. hydrodynamic, model calculations. Three applications of this description are presented:

First, the stable radiative equilibrium states of the gas are calculated for the circumstellar envelopes of R Coronae Borealis (RCB) stars. It is found that the condition of radiative equilibrium is not sufficient in order to determine the temperature of the gas. More than one temperature solution may exist for fixed conditions of pressure and radiation field. Thus, a spatial coexistence of hot, atomic and cool, molecular phases is principally conceivable ("thermal bifurcations").

Second, the relaxation process towards radiative equilibrium is studied in the circumstellar envelopes of C–stars. The character of the thermal relaxation behind propagating shock waves, which are caused by a pulsation of the central star, is discussed. It is found that the gas must be sufficiently dense in order to be capable to reestablish radiative equilibrium after the passage of such shocks. For densities $\lesssim 10^8\,\mathrm{cm}^{-3}$, the behavior of the gas becomes more and more adiabatic, so that finally the condition of radiative equilibrium looses its significance concerning the determination of the temperature structure.

Third, the time–dependent behavior of the gas in the circumstellar envelopes of pulsating RCB stars is investigated more detailed. A model for shock levitated atmospheres is developed, where the gas is periodically heated and compressed by shock waves and re–expands between the shocks. Within a distinct density interval the gas is found to undergo a two–step cooling process, consisting of radiative cooling at high temperatures followed by adiabatic expansion at low temperatures. In this case a considerable supercooling of the gas occurs, temporarily producing temperatures below 1500 K (far below the values expected from radiative equilibrium) at radial distances as small as $1.5-3\,R_*$, despite of the high effective temperatures of these stars. Thus, this thesis states the hypothesis that the onset of dust formation close to RCB stars is caused by shock waves, which might trigger the spectacular decline events.

Contents

List of Symbols

symbol	description	unit	page
A_{ul}	Einstein coefficient for spontaneous emission	$\mathrm{s^{-1}}$	25
B	frequency integrated Planck function	$\mathrm{erg\,s^{-1}\,cm^{-2}}$	3
B	rotational constant	Hz	35
B_{lu}	Einstein coefficient for absorption	$\mathrm{erg^{-1}\,cm^2\,s^{-1}}$	25
B_{ul}	Einstein coefficient for stimulated emission	$\mathrm{erg^{-1}\,cm^2\,s^{-1}}$	25
B_ν	Planck function	$\mathrm{erg\,s^{-1}\,cm^{-2}\,Hz^{-1}}$	2
C_{lu}	rate coefficient for collisional excitation	$\mathrm{s^{-1}}$	25
C_{ul}	rate coefficient for collisional de–excitation	$\mathrm{s^{-1}}$	25
D^0_{mol}	dissociation potential	erg	67
E_a	activation energy of a chemical reaction	erg	54
E_{diss}	total dissociation potential energy	erg	67
E_{el}	total electronic excitation energy	erg	67
E_{ion}	total ionic potential energy	erg	67
E_{rot}	total rotational excitation energy	erg	67
E_{trans}	total translational energy	erg	67
E_{vib}	total vibrational excitation energy	erg	67
ΔE_{ul}	energy difference between upper and lower state	erg	25
$\Delta_{\mathrm{f}} G^{\ominus}$	free enthalpy of formation at standard pressure $p^{\ominus}$	erg	54
$I^{\mathrm{inc}}_\nu(\mu)$	incident continuous intensity from direction μ	$\mathrm{erg\,s^{-1}\,cm^{-2}\,Hz^{-1}\,str^{-1}}$	25
J_ν	mean spectral intensity	$\mathrm{erg\,s^{-1}\,cm^{-2}\,Hz^{-1}}$	2
J	frequency integrated mean intensity	$\mathrm{erg\,s^{-1}\,cm^{-2}}$	3
J	rotational quantum number	–	35
$J^{\mathrm{cont}}_{\nu_{ul}}$	continuous mean intensity at line center frequency	$\mathrm{erg\,s^{-1}\,cm^{-2}\,Hz^{-1}}$	25
$\overline{J}_{ul}$	line averaged continuous mean intensity	$\mathrm{erg\,s^{-1}\,cm^{-2}\,Hz^{-1}}$	25
J_*	nucleation rate, i. e. the number of seed particles forming per volume and per second	$\mathrm{cm^{-3}\,s^{-1}}$	115
Ω	solid angle	–	25
Ω_{ul}	temperature–independent rate coefficient for collisional de–excitation	$\mathrm{cm^3\,s^{-1}}$	32
$P^{\,\mathrm{e}}$	mean escape probability	–	25
$\widetilde{P}^{\,\mathrm{e}}$	simplified mean escape probability	–	26
Q_{rad}	total net radiative heating function	$\mathrm{erg\,s^{-1}\,cm^{-3}}$	22
$\widehat{Q}_{\mathrm{rad}}$	total net radiative heating rate per mass	$\mathrm{erg\,s^{-1}\,g^{-1}}$	22
$\widehat{Q}_{\mathrm{dust}}$	total net heating rate per mass due to presence of dust grains	$\mathrm{erg\,s^{-1}\,g^{-1}}$	22
$Q^{\mathrm{bf}}_{\mathrm{rad}}$	net radiative heating function due to bound–free transitions	$\mathrm{erg\,s^{-1}\,cm^{-3}}$	45
$Q^{\mathrm{ff}}_{\mathrm{rad}}$	net radiative heating function due to free–free transitions	$\mathrm{erg\,s^{-1}\,cm^{-3}}$	58

symbol	description	unit	page
$Q_{\rm rot}$	rotational net heating function	$\rm erg\,s^{-1}\,cm^{-3}$	37
$Q_{\rm vib}$	vibrational net heating function	$\rm erg\,s^{-1}\,cm^{-3}$	41
$Q_{\rm rad}^{\rm chem}$	net radiative heating function of a photo–chemical reaction	$\rm erg\,s^{-1}\,cm^{-3}$	54
R_*	stellar radius	cm	4
R_{ij}	total rate coefficient for transition $i \to j$	$\rm s^{-1}$	24
S	supersaturation ratio of the gas with respect to graphite	–	115
$S_{ul}^{\rm L}$	line source function	$\rm erg\,s^{-1}\,cm^{-2}\,Hz^{-1}$	25
$S_i(T_{\rm g})$	Saha function of level i	$\rm cm^{-3}$	45
T	temperature	K	2
TM	vibrational transition moment	[cgs]	39
$T_{\rm rot}$	rotational excitation temperature	K	36
$T_{\rm rot}$	vibrational excitation temperature	K	39
$T_{\rm bb}$	black body temperature	K	3
$T_{\rm eff}$	effective stellar temperature	K	4
$T_{\rm g}$	unique kinetic temperature of the gas	K	17
$T_{\rm rad}$	radiation temperature	K	3
$T_{\rm g}^{\rm RE}$	radiative equilibrium temperature	K	3
V	specific volume $1/\rho$	$\rm cm^3\,g^{-1}$	22
W	dilution factor	–	3
$Z_{\rm II}$	partition function of an singly ionized atom	–	45
$Z_{\rm rot}$	rotational partition function	–	36
$Z_{\rm vib}$	vibrational partition function	–	39
amu	atomic mass unit $m_{\rm C12}/12$	g	39
atm	standard atmospheric pressure $1.013 \cdot 10^6$	$\rm dyn\,cm^{-2}$	39
α_i	photo–recombination coefficient to level i	$\rm cm^{-3}\,s^{-1}$	46
b_i	departure coefficient from LTE $b_i = n_i/n_i^*$	–	50
$\beta_i(T_{\rm g})$	rate coefficient for collisional ionization from level i	$\rm cm^3\,s^{-1}$	45
c	speed of light	$\rm cm\,s^{-1}$	25
e	internal energy of the gas	$\rm erg\,g^{-1}$, 18	
$\epsilon_{\rm El}$	element abundance by number	–	66
ϵ_ν	gas emission coefficient	$\rm erg\,s^{-1}\,cm^{-3}\,Hz^{-1}\,str^{-1}$	2
j_{ul}	dimensionless mean intensity at ν_{ul}	–	26
$f_{\rm rot}$	number of rotational degrees of freedom	–	67
g_l, g_u	statistical weights of lower and upper level	–	25
γ_{ul}	rate coefficient for collisional de–excitation	$\rm cm^3\,s^{-1}$	32
h	Planck's constant	$\rm erg\,s$	25
h	enthalpy per mass unit $h = e + p/\rho$	$\rm erg\,g^{-1}$	70
$\hbar$	$h/(2\pi)$	$\rm erg\,s$	39
$\langle h\nu\rangle^{\rm abs}$	mean absorbed photon energy	erg	47
$\langle h\nu\rangle^{\rm em}$	mean emitted photon energy	erg	47
k	Boltzmann constant	$\rm erg\,K^{-1}$	3
$k_{\rm f}$	rate coefficient of a forward chemical reaction	depends	54
$k_{\rm r}$	rate coefficient of a reverse chemical reaction	depends	54
κ_ν	gas absorption coefficient	$\rm cm^{-1}$	2
κ_B	Planck mean absorption coefficient	$\rm cm^{-1}$	3
κ_J	intensity mean absorption coefficient	$\rm cm^{-1}$	3
λ	wavelength	cm	2
$m_{\rm El}$	mass of neutral atom of element El	g	66

symbol	description	unit	page
$m_{\rm e}$	electron mass	g	45
$m_{{\rm red},i}$	reduced mass for collisions between the considered species and collision partner i	g	35
μ	$\cos\theta$	–	25
μ_D	dipole moment of a molecule	[cgs]	35
n^*	particle density in LTE, chemical equilibrium	$\rm cm^{-3}$	50
n_i	population of level i	$\rm cm^{-3}$	24
n_l	level population of the lower level	$\rm cm^{-3}$	25
n_u	level population of the upper level	$\rm cm^{-3}$	25
$n_{\rm at}^{\rm El}$	total neutral atom particle density	$\rm cm^{-3}$	66
$n_{\rm II}^{\rm El}$	singly ionized atom particle density	$\rm cm^{-3}$	66
$n_{<{\rm H}>}$	total density of H-nuclei in all ionic, atomic and molecular forms $\epsilon_{\rm H}\rho/(\sum_{\rm El}\epsilon_{\rm El}m_{\rm El}))$	$\rm cm^{-3}$	29
$n_{<{\rm He}>}$	total helium particle density in atomic or ionized form	$\rm cm^{-3}$	74
$n_{\rm cr}$	critical density ($n_{<{\rm H}>}$–value) for thermal population	$\rm cm^{-3}$	31
$n_{\rm thick}$	critical density ($n_{<{\rm H}>}$–value) for optical depths effects	$\rm cm^{-3}$	31
$n_{\rm e}$	electron density	$\rm cm^{-3}$	32
$n_{\rm mol}$	total particle density of molecule mol	$\rm cm^{-3}$	36
$n_{\rm sp}$	total particle density of one species	$\rm cm^{-3}$	25
ν	frequency	Hz	2
$\nu_{\rm thr}^i$	threshold frequency for photoionization	Hz	45
ν_{ul}	line center frequency	Hz	25
ω	eigenfrequency of the harmonic oscillator	Hz	39
$\omega_j^{\rm mol}$	j-th vibrational eigenfrequency of a molecule	Hz	67
p	gas pressure	$\rm dyn\,cm^{-2}$	22
$p^{\ominus}$	standard pressure	$\rm dyn\,cm^{-2}$	54
$p_{\rm sat}$	vapor pressure of neutral atoms over the bulk material	$\rm dyn\,cm^{-2}$	115
$\phi_{ul}(\nu,\mu)$	profile function of the considered transition	$\rm Hz^{-1}$	25
r	radial distance to the center of the star	cm	4
ρ	mass density of the gas	$\rm g\,cm^{-3}$	4
$s_{\rm mol}^{\rm El}$	stoichiometric coefficient of molecule mol for element El	–	66
σ	Stefan Boltzmann constant	$\rm erg\,cm^{-2}\,K^{-4}$	3
$\sigma^{\rm f}(\nu)$	photodissociation cross section	$\rm cm^2$	54
σ_0	total cross section for rotational de–excitation	$\rm cm^2$	35
$\sigma_i^{\rm bf}(\nu)$	bound–free absorption cross section from level i	$\rm cm^2$	45
$\tau_{ul}^{\rm S}$	Sobolev optical depth	–	25
$\widetilde{\tau}_{ul}^{\rm S}$	mean Sobolev optical depth	–	26
$\tau_{\rm cool}$	radiative heating/cooling time scale	s	86
θ	angle between the considered ray and the radial direction	–	25
θ	characteristic temperature of vibrational transitions	K	39
v	vibrational quantum number	–	39
v	hydrodynamic gas velocity	$\rm cm\,s^{-1}$	25
v_∞	terminal wind velocity	$\rm km\,s^{-1}$	28
$\left\langle\frac{dv}{dl}\right\rangle$	local mean velocity gradient	$\rm s^{-1}$	26

List of Figures

List of Tables

Chapter 1

Introduction

1.1 The Importance of Temperature Determination for Models of Dust Formation

Compared to the usual organizational forms of matter in space like stars and the interstellar medium (ISM), there are remarkable and exceptional thermodynamic conditions in extended circumstellar envelopes (CSEs). Here, the densities are lower by orders of magnitude than in the interior and the atmospheres of stars, but — due to mass loss — still higher by orders of magnitude than in the ISM. If the central star is sufficiently cool that its radiation field does not ionize the surrounding CSE, temperatures can exist, which are on one hand low enough to ensure the stability of complex chemical structures, but on the other hand high enough to bridge the energy barriers during their formation.

Therefore, the circumstellar envelopes of cool stars are a cosmic laboratory, where large amounts of complex chemical and physical processes can occur. These processes are of fundamental importance for the evolution of matter, especially for the transition from molecules to dust grains, i. e. the primary formation of solids in space. The high densities combined with low, but not too low, temperatures provide almost ideal preconditions for condensation processes.

Besides the CSEs of cool stars only a few classes of astrophysical objects are known which show similar thermodynamic conditions. These are the rare explosive phenomena like novae and supernovae, shock waves in the most dense parts of the ISM (probably connected with star formation) or comet impacts on planets. Therefore, the CSEs of cool stars are supposed to be the main production sites of small solid particles (dust grains) in space. These particles are carried into the ISM by stellar winds and finally can be observed everywhere in the universe. This ubiquitous existence of dust particles is of greatest importance for the appearance of the present universe, for the circulation of matter, for the formation of stars and planets and, last but not least, also for the existence of life, including mankind.

The chemical reactions, which successively lead to increasing complexity in gases and finally to the formation of seed and dust particles, show such a strong temperature dependence that even slight temperature deviations can change the formation rates by orders of magnitude. Therefore, effective nucleation is generally restricted to a small temperature window of a few hundred degrees below the sublimation temperature of the solid material, which is to be considered[1]. Thus it is immediately clear that the results of theoretical model calculations of dust formation critically depend on the proper determination of the temperature in the medium. Questionable or insufficient methods for temperature determination can easily induce severe errors in the results of such calculations.

> *For the modeling and the understanding of dust formation from the gas phase, the most precise information about the thermodynamic state of the gas is absolutely required.*

How profound is our knowledge of the true thermodynamic state of the gases (especially their temperature) in astrophysical objects? In exceptional cases a direct determination of the temperature stratification from observations of the objects might be possible. However, theoretical methods are usually required which may still suffer from large intrinsic uncertainties (see next section). Astonishingly, most model calculations concerning dust formation in cool stellar envelopes use rather simple and not very reliable methods for temperature determination. At least, the expenditure for the theoretical temperature determination often seems to be inadequate compared to the detailed treatment of the chemistry and dust formation processes in such investigations.

These questions get even more important, when the gas elements are subject to dynamic processes which directly affect the internal energy of the gas. For instance, in shock waves, in the heating by magneto–acoustic waves or during fast expansions accompanied by adiabatic cooling. Which temperature does one use in such cases? How reliable are those results? In this way new potential sites (e. g. close to hot stars) for dust formation not previously considered might be discovered.

1.2 Critical Comments on the Usual Method of Temperature Determination

The temperature structure in extended CSEs is usually calculated by means of the solution of a radiative transfer. Assuming that solely radiative processes are important for the heating and cooling of the gas, the gas will relax to radiative equilibrium (RE), where the total amount of absorbed radiative energy is locally balanced by the total amount of emitted radiative energy everywhere in the envelope.

$$\text{RE:} \qquad 4\pi \int \kappa_\nu J_\nu \, d\nu = 4\pi \int \epsilon_\nu \, d\nu \tag{1.1}$$

The meaning of the physical quantities is explained in the List of Symbols on page x. In case of local thermodynamic equilibrium (LTE), the emissivity can be eliminated by means of Kirchhoff's law $\epsilon_\nu = \kappa_\nu B_\nu(T)$:

$$\text{LTE:} \qquad \int \kappa_\nu J_\nu \, d\nu = \int \kappa_\nu B_\nu(T^{\rm RE}) \, d\nu \tag{1.2}$$

[1] This statement refers to both the "classical" and kinetic treatment of the problem.

In order to arrive at a short notation, appropriate means of the absorption coefficient (κ_J and κ_B) can be defined such that Eq. (1.2) simplifies to $\kappa_J J = \kappa_B B(T^{\rm RE})$ and the temperature of the gas in radiative equilibrium can be expressed by

$$T^{\rm RE\;4} = \frac{\kappa_J}{\kappa_B}\,\frac{\pi}{\sigma} J \quad . \tag{1.3}$$

As far as the assumptions of RE and LTE are appropriate, Eq. (1.3) together with a solution of the radiative transfer determines the proper temperature structure in the considered astrophysical object. The uncertainty of this method lies within the calculation of the gas absorption coefficients κ_ν. This calculation, however, is one of the key problems in astrophysics and a very difficult task, especially in those cases, where the gas is sufficiently cool for molecule formation. Considering the H_2O molecule, for example, which is one of the most abundant species in a cool gas with a solar elemental composition, over a billion of line transitions are known ranging from the near IR to the micro–wave spectral region. Furthermore electronic and bound–free transitions in the UV may be important. In principle, all these transition must be taken into account for a proper calculation of κ_ν. Additional questions concerning the individual line profiles and the effects caused by Doppler shifts due to hydrodynamic velocities and self shielding come into play.

Therefore, due to the lack of knowledge of the exact frequency dependency of κ_ν, the simplifying assumption $\kappa_J = \kappa_B$ is often made. In this case we have $J = B$, which gives the black body temperature

$$\text{grey:} \qquad T_{\rm bb}^4 = \frac{\pi}{\sigma} J \quad . \tag{1.4}$$

Alternatively, Eq. (1.4) can be derived directly from Eq. (1.2) by assuming $\kappa_\nu = const.$ $\kappa_J = \kappa_B$ is henceforth called the "quasi–grey assumption". In the following, the intrinsic uncertainty of this approximation for the resulting temperature structure is explored. First, Eq. (1.4) obviously has always exactly one temperature solution for a given J, whereas Eq. (1.3) may have two or more stable solutions, because the fraction κ_J/κ_B can be temperature–dependent itself. Thereby, the quasi–grey assumption ignores the possibility of thermal bifurcations, which we will encounter later in this work.

The maximum effect caused by true frequency–dependent absorption can be estimated by considering the extreme case of a δ–function

$$\kappa_\nu = \kappa_0\,\delta(\nu - \nu_0) \quad . \tag{1.5}$$

This case is not as artificial as it might first appear, because there is often one special radiative process which dominates the heating and cooling of the gas and which has a certain characteristic wavelength. We consider the effects in a diluted Planck field of type

$$J_\nu = W B_\nu(T_{\rm rad}) \quad , \tag{1.6}$$

which is a useful approximation of the radiation field if the gas element mainly receives light from a distant black body source. In a spherically symmetric, optically thin CSE with $T_{\rm rad}=T_{\rm eff}$ we find the dilution factor to be

$$W(r) = \frac{1}{2}\left(1-\sqrt{1-\frac{R_*^2}{r^2}}\right) \quad . \tag{1.7}$$

Allain (1996) has shown that even for an optically thick CSE Eq. (1.6) still provides a reasonable fit to the results of frequency–dependent radiative transfer calculations (Winters 1994). In general, the parameter $T_{\rm rad}$ is smaller than $T_{\rm eff}$ and W is larger compared to Eq. (1.7). For the assumed κ_ν we find $WB_{\nu_0}(T_{\rm rad})=B_{\nu_0}(T^{\rm RE})$ or

$$T^{\rm RE} = \frac{h\nu_0}{k} \Bigg/ \ln\left(1+\frac{1}{W}\left(\exp\left(\frac{h\nu_0}{kT_{\rm rad}}\right)-1\right)\right) \quad , \tag{1.8}$$

which can be compared to the black body temperature given by Eq. (1.4)

$$T_{\rm bb} = W^{1/4}\,T_{\rm rad} \quad . \tag{1.9}$$

Figure 1.1 depicts the results for some arbitrarily chosen central wavelengths $\lambda_0 = c/\nu_0$. First, if the radiation field is not diluted ($W=1$), the RE temperature always equals $T_{\rm rad}$. In this case (typical for the deep atmosphere and the interior of the star) the frequency dependency of κ_ν is meaningless for the resulting temperature, which makes the temperature determination very reliable.

Farther out in the envelope, however, where $W<1$, a wide spread of possible temperature solutions exist depending on the central wavelength (note the logarithmic scaling of the temperature axis). The possible solutions lie between the UV–limit $h\nu_0 \gg {\rm Max}\{kT_{\rm rad}, kT\}$ ($T_{\rm UV}=T_{\rm rad}$) and the IR–limit $h\nu_0 \ll {\rm Min}\{kT_{\rm rad}, kT\}$ ($T_{\rm IR}=WT_{\rm rad}$). The black body temperature $T_{\rm bb}$ (cf. Eq. 1.9) is just one solution in between, concerning a special type of frequency dependency of κ_ν.

The theoretically determined temperature structure is therefore very sensible for the frequency dependency of κ_ν. For example at $r=2R_*$, the result is 620 K, if the interaction between matter and radiation field mainly takes place at $\lambda_0=10\,\mu$m, but is 1920 K, if $\lambda_0=1\,\mu$m:

$$r = 2\,R_*: \qquad \lambda_0 = (1\ldots10)\,\mu{\rm m} \quad \Rightarrow \quad T^{\rm RE} = (1270\pm650)\,{\rm K}$$

If we compare these values to the small temperature window, where efficient dust condensation may take place, it is obvious that an uncertainty concerning the frequency dependency of κ_ν as considered above can easily change the temperatures to values well above or well below possible condensation, respectively. Let's generously assume $T_{\rm cond}=(1100\pm200)$ K for the temperature, where efficient nucleation from the gas phase may occur. The corresponding radius intervals $r_{\rm cond}$ in the optically thin limit are then given by

$$T_{\rm cond} = (1100\pm200)\,{\rm K}: \qquad \begin{array}{lcl} \lambda_0 = 10\,\mu{\rm m} & \Rightarrow & r_{\rm cond} = (1.1\ldots1.35)\,R_* \\ \text{grey} & \Rightarrow & r_{\rm cond} = (2.7\ldots5.5)\,R_* \\ \lambda_0 = 1\,\mu{\rm m} & \Rightarrow & r_{\rm cond} = (11.5\ldots135)\,R_* \end{array}$$

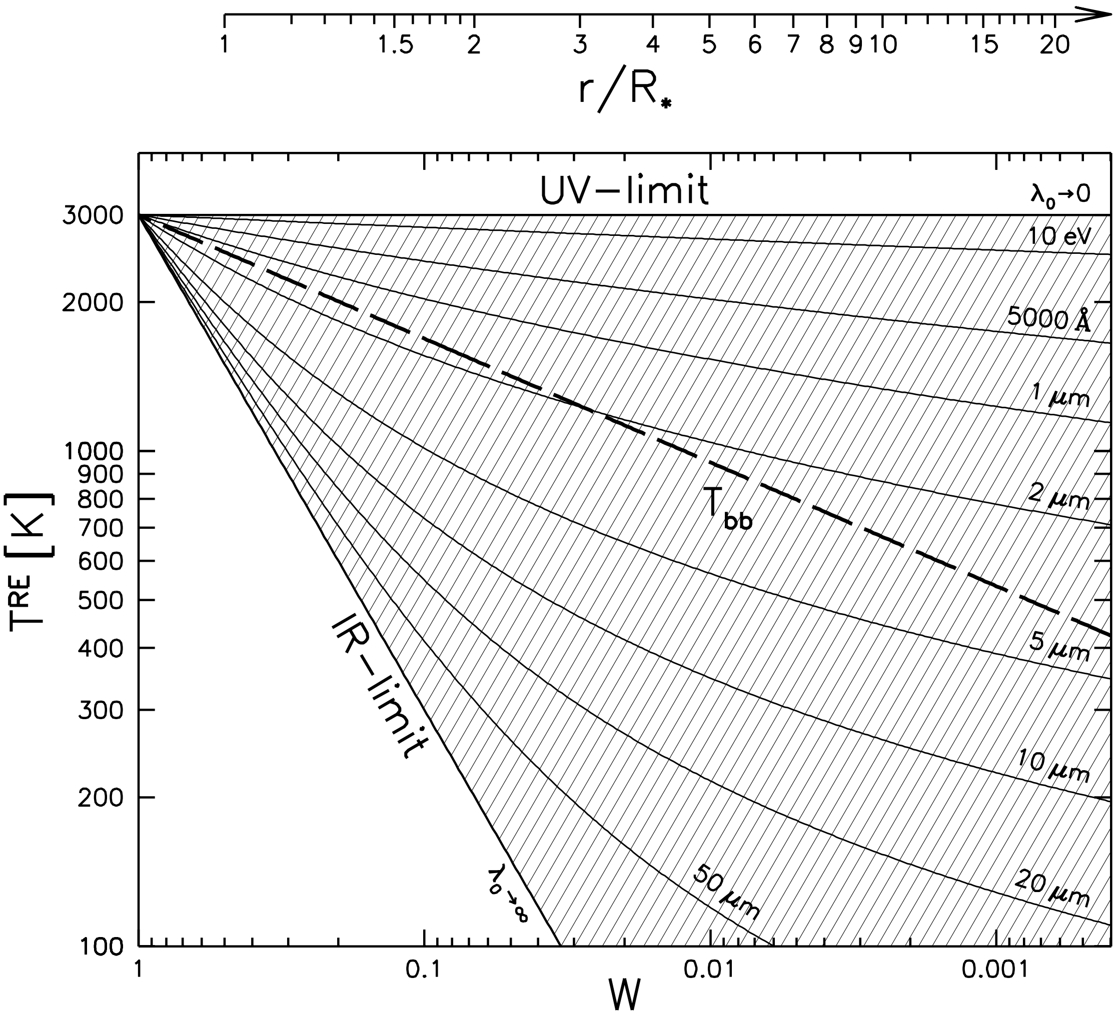

Figure 1.1: Radiative equilibrium temperatures over dilution factor W in a Planck–type radiation field with $T_{\rm rad} = 3000\,$K (cf. Eq. 1.6) according to a δ–function–type gas absorption coefficient. The radius axis belongs to the optical thin limit (pure radial dilution) according to Eq. (1.7). The shaded region indicates the range of possible RE temperatures between the UV and the IR-limit, where the central wavelength (see labels on solid curves) is small and large, respectively. The dashed line shows the black body temperature.

These estimates clearly indicate that the assumption $\kappa_J = \kappa_B$ has a decisive influence on the calculated temperature structure with severe consequences for the modeling of dust formation in the circumstellar envelopes of cool stars.

A lot of simplifying or even unphysical assumptions have been made in this section, so that the calculated numbers are meaningless. However, what is important is the clear trends in the results. Uncertainties concerning the frequency dependency of κ_ν can easily change the results of the theoretically determined temperature structure by 1000 K. The results are even less reliable, if the assumptions of RE and LTE become questionable, which is another topic of this work. More detailed studies on the important heating and cooling processes are required to tackle the problem of theoretical temperature determination in CSEs. Which spectral regions are important and which are the corresponding rates? Remembering the strong temperature dependency of nucleation from the gas phase, such investigations can lead to a new and distinct theoretical view on dust formation in CSEs.

1.3 The Puzzle of Dust Formation around RCB Stars

An example to the above conclusion can possibly be found in the CSEs of R Coronae Borealis stars.

More than two centuries ago, the German astronomer Eduard Pigott discovered that the 25th brightest star in the northern constellation *Coronae Borealis*, previously known to be about 6th magnitude, had suddenly disappeared from the sky. The star remained invisible for several months and finally recovered slowly. In the following years, Pigott observed similar disappearances at irregular intervals. He published his article on this remarkable star exactly 200 years ago (Pigott 1797), which established a new class of objects — the class of *irregular variable stars*. R Coronae Borealis became its first member. Since then, the unpredictable R Coronae Borealis (RCB) type decline events with decreases in visual brightness of up to 8 magnitudes within a few weeks, and the eye–catching shape of the light curve, always attracted much interest and fascination in the astrophysical community. The uniqueness and distinctiveness of this extreme type of variability in contrast to the broad variety of stellar parameters among the RCB stars immediately suggests that there must be *one unique physical mechanism* which triggers all the events.

Over the years, much observational efforts have been undertaken and more and more complete observational data have been collected covering the RCB decline events: photometry, spectroscopy and polarimetry. These observations form a comprehensive data set for this extreme type of stellar variability. A summary of the observations is outlined in Appendix A.

In spite of the completeness and the quality of observational data, our understanding of the physical processes causing the RCB decline events is still rather poor. Since Loreta's (1934) and O'Keefe's (1939) basic suggestion that the decline events are caused by the sudden occurrence of dust somewhere in the line of sight towards the

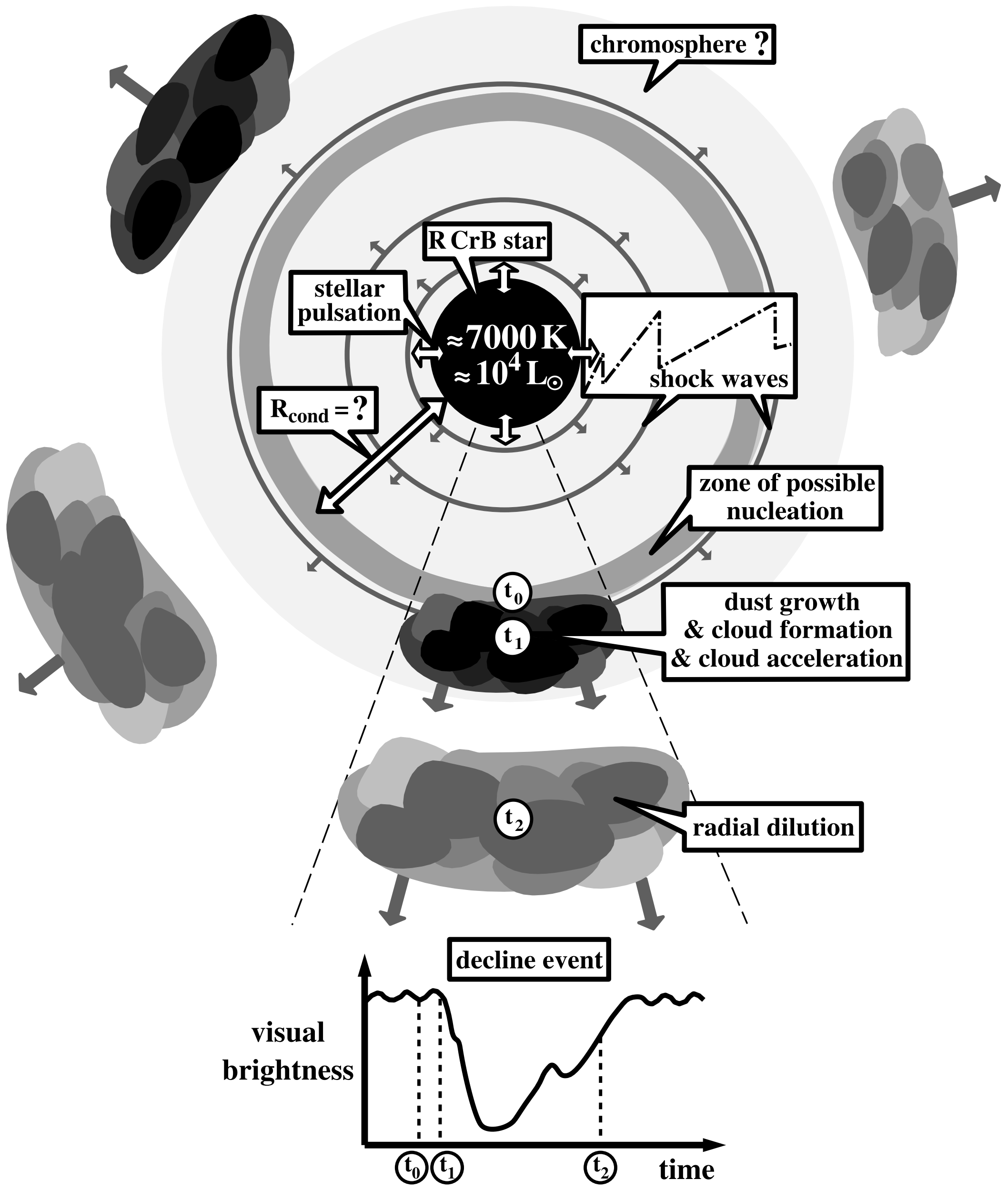

Figure 1.2: Sketch of the physical processes, the geometry and the time evolution of an RCB decline event. A visualization like this is always a mixture of observational facts and interpretation. In this case, the stellar parameters, the pulsation of the star, the occurrence of shock waves and dust clouds and the shape of the light-curve are supported by observations. The geometry of the scenario and the nucleation zone refer to the hypothesis of this work.

observer, the progress during the last six decades concerning a physical explanation of the phenomenon has been slow. The most favorable picture today is that clouds of carbon dust occasionally form from the gas phase near to the star, which are then radially accelerated by radiation pressure in random directions away from the star. If the dust cloud forms in the line of sight it successively eclipses the star and blocks the stellar light. In the late phases of a decline, the dust cloud moves outward and disperses due to radial dilution. The star slowly returns to normal light. This overall picture (sketched in Fig. 1.2) and the fact that it is some form of *carbon* dust which actually condenses is now generally accepted.

All further details, however, e. g. the distance of the dust clouds to the star in the early phases of a decline, the physics and chemistry of the decline phase, the survival of the dust clouds close to the star, the dynamic behavior of dust clouds in the circumstellar envelope etc., are still controversial. Especially so are the physical reasons for the occasional onset of dust formation and for the formation of dust *clouds* rather than spherical dust *shells*. Thus, the whole phenomenon is still waiting for a convincing explanation.

One key towards a better understanding of the RCB decline events is given by the radial distance to the stellar photosphere, where fresh carbon dust condenses from the gas phase. By means of a reliable determination of this quantity, many of the proposed models and scenarios could be ruled out immediately. The distance to R CrB is about 1000 pc and in order to detect a dust cloud with a diameter of one stellar radius, an angular resolution of $\sim 5 \cdot 10^{-4}$ arc-seconds would be required. Therefore, according to the present state of observational techniques this highly controversial quantity cannot be observed directly. However, there exist some indirect observational clues on the nucleation distances, indicating that dust formation occurs rather close to the photosphere:

Temporal evolution of emission lines: During a typical decline event, a rich "chromospheric" emission line spectrum appears, similar to a solar eclipse. A special temporal evolution of three distinguishable classes of emission lines can be observed (see Appendix A). It is natural to suggest that the expanding dust cloud subsequently covers the regions responsible for the line emissions. In this case, the dust cloud must form below these regions. Additionally, the emission lines are apparently less polarized than the continuum (see Appendix A), which supports this scenario. Corresponding observational estimates claim a nucleation distance of $1.5 - 2\,R_*$ (Clayton et al. 1992).

Dust acceleration time scale: In many cases strongly blue shifted ($\gtrsim 200\,\mathrm{km\,s^{-1}}$) absorption lines have been detected just in the beginning of a decline (see Appendix A). Since such blue shifts are only seen in the context of decline events, radiation pressure on dust seems to be responsible for the acceleration of the gas. Accelerations to velocities of a few hundred km/s within a few weeks, however, are only possible rather close to the star, where the radiation flux is sufficiently intense (Whitney et al. 1993), yielding nucleation distances of $4 - 6\,R_*$ (Goeres 1996).

Decline time scale: The initial decline phase typically lasts a few weeks. If the changes of the brightness and the spectra observed during this phase are caused by an optically thick dust cloud, radially expanding and subsequently obscuring the stellar disk, the dust cloud must be located close to the star (Clayton et al. 1992). Only in this case, the tangential projections of the measured radial velocities can be as large as one stellar radius per week. From this argument, Feast (1997) estimates the initial radial distance of the dust cloud to be $\sim 2\,R_*$.

Dust dilution time scale: The recovery phase in late decline is supposed to be a consequence of the dust cloud moving away from the star at a constant velocity while radially diluting. By simultaneous measurement of the expansion velocity (via absorption line blue shifts) and the gradient of light increase, an absolute distance of the cloud can be derived, compatible with nucleation distances of $4-7\,R_*$ (Goeres 1996).

IR flux constancy: The fact that the IR fluxes only show minor changes during the declines can be used to estimate the angular coverage of a single dust cloud (Forrest et al. 1972). The semi–cone angle together with the condition that such a cloud must have at least the size of the stellar disk in order to occult the star, leads to a minimum distance of the dust clouds at the beginning of the declines, which provides an estimate for the nucleation distance of $2.5-6\,R_*$ (Goeres et al. 1996).

Pulsation phase correlation: There is some observational evidence for certain individual objects that the decline events always begin at fixed pulsation phases (e. g. Pugach 1977, Lawson et al. 1992). For such a correlation, a physical connection between the photosphere of the star and the condensation zone with a constant time delay is required. The closer the condensation zone to the star, the more plausible this type of connection appears. The character of this argument is only qualitative.

Although at least one weak link can be found in every chain of the above arguments, the clear common tendency of the observational findings is that dust condensation in RCB envelopes in fact occurs fairly close to the photosphere of the star.

> *The small nucleation distances derived from observations at first sight seem to contradict the basics of dust formation theory.*

According to all known theories (classical nucleation theory, chemical pathway calculations or the modeling of chemical reaction networks) the formation of a solid body demands temperatures well below the sublimation temperature of the considered solid material. This yields lower temperatures than 2000 K under the density conditions present in CSEs for all high temperature condensates (including graphite and SiC). Considering the typical chemical conditions present in the envelopes of RCB stars, temperatures below 1500 K are inevitably required for carbon nucleation (Goeres & Sedlmayr 1992).

In standard models for CSEs (cf. last section), such temperature conditions are only present outside about $11\,R_*$ for $T_{\rm eff} = 7000\,$K. Furthermore, if we ask for the

Table 1.1: Observational and theoretical constraints on the nucleation distance in RCB envelopes. Distances are given in units of stellar radii.

observations		theory	
• temporal evolution and polarimetry of chromospheric emission lines	$1.5 - 2$	• sufficiently low gas temperature for nucleation	$\gtrsim 11$
• dust acceleration time scale	$4 - 6$		
• decline time scale	~ 2		
• dust dilution time scale	$4 - 7$	• sufficiently low dust temperature for dust stability	$\gtrsim 20$
• IR flux constancy	$2.5 - 6$		
• pulsation phase correlation	(close)		

minimum distance required to assure the stability of small carbon dust particles in an optically thin stellar radiation field, the result is about $20\,R_*$ for $T_{\rm eff} = 7000\,$K (Fadeyev 1988). In the case of hot RCB stars with effective temperatures up to 20 000 K, one derives distances as large as $50\,R_*$ and so the problem of nearby dust formation appears to be even more serious.

To summarize Table 1.1, two contradictory points of view can be distinguished. On one hand, the observational astronomers argue for dust formation near to the star on the basis of several supporting, independent scientific findings. On the other hand, theoretical models for dust formation predict large nucleation distances as a consequence of thermodynamic constraints. This obvious conflict between theory and observation traces through the whole literature and constitutes the central problem of the present understanding of the RCB type decline events. Once one accepts that dust formation occurs close to the star, as indicated by observations, there are only two ways out of this dilemma:

(i) There are fundamental errors in the current dust formation theory. Carbon dust can be formed from the gas phase already at temperatures of $3500 - 5000\,$K as present at $2\,R_*$ according to the standard models of CSEs.

or

(ii) There is a mistake in the previous applications of standard dust formation theory to RCB envelopes concerning the temperature determination of the gas. The conventional theories on dust formation are applicable, but have to be discussed in the context of more careful methods for the temperature determination, taking into account the dynamic conditions in the CSEs of RCB stars.

All RCB stars measured thus far seem to be pulsating variables (Lawson & Kilkenny 1996). The pulsation periods are of the order of 40 days and the radial velocity variations at the photosphere range from about $\pm\,3\,\mathrm{km\,s^{-1}}$ to $\pm\,20\,\mathrm{km\,s^{-1}}$ (cf. Appendix A). The stellar pulsation creates shock waves, which further steepen up in the atmosphere and propagate into the CSE (e. g. Bowen 1988, Fleischer et al. 1992). Consequently, a fixed fluid element in the envelope is hit by shock waves time and time again. The shocks dissipate mechanical energy and furthermore initiate a more or less periodical compression and re–expansion of the gas, both of which may cause strong deviations from RE in the gas phase. If, however, one of the three usual assumptions for temperature determination (RE, LTE, grey gas opacities) is abandoned, the radial range of nucleation distances prescribed by observations could easily open up.

1.4 Requirements for Different Approaches of Temperature Determination

The most promising scientific method to gain insight into the complex processes of astrophysical objects is the modeling by full time–dependent computer simulations. The basis of these models is a hydro- and thermodynamic description of the gas, where the physical interactions are formulated in terms of ordinary differential equations which are integrated in time. Besides hydro- and thermodynamics, these models may include radiative transfer, chemistry and dust formation, according to the chosen degree of approximation. Thereby, all the necessary physical and chemical processes can be investigated simultaneously, so that just the complex interplay among these processes can become the main topic of examination. Therefore, computer models can help to build up a higher level of completeness in science.

However, the results of this rather new method of scientific computing cannot be better than our physical understanding of the basic processes involved and our ability to abstract and to simplify. In this context, the "best" description of a physical process under investigation is not necessarily the most accurate and detailed one — but a description, which correctly describes the most important features of the process while using the least amount of resources. Such a description must be sufficiently simple in order to be included in more complex model calculations as part of the investigations of astrophysical objects.

Concerning the temperature determination in the CSEs of pulsating stars (such as Miras and long–period variables on the AGB and RCB stars, Cepheids and RV Tauri stars near to the Instability Strip) the presence of shock waves caused by the stellar pulsation calls for a time–dependent treatment of the thermodynamics. As argued above, strong deviations from RE may occur and the gas temperature structure cannot be obtained by means of radiative transfer calculations alone.

According to the present state of approximation in such models (Bowen 1988, Fleischer et al. 1992, Feuchtinger et al. 1993), the gas temperature structure is calculated as follows. Bowen (1988) first carries out a frequency integrated radiative transfer, using the basic assumptions of RE, LTE and grey gas opacities as described in Sect. 1.2, which determines the instantaneous RE–temperature structure. Secondly, he calculates the current gas temperature by assuming a local relaxation

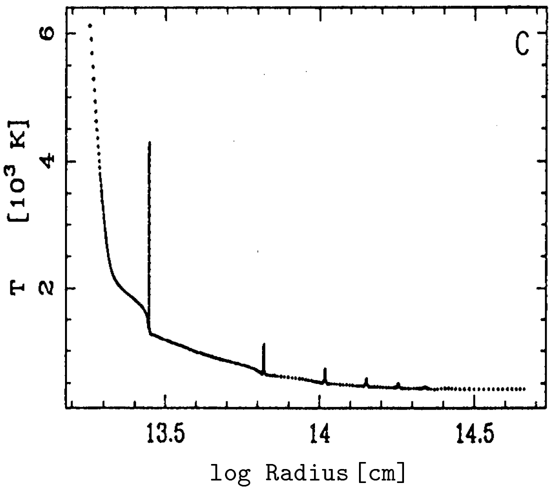

Figure 1.3: Temperature structure adopted from Feuchtinger et al. (1993).

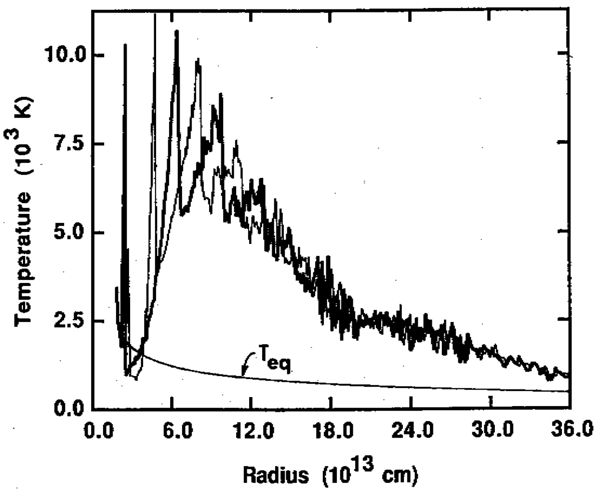

Figure 1.4: Adopted from Bowen (1988)

toward RE at a finite rate. Fleischer et al. (1992) consider the isothermal limiting case, assuming that the gas instantaneously relaxes to RE everywhere in the envelope. Applying radiation hydrodynamics, Feuchtinger et al. (1993) use an approach, which is similar to Bowen's, but more consistent. In order to treat the thermodynamics in these models, the total net heating rate due to radiative gains and losses, $Q_{\rm rad}$, is an important ingredient. $Q_{\rm rad}$ vanishes in RE and otherwise determines the time scale for relaxation toward RE.

Concerning the calculation of $Q_{\rm rad}$ in the models cited above, crucial assumptions have been made (LTE or, in contrast, $Q_{\rm rad} \propto \rho^2$), yielding simple analytical expressions for $Q_{\rm rad}$. But depending on which of these assumptions is applied, the gas temperature structure turns out to be quite different. In the LTE case, the calculated radiative heating/cooling rates are very efficient, resulting in gas temperatures usually very close to the RE–temperature structure except for some thin gas temperature peaks at the locations of the shock fronts (cf. Fig. 1.3). In contrast, at small densities in the $Q_{\rm rad} \propto \rho^2$ case, rather broad regions of enhanced gas temperatures behind the shocks are produced, almost entirely decoupled from the RE–temperature structure (cf. Fig. 1.4). These results are typical examples for shock waves of predominantly "isothermal" or predominantly "adiabatic" character, respectively. The resulting gas temperature structure affects all other results of these model calculations, e. g. the mass loss rate, and even the model stability (Wood 1979). An important feedback between the gas temperature structure and the dynamics of these envelopes is given by the condensation of seed particles from the gas phase (nucleation), which is very sensitive to the gas temperature. It triggers the further evolution of the dust component and hence the acceleration of the gas due to radiation pressure on dust grains (Fleischer et al. 1991).

Considering the determination of $Q_{\rm rad}$ in other astrophysical environments extensive model calculations have been made for stationary plane-parallel shocks, e. g. in the interstellar medium, where all physical properties are purely determined by the distance from the shock front, but are not explicitly time–dependent (Hollenbach & McKee 1979, Fox & Wood 1985, Hollenbach & McKee 1989, Gillet & Lafon 1989, Neufeld & Hollenbach 1994). This situation allows for a very accurate physical description, including non–LTE ionization, non–equilibrium chemistry and radiative transfer. However, this scheme cannot be easily applied to the time–dependent models for pulsating stars for essentially two reasons. First, the shocks in the envelopes of pulsating stars are not stationary (e. g. a fixed fluid element will start to re–expand after it has been compressed by an propagating shock as opposed to the stationary situation) and second, the detailed description given in the papers cited above is much too elaborate to be included within time–dependent hydrodynamic models, at least at the present state of computer speed.

Thus, there is a great need for a realistic calculation of $Q_{\rm rad}$. On the one hand, it must be physically based on the relevant heating and cooling processes, taking into account important features such as the non–LTE population of excited states or radiative trapping. On the other hand, it must be sufficiently simple to be included in time–dependent hydrodynamic models.

1.5 Aim and Structure of this Work

The basic aim of this work is to gain more theoretical insights on the temperature structure of circumstellar envelopes, especially those of pulsating stars, where shock waves propagate through the envelopes. This work focuses on the problem of theoretical temperature determination in a *given* radiation field — radiation transfer calculations are explicitly not considered and are not performed.

For this purpose, the radiative heating and cooling of the gas in circumstellar envelopes is investigated from the very beginning, examining densities from 10^5 to $10^{14}\,\mathrm{cm}^{-3}$. Preceding studies in the literature are usually not applicable in this density range typical for CSEs. However, there is detailed knowledge available at both extremes of this density interval. For large densities, extensive calculations of gas absorption coefficients in stellar atmospheres exist which, in case of LTE, determine the net radiative heating rate. At low densities, the important radiative heating and cooling processes are known from studies of interstellar clouds and interstellar shock waves. This work derives advantages from both and intends to close the gap between these density limits.

Due to the time–dependent conditions present in CSEs of pulsating stars, the determination of the temperature stratification must involve time–dependent hydrodynamic model calculations. The possibility of a fast and proper inclusion of the calculated heating and cooling rates into hydrodynamic models is an essential constraint for these investigations. It is the aim of this work to lay the foundations for a more reliable treatment of the time–dependent thermodynamics in such hydrodynamic model calculations.

Although dust formation is rarely discussed in this work explicitly, the work is guided by the certainty that the formation of solids in CSEs requires large densities and very special temperature conditions. The question, which always stands behind the investigations and is the basic motivation for this work is:

Where in the envelope such thermodynamic conditions may occur?

The work is organized as follows:

Chapter 2 describes the basic concept for the treatment of the time–dependent thermodynamics. The level of approximation for this work is fixed and the internal energy of the gas is defined according to the basic assumption of steady–state non–LTE.

Chapter 3 contains the calculations of the various heating and cooling rates considering arbitrary radiation fields. Computational methods are developed which include the important effects of non–LTE and of optical thickness in spectral lines. Due to the wide temperature range to be considered, a variety of different radiative processes is investigated: rotational and ro–vibrational transitions of polar molecules and of H_2; line transitions of neutral atoms and ions; bound–free transitions; free–free transitions and photochemical reactions. Special attention is paid to which kind of atomic and molecular data has to be known for a reliable determination of the corresponding rates. A short list of radiative processes, which have not been considered so far, but might be of further interest for the heating and cooling of the gas, completes the theoretical part of this work.

Chapter 4 outlines some common features for the following applications. The technical details of the calculation of the various particle concentrations and the internal energy of the gas are explained. The particle concentrations and the state of the gas are determined from the element abundances ϵ_i, the mass density ρ of the gas, its temperature $T_{\rm g}$, and the continuous radiation field J_ν.

In the following chapters, three applications of the theoretical methods are presented:

Chapter 5 examines the topology of the radiative equilibrium temperature solutions in the CSEs of RCB stars. It is shown that the condition of radiative equilibrium may not be unique, but can have two or more stable temperature solutions. These "thermal bifurcations", in principle, allow for a spatial coexistence of hot and cool phases in the circumstellar envelope.

Chapter 6 investigates the relaxation towards radiative equilibrium, especially in response to propagating shock waves. For this purpose, radiative cooling time scales for a carbon–enriched gas typical for C–stars are calculated as function of gas density and temperature. The importance of the different heating/cooling processes is discussed and the most efficient process in the various density and temperature regions is determined. The results of the cooling time scales are compared to those derived from formerly applied analytical heating/cooling functions in previous research. The character of the thermal relaxation of the gas after the passage of shock waves is discussed, providing new fuel to the controversy about whether the shocks in CSEs behave predominantly "isothermally" or "adiabatically".

Chapter 7 again considers RCB stars. A physical mechanism is presented, which may be essential for the occasional onset of dust formation in the circumstellar envelopes of pulsating RCB stars. A model for fixed fluid elements, which are periodically hit by strong shock waves produced by the stellar pulsation, is developed and the thermal energy balance, the chemistry and the nucleation in such fluid elements, are investigated. According to this model, the preconditions for effective carbon nucleation may be temporarily present quite near to the photosphere of a pulsating RCB star, despite their high effective temperatures. Thus, this work might bridge the gap between observations and theory concerning RCB stars as outlined in Sect. 1.3.

Chapter 8 summarizes the results and presents the conclusions of this work.

Appendix A gives an overview of the current status of observational knowledge on the fascinating class of RCB stars and summarizes previous models. This Appendix provides an important background for the investigations in Chapter 5 and 7.

Chapter 2

The Thermodynamic Concept

This chapter intends to state the basic assumptions of this work and to clarify the meaning of some terms frequently used.

The central physical quantity of this work is the temperature of the gas. The velocity distribution of the gas at rest is assumed to be given by a unique Maxwellian distribution, characterized by a single kinetic temperature, which is henceforth called the "gas temperature" and denoted by T_{g}. Differences in the kinetic temperatures of different kinds of particles (e. g. electrons and atoms) are neglected. The processes responsible for the relaxation towards the Maxwellian distribution are elastic collisions which distribute the total translational energy present among the gas particles. The corresponding relaxation time scale is assumed to be considerably shorter than any other time scale inherent in the physical system under investigation. With regard to this relaxation, the most critical process is the equalization of the translational energies between light and heavy particles, because of the inefficient energy transfer rates of such collisions. For conditions in stellar atmospheres, Mihalas & Weibel Mihalas (1984, see p. 29 and p. 387 for a more comprehensive discussion) arrive at the conclusion that the existence of a unique Maxwellian can safely be assumed.

2.1 First Law of Thermodynamics and Equation of State

The aim of this work is to develop a time–dependent method for temperature determination based on the first law of thermodynamics

$$dE = \delta\mathcal{Q} + \delta\mathcal{W} \quad . \tag{2.1}$$

Equation (2.1) states that the change of internal energy dE is given by the amount of heat transfered to the gas $\delta\mathcal{Q}$ (counted positive for gains) plus the work done to the gas $\delta\mathcal{W}$ (counted positive when the surroundings deliver work to the gas).

How are the gas temperature and the internal energy related to each other? The answer of this questions seems to be trivial (given by the well–known caloric equation of state), but in fact deserves some further discussion for diluted gases under astrophysical conditions. Besides the translational degrees of freedom, a real gas – consisting of neutral atoms, electrons, ions and molecules – has additional possibilities to store energy, which are henceforth called "the pools of energy". The population of excited electronic, vibrational and rotational states represent such pools. Furthermore, energy is stored in potential form according to the binding forces between electrons and atoms (ionization potential) and between the constituting atoms of molecules (dissociation potential). Consequently, the internal energy of the gas is defined as

$$e = \frac{1}{\rho}\left(E_{\rm trans} + E_{\rm ion} + E_{\rm diss} + E_{\rm el} + E_{\rm vib} + E_{\rm rot}\right) \tag{2.2}$$

The details of the evaluation of the various energy terms are stated in Chapter 4 (Eq. 4.1 – 4.6). In case of Local Thermodynamic Equilibrium (LTE), the relationship between the gas temperature $T_{\rm g}$ and the internal energy e is well–defined. The degree of ionization, the concentration of the molecules and the population of the excited levels can be determined by means of Saha equations, the law of mass action and Boltzmann distributions, respectively. All energy terms in Eq. (2.2) can be calculated straightforwardly, yielding $e = e(\rho, T_{\rm g})$ or, more generally, e as function of any suitable set of two local state variables.

2.2 LTE and Non–LTE

Considering the diluted gases in CSEs, however, LTE is not valid. Radiative processes alter the state of the gas in various ways. Figure 2.1 sketches this situation. The gas is represented by the big grey box, containing the internal pools of energy. The gas interacts with the radiation field via the exchange of photons and with the dust component, e. g. via inelastic collisions. At the same time, internal processes (grey arrows) redistribute the total internal energy among the various degrees of freedom of the gas. Work can be done to the gas $\delta\mathcal{W} = -p\,dV$ as indicated by the arrow on the l.h.s in the figure and the gas may exchange heat with its surroundings (not shown). Examples for the such processes are heat conduction, viscous processes and shock dissipation.

The radiative processes generally drive the gas away from LTE[1], whereas the internal processes (processes not involving photons or dust grains, that is) drive the gas toward LTE. In general, the energy transport between the radiation field and the translational energy pool is indirect, so to speak, because a transmitting state is involved. Usually, a two–step process is required, for example a collisional ionization followed by radiative recombination or the absorption of a photon followed by collisional de–excitation[2]. These transmitting states (e. g. the excited electronic states of the atoms) are considerably affected by the radiation field and hence, the state of the gas cannot be calculated by thermodynamic considerations.

Thus, a non–LTE treatment for the diluted gases in CSEs is required. Balancing the gains and losses by all collisional, radiative and chemical processes, the change

[1]Except for the case that the radiation field exactly equals a Planckian of the gas temperature.

[2]Direct links between the radiation filed and the translational energy pool do also exist, but are usually less important, e. g. free–free emission (bremsstrahlung).

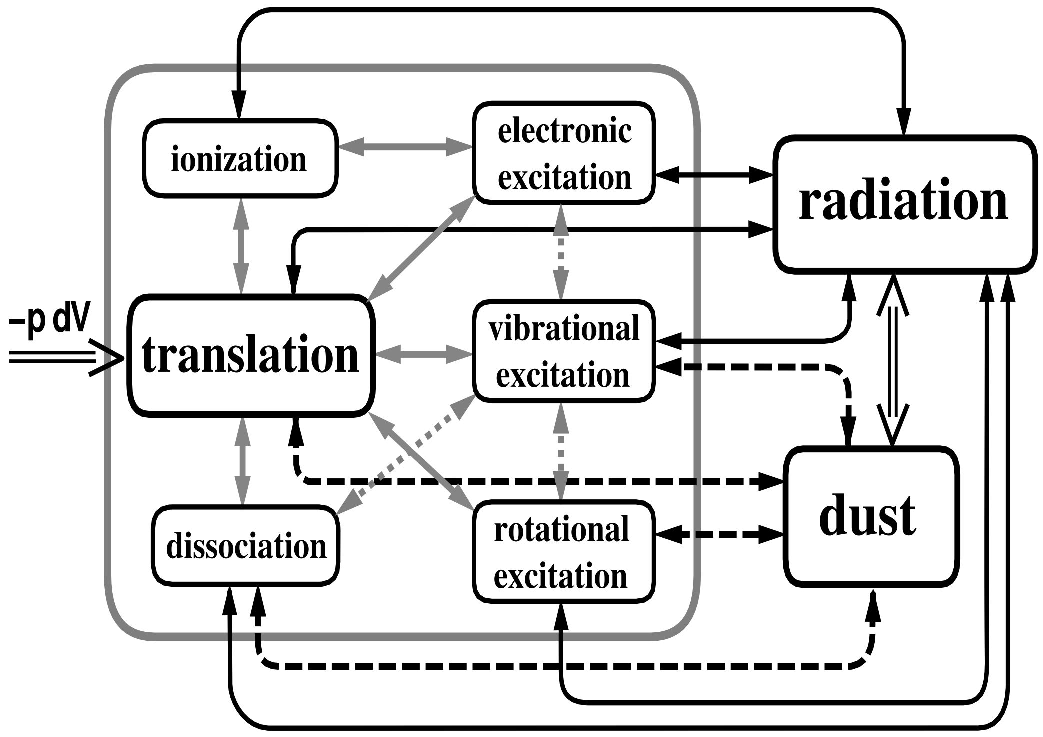

Figure 2.1: The pools and fluxes of energy. Black full arrows indicate energy fluxes via photons. From top to bottom: photoionization/radiative recombination; bound–bound, free–free, vibrational and rotational emission/absorption; photodissociation/radiative association. Black dashed arrows show energy exchange rates between dust and gas (via collisions and surface chemical reactions). Full grey arrows represent “internal” energy fluxes via collisional (de-)excitation or particle creation/destruction, respectively. Dotted grey arrows show additional examples of internal energy fluxes not explicitly considered in this work, such as pumping by fluorescence, ro–vibrational pumping or the excitation of vibrational states via chemical reactions.

of the particle density n_i^j of chemical species i in quantum state j can be expressed by (e. g. Mihalas & Weibel Mihalas 1984, p. 389)

$$\rho\,\frac{d(n_i^j/\rho)}{dt} \;=\; \sum_{\{kl\}\neq\{ij\}} n_k^l\,R_{k\to i}^{l\to j} \;-\; n_i^j \sum_{\{kl\}\neq\{ij\}} R_{i\to k}^{j\to l} \quad . \tag{2.3}$$

Diffusion processes are neglected in Eq. (2.3) and d/dt denotes the Lagrangian derivative with respect to time, considering a comoving-moving frame. The rate coefficient $R_{i\to k}^{j\to l}$ [Hz] denotes the total rate of all collisional, radiative and chemical processes which destroy a particle of species i in state j and create a particle of species k in state l. For simple collisional, absorption or emission processes we have $i=k$. For chemical processes ($i\neq k$), the quantum indices j and l usually refer to the ground state. The rate coefficients may contain further particle densities (collision partners or chemical reactants) or the radiation field J_ν, depending on which type of process is considered. The rate coefficients will be quantified in Chapter 3.

2.3 Steady State

If the gas is exposed to static outer conditions (radiation field, properties of the dust component, volume etc.), the gas will relax towards a *steady state*[3], i. e. the concentrations of all species in all quantum states become time–independent

$$\frac{d(n_i^j/\rho)}{dt} = 0 \quad . \tag{2.4}$$

In case of a steady state the l.h.s of Eq. (2.3) vanishes. The particle densities can be calculated by solving the coupled algebraic equations of type Eq. (2.3) for all species and states under investigation. The results are time–independent and can formally be expressed by

$$n_i^j = n_i^j(\rho, T_{\rm g}, J_\nu) \quad , \tag{2.5}$$

Consequently, the caloric equation of state (2.2) of the gas writes as $e=e(\rho, T_{\rm g}, J_\nu)$. Therefore, in addition to the two local state variables sufficient in LTE, the radiation field occurs as additional external parameter for the determination of the particle densities and the equation of state[4,5]. The resulting steady state of course differs from LTE in general. In the limiting case of large densities, however, where the internal (e. g. collisional) processes dominate, LTE is valid and the dependency on J_ν disappears.

[3]Other terms used in the literature are "kinetic equilibrium" or "statistical equilibrium".

[4]In Chapter 3 it will be stated that another external parameter enters into the determination of the steady state, which is the mean local velocity gradient $\langle\frac{dv}{dl}\rangle$. This parameter is involved in the calculation of the rate coefficients for bound–bound transitions concerning optically thick lines. However, the influence of this parameter is small.

[5]The influence of the dust component on the state of the gas is neglected in Eq. (2.5)

The condition of a static environment can be relaxed to some extend concerning those time–dependent situations where the changes of the outer conditions occur *slowly*. In this case the gas rapidly accommodates to the varying environment. This work assumes that this accommodation in fact occurs instantaneously:

> *The internal relaxation of the gas toward steady state is assumed to occur on a short time scale compared to the changes of the outer conditions.*

In this case, a caloric equation of state exists, as stated above, although the gas is not in LTE. A thermodynamic description of the gas is appropriate[6]. Of course, the

[6]Considering the excited electronic states of atoms and ions, the relaxation time scale is given by the radiative lifetimes of the levels at small densities and is even shorter at large densities. Allowed electronic transitions have radiative lifetimes of typically 10^{-8}s, but actually the slowest rate within the level system decides upon the relaxation time toward a complete steady state, which can be as large as 10^{2}s for the meta–stable levels included in this work. The radiative lifetimes of the vibrational and rotational levels of polar diatomic molecules are found to be typically $10^{-2}-10^{1}$s. These time scales are to be compared to typical hydrodynamic time scales, which for the CSEs of pulsating stars are approximately given by one pulsation period, which is about 10^{7}s for Miras and 10^{6}s for RCB stars. Hence, the relaxation of the electronic, vibrational and rotational states can be assumed to be fast.

Considering the relaxation towards ionization equilibrium (balance between ionization and recombination rates), the corresponding time scales are very different. If photoionization dominates, e. g. considering the case $J_\nu = B_\nu(7000\,K)$, the relaxation time scales are found to be $10^{-1}-10^{1}$ s for all atoms under investigation, independent of density and temperature. If collisional ionization dominates, the relaxation time scale strongly depends on the density. In the case $J_\nu = B_\nu(3000\,K)$ the relaxation lasts $\sim 10^{4}$ s at a density of $10^{13}\,\mathrm{cm}^{-3}$, $\sim 10^{6}$ s at $10^{9}\,\mathrm{cm}^{-3}$ and $\sim 10^{9}$ s at $10^{5}\,\mathrm{cm}^{-3}$, concerning low temperatures. If the temperature is high enough to cause considerable collisional ionization, the relaxation time scale becomes much shorter. Hence, the relaxation of the degree of ionization is fast in those cases, where is it important for the calculation of the radiative heating/cooling rates, but can exceed the hydrodynamic time scales otherwise.

The chemical processes usually introduce the largest time scales to the gas (disregarding dust formation processes). The chemical relaxation time scales can indeed exceed hydrodynamic time scales in CSEs (e. g. Beck et al. 1992). However, the chemical processes themselves do not provide first order radiative heating and cooling rates — the most important heating and cooling processes usually involve the degrees of freedom discussed above, which can be assumed to be populated according to a steady state.

Thus, one has to conclude that the relaxation of the gas in CSEs towards its steady steady may not always be complete. A full time–dependent non–LTE approach would be required for a more accurate modeling of the gas. In this case, the first law of thermodynamics has to be applied to the translational energy alone $e = E_{\rm trans}/\rho$. A caloric equation of state does not exist in the usual sense or becomes obsolete. One has to determine the internal energy distribution processes in this case, e. g. how much translational energy is consumed or liberated during a chemical reaction. A time–dependent treatment of ionization and chemistry within hydrodynamic models seems to be out of question, at least at the current state of computer speed. This would introduce a large number of new (stiff) differential equations to the usual set of hydrodynamic equations to be solved, which requires much more computational efforts. However, the possibility to include the results of this work into such calculations is regarded as essential, concerning future investigations. Therefore, the assumption of a steady state is made nevertheless. It represents an appropriate *compromise* between accuracy and expense: it accounts for the most important non–LTE effects, but keeps things simple enough for a thermodynamic description compatible to hydrodynamic calculations. For a further discussion of this topic, see Mihalas & Weibel Mihalas (1984, p. 386–396) particle densities can only be determined, if the radiation field is known; that is, there are as many new external parameters as are required to specify J_ν. However, the circumstellar envelopes are optically thin by definition, maybe except for some strong spectral lines. The radiation field is mainly provided by external sources, eventually modified by dust in the CSE, which is also considered as "external". Therefore, it seems appropriate to prescribe the radiation field in CSEs (e. g. by a radially diluted photospheric radiation field) or to use the results of radiative transfer calculations concerning the dust component. The gas itself is not, or at least not much, responsible for the radiation field. Therefore, the non–LTE radiative transfer problem decouples in CSEs (in contrast to the situation in stellar atmospheres) and the thermodynamic behavior of the gas can be studied in the proposed way.

The first law of thermodynamics Eq. (2.1) is further specialized in the following. According to the definition of the internal energy (cf. Eq. 2.2), the internal energy transfer rates do not cause any heating or cooling, since they only transfer energy from one internal pool to another (cf. Fig. 2.1). The net heating rate $\widehat{Q} = \delta\mathcal{Q}/dt$ is given by the sum of energy fluxes from the remaining external pools (the radiation field and the dust, that is) to the gas. Let $\widehat{Q}_{\rm rad}$ denote the total net heating rate per unit mass and time due to radiative processes, which is given the amount of net absorbed photon energy, and $\widehat{Q}_{\rm dust}$ the total net heating caused by the presence of dust grains. Disregarding other heating/cooling mechanisms as heat conduction, convection and viscous processes, which are usually negligible at the low densities in CSEs, the first law of thermodynamics writes

$$\frac{de}{dt} = -p\,\frac{dV}{dt} + \widehat{Q}_{\rm rad} + \widehat{Q}_{\rm dust} \quad , \tag{2.6}$$

p is the gas pressure and $V = 1/\rho$ the specific volume. The gas temperature can be regarded as an implicit result of the solution of Eq. (2.6), inferred from the caloric equation of state.

The main task of the following Chapter 3 will be to quantify all the important internal and external rates, as far as possible. By means of these rates, the steady state of the gas is determined. The net radiative heating rate $\widehat{Q}_{\rm rad}$ is a kind of useful byproduct of these calculations.

As a consequence of the steady–state assumption, the internal energy and the net heating function are entirely determined by means of local physical quantities, which are readily available in hydrodynamic model calculations. It is hence possible to tabulate $\widehat{Q}_{\rm rad}$ and e as function of two state variables, say ρ and $T_{\rm g}$, and a suitable parametric specification of J_ν. Thus, it is guaranteed that the proposed time–dependent method of temperature determination can be included in hydrodynamic model calculations with regard to future investigations.

Chapter 3

Radiative Heating and Cooling

The determination of the total radiative heating/cooling rate of the gas in CSEs requires a quantitative analysis of all radiative processes occurring in the considered fluid element — a difficult and principally infinite task. What is feasible, however, is the investigation of the *most important* heating and cooling processes, mainly relying on the experience of preceding studies.

From stellar atmosphere calculations it is generally known, that bound–free transition usually are the primary cause for the shape and the magnitude of the absorption coefficient (e. g. Unsöld 1968) and hence for the heating and cooling of the gas. The additional consideration of line transitions ("line blanketed" models) is only a second–order–effect in this context[1]. In predominantly neutral stellar atmospheres, the bound–free transitions of H^- are important. Below about 3500 K, molecules enter into competition and soon dominate the absorption coefficient by their electronic bands, vibrational and rotational spectra, especially those molecules with permanent dipole moment (Jørgensen 1994).

Concerning interstellar conditions, Hollenbach & McKee (1979, 1989) pointed out that forbidden fine–structure lines, meta-stable transitions and some low–lying permitted line transitions of the various neutral and singly ionized metal atoms often provide the dominant cooling mechanism for a shocked non–molecular gas. If present, polar molecules contribute by their large amount of allowed vibrational and rotational line transitions. Bound–free transitions (mainly of hydrogen), Lyα and Hα are important at temperatures $T \gtrsim 8000$ K, especially for large densities.

Reviewing these experiences, it is important to tackle at least all the heating and cooling processes mentioned above in order to unify the picture of important heating/cooling rates for CSEs. A general theoretical description must be developed which is applicable to both, stellar atmospheres as well as interstellar density conditions.

In the following the *net heating rate* of one particular radiative process and its reverse process is always discussed simultaneously, which is different from other approaches concerning interstellar matter (e. g. Spitzer 1978), where the heating and cooling rates are usually discussed strictly apart.

[1] This statement refers to a static atmosphere, where self shielding diminishes the influence of spectral lines — the effects of lines in a moving medium may be larger by orders of magnitude

3.1 Bound–Bound Transitions

The most basic form of interaction between matter and radiation field is given by the absorption and emission of line photons. In this section, a general theoretical method for the calculation of the heating/cooling rate of an arbitrary N–level–system of bound states is presented. The method is applicable to line transitions of atoms and ions, to vibrational and rotational transitions of molecules and also to quadrupole transitions of H_2. It has the following features:

a) The calculation of the level population is performed under the assumption of steady-state non–LTE. It is absolutely necessary to consider non–LTE under the density conditions present in circumstellar envelopes, especially for allowed atomic transitions.

b) Compared to interstellar conditions, the high densities encountered in circumstellar envelopes may cause large optical depths in the lines, which significantly change the heating/cooling rates due to radiative trapping. These effects are tackled by applying an escape probability method.

c) Since propagating shock waves may be present in the circumstellar envelopes of pulsating stars, large velocity gradients occur. In contrast to steady, plane–parallel shocks (e. g. in the ISM), the explicit time–dependence and the geometry of the flow requires a different method to calculate the escape probabilities as outlined by Hollenbach & McKee (1979). This work uses the Sobolev theory in case of spherical symmetry.

d) Line absorption is completely taken into account. The intense continuous radiation field in circumstellar envelopes changes the cooling rates significantly and can in fact lead to net line heating — in contrast to interstellar conditions.

3.1.1 Escape Probability Method for an N–Level–System without Continuum

An atomic or molecular N–level system is considered. The quantity to be determined is the total rate of energy which is transferred to/from the radiation field via line emission/absorption. This total energy transfer rate is calculated in two steps. First, the level populations n_i are calculated by means of the statistical equations ("steady state non–LTE") and secondly, the energy transfer rate is determined. The statistical equations are given by

$$n_i \sum_{j \neq i} R_{ij} = \sum_{j \neq i} n_j R_{ji} \quad , \tag{3.1}$$

and can be solved together with the equation for the conservation of the total particle density of the considered species $n_{\rm sp} = \sum_i n_i$. The rate coefficients are defined by

$$R_{ul} = A_{ul} + B_{ul}\overline{J}_{ul} + C_{ul} \tag{3.2}$$

$$R_{lu} = B_{lu}\overline{J}_{ul} + C_{lu} \quad , \tag{3.3}$$

where u and l label an upper and lower level, respectively. The rate coefficients for stimulated emission B_{ul} and absorption B_{lu} can be calculated from those for spontaneous emission A_{ul} by applying the Einstein relations. Similarly, the rate coefficients for collisional excitation C_{lu} can be calculated from those for collisional excitation C_{ul} by applying a detailed balance relation:

$$B_{ul} = \frac{c^2}{2h\nu_{ul}^3}\,A_{ul} \tag{3.4}$$

$$B_{lu} = \frac{g_u}{g_l}\,B_{ul} \tag{3.5}$$

$$C_{lu} = \frac{g_u}{g_l}\,C_{ul}\,\exp\left(-\Delta E_{ul}/kT_{\rm g}\right) \tag{3.6}$$

The frequency integrated mean intensity

$$\overline{J}_{ul} = \frac{1}{4\pi}\iint \phi_{ul}(\nu,\mu) I_\nu(\mu)\,d\nu\,d\Omega \tag{3.7}$$

is not solely given by the incident continuous intensities $I_\nu^{\rm inc}(\mu)$ (which are regarded as known), but is modified by line emission and absorption in the considered resonance region itself, which becomes important for optically thick lines. An exact solution of this problem can only be achieved by frequency dependent non–LTE radiative transfer calculations in the moving medium, which goes far beyond the scope of this work. Fortunately, there are approximate escape probability techniques available, which can account for the most important resonance effects. This work uses the Sobolev approximation in the case of spherical symmetry (e. g. Puls & Hummer 1988, for a detailed description see Woitke 1992)[2]:

$$\overline{J}_{ul} = P^{\rm e}_{ul}\,J^{\rm cont}_{\nu_{ul}} + (1-P^{\rm e}_{ul})\,S^{\rm L}_{ul} \tag{3.8}$$

$$J^{\rm cont}_{\nu_{ul}} = \frac{1}{4\pi}\int I^{\rm inc}_{\nu_{ul}}(\mu)\,d\Omega \tag{3.9}$$

$$S^{\rm L}_{ul} = \frac{2h\nu_{ul}^3}{c^2}\left(\frac{g_u n_l}{g_l n_u} - 1\right)^{-1} \tag{3.10}$$

$$P^{\rm e}_{ul} = \frac{1}{4\pi}\int \frac{1-\exp\left(-\tau^{\rm S}_{ul}(\mu)\right)}{\tau^{\rm S}_{ul}(\mu)}\,d\Omega \tag{3.11}$$

$$\tau^{\rm S}_{ul}(\mu) = \frac{c^3 A_{ul}}{8\pi\nu_{ul}^3}\left(\frac{g_u}{g_l}n_l - n_u\right)\left|\frac{dv_\parallel}{dl}(\mu)\right|^{-1} \tag{3.12}$$

$$\frac{dv_\parallel}{dl}(\mu) = \left(1-\mu^2\right)\frac{v}{r} + \mu^2\,\frac{\partial v}{\partial r} \tag{3.13}$$

$P^{\rm e}_{ul}$ is the mean escape probability and $S^{\rm L}_{ul}$ the line source function. $J^{\rm cont}_{\nu_{ul}}$ is the continuous mean intensity at line center frequency caused by incident radiation ignoring radiation transfer effects in the considered resonance region itself.

[2] A discussion of the applicability of Sobolev theory to the shocked envelopes of pulsating stars is given on p. 28.

$J^{\rm cont}_{\nu_{ul}}$, in principle, results from the calculation of a continuous radiative transfer (without the considered line). For simplicity, the incident intensities are assumed to be isotropic in Eq. (3.8)[3]. $\tau^{\rm S}_{ul}$ is the so–called Sobolev optical depth of the line and $\frac{dv_\parallel}{dl}$ the velocity gradient on a considered ray. The following approximation is used in order to avoid the elaborate and time–consuming integration over the solid angle in Eq. (3.11): An appropriate mean velocity gradient $\left\langle\frac{dv}{dl}\right\rangle$ is defined and the escape probabilities are calculated according to

$$\left\langle\frac{dv}{dl}\right\rangle = \frac{1}{3}\left|\frac{\partial v}{\partial r}\right| + \frac{2}{3}\left(2\,x_0^{-1/2}-1\right)\left|\frac{v}{r}\right| \tag{3.14}$$

$$x_0 = 1+\max\left\{0,-\frac{\partial v}{\partial r}\Big/\frac{v}{r}\right\} \tag{3.15}$$

$$\widetilde{\tau}^{\rm S}_{ul} = \frac{c^3 A_{ul}}{8\pi\nu_{ul}^3}\left(\frac{g_u}{g_l}n_l - n_u\right)\left\langle\frac{dv}{dl}\right\rangle^{-1} \tag{3.16}$$

$$\widetilde{P}^{\rm e}_{ul} = \frac{1-\exp\left(-\widetilde{\tau}^{\rm S}_{ul}(\mu)\right)}{\widetilde{\tau}^{\rm S}_{ul}} \quad , \tag{3.17}$$

The error of this procedure vanishes for the two important cases $P^{\rm e}\to 0$ and $P^{\rm e}\to 1$ and reaches a maximum value of 33% around $P^{\rm e}\approx 0.5$. Different flow geometries and cases with vanishing velocity gradients can be tackled by using different expressions for $\left\langle\frac{dv}{dl}\right\rangle$ in Eq. (3.14) as summarized in Neufeld & Kaufman (1993).

For the numerical solution of the statistical equations (3.1) it is very advantageous to eliminate the unknown line source functions $S^{\rm L}_{ul}$. It is straight forward to show that

$$n_u A_{ul} + (n_u B_{ul} - n_l B_{lu})\,\overline{J}_{ul} = n_u A_{ul}\widetilde{P}^{\rm e}_{ul}\left(1-\frac{J^{\rm cont}_{\nu_{ul}}}{S^{\rm L}_{ul}}\right) \tag{3.18}$$

$$= A_{ul}\widetilde{P}^{\rm e}_{ul}\left(n_u\,(1+j_{ul}) - n_l\frac{g_u}{g_l}j_{ul}\right) \tag{3.19}$$

where $j_{ul} = c^2/(2h\nu_{ul}^3)\,J^{\rm cont}_{\nu_{ul}}$ is a dimensionless quantity which characterizes the local continuous radiation field. By means of Eq. (3.19) all above equations can be combined into the following set of effective rate coefficients

$$\widetilde{R}_{ul} = A_{ul}\widetilde{P}^{\rm e}_{ul}\,(1+j_{ul}) + C_{ul} \tag{3.20}$$

$$\widetilde{R}_{lu} = \frac{g_u}{g_l}\left(A_{ul}\widetilde{P}^{\rm e}_{ul}\,j_{ul} + C_{ul}\exp\left(-\frac{\Delta E_{ul}}{kT_{\rm g}}\right)\right) \quad . \tag{3.21}$$

The level populations can now be calculated by solving Eq. (3.1) with $\widetilde{R}_{ij}$ instead of R_{ij}, where the line source functions do not appear anymore.

[3]Strictly speaking, the influence of incident continuous radiation increases or decreases compared to Eq. (3.8), if the considered fluid element mainly receives the light from a particular direction, where the velocity gradient is smaller or larger than the mean velocity gradient, respectively: the effect of the incident intensities is proportional to the escape probability in that particular direction, but the (isotropic) re-emission is proportional to the mean escape probability.

Finally, after having determined the level populations, the net heating rate can readily be calculated either from

$$Q_{\rm coll} = \sum_l \sum_{u>l} \Delta E_{ul} C_{ul} \left(n_u - n_l \frac{g_u}{g_l} \exp\left(-\frac{\Delta E_{ul}}{kT_{\rm g}} \right) \right) \tag{3.22}$$

or by multiplying the radiative rate in Eq. (3.18) by $-\Delta E_{ul}$ and summing up the contributions from all transitions:

$$Q_{\rm rad} = \sum_l \sum_{u>l} \Delta E_{ul} n_u A_{ul} \widetilde{P}^{\rm e}_{ul} \left(\frac{J^{\rm cont}_{\nu_{ul}}}{S^{\rm L}_{ul}} - 1 \right) \tag{3.23}$$

$$= \sum_l \sum_{u>l} \Delta E_{ul} A_{ul} \widetilde{P}^{\rm e}_{ul} \left(n_l \frac{g_u}{g_l} j_{ul} - n_u \left(1+j_{ul}\right) \right) \tag{3.24}$$

Both expressions are equivalent and must yield the same result ($Q_{\rm coll}=Q_{\rm rad}$), since the gains and losses from the translational and the radiative pool (the only considered source terms) balance each other (cf. Fig. 2.1). This equality demonstrates the physical meaning of the basic assumption of steady state: A fast relaxation of the degree of excitation of the considered species is assumed such, that $Q_{\rm coll} = Q_{\rm rad}$ is assured. Equation (3.23) shows the modifications from the usual expression $-\sum \Delta E_{ul} n_u A_{ul}$ caused by optical thickness and incident continuous radiation (note however that the level populations are also affected).

3.1.1.1 Numerical Iteration Scheme

The solution of the statistical equations still requires an iteration, since the escape probabilities depend on the level populations. In most cases, a direct λ–iteration converges rapidly, but there are also cases in which this procedure fails. The following scheme, which may be called a decelerated λ–iteration, converges for all considered model atoms under all considered density–, temperature– and radiation field–conditions, where $X(it)$ means quantity X at iteration step it:

1. Put $\tilde{\tau}^{\rm S}_{ul}(0) = 0$; $\widetilde{P}^{\rm e}_{ul}(0) = 1$; $Q_{\rm rad}(0) = 10^{99}$.
2. Calculate $\widetilde{R}_{ul}(it)$ and $\widetilde{R}_{lu}(it)$ according to Eqs. (3.20) and (3.21).
3. Determine $n_j(it)$ from the statistical equations (3.1).
4. Calculate $Q_{\rm coll}(it)$ and $Q_{\rm rad}(it)$ according to Eqs. (3.22) and (3.24).
5. Define $\delta = |1 - Q_{\rm rad}(it)/Q_{\rm rad}(it-1)|$.
6. Calculate $\tilde{\tau}^{\rm S}_{ul}$ according to Eq. (3.16).
7. Put $\tilde{\tau}^{\rm S}_{ul}(it) = \tilde{\tau}^{\rm S}_{ul}(it-1) + [\tilde{\tau}^{\rm S}_{ul} - \tilde{\tau}^{\rm S}_{ul}(it-1)] \cdot \exp(-\max\{0, (it-30)/10\})$.
8. Calculate $\widetilde{P}^{\rm e}_{ul}(it)$ from Eq. (3.17).
9. Go back to step 2 unless $\delta < 10^{-10}$.
10. Take $Q_{\rm rad}$ as final result, if the population is close to LTE — otherwise rely on $Q_{\rm coll}$ (to avoid the errors produced by the subtraction of large, almost equally large numbers.)

The total line heating/cooling rate depends on the following physical parameters: The particle density of the considered species $n_{\rm sp}$, the particle densities of the collision partners, the gas temperature $T_{\rm g}$, the continuous background radiation field $J^{\rm cont}_{\nu_{ul}}$ and the local mean velocity gradient $\left\langle\frac{dv}{dl}\right\rangle$.

The following atomic or molecular data are required: the statistical weights g_i and energies E_i of the considered levels, the Einstein coefficients for spontaneous emission A_{ul} and the rate coefficients for collisional de–excitation $C_{ul}(T_{\rm g})$ (where the particle densities of the collision partners enter into the calculation).

The presented method is an universal and rapidly converging tool for the calculation of the total line heating/cooling rate of an arbitrary N–level–system. It is applicable to arbitrary conditions of density, temperature and radiation field and can be applied to a variety of flow geometries, as far as the involved escape probability concept makes sense.

3.1.1.2 Discussion of the Applicability of Sobolev Theory

The application of Sobolev theory to the shocked envelopes of pulsating stars requires some critical remarks:

1) Sobolev theory is applicable only in case of large velocity gradients, where the sizes of the resonance regions (where an emitted line photon can still be re-absorbed) are small compared to typical scale heights of the envelope. In case of thermal broadening, this condition can be written as

$$\frac{\left\langle\frac{dv}{dl}\right\rangle}{v_{\rm th}} \gg \max\left\{\frac{d\ln\rho}{dr},\frac{d\ln T}{dr},\frac{d\ln n_{\rm sp}}{dr},\ldots\right\} \quad . \tag{3.25}$$

Regarding the results of time–dependent models for the envelopes of long–periodic variable stars (Bowen 1988, Fleischer 1994), this condition seems to be just even fulfilled. The thermal velocities are a few $\rm km\,s^{-1}$, the mean velocity gradient (cf. Eq. 3.14) is typically 5 to 50 $\rm km\,s^{-1}/R_*$ and the scale height (the r.h.s. of Eq. 3.25) is typically $1\,R_*$. Problems can occur very close to the star, where the scale height can be much smaller, and close to shock fronts in the post–shock regions, where the temperature gradients can be fairly large.

2) Due to the strict division between considered line and continuum, line overlaps are an intrinsic problem of Sobolev theory. The Sobolev theory requires that the emitted line photons of one particular transition cannot be re-absorbed by any other line transition anywhere else in the envelope:

$$\frac{v_\infty}{c} < \frac{\Delta\nu}{\nu} \tag{3.26}$$

The maximum relative shift of the lines due to hydrodynamic velocities (the l.h.s. of Eq. 3.26) is about 10^{-4} for AGB–stars, which is usually much smaller than the relative spacing of the considered spectral lines (the r.h.s. of Eq. 3.26, where $\Delta\nu$ is the frequency difference of two considered lines). This condition becomes more serious for the vibrational bands of diatomic polar molecules, where the r.h.s. of Eq. (3.26) is given by $2hB/\hbar\omega \approx 2 \cdot 10^{-3}$ (cf. Sect. 3.1.4). But even in this case, condition (3.26) remains valid. Problems can occur in electronic bands of molecules, where the spacing of the individual lines is even more narrow or in very narrow spaced atomic multiplets.

3) The problem of non–monotonic velocity gradients in the saw–tooth like velocity fields of CSEs of pulsating stars coupled with the question of the difference between local and global escape is ignored. Thereby, the radiative heating of e. g. one post–shock layer by line emissions from the post–shock region of another shock wave is neglected in this work.

4) Close to the location of a velocity discontinuity (caused by a shock front), most of the disturbing absorber are missing in the directions across the discontinuity. Therefore, larger escape probabilities can occur in this case and the radiative cooling of otherwise optically thick lines increases, which may be important just for the hot emitting post–shock regions directly behind shock waves.

The advantages of the presented escape probability method, however, clearly outweigh these short–comings. As long as no better and comparable simple methods are available, the Sobolev theory is just the appropriate compromise between simplicity and accuracy of the physical description. Using this theory, the results of the line heating/cooling rates are entirely determined by *local* physical properties (which are available in hydrodynamic models), still including the most important line transfer effects. The only real alternative would be to ignore optical depth effects of the lines completely, which would induce much larger errors.

3.1.1.3 An Exemplary Two–Level–Atom

In order to demonstrate the basic features of the line heating/cooling functions, an exemplary two–level–atom is examined. The following (typical) atomic parameters and physical conditions are considered:

$$g_1 = g_0, \quad \Delta E/k = 10000\,\mathrm{K}, \quad A_{10} = 10^{-2}\,\mathrm{Hz}, \quad C_{10} = n_{<\mathrm{H}>} \cdot 10^{-10}\,\mathrm{Hz\,cm^3}$$
$$n_\mathrm{H} : n_{\mathrm{H}_2} : n_\mathrm{He} : n_\mathrm{sp} = 1 : 0 : 0.1 : 10^{-4}, \quad \left\langle \frac{dv}{dl} \right\rangle = \frac{20\,\mathrm{km\,s^{-1}}}{500\,R_\odot}$$

The resulting line heating/cooling rate per mass Q_rad/ρ as function of the total hydrogen particle density $n_{<\mathrm{H}>}$ is depicted in Fig. 3.1 for the case of negligible continuous radiation field $J^\mathrm{cont} = 0$. The figure demonstrates the fundamental density–dependence of the two–level cooling rate. Three different cases can be distinguished, depending on the relation between the density of the gas $n_{<\mathrm{H}>}$ and two critical densities n_cr and n_thick, which are defined below:

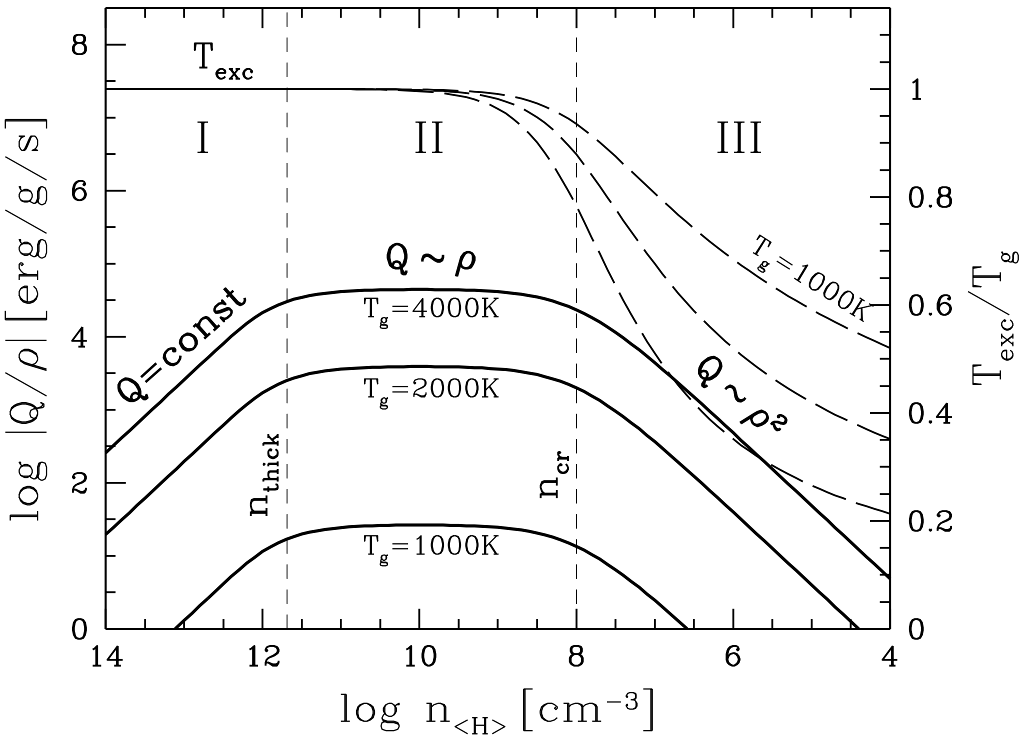

Figure 3.1: The cooling rate (full lines, left axis) and the excitation temperature, defined by $kT_{\rm exc} = \Delta E_{ul}/\ln((g_u n_l)/(g_l n_u))$, in units of $T_{\rm g}$ (dashed lines, right axis) of an exemplary two–level–atom in the case of negligible continuous radiation field $J_\nu^{\rm cont} = 0$.

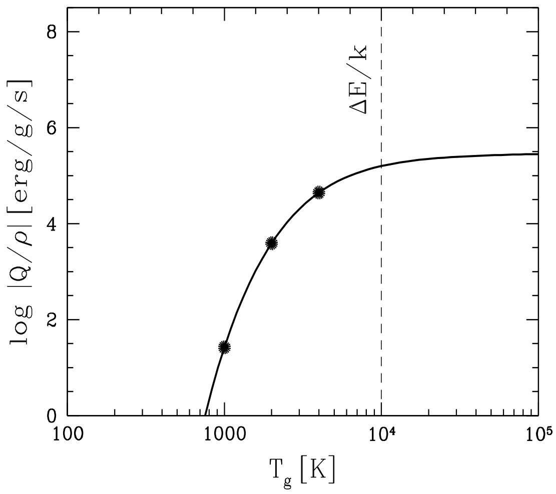

Figure 3.2: The temperature dependence of the line cooling rate per mass for $n_{<\rm H>} = 10^{10}\rm cm^{-3}$ and $J_\nu^{\rm cont} = 0$. Full circles indicate points already depicted in Fig. 3.1.

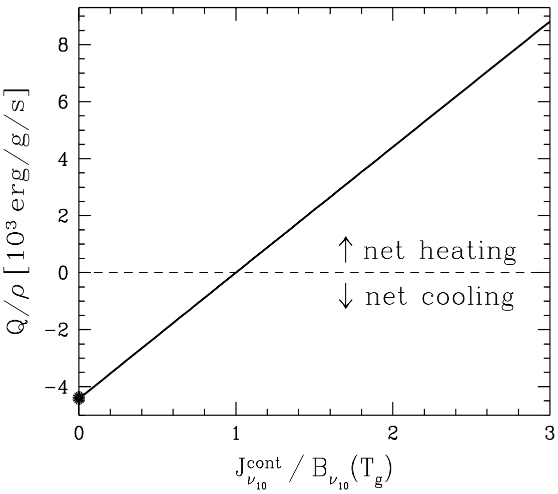

Figure 3.3: The dependency of the line cooling rate per mass on the radiation field for $n_{<\rm H>} = 10^{10}\rm cm^{-3}$ and $T_{\rm g} = 2000\,K$.

I. $n_{<\mathrm{H}>} > n_{\mathrm{thick}}$: The line is optically thick and the cooling rate is limited by radiative trapping, where only a fraction of the emitted line photons can escape the local surroundings. LTE is valid. In the limiting case $n_{<\mathrm{H}>} \to \infty$ the escape probability scales as $P^{\mathrm{e}} \to 1/\tau^{\mathrm{S}} \propto \rho^{-1}$. Thereby, Q_{rad} becomes density–independent.

II. $n_{\mathrm{cr}} < n_{<\mathrm{H}>} < n_{\mathrm{thick}}$: The atom is thermally populated (LTE) and the line is optically thin. The cooling rate is simply given by the thermal rate of emitted photons, leading to $Q_{\mathrm{rad}} \propto \rho$.

III. $n_{<\mathrm{H}>} < n_{\mathrm{cr}}$: The atom is populated sub–thermally (non–LTE) and the cooling rate is limited by the rate of energy transferred from the gas via collisions, which yields $Q_{\mathrm{rad}} \propto \rho^2$. In the limiting case $n_{<\mathrm{H}>} \to 0$, each exciting collision is followed by spontaneous emission.

n_{cr} denotes the usual critical density for thermal population and n_{thick} corresponds to $\tau^{\mathrm{S}} = 1$. The critical densities are defined by

$$n_{\mathrm{cr}} = \frac{A_{10}}{C_{10}/n_{<\mathrm{H}>}} \tag{3.27}$$

$$n_{\mathrm{thick}} = \frac{8\pi}{A_{10}} \frac{g_0}{g_1} \left(\frac{\nu_{10}}{c}\right)^3 \left\langle \frac{dv}{dl} \right\rangle \frac{n_{<\mathrm{H}>}}{n_{\mathrm{sp}}} \quad . \tag{3.28}$$

In some cases, the two critical densities will overlap ($n_{\mathrm{cr}} > n_{\mathrm{thick}}$). If this happens, as e. g. in case of the large Einstein coefficients of allowed transitions, the cooling rate directly changes from the $Q_{\mathrm{rad}} \propto \rho^2$ to the $Q_{\mathrm{rad}} = \mathrm{const}$ behavior.

Figure 3.2 shows the "freezing out" of the concerned degree of freedom. A minimum temperature of about $T_{\mathrm{g}} \gtrsim \Delta E/5k$ is required for efficient collisional excitation and, hence, for efficient line cooling[4]. A further increase of the temperature does not increase the cooling rate much. However, since at the same time other cooling lines enter into competition and become much more efficient, the considered spectral line gets less important in comparison. Hence, a spectral line requires very special density and temperature conditions in order to be an efficient coolant. The depicted temperature–dependence is unique for all densities: The $Q_{\mathrm{rad}}(n_{<\mathrm{H}>})$-curve is simply shifted up- and downwards in Fig. 3.1 according to that temperature–dependence.

Line transitions can cause net cooling of the gas, but can in fact also cause *net heating* in the case of intense continuous radiation fields as shown in Fig. 3.3. This result is straightforward, but fundamentally different from the experience with interstellar matter, where the continuous radiation field may be neglected and where line transitions generally cause radiative cooling. Equation (3.23) expresses the linear dependency shown in Fig. 3.3.

All the discussed dependencies of the two–level line heating/cooling function are quite general and approximately apply also to the other heating/cooling mechanisms outlined in this work.

[4]However, the considered line can still be interesting for radiative heating as far as $E_l \lesssim kT_{\mathrm{g}}$ concerning a multi–level–atom.

3.1.2 Lines of Atoms and Ions

For a general discussion of the importance of line heating and cooling in circumstellar envelopes, the selection of species and lines is crucial. The selection depends on the considered elemental abundances and on the considered density and temperature conditions. As argued above, one should especially include a variety of lines with different ΔE_{ul} values (different spectral regions). Furthermore, the availability of atomic data (especially the collision rates) can be problematic. The selection of lines in this work is mainly based on the experience of Hollenbach & McKee (1989). Since their work relates to interstellar conditions, mainly the few, low–lying levels of the more abundant atoms and ions are taken into account.

In case of larger densities, where the population is generally closer to LTE, more lines enter into competition and the chosen selection may be insufficient. Especially for high gas temperatures, even the population of very high–lying levels may become important (which immediately causes troubles due to the rapidly increasing number of transitions to be considered). However, since spectral lines have generally proven to be important solely at small densities, a troublesome expansion of the line list would be rather fruitless, because the bound–free heating and cooling rates will dominate at larger densities anyway.

Therefore, only a few further lines, which satisfy the conditions

- large elemental abundance,
- neutral or singly ionized,
- low excitation energy E_l,
- large A_{ul}, different ΔE_{ul} values and
- collisional data available

have been additionally included, especially from Mendoza (1983) and the references therein. The *completeness of the model atoms* is another necessary precondition for non–LTE investigations. If, for example, a transition with the principal quantum number jump $9 \to 5$ looks interesting, *all* the 55 transitions up to levels 9 should be taken into account. Table 3.1 summarizes the selection of species and line transitions in this work, comprising 15 species and 85 lines. The list includes most of the existing low–lying energy levels of the considered species.

The rates for collisional de-excitation are assumed to be given by the collision rates with free electrons (which are usually dominant unless the degree of ionization is lower than $\sim 10^{-4}$) and with neutral H atoms:

$$C_{ul}(T_{\rm g}) = n_{\rm e}\gamma^{e}_{ul}(T_{\rm g}) + n_{\rm H}\gamma^{\rm H}_{ul}(T_{\rm g}) \tag{3.29}$$

$$\gamma^{\rm x}_{ul}(T_{\rm g}) = \Omega^{\rm x}_{ul}\Big(T_{\rm g}/T_{\rm ref}\Big)^{\alpha^{\rm x}_{ul}} \tag{3.30}$$

The collisional rates are often represented as Eq. (3.30), so that for one collision rate usually two parameters (Ω_{ul}, and α_{ul}) are to be collected for electrons and H–atoms. There are often different fits for different temperature regimes $T_{\rm ref}$.

Table 3.1: Atomic line heating and cooling: considered species and transitions

	Levels[(1)]	λ_{ul} [μm] [(2)]	Ref.
H	$n=1$, $n=2$, $n=3$	0.1215, 0.1025, 0.656	5
He	1^1S, 2^3S, 2^1S, 2^3P^0, 2^1P^0	0.0626, 0.0601, 0.0591, 0.0584, 1.56, 1.08, 0.887, 3.56, 2.06, 4.88	4
He^+	$n=1$, $n=2$, $n=3$, $n=4$, $n=5$	0.0304, 0.0256, 0.0243, 0.0237, 0.164, 0.122, 0.109, 0.469, 0.321, 1.01	6
C	$^3P_0$, $^3P_1$, $^3P_2$	609.2, 229.9, 369.0	3
	^3P, $^1D_2$, $^1S_0$	0.984, 0.462, 0.873	3
C^+	$^2P_{1/2}$, $^2P_{3/2}$	157.7	3
	^2P, ^4P	0.233	3
N	$^4S_{3/2}$, ^2D, ^2P	0.520, 0.347, 1.04	3
N^+	^3P, $^1D_2$, $^1S_0$	0.656, 0.306, 0.576	3
O	$^3P_2$, $^3P_1$, $^3P_0$	63.1, 44.2, 145.6	3
	^3P, $^1D_2$, $^1S_0$	0.633, 0.297, 0.558	3
O^+	$^4S_{3/2}$, $^2D_{5/2}$, $^2D_{3/2}$	0.373, 0.372, 508	3
Si	$^3P_0$, $^3P_1$, $^3P_2$	129.6, 44.8, 68.4	3
	^3P, $^1D_2$, $^1S_0$	1.62, 0.653, 1.10	3
Si^+	$^2P_{1/2}$, $^2P_{3/2}$	34.8	3
	^2P, ^4P	0.224	3
S	$^3P_2$, $^3P_1$, $^3P_0$	25.2, 17.4, 56.6	3
	^3P, $^1D_2$, $^1S_0$	1.10, 0.459, 0.773	3
S^+	$^4S_{3/2}$, $^2D_{3/2}$, $^2D_{5/2}$, $^2P_{1/2}$, $^2P_{3/2}$	0.673, 0.672, 0.408, 0.407, 314.5, 1.034, 1.029, 1.037, 1.032, 213.2	4
Fe	$^5D_4$, $^5D_3$, $^5D_2$	24.0, 14.2, 34.2	3
	$^5D_4$, $^5F_5$, $^5F_4$	1.44, 1.36, 22.3	3
Fe^+	$^6D_{9/2}$, $^6D_{7/2}$, $^6D_{5/2}$	26.0, 15.0, 35.4	3
	$^6D_{9/2}$, $^4F_{9/2}$, $^4F_{7/2}$, $^4D_{7/2}$	5.34, 4.12, 1.26, 17.9, 1.64, 1.80	3

(1): Levels are listed in the order of energy (first level = ground level). Levels without lower index are multiplets which are treated as single levels.

(2): Order of transitions: $1\to0$ for two-level-atoms, $1\to0$, $2\to0$, $2\to1$ for three-level-atoms, $1\to0$, $2\to0$, $3\to0$, $2\to1$, $3\to1$, $3\to2$ for four-level-atoms, $1\to0$, $2\to0$, $3\to0$, $4\to0$, $2\to1$, $3\to1$, $4\to1$, $3\to2$, $4\to2$, $4\to3$ for five-level-atoms.

3: Hollenbach & McKee (1989) and references therein
4: Mendoza (1983) and references therein, $\gamma_{ul}^{\rm H} = 10^{-12}\rm cm^3\,s^{-1}$ is assumed
5: Luttermoser & Johnson (1992)
6: Einstein coefficients from Mihalas (1978), collisional de-excitation rates from Mihalas & Stone (1968)

In conclusion, the selection of lines has been performed *in view of the importance for the gas — not from the observational point of view*. At first sight, an astronomer would probably suggest to consider those lines, which can be *seen*. These lines, however, refer to an optical depth $\tau_\nu \approx 1$, i. e. to a particular shell of the CSE (usually close to the photosphere of the star) where the density is large. In contrast, the lines listed in Table 3.1 may not even occur in the stellar spectra.

The calculation of the various line heating/cooling functions straightforwardly proceeds according to the methods outlined in Sect. 3.1.1. Each row in Table 3.1 is thereby considered as closed multi–level–system with $\sum_{\rm row} n_i = n_{\rm sp}$. The results roughly are a superposition of several two–level–type functions as depicted in Fig. 3.1. The behavior of lines with larger excitation energy, however, is usually more complex, since the population of the lower level changes and the upper level can be pumped by another transition etc. In a real physical situation, the concentrations of the carriers of the lines $n_{\rm sp}/n_{<\rm H>}$ additionally depend on the temperature, the density and the radiation field. The same occurs for the electron concentration, which is of crucial importance for the collision rates.

3.1.3 Rotational Transitions of Linear Polar Molecules

As soon as molecules become abundant in the gas phase, they usually dominate the radiative energy exchange. Especially the ro–vibrational transitions of *abundant polar molecules* have proven to be important under interstellar conditions (e. g. Neufeld & Kaufman 1993), in the atmospheres of cool stars and even in the outer atmosphere of the sun (e. g. Ayres 1981). The general problem of the treatment of molecules in radiative transfer arises from the large number of line transitions to be considered. For non–LTE investigations, a huge amount of molecular data has to be collected (individual radiative lifetimes, collision rates etc.). This procedure is only feasible for a very few well–known molecules and subsets of transitions. Fortunately, there are some approximate analytical expressions available for certain types of molecules (e. g. diatomic molecules). Since we are not interested in any spectroscopic details, but in the total effect of molecules for the radiative heating and cooling of the gas, these analytical approximations are just appropriate.

Concerning the rotational transitions of linear polar molecules, the basic model of a rigid rotator provides the statistical weights g_J and energies E_J of the levels. The Einstein coefficients for the allowed dipole transitions with selection rule $J \to J-1$ (for spontaneous emission) can be derived from the rotational constant B and the dipole moment μ_D (Chin & Weaver 1984). The rates for collisional de-excitation C_{ul} are adopted from Hollenbach & McKee (1979)

$$E_J = J(J+1)\,hB \tag{3.31}$$

$$g_J = 2J+1 \tag{3.32}$$

$$A_{J\to J-1} = \frac{64\pi^4}{3h}\left(\frac{\nu_{J\to J-1}}{c}\right)^3 \mu_D^2\,\frac{J}{2J+1} \tag{3.33}$$

$$C_{ul} = \sigma_0 \frac{g_l h B}{k T_g} \exp\Big(-\frac{E_l}{k T_g}\Big) \sum_i n_i v_{th,i} \tag{3.34}$$

$$v_{th,i} = \sqrt{8 k T_g / \pi m_{red,i}} \quad , \tag{3.35}$$

where $\nu_{J \to J-1} = 2JB$ is the frequency of the transition, $v_{th,i}$ the most probable thermal velocity and σ_0 is the total collisional cross section, which is usually estimated to be $10^{-15}\,cm^2$.

The molecular data required for the calculation of the rotational heating/cooling rate are the total collisional cross section σ_0, the rotational constant B and the dipole moment μ_D, which can be taken from various molecular data tables, e. g. Landolt–Börnstein (Hellwege 1982). Table 3.2 summarizes these molecular data of the considered molecules in this work.

Table 3.2: Vibrational and rotational heating and cooling: considered species and molecular data

Species(3)	θ [K]	$1/\tau_{10}$ [Hz]	B [MHz]	μ_D [D]	σ_0 [cm^2]
CO	3084	34.4	57636	0.1098	10^{-15}
OH	5134	15.9	556141	1.667	10^{-15}
CH	4113	115	425473	1.46	10^{-15}
C_2H	– (1)	–	43675	0.8	10^{-15}
HCN	– (1)	–	44316	2.985	10^{-15}
CN	2939	2.3	56694	1.45	10^{-15}
C_2N	– (1)	–	11863	0.6	10^{-15}
SiC	1830	10 (2)	20298	1.7	10^{-15}
SiN	1638	10 (2)	21882	2.3	10^{-15}
SiO	1769	10 (2)	21788	3.098	10^{-15}
SiS	1058	10 (2)	9077	1.73	10^{-15}
CS	1830	10 (2)	24496	1.957	10^{-15}

(1): The vibrational heating/cooling function of this molecule cannot be treated according to Sect. 3.1.4, since it is not diatomic.

(2): Estimated. The corresponding net vibrational heating function, however, is not significantly affected by the choice of this parameter (cf. Sect. 3.1.4).

(3): Since only applications for carbon–enriched cases are made, H_2O is not considered in this work. In the case $\epsilon_C > \epsilon_O$, water it is almost absent from the gas phase.

The calculation of the rotational heating/cooling function can be performed similarly to the last paragraph. Instead of solving the statistical equations (3.1) for all considered rotational level populations n_J, however (which would also be possible, but too elaborate for our purpose), I use the following approximate method proposed by Krüger et al. (1994). The rotational states are assumed to be populated according to a Boltzmann–distribution with a yet unknown rotational excitation temperature $T_{\rm rot}$:

$$Z_{\rm rot} = \frac{kT_{\rm rot}}{hB} \tag{3.36}$$

$$n_J = n^{\rm mol}\frac{g_J}{Z_{\rm rot}}\exp\Big(-\frac{E_J}{kT_{\rm rot}}\Big) \tag{3.37}$$

By means of Eqs. (3.31), (3.32), (3.34), (3.36) and (3.37) and by replacing the sums over the rotational states in Eq. (3.22) by integrals, it can be shown that the total rate of collisional energy transfer simplifies to

$$Q_{\rm coll} = \sigma_0\, n^{\rm mol} k\,(T_{\rm rot} - T_{\rm g}) \sum_i n_i\, v_{{\rm th},i} \quad . \tag{3.38}$$

The rotational temperature is found by iteration, until the both results for $Q_{\rm coll}$ and $Q_{\rm rad}$ from Eqs. (3.38) and (3.24) are equal. The evaluation of the radiative net heating rate according to Eq. (3.24), which properly includes the optical depth effects in the individual lines, is thereby carried out over the first $J_{\rm max} = (7kT_{\rm rot}/hB)^{1/2}$ (typically $\sim 10^2$) rotational states by $\sum_{l,u} \to \sum_{J=1}^{J_{\rm max}} (u\!=\!J\,;\ l\!=\!J\!-\!1)$, yielding about 97% of the total thermal emission rate in the optically thin limit.

3.1.3.1 Rotational Heating and Cooling by CO

For example, the rotational heating cooling function of CO is briefly discussed, which is of special importance due to its large abundance. The molecular data of CO are outlined in Table 3.2 and the following physical conditions are considered:

$$n_{\rm H} : n_{\rm H_2} : n_{\rm He} : n_{\rm CO} = 0 : 1 : 0.2 : 10^{-3}, \quad \Big\langle \frac{dv}{dl} \Big\rangle = 20\,{\rm km\,s^{-1}}/500\,R_\odot$$

Figure 3.4 depicts the results for the case $J_\nu^{\rm cont}\!=\!0$. The density–dependence of the rotational cooling function is generally similar to a two–level–type cooling function (with the critical densities $n_{\rm cr}\!\approx\!10^{6}\,{\rm cm^{-3}}$ and $n_{\rm thick}\!\approx\!10^{9}\,{\rm cm^{-3}}$ for CO, cf. Eqs. 3.41 and 3.42 below). Due to the increasing population of the higher rotational levels and the smaller radiative life times of these levels, however, the rotational cooling function scales as $Q_{\rm rot}\!\propto\!T_{\rm g}^2$, which is different from a two–level–type cooling function.

3.1.3.2 Fast, Approximate Method

For certain applications, even the rather simple method described above for the calculation of the rotational heating/cooling functions may be too time expensive (e. g. for the model calculations in Chapter 7). In such cases, the following fit to the upper results can be used, if the continuous radiation field in the micro–wave spectral

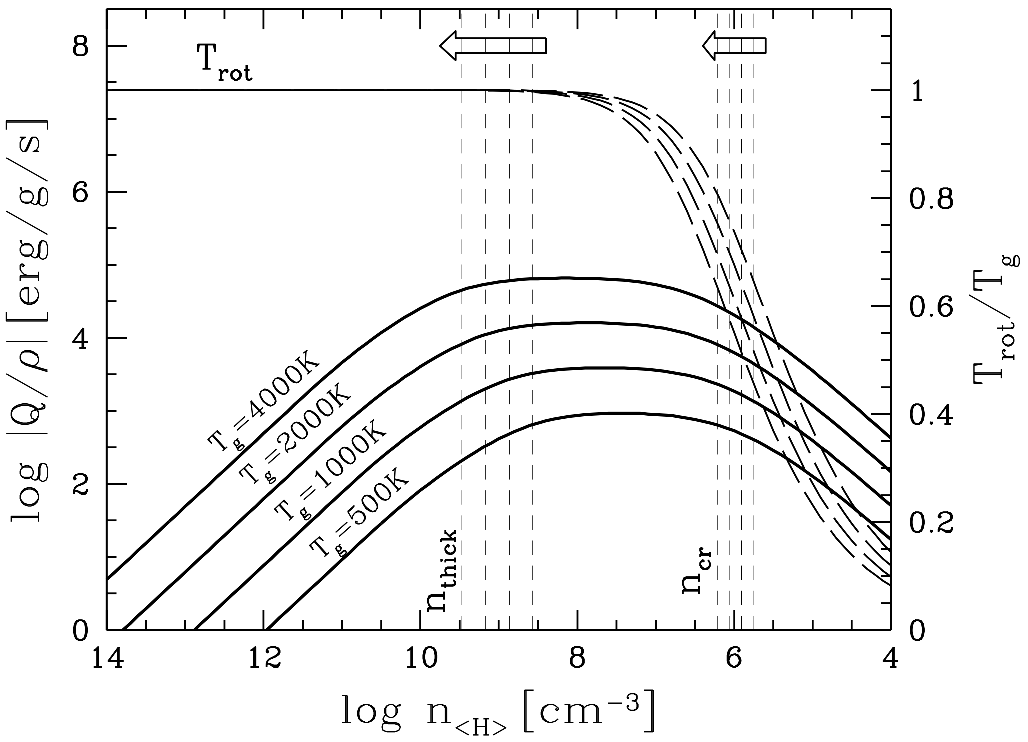

Figure 3.4: Rotational cooling rate and excitation temperature of CO in case $J_\nu^{\rm cont}\!=\!0$. Arrows indicate the trend for increasing gas temperature.

region fits like $J_\nu^{\rm cont}\!\approx\!W B_\nu(T_{\rm rad})\!\approx\!W 2kT_{\rm rad}(\nu/c)^2$ (Rayleigh–Jeans approximation):

$$Q_{\rm rot} = Q_{\rm rot,LTE}\left(\frac{n_{\rm cr}}{n_{<{\rm H}>}}+1+\frac{n_{<{\rm H}>}}{n_{\rm thick}}\right)^{-1} \quad (3.39)$$

$$Q_{\rm rot,LTE} = \frac{1024\pi^4\mu_D^2B^2}{3c^3h^2}\,n_{\rm mol}\,k^2T_{\rm g}\Big(WT_{\rm rad}-T_{\rm g}\Big) \quad (3.40)$$

$$n_{\rm cr} = \frac{1024\pi^4\mu_D^2B^2kT_{\rm g}}{3h^2c^3\sigma_0\overline{v_{\rm th}}} \quad (3.41)$$

$$n_{\rm thick} = 0.08\frac{kT_{\rm g}}{\mu_D^2B}\left\langle\frac{dv}{dl}\right\rangle\frac{n_{<{\rm H}>}}{n_{\rm mol}} \quad , \quad (3.42)$$

where $\overline{v_{\rm th}}=n_{<{\rm H}>}^{-1}\sum_i n_i\,v_{{\rm th},i}$ is the mean thermal velocity with respect to the concentrations of the collision partners. Considering typical astrophysical relevant molecules, the critical densities for thermal population of the rotational states $n_{\rm cr}$ range between about $10^5\,{\rm cm}^{-3}$ (e. g. SiS) and $10^8\,{\rm cm}^{-3}$ (e. g. HCN).

Equation (3.39) is a very useful fit formula with acceptable accuracy (error $<35\%$ at the critical densities, $<10\%$ elsewhere). $Q_{\rm rot,LTE}$ is the rotational heating/cooling function in case of LTE ($T_{\rm rot}\!=\!T_{\rm g}$) and vanishing optical depths ($\widetilde{P}_{ul}^{\rm e}\!=\!1$), which can be analytically derived from Eq. (3.23). Equation (3.40) expresses the dependencies of the rotational heating/cooling function upon the temperature and the radiation field. As the rotational frequencies are located in the micro–wave spectral region ($h\nu_{1\to 0}/k = 2hB/k \approx 5.5\,$K for CO), radiative heating via rotational pumping solely occurs in case $WT_{\rm rad} > T_{\rm g}$ which seems unlikely to occur in circumstellar envelopes (cf. the IR–limit in Fig. 1.1). The opposite case is much more probable: the rotational transitions will almost always cause net radiative cooling. According to the comparatively weak temperature–dependence, rotational heating/cooling is especially significant at low gas temperatures. The relevance of a considered molecule scales as $n^{\rm mol}\mu_D^2 B^2$, which is important for the choice of the molecules to be taken into account.

3.1.4 Vibrational Transitions of Diatomic Polar Molecules

The allowed vibrational transitions of polar molecules also provide an effective heating/cooling mechanism for the gas. The vibrational spectra of polyatomic molecules are already rather complex, so that no closed analytical expressions for the mean radiative life times and the collision rates are known. Therefore, this work restricts to the vibrational transitions of diatomic polar molecules with selection rules ${\rm v}\to{\rm v}-1$; $J\to J\pm 1$ (for spontaneous emission). Fortunately, these molecules are usually the most abundant polar molecules in the gas phase (e. g. CO). The vibrational heating/cooling by polyatomic molecules probably is a second–order–effect[5]. The corresponding wavelengths typically range from $4\,\mu$m to $12\,\mu$m[6].

For the level energies, the most simple model of a harmonic oscillator and a rigid rotator is applied, which is sufficient for the purpose of this work.

$$E_{{\rm v},J} = \hbar\omega\Big({\rm v}+\frac{1}{2}\Big) + J(J+1)\,hB \tag{3.43}$$

$$g_{{\rm v},J} = g_J \tag{3.44}$$

$$A^{{\rm v}\to{\rm v}-1}_{J\to J+1} = {\rm v}\,\frac{64\pi^4}{3h}\left(\frac{\nu^{{\rm v}\to{\rm v}-1}_{J\to J+1}}{c}\right)^3 (TM)^2\,\frac{J+1}{2J+1} \qquad (\text{“P–branch”}) \tag{3.45}$$

$$A^{{\rm v}\to{\rm v}-1}_{J\to J-1} = {\rm v}\,\frac{64\pi^4}{3h}\left(\frac{\nu^{{\rm v}\to{\rm v}-1}_{J\to J-1}}{c}\right)^3 (TM)^2\,\frac{J}{2J+1} \qquad (\text{“R–branch”}) \tag{3.46}$$

$$C_{10} = \frac{kT_{\rm g}/1\,{\rm atm}}{1-\exp\left(-\theta/T_{\rm g}\right)}\sum_i n_i \exp\Big(B_i - A_i T_{\rm g}^{-1/3}\Big) \tag{3.47}$$

$$\theta = \hbar\omega/k \tag{3.48}$$

$$A_i = 1.16\cdot 10^{-3}\left(\frac{m_{{\rm red},i}}{1\,{\rm amu}}\right)^{1/2}\theta^{4/3} \tag{3.49}$$

$$B_i = 18.42 + 0.015\,A_i\left(\frac{m_{{\rm red},i}}{1\,{\rm amu}}\right)^{1/4} \tag{3.50}$$

$$C_{{\rm vv}'} = ({\rm v}-{\rm v}')\,C_{10}\,\exp\left(-\frac{({\rm v}-{\rm v}'-1)\,1.5\,\theta/T_{\rm g}}{1+1.5\,\theta/T_{\rm g}}\right) \tag{3.51}$$

[5]An exception is the H_2O molecule in case of an oxygen rich elemental composition of the gas.
[6]Note that overtone transitions are not considered here (cf. discussion in Sect. 3.6).

v is the vibrational quantum number, ω the eigenfrequency of the harmonic oscillator and TM its transition moment, which is related to the mean radiative life time of the first excited vibrational state via $1/\tau_{10} = A^{1\to0}_{J\to J+1} + A^{1\to0}_{J\to J-1}$. The analytical representation of the Einstein coefficients is adopted from Nuth & Donn (1981). The analytical representation of the rate of collisional de-excitation of the first vibrational state C_{10} is taken from Millikan & White (1964). The Landau–Teller coefficients A_i and B_i are to be determined by experiments or can be estimated for "simple systems" (diatomic molecule plus atom or diatomic molecule as collision partner) according to Eqs. (3.49) and (3.50). The corresponding collisional cross sections for vibrational de-excitation are much less than the geometric cross sections of the molecules and show a strong temperature–dependence. The collisional de-excitation rates for higher quantum numbers $\mathrm{v} > \mathrm{v}'$ according to Eq. (3.51) are estimated by "surprisal analysis" (Elitzur 1983).

Equations (3.43)–(3.51) form a useful set of approximate analytical expressions for the required molecular data in terms of a few basic quantities, which are the eigenfrequency ω, the rotational constant B and the transition moment TM (or the mean life time of the first excited vibrational state τ_{10}, respectively). The first two data can easily be obtained from various molecular data tables, whereas the latter is available only for a few well-known molecules (from laboratory experiments or ab initio quantum mechanical calculations). Typical values for $1/\tau_{10}$ range from about 1 to 100 Hz. The obvious advantage of the analytical expressions above is their broad applicability to diatomic polar molecules. The disadvantage is the modest accuracy. Of course, more accurate Einstein coefficients and collisional data can be used for particular molecules, if available.

As in the last section, the ro–vibrational states are assumed to be populated according to Boltzmann distributions:

$$Z_{\rm vib} = \frac{1}{1-\exp\left(-\hbar\omega/kT_{\rm vib}\right)} \tag{3.52}$$

$$n_{\mathrm{v},J} = \frac{n^{\rm mol} g_J}{Z_{\rm vib} Z_{\rm rot}} \exp\left(-\frac{\mathrm{v}\hbar\omega}{kT_{\rm vib}} - \frac{J(J+1)hB}{kT_{\rm rot}}\right) \tag{3.53}$$

The rotational temperature is considered as known from the calculation of the rotational heating/cooling function and the vibrational excitation temperature $T_{\rm vib}$ is again found by iteration, until the results for $Q_{\rm rad}$ and $Q_{\rm coll}$ derived from Eq. (3.24) and Eq. (3.22) are equal. Equation (3.22) is thereby evaluated solely for the vibrational states and restricted to the first $\mathrm{v}_{\max} = 1 + 6kT_{\rm vib}/\hbar\omega$ vibrational levels $\sum_{l,u} \to \sum_{\mathrm{v}=1}^{\mathrm{v}_{\max}} \sum_{\mathrm{v}'=0}^{\mathrm{v}-1} (u = \mathrm{v}\ ;\ l = \mathrm{v}')$, yielding about 99% of the total collisional rate. Equation (3.24) is evaluated according to $\sum_{l,u} \to \sum_{\mathrm{v}=1}^{\mathrm{v}_{\max}} \sum_{J=0}^{J_{\max}} (u = \{\mathrm{v}, J\};\ l = \{\mathrm{v}-1, J\pm1\})$, which yields $\sim$ 98% of the total thermal emission rate in the optically thin limit.

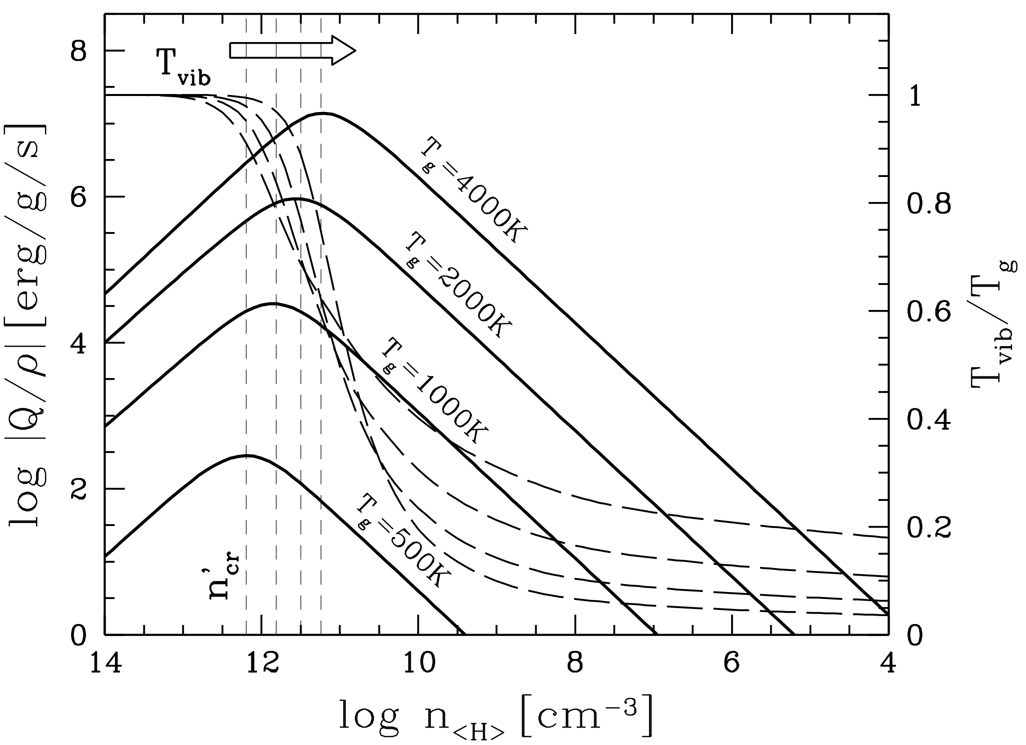

Figure 3.5: Vibrational cooling rate and excitation temperature of CO in case $J_\nu^{\rm cont}=0$.

3.1.4.1 Vibrational Heating and Cooling by CO

In order to illustrate the outlined procedure, the vibrational heating/cooling function of the CO molecule is calculated. The molecular data for CO are given in Table 3.2 and the considered velocity gradient and gas abundances are given in the last section. In case of CO, more accurate collisional data are available: The $1 \to 0$ rate coefficients for collisions with H atoms are taken from Glassgold (1993, see Neufeld & Hollenbach 1994) and for collisions with H_2 molecules from Rosenberg et al. (1971, see Hollenbach & McKee 1989). Landau–Teller coefficients have been explicitly measured for the CO–He collisions (Millikan & White 1964).

Figure 3.5 depicts the results for the case $J_\nu^{\rm cont} = 0$. The vibrational cooling rate essentially is a two–level–type cooling function and consequently shows all the features discussed in Sect. 3.1.1.3. The higher vibrational levels $\rm v \geq 2$ are usually not very significant. According to the large Einstein coefficients of the vibrational transitions, the maximum possible emission rate in the optically thin LTE case is never realized, because the emission is limited either by insufficient collisional pumping or by radiative trapping, which is the typical behavior of allowed transitions. Consequently, the vibrational cooling function directly changes from the $Q_{\rm rad} \propto \rho^2$ to the $Q_{\rm rad} = {\rm const}$ case at about $n'_{\rm cr} \approx 10^{11.5}{\rm cm^{-3}}$ for CO. The basic slope of the temperature–dependence is the same as depicted in Fig. 3.2, although for temperatures $T_{\rm g} \gtrsim \theta$, the higher vibrational levels cause some modifications. The main difference to an ordinary two–level–type cooling function arises from the weak sensibility of the vibrational heating/cooling to optical thickness, since the emitted photons are spread among the fine structure of the P– and R–branch of the vibrational band.

3.1.4.2 Fast, Approximate Method

Similar to the rotational heating/cooling function in the previous section, a fast fit formula is designed, which can be applied in time–critical model calculations. It is assumed that the background radiation field is constant over the vibrational band and equals $J^{\rm cont}_{\nu_{1\to 0}}$:

$$Q_{\rm vib} = Q_{\rm vib,LTE}\left(\frac{n_{\rm cr}}{n_{\rm <H>}} + 1 + \frac{n_{\rm <H>}}{n_{\rm thick}}\right)^{-1} \quad (3.54)$$

$$Q_{\rm vib,LTE} = \frac{n_{\rm mol}}{\tau_{10}}\,\frac{\hbar\omega}{\exp\left(\theta/T_{\rm g}\right)-1}\left(\frac{J^{\rm cont}_{\nu_{1\to 0}}}{B_{\nu_{1\to 0}}(T_{\rm g})} - 1\right) \quad (3.55)$$

$$n_{\rm cr} = \frac{n_{\rm <H>}}{\tau_{10}\,C_{10}} \quad (3.56)$$

$$n_{\rm thick} = 26.4\,\tau_{10}\left\langle\frac{dv}{dl}\right\rangle\frac{kT_{\rm g}}{hB}\left(\frac{\hbar\omega}{hc}\right)^3\frac{n_{\rm <H>}}{n_{\rm mol}} \quad (3.57)$$

$$n'_{\rm cr} = \sqrt{n_{\rm cr}\,n_{\rm thick}} \quad (3.58)$$

The accuracy of formula (3.54) is about 35% at $n_{\rm <H>} \approx n'_{\rm cr}$ and better than 10% elsewhere. The dependency of the vibrational heating/cooling function on the radiation field is expressed by Eq. (3.55), once more indicating that radiative heating occurs in case $J^{\rm cont}_\nu > B_\nu$ and radiative cooling otherwise. $Q_{\rm vib,LTE}$ is the energy exchange rate in case of LTE ($T_{\rm vib} = T_{\rm g}$) and negligible optical depths ($\widetilde{P}^{\rm e}_{ul} = 1$). Although this maximum possible rate is usually not realized (see above), it scales the results as formulated in Eq. (3.54). As far as $n_{\rm cr} > n_{\rm thicks}$ is valid, the vibrational heating/cooling rate is almost entirely independent from the mean life time τ_{10}. This allows for the determination of the vibrational heating/cooling rates also of those diatomic polar molecules, for which the τ_{10}–values are not exactly known. Considering typical values for τ_{10} and C_{10} for diatomic polar molecules and gas temperatures $500 - 2000\,$K, the critical densities for thermal excitation of the vibrational states $n_{\rm cr}$ are of the order $10^{10} - 10^{17}\,{\rm cm^{-3}}$, which due to radiative trapping are usually significantly reduced ($n_{\rm cr} \to n'_{\rm cr}$) by up to 4 orders of magnitude[7]. Considering the

[7]Consequently, strong non–LTE effects concerning the population of the vibrational states of polar molecules can be expected in circumstellar envelopes (in contrast to the population of the rotational states). Chemical reactions might be affected by these effects, since many reactions are extremely temperature–dependent and the vibrational energies of the reactants may be involved. This situation may have severe consequences for the chemistry and also for the nucleation of dust grains in these envelopes. A first approach to handle reactants of different temperatures has been presented by Cherchneff et al. (1992).

mostly realized case $Q_{\rm vib} \propto \rho^2$, the importance of a molecular species under examination concerning its contribution to the total heating/cooling of the gas scales as $n_{\rm mol}\,\hbar\omega\,C_{10}$.

3.1.5 Quadrupole Transitions of H_2

Unpolar molecules may usually be neglected considering the total energy exchange between the gas and the radiation field, because these molecules have extremely small radiative transition probabilities. The H_2 molecule, however, may be sufficiently abundant in order to compensate for this. Its ro–vibrational quadrupole transitions are known to be significant in warm interstellar clouds and are located roughly between 1 μm and 25 μm.

The radiative heating/cooling function of H_2 is calculated analogously to Sect. 3.1.4. Since no analytical expressions are available, an extensive list of individual transition probabilities must be used, which means a much larger expense compared to Sect. 3.1.4. The level energies are derived from the spectroscopic constants

$$E({\rm v},J) = hc\left[w_e\Big({\rm v}+\tfrac{1}{2}\Big) - w_e x_e\Big({\rm v}+\tfrac{1}{2}\Big)^2 + B_{\rm v}J(J+1) - D_e J^2(J+1)^2\right] \qquad (3.59)$$

$$w_e = 4401.2,\ x_e = 121.33,\ B_{\rm v} = 60.853 - 3.062\Big({\rm v}+\tfrac{1}{2}\Big),\ D_e = 0.0471 \quad [{\rm cm}^{-1}]$$

as given by Huber & Herzberg (1979) and the Einstein coefficients for spontaneous emission of the (forbidden) ro–vibrational quadrupole transitions ${\rm v} \rightarrow {\rm v}'$; $J \rightarrow \{J-2,\ J,\ J+2\}$ are taken from Turner et al. (1977), where all transitions with ${\rm v} \le 5$ and $J \le 20$ are taken into account (comprising 114 pure rotational and 898 ro–vibrational transitions).

The collisional vibrational de-excitation rates $1 \rightarrow 0$ for H–atoms and H_2–molecules are adopted from Lepp & Shull (1983) and references therein. Those for He–atoms are estimated according to Eq. (3.47) with $A_{\rm He} = 145.5$ and $B_{\rm He} = 20.77$. The collisional rates for the higher vibrational states are again estimated according to Eq. (3.51). The collisional (de–) excitation of the rotational states is not considered in detail here — instead, the rotational temperature of H_2 is assumed to equal the gas temperature. According to the calculations of Lepp & Shull (1983), this approximation is reliable, unless the gas density is lower than $\sim 10^5\,{\rm cm}^{-3}$.

If the optical depths in the lines are neglected as assumed in the work of Lepp & Shull (1983), their results can be reproduced within a maximum factor of 2 (generally much better) for all considered gas temperatures and for densities larger than $10^5\,{\rm cm}^{-3}$, proving that the presented method including the introduction of excitation temperatures works properly. Figure 3.6 shows the results once more for the case $J_\nu^{\rm cont} = 0$, $n_{\rm H} : n_{\rm H_2} : n_{\rm He} = 0 : 1 : 0.2$ and $\left\langle \frac{dv}{dl} \right\rangle = 20\,{\rm km\,s^{-1}}/500\,R_\odot$. According to the assumption $T_{\rm rot} = T_{\rm g}$, the rotational cooling rate is proportional to ρ for all densities unless $n_{\rm <H>} \gtrsim 10^{12}{\rm cm}^{-3}$, where even the quadrupole transitions become optically thick. The vibrational cooling rate is more important for high temperatures ($T_{\rm g} > 1000\,{\rm K}$) and high densities, where it exceeds the rotational cooling rate

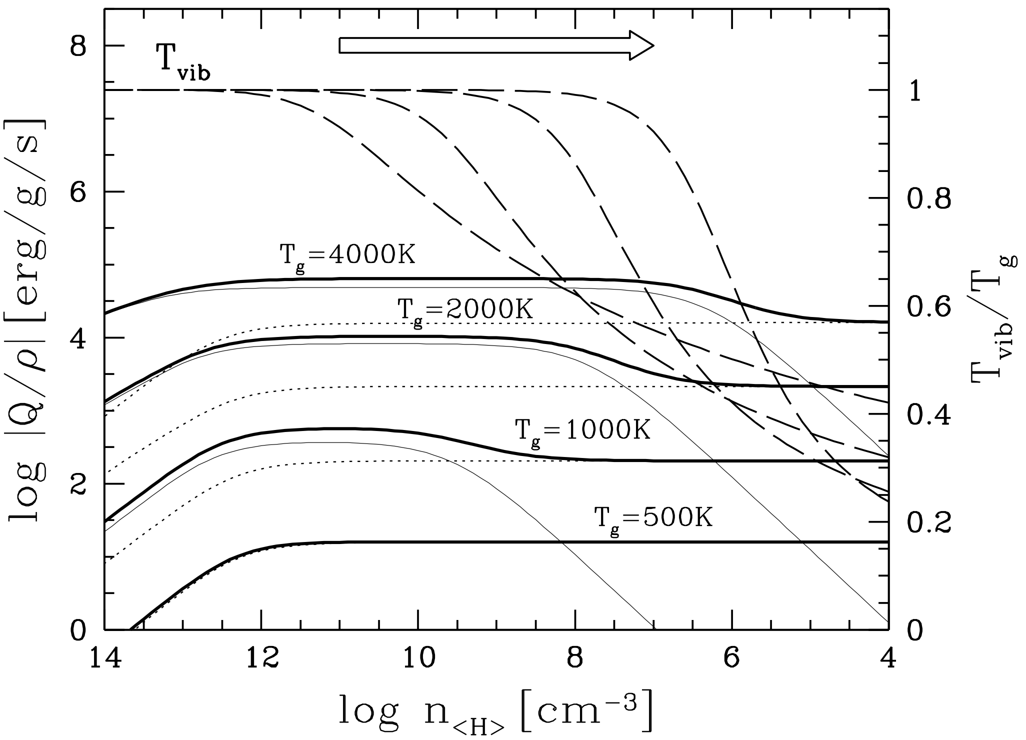

Figure 3.6: The total quadrupole cooling rate (thick full lines), the vibrational cooling rate (thin full lines), the rotational cooling rate (dotted lines, left axis) and the vibrational excitation temperature (dashed lines, right axis) of H_2 in case $J_\nu^{\rm cont}=0$.

by about one order of magnitude. The critical density for thermal population of the vibrational states of the H_2 molecule strongly depends on the gas temperature and ranges from 10^6 to $10^{10}\,{\rm cm}^{-3}$.

The total contribution of H_2 heating and cooling roughly stays proportional to the gas density over the whole considered density range of circumstellar envelopes (with an accuracy of about one order of magnitude). This behavior is a natural consequence from the low transition probabilities of the quadrupole transitions, and is typical for forbidden lines. In comparison to other heating/cooling rates, which decrease as $Q_{\rm rad} \propto \rho^2$ for small densities, the H_2 quadrupole heating/cooling is especially significant at low density (e. g. interstellar) conditions.

3.2 Bound–Free Transitions

Bound–free transitions (photoionisation and radiative recombination) generally provide important heating and cooling rates as soon as considerable fractional ionization is present in the gas, which occurs in the following two cases:

i) A strong UV radiation field is present which causes both, photoionisation and net radiative heating of the gas. This case is generally realized in the overwhelming part of the ISM (except for the dense and shielded molecular clouds), where the interstellar UV radiation field interacts with the gas.

ii) The gas is dense and hot, so that collisional ionization causes considerable fractional ionization. High temperatures ($\gtrsim 8000\,\mathrm{K}$ for hydrogen) are usually required for effective collisional ionization which, followed by radiative recombination, preferably causes net cooling of the gas (the details, however, depend on the relation between the gas temperature and the present UV radiation field, see below). The competitive processes of collisional ionization and three–body recombination are furthermore responsible for keeping the ionization equilibrium close to LTE in stellar atmospheres. In return, the large bound–free opacities in the case of LTE control the radiative transfer and the radiative heating and cooling of the gas as e. g. in the atmospheres of hot stars.

Considering the physical conditions in CSEs, large fractional ionization especially occurs around warm and hot stars, where the photospheric UV radiation field is already sufficiently intense to cause considerable bound–free radiative heating can be expected.

The conditions in the predominantly neutral CSEs of cool (e. g. AGB) stars do generally not favor large bound–free heating/cooling rates. There are, however, important exceptions from this rule: First, if chromospheric activity is present, radiative heating by bound–free transitions of the gas can be effective. Second, if the interstellar UV radiation field can penetrate into the considered layer of the CSE, it will cause considerable fractional ionization and radiative heating. Third, concerning the hot post–shock gas layers in the CSEs of pulsating stars, collisional ionization followed by radiative recombination can be an important cooling processes.

3.2.1 The Rate Equations for an N–Level System with Continuum

A level system consisting of N bound electronic states plus one additional level (denoted by "II") for the first ionized state of the considered species is examined. Besides the bound–bound processes discussed before, the processes of photoionisation, radiative recombination, collisional excitation and three–body recombination are taken into account. Analogously to Sect. 3.1.1 the level populations $n_1, n_2, \ldots, n_N, n_{\mathrm{II}}$ are derived from the statistical equations (3.1), assuming that the net production rates of all considered states vanish (steady–state non–LTE). This assumption is more restrictive in this section, because the time scale for relaxation towards ionization equilibrium ($n_{\rm II}\sum_i R_{{\rm II}\,i} = \sum_i n_i R_{i\,{\rm II}}$) can be much larger compared to the time scales for relaxation of the excited bound states under certain circumstances (e. g. in the case of low fractional ionization) and might exceed other, e. g. hydrodynamic time scales. Furthermore, the level system is assumed to be "closed" in the sense that other processes, which might provide additional source terms for the particle densities of the neutral and singly ionized atoms (e. g. chemical reactions, charge exchange reactions) are neglected.

The rate coefficients for the bound–bound transitions are given by Eqs. (3.20) and (3.21), whereas those for the bound–free transitions are formulated according to Mihalas (1978):

$$R_{i\,{\rm II}} = 4\pi\int\limits_{\nu^i_{\rm thr}}^{\infty}\frac{J_\nu}{h\nu}\,\sigma_i^{\rm bf}(\nu)\,d\nu \;+\; n_e\beta_i(T_{\rm g}) \tag{3.60}$$

$$R_{{\rm II}\,i} = \frac{n_{\rm e}}{S_i(T_{\rm g})}\left(4\pi\int\limits_{\nu^i_{\rm thr}}^{\infty}\left(\frac{2\nu^2}{c^2}+\frac{J_\nu}{h\nu}\right)\exp\left(-\tfrac{h\nu}{kT_{\rm g}}\right)\sigma_i^{\rm bf}(\nu)\,d\nu \;+\; n_e\beta_i(T_{\rm g})\right) \tag{3.61}$$

$$S_i(T_{\rm g}) = \frac{2Z_{\rm II}}{g_i}\,\frac{(2\pi m_{\rm e}\,kT_{\rm g})^{1.5}}{h^3}\exp\left(-\frac{\chi_i}{kT_{\rm g}}\right) \tag{3.62}$$

i labels a bound state, $\sigma_i^{\rm bf}(\nu)$ is the bound–free absorption cross section and $\beta_i(T_{\rm g})$ the rate coefficient for collisional ionization (we only consider collisions with electrons here). χ_i is the energy difference between the i-th level and the continuum, $\nu^i_{\rm thr} = \chi_i/h$ the corresponding threshold frequency, $S_i(T_{\rm g})$ the Saha function and $Z_{\rm II}$ the partition function of the ionized state.

The total radiative heating/cooling function of such a multi–level system comprises contributions from bound–bound transitions, which are calculated according to Eq. (3.24) and from bound–free transitions:

$$Q^{\rm bf}_{\rm rad} = 4\pi\sum_{i=1}^{N}\int\limits_{\nu^i_{\rm thr}}^{\infty}\left(n_iJ_\nu - \frac{n_{\rm II}n_{\rm e}}{S_i(T_{\rm g})}\left[\frac{2h\nu^3}{c^2}+J_\nu\right]\exp\left(-\tfrac{h\nu}{kT_{\rm g}}\right)\right)\sigma_i^{\rm bf}(\nu)\,d\nu \tag{3.63}$$

It is important to note that the evaluation of the radiative heating/cooling rate depends on the definition of the internal energy. In this work, the total absorbed/emitted photon energy is calculated and the ionization energies χ_i occur as potentials in the internal energy (cf. Eq. 2.2). Concerning other publications, the radiative heating and cooling rates occasionally refer to the pool of translational energy alone. In this case, no internal ionization potentials are considered, but an additional factor $(h\nu-\chi_i)/h\nu$ appears in Eq. (3.63), describing the gain or loss of pure *translational* energy.

Besides the data for the level energies χ_i, the statistical weights g_i and the partition function $Z_{\rm II}$, only $\sigma_i^{\rm bf}(\nu)$ and $\beta_i(T_{\rm g})$ are required for the calculation of the bound–free radiative heating/cooling functions. The so–called photo–recombination coefficients are principally not needed[8], since they can be deduced from the Einstein–Milne relations for bound–free transitions, which are already included in Eqs. (3.61, 3.63).

For the actual solution of the outlined system of equations, all integrals are evaluated numerically. The solution of the statistical equations (3.1) for the level populations including $n_{\rm II}$ requires an (inner) iteration of the escape probabilities of the bound–bound transitions, where the same procedure as outlined in Sect. 3.1.1.1 is applied. The system of equations is well–defined for given total particle density $n_{\rm sp} = n_{\rm II} + \sum n_i$, given temperature $T_{\rm g}$, given radiation field J_ν and given electron density $n_{\rm e}$. Another (outer) iteration is necessary to achieve the physical condition of charge conservation $n_{\rm e} = \sum n_{\rm II}$, comprising all ions under consideration, which in return yields the electron density.

According to the outlined equations, the degree of ionization of the gas and the bound–free heating/cooling rates are calculated simultaneously. Optical depths effects are not included concerning the bound–free transitions — in contrast to the bound–bound transitions discussed before, where it was possible to apply Sobolev theory[9]. This problem could only be handled by means of non–local (non–LTE) radiative transfer calculations. Since the basic approach of this work is to determine the radiative heating and cooling of single gas elements, we ignore these effects, assume the gas to be optically thin in the continuum and put $J_\nu = J_\nu^{\rm cont}$, where $J_\nu^{\rm cont}$ is the continuous *background* radiation field.

3.2.1.1 Fast, Approximate Method

A useful and quite illuminating form for the general bound–free rates and heating/cooling functions can be derived by introducing the photo–recombination coefficients as

$$\alpha_i(T) = \frac{4\pi}{S_i(T)} \int\limits_{\nu_{\rm thr}^i}^{\infty} \frac{2\nu^2}{c^2} \exp\left(-\tfrac{h\nu}{kT}\right) \sigma_i^{\rm bf}(\nu)\, d\nu \;\approx\; a_i\, T^{\,b_i} \tag{3.64}$$

The second part of Eq. (3.64) provides a common fit formula, where the parameters a_i and b_i are occasionally stated in the literature. As far as stimulated bound–free emission can be neglected (which usually is a very accurate approximation in the UV[10]), the recombination rates can be re-written as

$$R_{{\rm II}\,i} \;=\; n_{\rm e}\alpha_i(T_{\rm g}) \;+\; \frac{n_{\rm e}^2}{S_i(T_{\rm g})}\beta_i(T_{\rm g}) \quad . \tag{3.65}$$

[8]The photo–recombination coefficients, however, are very useful for quick, approximate calculations, see below.

[9]Such optical depth effects are expected to reduce the bound–free heating/cooling rates and drive the gas towards LTE–ionization already at comparatively smaller gas densities.

[10]Note, however, that the corresponding wavelengths of recombinations to highly excited states can be located in the optical or even IR spectral region.

If the continuous radiation field fits like $J_\nu \approx W B_\nu(T_{\rm rad}) \approx W 2h\nu^3/c^2 \exp(-\frac{h\nu}{kT_{\rm rad}})$ (Wien approximation), also the ionization rates can partly be expressed in terms of the photo–recombination coefficient:

$$R_{i\,\rm II} \;=\; W S_i(T_{\rm rad})\,\alpha_i(T_{\rm rad}) \;+\; n_{\rm e}\beta_i(T_{\rm g}) \tag{3.66}$$

By determining the derivative $\partial\alpha_i/\partial(1/kT)$ from Eq. (3.64), it can be shown that the net bound–free heating rate then reduces to

$$Q^{\rm bf}_{\rm rad} \;=\; \sum_{i=1}^{N} n_i\, W S_i(T_{\rm rad})\;\alpha_i(T_{\rm rad})\,\langle h\nu\rangle_i^{\rm abs} \;-\; n_{\rm II} n_{\rm e}\,\alpha_i(T_{\rm g})\,\langle h\nu\rangle_i^{\rm em} \tag{3.67}$$

$$\langle h\nu\rangle_i^{\rm abs} \;=\; \chi_i + (1.5{+}b_i)\,kT_{\rm rad} \tag{3.68}$$

$$\langle h\nu\rangle_i^{\rm em} \;=\; \chi_i + (1.5{+}b_i)\,kT_{\rm g} \quad , \tag{3.69}$$

where $\langle h\nu\rangle^{\rm abs/em}$ is the mean absorbed and emitted photon energy, respectively. Equation (3.67) is exact as far as the upper conditions are valid and the derivative $dZ_{\rm II}/dT$ can be neglected. The big technical advantage of Eqs. (3.65), (3.66) and (3.67) is that no integrals occur and that instead of a function $(\sigma_i^{\rm bf}(\nu))$ only two parameters (a_i and b_i) have to be known for each considered bound–free transition.

Equation (3.67) demonstrates that even if the number of bound–free absorbed photons equals the number of free–bound emitted photons (as in the case of negligible collisional ionization), the net rate of transferred energy does usually not vanish, in contrast to all bound–bound–type transitions discussed in the previous section. The reason lies within the integration over the absorbed/emitted photon spectrum, since the *mean* absorbed photon energy usually differs from the *mean* emitted photon energy. In the case of thermodynamic equilibrium, however, where $J_\nu{=}B_\nu(T_{\rm g})$ and $n_i = n_{\rm II} n_{\rm e}/S_i$, the net bound–free radiative heating rate according to Eq. (3.63) or according to Eq. (3.67) is indeed zero — as demanded by detailed balance.

The most simple case occurs, if solely the ground state of the neutral atom is considered and if the collisional ionization rates are neglected. From the condition of steady state $n_1 R_{1\,\rm II}{=}n_{\rm II} R_{\rm II\,1}$ it follows that in this case the net heating/cooling rate simplifies to

$$Q^{\rm bf}_{\rm rad} \;=\; n_{\rm II} n_{\rm e}\,\alpha_1(T_{\rm g})\Big(1.5{+}b_1\Big)\,k(T_{\rm rad} - T_{\rm g}) \quad . \tag{3.70}$$

In this case, radiative heating occurs for $T_{\rm rad} > T_{\rm g}$ and radiative cooling otherwise (independent of the value of the dilution factor W), which corresponds to the UV–limit depicted in Fig. 1.1.

3.2.2 The H–Atom

According to its overwhelming abundance, hydrogen is always important for both, the total degree of ionization and the radiative heating and cooling of the gas. However, the high–lying energy levels of hydrogen make it almost inaccessible for collisional excitation and collisional ionization at lower temperatures, so that the importance of hydrogen is mainly restricted to high temperatures.

For demonstration, a pure hydrogen plasma is examined in the following, consisting of the first three bound levels and the ionized state[11]. The following data of hydrogen and physical conditions are considered:

$$\chi_n = 13.598\,\mathrm{eV}/n^2, \quad g_n = 2n^2, \quad Z_{\rm II} = 1, \quad \sigma_n^{\rm bf}(\nu) = 2.815(+29)\,\frac{G_{\rm II}^n}{n^5\,\nu^3}$$
$$n_{<\rm H>} = n_1 + n_2 + n_3 + n_{\rm II}, \quad n_{\rm e} = n_{\rm II}, \quad \left\langle\frac{dv}{dl}\right\rangle = 20\,\mathrm{km\,s^{-1}}/500\,R_\odot$$

The bound–free absorption cross sections are taken from Mihalas (1978) with the abbreviation $X(Y) = X\cdot 10^Y$ in cgs–units. $G_{\rm II}^n$ are the bound–free Gaunt factors, which are of the order of unity. The collisional ionization rate coefficients $\beta_n(T_{\rm g})$ are taken from Luttermoser & Johnson (1992) and the references therein. The hydrogen bound–free transitions $\mathrm{II}\to 1$ (Lyman–continuum), $\mathrm{II}\to 2$ (Balmer–continuum) and $\mathrm{II}\to 3$ (Paschen–continuum) are calculated by means of the exact equations given in Sect. 3.2.1. The treatment of the hydrogen bound–bound transitions $2\to 1$ (Lyα), $3\to 1$ (Hα) and $3\to 2$ (Hβ) has been described in Sect. 3.1.

Figures 3.7 and 3.8 show the resulting total (bound–free plus bound–bound) cooling rates of hydrogen. Two figures are presented here, since the degree of ionization and the heating/cooling rates strongly depend on the continuous back–ground radiation field, which is chosen to be zero in the first and to equal a Planckian of 3000 K in the second figure. Note the scaling of the y–axis which is different from the other plots before.

Compared to the magnitude of the heating/cooling rates discussed so far, hydrogen heating and cooling is found to be unimportant for $T_{\rm g} \lesssim 6000\,$K. However for higher gas temperatures, hydrogen cooling soon becomes efficient and finally hydrogen provides the dominant cooling rate of the gas at temperatures above $\sim 8000\,$K. This temperature–dependency is a consequence of the high–lying energy levels of hydrogen, which can be collisionally excited or ionized solely in the case of high gas temperatures.

The total hydrogen cooling rate is found to scale roughly as $Q \propto \rho^2$, which is an indicator for strong non–LTE effects in the level populations[12].

[11] Luttermoser et al. (1989) have shown that a three–level model for hydrogen is sufficient in cool stellar environments for describing accurately both the emergent Hα spectrum and the contribution of hydrogen to the electron density.

[12] LTE without optical depth effects implies $Q \propto \rho$ for spectral lines as already discussed in Sect. 3.1. Concerning the bound–free heating/cooling functions, we have $n_{\rm II} n_{\rm e} \equiv S_i n_i$ in LTE, which according to Eq. (3.63) also implies $Q \propto \rho$ as far as hydrogen is mostly neutral.

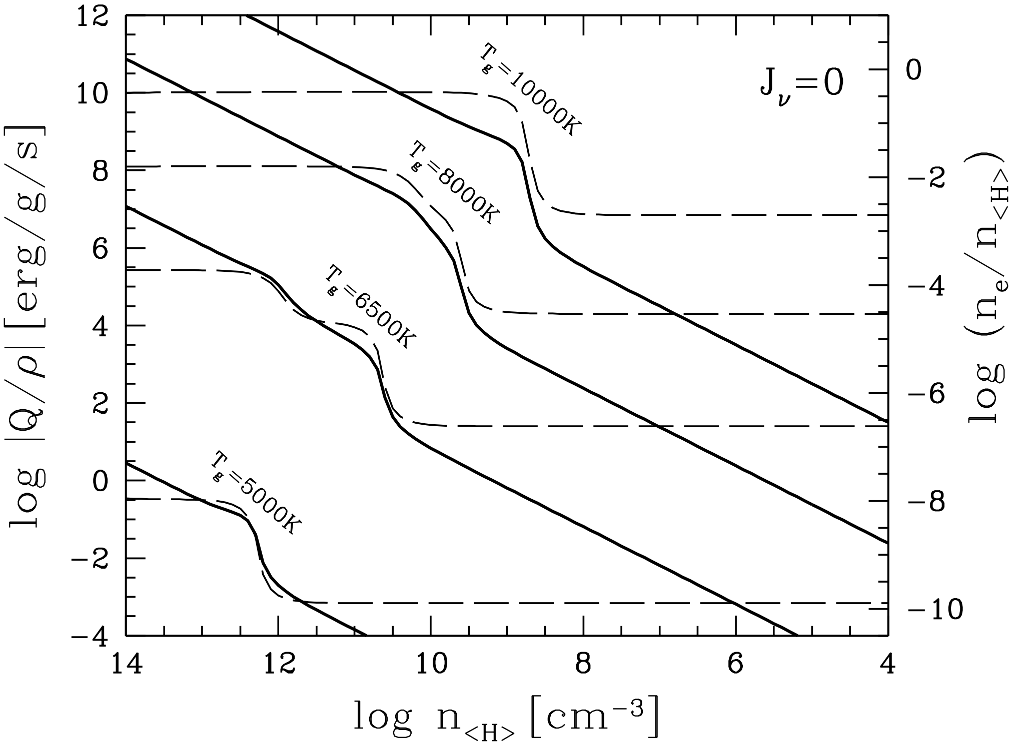

Figure 3.7: The total (bound–free plus bound–bound) hydrogen cooling rate (full lines, left axis) and the degree of ionization (dashed lines, right axis) in the case without continuous radiation field.

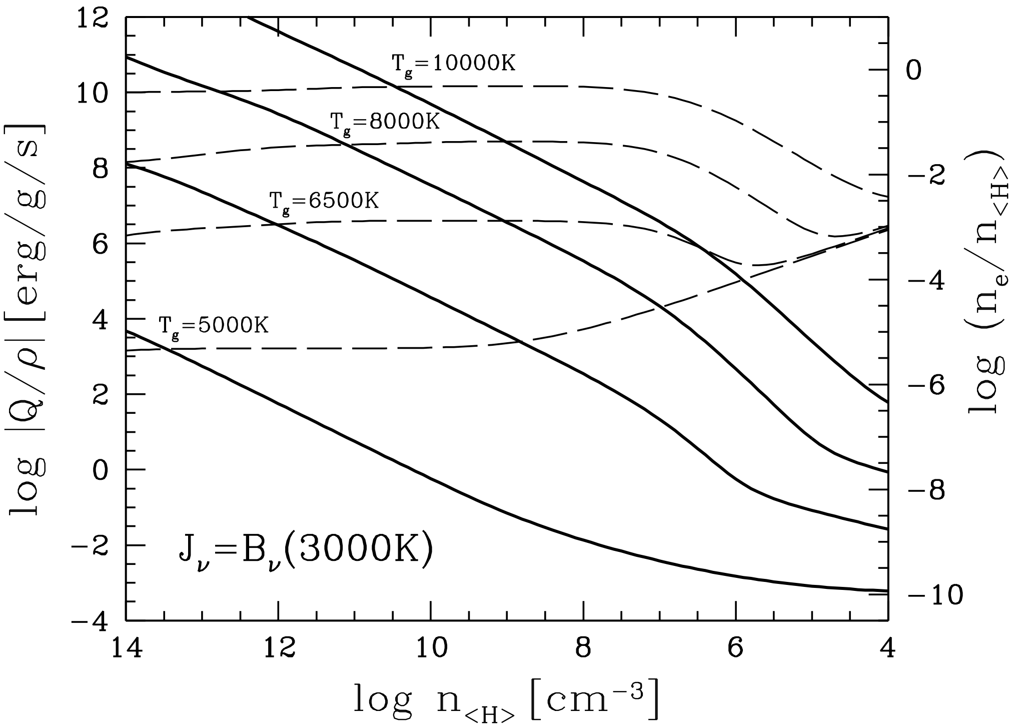

Figure 3.8: Same as Fig. 3.7, but with an underlying continuous radiation field.

The degree of ionization in Fig. 3.7 shows a step–like behavior. This is an effect caused by the varying optical depths of the hydrogen lines: With increasing gas density, Lyα and for larger densities also Hα become optically thick. Consequently, the effective radiative bound–bound rates according to Eqs. (3.20) and (3.21) become negligible compared with the collisional rates, forcing the upper level of the considered transition to achieve thermal population with respect to the lower level. Therefore, the collisional ionization rate from that upper level is increased by orders of magnitude, leading to successively enhanced electron concentrations from the right to the left in Fig. 3.7. In Fig. 3.8, this behavior is smeared out, since the rates for photoionisation enter into competition.

The hydrogen net cooling rates in the case $J_\nu = B_\nu(3000\,\mathrm{K})$ depicted in Fig. 3.8 are found to be larger than in the case $J_\nu = 0$, since photoionisation produces considerably higher electron concentrations, providing more collision partners[13].

Further details concerning the relative contributions of the different transitions and the level populations are presented in Fig. 3.9, considering the case $T_\mathrm{g}=8000\,\mathrm{K}$ and $J_\nu=0$. The b–factors for departures from LTE are calculated as

$$b_i = n_i/n_i^* = n_i\,S_i(T_\mathrm{g})/n_\mathrm{e}^{*\,2} \tag{3.71}$$

$$n_\mathrm{e}^* = \frac{n_{<\mathrm{H}>}}{0.5+\sqrt{0.25+n_{<\mathrm{H}>}\,(1/S_1+1/S_2+1/S_3)}} \tag{3.72}$$

Hydrogen bound–free cooling is found to dominate in hot dense media, whereas emission in hydrogen lines dominates the cooling of a hot thin gas, which is a straightforward consequence of the increasing optical depths in the hydrogen lines with increasing gas density. The transition between these two cases occurs at a particular density, which depends on the considered gas temperature and velocity gradient. In Fig. 3.9, this transition density is about $n_{<\mathrm{H}>}=10^{10}\,\mathrm{cm}^{-3}$. The bumps on the total cooling rates depicted in Fig. 3.7 correspond to these transitions.

The Lyman–continuum always provides the most important bound–free cooling rate. The relative contributions of the other continua with respect to the Lyman–continuum scale as $1/n^3$, which can be analytically derived from Eq. (3.63).

Lyα is usually the most important hydrogen cooling line as has already been pointed out by Hollenbach & McKee (1989) and Neufeld & Hollenbach (1994), although Lyα is optically thick for all considered densities ($\widetilde{P}^\mathrm{e}_{21}\approx 0.5/n_{<\mathrm{H}>}$ for the chosen velocity gradient). However, for large densities, Hα becomes more efficient than Lyα, because the Hα transition ($3\to 2$) does not involve the ground level and, hence, is not so much affected by optical thickness. Therefore, there is in fact a small density–interval, where Hα is the most efficient cooling process, already more important than Lyα and still more important than bound–free transitions (around $n_{<\mathrm{H}>}=10^{10}\,\mathrm{cm}^{-3}$ in

[13]This is different from all cooling rates discussed so far, since we have not yet considered a change of the concentrations of the collision partners. If the concentration of the collision partners are constant, an increase of the background continuous radiation field always implies reduced net cooling rates and finally causes net radiative heating.

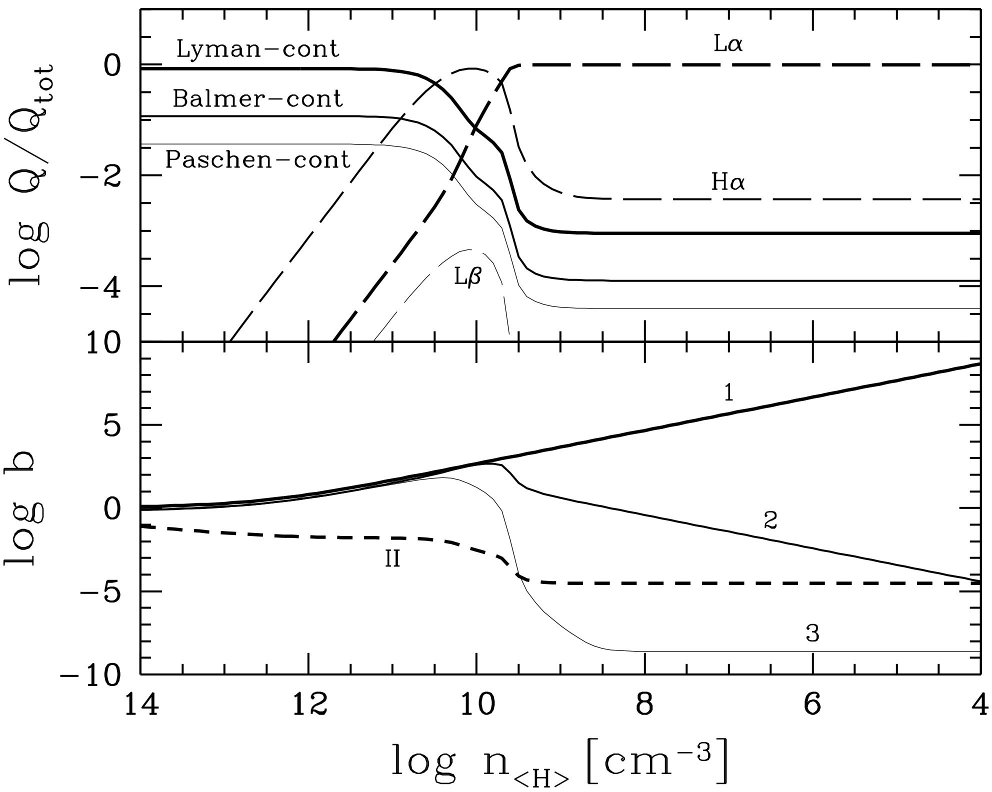

Figure 3.9: Details for the case $T_{\rm g} = 8000\,{\rm K}$ and $J_\nu = 0$. Upper panel: relative contributions of the different bound–bound and bound–free transitions. Lower panel: b–factors for the hydrogen levels.

Fig. 3.9). Lyβ is also always optically thick (similar to Lyα) and hence always much less important than Hα.

The lower panel of Fig. 3.9 shows the gradual change from almost LTE–ionization and LTE–population ($b_n \approx 1$) at large densities to pronounced non–LTE conditions at small densities, caused by the decreasing relevance of the collisional processes. The $b_{\rm II}$–factor indicates that the degree of ionization of hydrogen is always sub–thermal (provided that $T_{\rm rad} < T_{\rm g}$ for a Planck field $J_\nu = B_\nu(T_{\rm rad})$). Consequently, the ground state is populated hyper–thermally, which is an important result for the CSEs of cool stars, since it keeps the gas predominantly neutral also at fairly high temperatures and low densities, where hydrogen would be strongly ionized according to LTE. The populations of the excited hydrogen levels are completely decoupled at small densities and are thermally coupled to the ground state for large densities, caused by the strongly decreasing escape probabilities of the lines photons. LTE population is established in direction of increasing gas densities successively from the lower to the higher excited levels, finally also for the ionized state. For complete LTE–ionization, however, extremely large densities are required (e. g. $n_{\rm <H>} \gtrsim 10^{16}\,{\rm cm}^{-3}$ for $T_{\rm g} = 10000\,{\rm K}$), where the three–body–recombination rates become relevant.

The situation in the case $J_\nu = B_\nu(3000\,\mathrm{K})$ is quite different. Here, the net bound–free cooling rates dominate over net bound–bound cooling rates unless the gas density is smaller than $\sim 10^7\,\mathrm{cm}^{-3}$ for all considered temperatures. Negative and positive net contributions from the different transitions may occur at the same time, although the sum of all contributions always results in a net cooling.

To summarize, hydrogen is mainly an important high–temperature coolant, approximately contributing as $Q \propto \rho^2$. For large densities the Lyman–continuum is most effective, whereas at small densities Lyα dominates.

3.2.3 Other Neutral Atoms

Concerning other atoms than hydrogen, solely the electronic ground states of the neutral atoms are considered in this work for practical reasons. Furthermore, since all bound–free transitions from the ground states are located in the UV, the approximate method outlined on p. 46 can be used for the calculation of the photo–recombination rates and the bound–free heating/cooling functions. The approximate photo–recombination rates derived from Eq. (3.65) are found to show reasonable agreement with those calculated from Eq. (3.61), when applying the photoionisation cross sections of the various metal atoms from Schmutzler (1987). Therefore, the application of the approximate method is rather accurate and very practical, since it avoids the time–consuming numerical frequency integrations.

The rates of collisional ionization are determined from the analytical expression given by Allen (1973)

$$\beta_1(T_\mathrm{g}) = 1.1(-8)\, o_1 \sqrt{T_\mathrm{g}} \left(\chi_1/\mathrm{eV}\right)^{-2} \exp\left(\frac{\chi_1}{kT_\mathrm{g}}\right) \quad , \tag{3.73}$$

where o_1 is the number of optical electrons of the neutral atom. Table 3.3 summarizes the data used for the determination of the the bound–free heating/cooling rates.

At the end of this section, the important features of the developed methods for the bound–free transitions are once more summarized. The methods are used for the determination of the electron concentration, the concentrations of the various ions and the calculation of the bound–free heating and cooling rates:

- Ionization equilibrium (steady state non–LTE) is assumed to determine the particle densities of the considered atoms, ions and electrons. The rates of photoionisation and –recombination, collisional ionization and three–body–recombination are taken into account for each atom.

- A couple of simplifying assumptions are used for other atoms than hydrogen. Hydrogen is treated more accurately, including of the first two excited levels.

- Bound-free optical depths effects are ignored.

Table 3.3: Bound–free heating and cooling: considered species and atomic data

Species	χ_1 [eV] [(1)]	$g_1^{(1)}$	$Z_{\rm II}^{(1,3)}$	$a_1^{(2)}$	$b_1^{(2)}$	$o_1^{(4)}$
He	24.587	1	2	2.06(-10)	-0.67	2
C	11.260	9	6	1.43(-10)	-0.61	2
N	14.534	4	9	1.30(-10)	-0.62	3
O	13.618	9	4	1.24(-10)	-0.63	4
S	10.360	9	4	1.40(-10)	-0.63	4
Mg	7.646	1	2	3.70(-10)	-0.86	2
Si	8.151	9	6	1.50(-10)	-0.64	2
Fe	7.870	25	30	1.50(-10)	-0.65	2
Na	5.139	2	1	1.40(-10)	-0.69	1

[(1)]: Allen (1973).
[(2)]: Beck (1993) and references therein.
[(3)]: For simplicity, the partition function $Z_{\rm II}$ is approximated by the statistical weight of the ground state of the ionized atom.
[(4)]: The number of "optical" electrons is the number of electrons in the last occupied quantum state

In conclusion, the outlined methods are approximate, but simple and applicable to the wide range of density conditions present in circumstellar envelopes. The gradual change from almost LTE ionization at large densities to non–LTE ionization at small densities can be reproduced.

3.3 Photodissociation and Radiative Association

Radiative gains and losses of the gas can also be caused by chemical reactions. According to the definition of the internal energy in this work (cf. Fig. 2.1), solely those reactions which are accompanied by an absorption or emission of a photon (photodissociation or radiative association) contribute to the radiative heating or cooling, respectively[14].

The dissociation potentials of the molecules of astrophysical interest typically range from 3 to 8 eV (exceptions CO: 11.1 eV and N_2: 9.9 eV), which already gives a first impression of the concerned wavelength region of the radiative processes under investigation. Compared to typical molecular ionization potentials of more than about 10 eV, the dissociation energies are substantially smaller. Thus, as far as hard

[14]Pure gas phase reactions, which do not involve photons, do not contribute to the *radiative* heating/cooling of the gas even if they are "exothermic" or "endothermic". Such reactions only convert dissociation potential energies into translational, ro–vibrational and electronic excitation energies and might be considered as additional source terms for these pools, but do not directly affect the total internal energy of the gas.

UV radiation is absent, photodissociation is expected to be more efficient for the heating of the gas than photoionisation in the molecular domain of circumstellar envelopes, even if the corresponding photo cross sections are smaller. In the following, a photo–chemical reaction of prototype

$$\mathrm{AB} + h\nu \underset{k_\mathrm{r}}{\overset{k_\mathrm{f}}{\rightleftharpoons}} \mathrm{A} + \mathrm{B} \tag{3.74}$$

is considered, where A and B label an atom, ion, molecule or electron and AB the corresponding composite species. k_f and k_r are the rate coefficients of the forward and reverse reaction, respectively. Irrespective of the fact that photodissociation is mostly initiated by absorption in electronic bands (e. g. the Lyman– and Werner–bands of $\mathrm{H_2}$), which are in principle narrow–spaced bound–bound transitions, the photodissociation cross sections $\sigma^\mathrm{f}(\nu)$ are assumed to be given in a quasi–continuous way

$$k_\mathrm{f} = 4\pi \int \frac{J_\nu}{h\nu}\,\sigma^\mathrm{f}(\nu)\,d\nu \quad . \tag{3.75}$$

From the detailed balance consideration $n^*_\mathrm{AB}\,k_\mathrm{f}\Big|_{J_\nu=B_\nu} = n^*_\mathrm{A} n^*_\mathrm{B}\,k_\mathrm{r}$ it is found

$$k_\mathrm{r}(T) = \left.\frac{n^*_\mathrm{AB}}{n^*_\mathrm{A} n^*_\mathrm{B}}\right|_T 4\pi \int \frac{B_\nu(T)}{h\nu}\,\sigma^\mathrm{f}(\nu)\,d\nu \;\approx\; A\,T^\alpha \exp\left(-\frac{E_a}{kT}\right) \quad . \tag{3.76}$$

The second part of Eq. (3.76) is the usual Arrhenius law for the backward reaction with E_a being the activation energy. Coming back to the first part, n^*_X is the particle density of species X in chemical equilibrium, i. e. the first fraction in Eq. (3.76) can be determined by means of the law of mass action from the corresponding free enthalpy of formation at standard pressure p°

$$\left.\frac{n^*_\mathrm{AB}}{n^*_\mathrm{A} n^*_\mathrm{B}}\right|_T = \frac{kT}{p^\circ} \exp\Big(-\frac{\Delta_\mathrm{f} G^\circ(T)}{kT}\Big) \tag{3.77}$$

$$\Delta_\mathrm{f} G^\circ(T) \;=\; \Delta_\mathrm{f} G^\circ_\mathrm{AB}(T) - \Delta_\mathrm{f} G^\circ_\mathrm{A}(T) - \Delta_\mathrm{f} G^\circ_\mathrm{B}(T) \;<\; 0 \tag{3.78}$$

The contribution of the photochemical reaction (3.74) to the total net heating function of the gas is given by

$$Q^\mathrm{chem}_\mathrm{rad} = 4\pi \int \left(n_\mathrm{AB} J_\nu - n_\mathrm{A} n_\mathrm{B} \left.\frac{n^*_\mathrm{AB}}{n^*_\mathrm{A} n^*_\mathrm{B}}\right|_{T_\mathrm{g}} B_\nu(T_\mathrm{g}) \right) \sigma^\mathrm{f}(\nu)\,d\nu\,. \tag{3.79}$$

n_X are the actual particle densities, which in this context have to be determined from the steady–state solution of a chemical reaction network. Especially interesting are those reactions, which have the largest net photo–rates (this does not necessarily imply that the involved molecule has be to abundant).

The general problem of the treatment of these processes is the large amount of different species to be considered and the poor availability of appropriate molecular data $\sigma^{\rm f}(\nu)$[15]. Therefore, the so far outlined equations do not look very promising, since they can solely be applied to a very few, well–known molecules (e. g. H_2, CO).

This problem can be avoided by the following consideration, analogously to the approximate method for the bound–free transitions discussed in the last section. We assume the continuous radiation field to fit like $J_\nu \approx W B_\nu(T_{\rm rad})$ and consider the case $\max\{kT_{\rm g}, kT_{\rm rad}\} \ll D^0_{\rm AB} < h\nu$, applying Wien's law as before. By differentiating Eq. (3.76) with respect to $1/kT$, the following expression can be derived:

$$Q^{\rm chem}_{\rm rad} = n_{\rm AB}\, W\, k_{\rm r}(T_{\rm rad}) \left.\frac{n^*_{\rm A} n^*_{\rm B}}{n^*_{\rm AB}}\right|_{T_{\rm rad}} \langle h\nu\rangle^{\rm abs} - n_{\rm A} n_{\rm B} k_{\rm r}(T_{\rm g})\, \langle h\nu\rangle^{\rm em} \qquad (3.80)$$

$$\langle h\nu\rangle^{\rm abs} = -\Delta_{\rm f} G^{\circ}(T_{\rm rad}) + E_a + (\alpha - 1)\, kT_{\rm rad} \qquad (3.81)$$

$$\langle h\nu\rangle^{\rm em} = -\Delta_{\rm f} G^{\circ}(T_{\rm g}) + E_a + (\alpha - 1)\, kT_{\rm g} \qquad (3.82)$$

Compared to Eq. (3.79), this expression for the net heating rate of a considered photo–reaction can easily be applied to the results of chemical reaction networks, since only the Gibbs energies $\Delta_{\rm f} G^{\circ}$ and the Arrhenius coefficients A, α and E_a have to be known. The considerations find the mean absorbed and emitted photon energies to be of order $-\Delta_{\rm f} G^{\circ} + E_a - kT \approx D^0_{\rm AB} + E_a$, i. e. the molecule dissociation energy plus the activation energy of the radiative association reaction. The net heating rate vanishes in the case of thermodynamic equilibrium, as expected.

For a comprehensive discussion of the importance of photodissociation and radiative association for the thermal balance of the gas in CSEs, the (steady state) results of chemical reaction network calculations are required providing the various concentrations of the species under examination. Such investigations go beyond the scope of this work and must be left to future investigations. However, an important example is considered in the following section.

3.3.1 The H^- Heating/Cooling Rate

The negative hydrogen ion H^- shows exceptionally large photo–rates in circumstellar envelopes (Beck 1993). Its bound–free and free–free transitions are furthermore well–known to be the most significant contributor to the gas opacity in the stellar atmospheres of warm stars as the sun. Therefore, it is important to consider the radiative heating and cooling by H^- in more details.

The concentration of H^- in circumstellar envelopes is mostly controlled by the following two reactions (Beck et al. 1992):

$$H^- + h\nu \underset{k_{\rm r,1}}{\overset{k_{\rm f,1}}{\rightleftharpoons}} H + e^- \qquad (3.83)$$

$$H^- + H \underset{k_{\rm r,2}}{\overset{k_{\rm f,2}}{\rightleftharpoons}} H_2 + e^- \quad . \qquad (3.84)$$

[15] Considering the frequency integration in Eq. (3.79), the soft end of $\sigma^{\rm f}(\nu)$ almost entirely determines the rates and the heating/cooling function — difficult to measure in laboratory experiments.

Thus, the concentration of H^- in steady state ("kinetic equilibrium") is always proportional to the electron concentration:

$$n_{\rm H^-} = n_{\rm e}\,\frac{n_{\rm H}\,k_{\rm r,1} + n_{\rm H_2}k_{\rm r,2}}{k_{\rm f,1} + n_{\rm H}\,k_{\rm f,2}} \qquad (3.85)$$

Reaction 3.83 ("H^- bound–free") is the process to be considered for the radiative heating and cooling of the gas. The above outlined methods are straightforwardly applied, although the bound–free transitions of H^- are classified as photoionisation and radiative recombination rather than as photodissociation and radiative association. The reaction rate coefficients $k_{\rm f,1}$ and $k_{\rm r,1}$ are calculated by means of the "exact" Eqs. (3.75) and (3.76), where A labels the H atom, B the electron and AB the negative ion H^-. The bound–free absorption cross section of H^- is interpolated from tables given by Wishart (1979). Stimulated recombinations are treated in LTE, for simplicity. The rate coefficients of the second reaction (3.84) are taken as

$$k_{\rm f,2} \;=\; 1.35(-9)\ {\rm cm^3\,s^{-1}}\ \ \text{(Schmetekopf et al. 1967)} \qquad (3.86)$$

$$k_{\rm r,2} \;=\; \frac{n^*_{\rm H^-}n^*_{\rm H}}{n^*_{\rm H_2}n^*_{\rm e}}\,k_{\rm f,2} \quad . \qquad (3.87)$$

Considering a gas of solar elemental abundances, the required particle densities $n_{\rm e}$, $n_{\rm H}$ and $n_{\rm H_2}$ are determined by means of the methods outlined in Chapter 4. The $n_{\rm H^-}$ density is calculated afterwards from Eq. (3.85)[16]. Accordingly, collisional ionization and photoionisation of metal atoms with low ionization potentials (Na, Mg, Fe, ...) are important low–temperature electron donators and provide electron concentrations of at least 10^{-5} for $T_{\rm g} > 5000\,{\rm K}$, leading to considerable H^- particle densities[17].

The radiative heating and cooling by H^- comprises bound–free and free-free contributions. The bound–free heating/cooling rate is calculated according to Eq. (3.79), and the free-free heating/cooling rate is determined by[18]

$$Q_{\rm rad}({\rm H^-}) \;=\; Q^{\rm bf}_{\rm rad}({\rm H^-}) + Q^{\rm ff}_{\rm rad}({\rm H^-}) \qquad (3.88)$$

$$Q^{\rm ff}_{\rm rad}({\rm H^-}) \;=\; 4\pi\, n_{\rm H}\, n_{\rm e}\int\Big(J_\nu - B_\nu(T_{\rm g})\Big)\,\sigma^{\rm ff}(\nu)\;d\nu \quad , \qquad (3.89)$$

where the free–free cross section $\sigma^{\rm ff}(\nu)$ is fitted on the dipole length calculations of Stilley & Callaway (1970):

$$\sigma^{\rm ff}(\nu) = \left(\frac{1.3727(-25)}{\nu} + \frac{4.3748(-10) - 2.5993(-7)/T_{\rm g}}{\nu^2}\right)\Big(1 - \exp\big(-\frac{h\nu}{kT_{\rm g}}\big)\Big)\ {\rm cm^5}$$

[16] This is an approximate procedure, since it neglects the feedback on the former particle densities.

[17] In contrast, the consideration of a pure hydrogen plasma leads to a systematic underestimation of the H^- concentration and heating/cooling rates: The resulting electron concentrations are smaller in this case, especially around $T_{\rm g} \approx 6000\,{\rm K}$, just where the heating and cooling of H^- turns out to be most significant.

[18] Kirchhoff's law $\epsilon^{\rm ff}_\nu = \kappa^{\rm ff}_\nu B_\nu(T_{\rm g})$ is applicable to free–free transitions also in non–LTE, since they solely refer to the thermal motion of the gas.

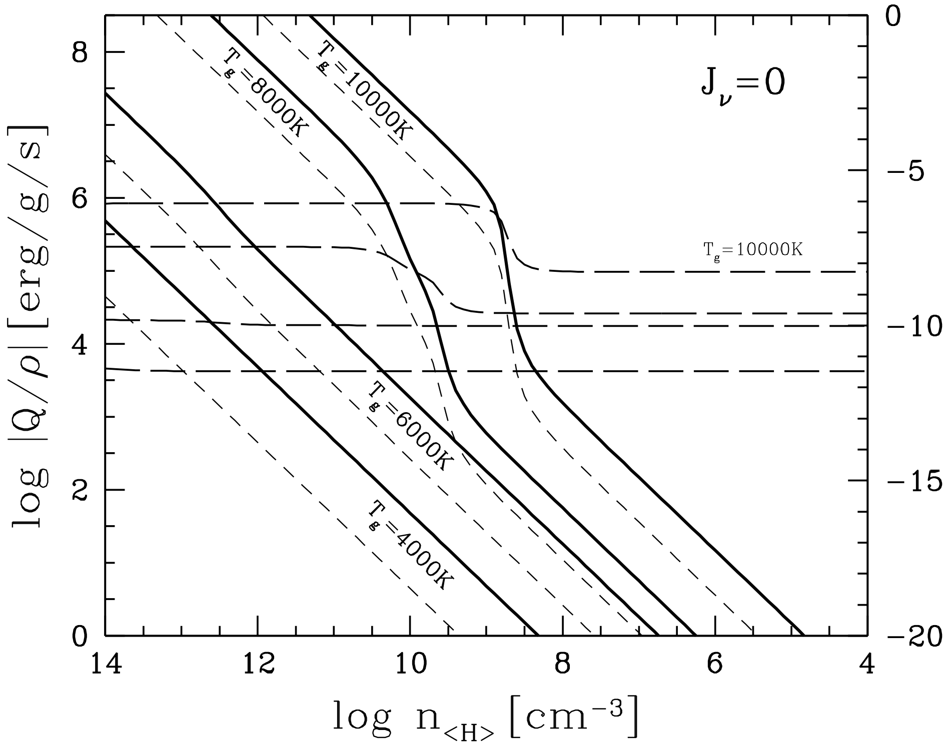

Figure 3.10: The total (bound–free + free–free) cooling rate (full lines), the free–free cooling rate (short dashed lines, left axis) and the concentration (long dashed lines, right axis) of H^- in the case without continuous radiation field.

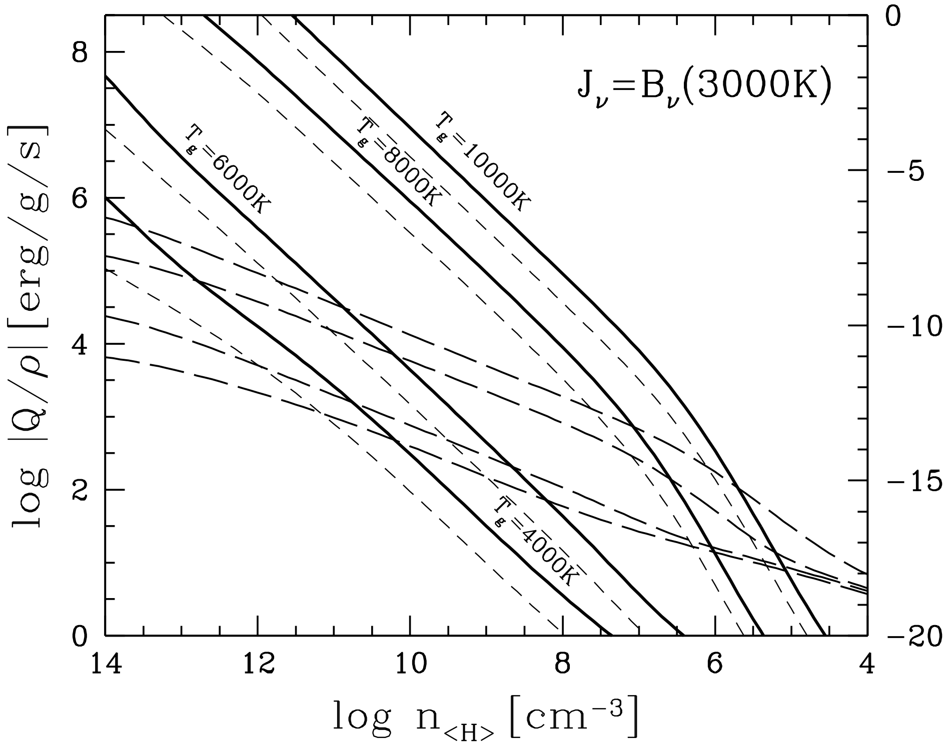

Figure 3.11: Same as Fig. 3.10, but with underlying continuous radiation field.

Figures 3.10 and 3.11 depict the results for the two cases $J_\nu = 0$ and $J_\nu = B_\nu(3000\,\mathrm{K})$. In both cases, the radiative cooling rate of H^- scales as $Q \propto n_\mathrm{H}\, n_\mathrm{e}$, which implies at least $Q \propto \rho^2$. Therefore, the radiative heating and cooling of H^- is only important for a dense medium, e. g. in stellar atmospheres. The step–like behavior of the H^- concentration and total cooling rates for $T_\mathrm{g} = 10000\,\mathrm{K}$ and $T_\mathrm{g} = 8000\,\mathrm{K}$ in Fig. 3.10 correspond to the step–like degree of ionization of hydrogen (cf. Figs. 3.7 and 3.8), whereas for lower gas temperatures the electron concentration is controlled by the metals with low ionization potentials. For even lower gas temperatures (not shown in the figures), hydrogen is mostly locked in H_2, and the concentration and the heating/cooling rates of H^- rapidly vanish.

The calculated H^- concentrations for the case $J_\nu = B_\nu(3000\,\mathrm{K})$ (cf. Fig. 3.11) are considerably smaller due to the large photoionisation rates $k_{\mathrm{f},1}$. However, since the radiative cooling rates of H^- are related to $n_\mathrm{H}\, n_\mathrm{e}$ and not to n_{H^-}, the cooling rates remain similar. The differences between Figs. 3.10 and 3.11 are mainly caused by the different electron concentrations. Free–free heating/cooling of H^- is always found to be less important than bound–free heating/cooling. For even more intense radiation fields (not shown), the bound–free transitions effectively destroy the negative ion, so that radiative heating by H^- is rarely found to be significant — only, if an active chemistry (at large densities) quickly restores the H^- ions.

In conclusion, H^- is mainly an important coolant for large densities and medium temperatures, where the product of electron and atomic hydrogen density is large.

3.4 Free–Free Transitions

If the gas is almost fully ionized and the density is large ($n_{<\mathrm{H}>} \gtrsim 10^{11}\mathrm{cm}^{-3}$), free-free emission (Bremsstrahlung) becomes an effective cooling process. We use the ordinary expression for free–free emission for a partially singly ionized gas given in Allen (1973) and include, for consistency, the reverse process of free–free absorption by means of the relation $\epsilon_\nu^\mathrm{ff} = \kappa_\nu^\mathrm{ff} B_\nu(T_\mathrm{g})$

$$\epsilon_\nu^\mathrm{ff}(T_\mathrm{g}) = 5.44(-39)\,\frac{n_\mathrm{e}^2}{\sqrt{T_\mathrm{g}}}\exp\Big(-\frac{h\nu}{kT_\mathrm{g}}\Big) \tag{3.90}$$

$$Q_\mathrm{rad}^\mathrm{ff} = 4\pi\int \epsilon_\nu^\mathrm{ff}(T_\mathrm{g})\left(\frac{J_\nu}{B_\nu(T_\mathrm{g})} - 1\right)\, d\nu \quad . \tag{3.91}$$

Free–free transitions always concern the whole electromagnetic spectrum. Consequently, free–free transitions principally provide one of lasting possibilities for radiative heating, if the incident radiation field mainly consists of IR photons, where other radiative heating processes become impossible. However, the gas must be considerably ionized ($Q_\mathrm{rad}^\mathrm{ff} \propto n_\mathrm{e}^2$) for such heating.

3.5 Overview of the Considered Radiative Processes

Figure 3.5 summarizes the radiative heating/cooling functions considered in this work. To what extend this selection is complete, must be left to the reader's discretion. The shown spectral positions of the various radiative processes already provide a first impression of their net effect and their importance for the heating and cooling of the gas. In general, radiative heating occurs in the case $J_\nu > B_\nu(T_g)$ and cooling in the opposite case[19]. For the depicted case of a diluted Planck–type radiation field, the radiative processes at short wavelengths (bound–free transitions, spectral lines) are responsible for radiative heating and those at long wavelengths (vibrational and rotational transitions, spectral lines) for cooling. Considering the thermal relaxation of the gas towards radiative equilibrium, the gas temperature will tune in such a way, that these gains and losses balance each other. Note that the formation of molecules in the gas intensifies the interaction between matter and radiation field at long wavelengths, thus reinforcing radiative cooling and consequently leading to lower radiative equilibrium temperatures (this effect can in fact cause thermal bifurcations in the gas as discussed in Chapter 6).

As part of this summary, the important features of the developed methods are once more placed together:

- All considered radiative processes are treated in non–LTE. The non–LTE description of the molecules is restricted to individual vibrational and rotational excitation temperatures. The heating/cooling rates are calculated in steady–state.

- All corresponding reverse processes are taken into account, relying on detailed balance considerations. Consequently, each considered pair of forward and reverse process can appear as both net radiative heating and cooling. Which case actually occurs depends upon a specific relation between the gas temperature and the radiation field. In the case $J_\nu = B_\nu(T_g)$ (as in thermodynamic equilibrium), all discussed net heating/cooling rates vanish ($Q_{\rm rad} = 0$).

- The heating/cooling rates are formulated for arbitrary radiation fields J_ν. Especially simple expressions are derived for diluted Planck fields of type $J_\nu = W B_\nu(T_{\rm rad})$[20].

- Optical depths effects are included for all bound–bound type transitions and neglected otherwise.

[19]These relations are not exact, but usually correct also in non–LTE, since the corresponding source functions (considering e. g. a two–level–atom) generally satisfy $J_\nu \gtrless S_\nu \gtrless B_\nu(T_g)$.

[20]The fit parameters W and $T_{\rm rad}$ can be different for different spectral regions (e. g. UV and IR), as far as the considered heating/cooling processes merely refer to such region.

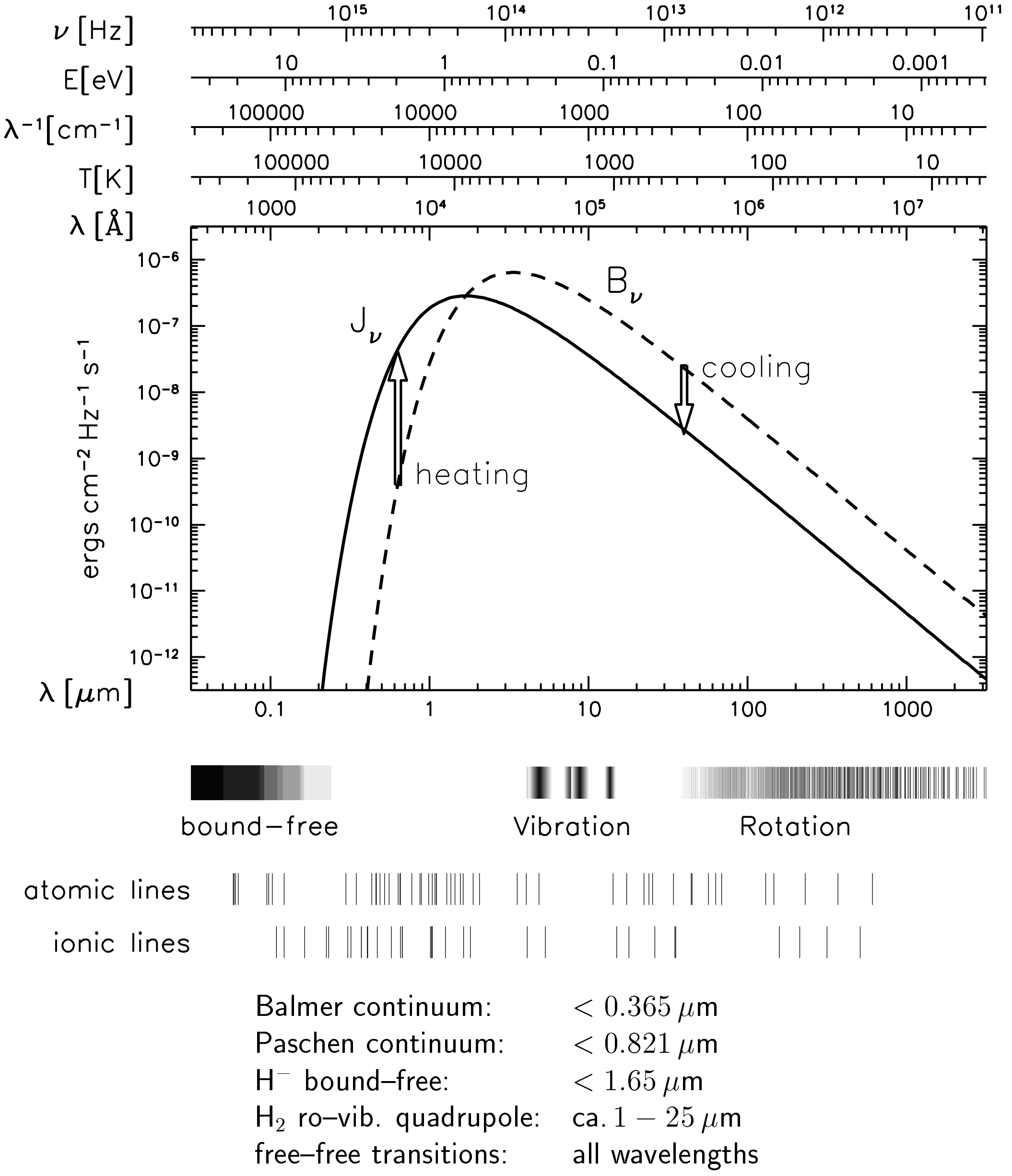

Figure 3.12: Overview of the considered heating and cooling processes. The full line shows an assumed continuous mean intensity J_ν according to Eq. (1.6) with $W = 0.029$ ($r = 3\,R_*$ for pure radial dilution) and $T_{\rm rad} = 3000\,$K. The dashed line is the Planck function for $T_{\rm g} = 1500\,$K. The arrows indicate the energy exchange between matter and radiation field, favoring radiative heating at short and radiative cooling at long wavelengths, respectively. The lower panel indicates the wavelength regions of the considered heating/cooling processes.

3.6 Further Heating and Cooling Processes

The theoretical part of this work ceases with some remarks on those heating and cooling processes which have *not* been taken into account.

Of course, the proper inclusion of *all* radiative processes is principally desirable. The construction of such an utmost "complete" set, however, is a long lasting process and cannot be carried out by one single work. The selection of heating/cooling functions of this work may be extended in two ways: First, to include a larger *number* of processes (more species, more lines, etc.) of the already considered types of processes, and second, to take into account further *types* of processes.

A pure quantitative extension will probably not lead to substantial changes compared to the forthcoming results of this work, since the most promising candidates of each considered type of process are already included. What may be crucial, however, are the additional types of processes not considered so far, which might prove to be important under certain circumstances. As the author started to study a few of them, more or less serious, specific obstacles occurred which prevent a simple quantitative discussion for the time being. Together with some valuations and remarks, these obstacles shall be fixed in this section.

Table 3.4 lists some interesting candidates of different types of processes, the expected spectral region of absorbed/emitted photons, the expected effect for the gas, the faced obstacles for the determination of the corresponding heating/cooling rates and some comments. Extensive explanations are not included, as Table 3.4 is mainly given for reasons of completeness and to open the discussion. Some additional comments, however, are necessary concerning the energy gains and losses caused by the presence of dust grains:

Due to the large time scales involved in the dust formation process, the dust component (here especially the total dust surface) should be treated time–dependently (e. g. Fleischer et al. 1992) and cannot be determined by any steady–state considerations. Therefore, the heating and cooling processes caused by the presence of dust are not explicitly included in this work.

Dust grains provide a similar external pool as the radiation field (see Fig. 2.1). Consequently, energy transfer rates directly occur by collisions. The corresponding rates can easily be added to the total net radiative heating rate of the gas, if the appropriate informations about the dust component (total surface, dust temperature, drift velocities, etc.) are available. The rates for thermal accommodation (energy transfer via inelastic gas–dust collisions) are given, for example, in Burke & Hollenbach (1983) and those for drift heating (energy transfer via gas collisions with moving dust grains caused by radiation pressure) in Goldreich & Scoville (1976) or in Krüger et al. (1994).

More difficult to determine are the heating/cooling rates caused by surface chemical reactions, which principally exchange all types of gas internal energies (especially dissociation and ionization potentials) with the dust component. Very detailed knowledge about these reactions is required.

Table 3.4: Overview of further heating and cooling processes not explicitly considered in this work.

process	spectral region (estimated)	important for what?	obstacles	comments
photo-dissociation	several eV	rad. heating in molecular domain	number of trans., $\sigma(\nu)$, concurring reaction channels and rates	(2)
electronic trans. of molecules	several eV	rad. heating in molecular domain, maybe important counterbalance for rot. and vib. cooling	number of trans., rad. lifetimes, coll. rates, line overlaps	probably strong non–LTE effects: short rad. lifetimes (typically $0.01 - 1\,\mu$s) and small coll. rates
vib. trans. of polyatomic molecules	$3 - 20\,\mu$m	heating and cooling	selection rules, rad. lifetimes (analytical expressions), coll. rates	unpolar polyatomic molecules may become polar during vibration, (1)
vib. overtone trans.	$1 - 5\mu$m	heating and cooling	rad. lifetimes (analytical expressions)	A–coeffs. about one magnitude smaller than for ground tone trans.
rot. trans. of non–linear molecules	$20 - 1000$ GHz	cooling	selection rules, rad. lifetimes (analytical expressions)	(1)
bf. trans. from excited states	several eV	heating and cooling, indirect (de–) excitation of bound levels	$\sigma(\nu)$, complete model atoms	(2)
bf. and ff. trans. of negative ions, molecules	several 0.1 eV	heating and cooling	$\sigma(\nu)$, concurring reaction channels and rates	(2)
gas phase chemical reactions	depends	indirect excitation of electronic and vib. levels of reaction products, probably followed by emission, i. e. cooling	reaction rates, reaction heats, energy distribution among the various degrees of freedom on the reactants	difficult, cooling approximately proceeds on chemical time scale

bf. = bound–free, **ff.** = free–free, **rad.** = radiative, **rot.** = rotational, **vib.** = vibrational, **A–coeffs.** = Einstein coefficients for spontaneous emission (inverse of the radiative lifetimes), **coll. rates** = collisional de-excitation rate coefficients, **trans.** = transitions, $\sigma(\nu)$ = corresponding photo cross sections.

(1) = polyatomic molecules (except for H_2O) are generally less abundant than diatomic molecules (e. g. CO) in CSEs

(2) = see the simple, approximate methods proposed in this work

Table 3.4 *continued from page 62*

process	spectral region (estimated)	important for what?	obstacles	comments
Raman scattering	UV and optical	rad. heating of molecular gases by inelastic scattering	absolute cross sections for Raman scattering (Stokes and Anti-stokes) of individual molecules , e. g. of H_2	applies to polar and unpolar molecules and to arbitrary wavelengths, however, cross sections are small
dust: thermal accommodation	–	heating and cooling	–	according to temperature difference between gas and dust
dust: drift heating	–	heating	–	efficient mechanism, see Krüger et al. (1994)
dust: surface reactions	–	gain or loss of dissociation potential energies (heating and cooling), desorption of excited reactants (heating)	reaction rates, reaction heats, energy distribution among the various degrees of freedom of the reaction products	difficult

Chapter 4

The Calculation of the Equation of State

The calculation of the equation of state provides the basic link between the microphysics and the thermodynamic description of the gas. Having once determined the microphysical quantities (the particle densities) as function of a suitable set of thermodynamic state variables (e. g. temperature and density), all macroscopic properties of the gas can be determined by means of statistical methods. Thus, the modeling of the gas can be performed on a higher, thermodynamic level without going back into the details of microphysics.

This chapter describes the assumptions and the numerical techniques used to determine the particle densities and the internal energy of the gas as function of $T_{\rm g}$ and ρ. As pointed out in Chapter 2, this work does not rely on LTE, but considers a steady state. Consequently, two additional external parameters enter into the usual thermodynamic description: the radiation field J_ν and the mean velocity gradient $\left\langle\frac{dv}{dl}\right\rangle$. Since the techniques are the same for all following applications, they are summarized in this separate chapter.

4.1 Calculation of the Particle Concentrations

The basis for the calculation of the particle concentrations are the element abundances. In this work, a mixture of the elements H, He, C, N, O, Na, Mg, Si, S and Fe is considered. Since different types of stars with different abundances are considered in the forthcoming applications (C–stars, RCB stars), the assumed abundances are stated separately (cf. Sect. 5.1.2 and Sect. 6.1.2). The following basic assumptions are made in order to calculate the various particle densities of the neutral atoms, ions, electrons and molecules:

- Neutral and singly ionized atoms are taken into consideration. The ratios between the particle densities of ions and neutral atoms are calculated by means of the statistical equations Eq. (3.1), taking into account the rates of photoionization, -recombination, collisional ionization and 3-body recombination (steady state non–LTE), as described in Chapter 3.
- For simplicity, the ratios between the particle densities of molecules and neutral atoms are calculated according to chemical equilibrium[1]. Negative ions

[1] This is of course a simplifying assumption. An improvement of the model may be achieved by calculating the steady state solution ("kinetic equilibrium") of a complete and reliable chemical

are treated like molecules (except for H^-, cf. Sect. 3.3.1). The chemistry comprises 130 species (Gail & Sedlmayr 1986), where some larger pure carbon molecules have additionally been included using the thermo–chemical data from Goeres & Sedlmayr (1992).

The particle densities are finally found by means of nested Newton–Raphson and λ–iteration techniques, until the conservation of charge and elements is assured. The following scheme is applied, where the quantities ρ, T_g, J_ν and $\left\langle\frac{dv}{dl}\right\rangle$ are given:

1. Estimate the electron density n_e and all neutral atom densities in the electronic ground state n_0^El.
2. Calculate the bound–free and free–bound rates $R_{i\,\mathrm{II}}$ and $R_{\mathrm{II}\,i}$, which depend on T_g, J_ν and n_e.
3. Perform an inner λ–iteration for each atomic species in order to solve the coupled equations for the level populations and the escape probabilities (compare Sect. 3.1.1.1), i. e.:

3a. Calculate the bound–bound rates $\widetilde{R}_{ul}$ and $\widetilde{R}_{lu}$, which depend on T_g, J_ν, the escape probabilities $\widetilde{P}^\mathrm{e}_{ul}$ and the densities of the collision partners.

3b. Determine the level populations and the ion particle densities $n_\mathrm{II}^\mathrm{El}$ from the statistical equations (3.1).

3c. Calculate the escape probabilities $\widetilde{P}^\mathrm{e}_{ul}$ which depend on the level populations and the local velocity gradient $\left\langle\frac{dv}{dl}\right\rangle$.

3d. Go back to step 3a unless the procedure has converged.

4. Calculate the particle densities of the molecules n_mol by assuming chemical equilibrium according to the total neutral atom densities $n_\mathrm{at}^\mathrm{El}$ and the gas temperature T_g.
5. Calculate the current errors of charge and element conservation, i. e.

$$\vec{\mathcal{F}}(n_\mathrm{e}, n_0^\mathrm{H}, \ldots, n_0^\mathrm{Fe}) = \begin{pmatrix} n_\mathrm{e} - \sum_\mathrm{El} n_\mathrm{II}^\mathrm{El} + \sum_\mathrm{mol} n_\mathrm{mol} s_\mathrm{mol}^\mathrm{e} \\ \frac{\epsilon_\mathrm{H}\,\rho}{\sum_\mathrm{El}\epsilon_\mathrm{El} m_\mathrm{El}} - n_\mathrm{at}^\mathrm{H} - n_\mathrm{II}^\mathrm{H} - \sum_\mathrm{mol} n_\mathrm{mol} s_\mathrm{mol}^\mathrm{H} \\ \vdots \\ \frac{\epsilon_\mathrm{Fe}\,\rho}{\sum_\mathrm{El}\epsilon_\mathrm{El} m_\mathrm{El}} - n_\mathrm{at}^\mathrm{Fe} - n_\mathrm{II}^\mathrm{Fe} - \sum_\mathrm{mol} n_\mathrm{mol} s_\mathrm{mol}^\mathrm{Fe} \end{pmatrix}$$

6. Perform one Newton–Raphson iteration step, i. e. solve $D\vec{\mathcal{F}} \cdot \Delta\vec{n} = \vec{\mathcal{F}}$ for the corrections $\Delta\vec{n}$ and put $\vec{n} \rightarrow \vec{n} - \Delta\vec{n}$, where the components of the vector $\vec{n}$ are shown as the argument of $\vec{\mathcal{F}}$ in the upper equation.
7. Go back to step 2 unless all further corrections become small $\delta = \max\limits_{j\,=\mathrm{e,H,\ldots,Fe}} \{\Delta n_j/n_j\} < 10^{-10}$.

reaction rate network, which, however, goes beyond the scope of this work. Concerning the RCB element abundances, most of the important reaction channels probably involve the abundant pure carbon molecules, which are all radicals and whose reaction rates are only poorly known.

The successful convergence of this iteration scheme critically depends on the quality of step 1, i. e. the first estimate of the electron and neutral atom densities. The inner λ–iteration (step 3 – 3d) is necessary, if bound–free transitions from excited levels are included. In this case, the degree of ionization of a considered atom (and hence the electron density) may depend on the escape probabilities, as demonstrated for hydrogen in Sect. 3.2.2. If no such bound–free transitions are considered (as for all other elements than hydrogen in this work), the system of equations decouples and the populations of the multi–level atoms without continuum can be determined after having solved the above iteration scheme. Especially all excited states of ions can be calculated afterwards, since only the first ionization stage is taken into account.

The described method yields all particles densities, including the considered level populations, as function of the mass density ρ, the gas temperature T_{g}, the continuous background radiation field J_ν and the velocity gradient $\left\langle\frac{dv}{dl}\right\rangle$.

4.2 Calculation of the Internal Energy

For dynamic considerations, the proper determination of the internal energy is as important as the determination of the radiative heating and cooling rates[2]. Having once determined the particle densities as outlined above, the evaluation of the internal energy is comparable simple and not very time–consuming.

According to the definition of the internal energy in this work (cf. Chapter 2), the internal energy comprises of translational, ionization and dissociation potential and electronic, vibrational and rotational excitation energies. The different terms are calculated as follows:

$$
\begin{aligned}
E_{\mathrm{trans}} &= \frac{3}{2}\, n\, kT_{\mathrm{g}} && (4.1)\\
E_{\mathrm{ion}} &= \sum_{\mathrm{El}} n_{\mathrm{II}}^{\mathrm{El}} \chi_{\mathrm{II}}^{\mathrm{El}} + \sum_{\mathrm{El}} n_{\mathrm{III}}^{\mathrm{El}} \left(\chi_{\mathrm{II}}^{\mathrm{El}} + \chi_{\mathrm{III}}^{\mathrm{El}}\right) + \ldots && (4.2)\\
E_{\mathrm{diss}} &= -\sum_{\mathrm{mol}} n_{\mathrm{mol}} D_{\mathrm{mol}}^{0} && (4.3)\\
E_{\mathrm{el}} &= \sum_{i,j} n_{ij} \Delta E_{ij} && (4.4)\\
E_{\mathrm{vib}} &= \sum_{\mathrm{mol}} n_{\mathrm{mol}} \sum_{j} \frac{g_j\, \hbar\omega_j^{\mathrm{mol}}}{\exp\left(\frac{\hbar\omega_j^{\mathrm{mol}}}{kT_{\mathrm{vib}}^{\mathrm{mol}}}\right) - 1} && (4.5)\\
E_{\mathrm{rot}} &= \sum_{\mathrm{mol}} \frac{f_{\mathrm{rot}}^{\mathrm{mol}}}{2} n_{\mathrm{mol}}\, kT_{\mathrm{rot}}^{\mathrm{mol}} \quad . && (4.6)
\end{aligned}
$$

[2]Warning: One should not take the radiative heating and cooling rates out of this work and consider $e = fkT/(2\mu)$ at the same time. The definitions of the internal energy and the radiative heating and cooling rates refer to each other. For example, the internal energy in the molecular domain turns out to be negative in this work.

n is the total gas particle density (atoms + ions + electrons + molecules). $\chi_{\rm II/III}$ is the ionization potential of the first/second ionization stage (the latter only given for reasons of completeness). $D^0_{\rm mol}$ is the total dissociation potential of a molecule (measured from the vibrational ground state), i. e. the energy required to totally dissociate the molecule into its constituting atoms at 0K. By definition, neutral atoms have zero potential energies.

n_{ij} is the particle density of species i in the j-th excited electronic state and ΔE_{ij} the corresponding energy difference to its electronic ground state. $\omega_j^{\rm mol}$ is the j-th eigenfrequency of a molecule and g_j the corresponding degeneracy. Equation (4.5) assumes independent, harmonic oscillators. Equation (4.6) is the classical limit for large rotational temperatures, which is sufficient in this context. $f_{\rm rot}$ is the number of rotational degrees of freedom (2 for linear molecules, 3 otherwise).

As far as possible, the vibrational and rotational excitation temperatures $T_{\rm rot}$ and $T_{\rm vib}$ are calculated by means of the methods outlined in the Sects. 3.1.3 and 3.1.4. For those molecules which are not considered therein, the excitation temperatures are assumed to equal the gas temperature.

For the calculation of the dissociation potential, vibrational and rotational excitation energies, only the abundant molecules must be taken into account. Table 4.1 lists the selected molecules and summarizes the necessary molecular data. The selection comprises the most abundant molecules in both cases, C–star and RCB star element abundances. Additional data for the ionization potentials $\chi_{\rm II}^{\rm El}$ and the excited electronic levels $\Delta E_{i,j}$ can be found in the Tables 3.1 and 3.3.

In summary, the outlined methods for the calculation of the particle densities and the internal energy provide the caloric and thermal equations of state in the form

$$e \;=\; e\Big(\rho, T_{\rm g}, J_\nu, \Big\langle\tfrac{dv}{dl}\Big\rangle\Big) = \frac{1}{\rho}\,\left(E_{\rm trans}+E_{\rm ion}+E_{\rm diss}+E_{\rm el}+E_{\rm vib}+E_{\rm rot}\right) \tag{4.7}$$

$$p \;=\; p\Big(\rho, T_{\rm g}, J_\nu, \Big\langle\tfrac{dv}{dl}\Big\rangle\Big) = \left(n_e + \sum_{\rm El}(n_{\rm at}^{\rm El}+n_{\rm II}^{\rm El}) + \sum_{\rm mol} n_{\rm mol}\right)\,kT_{\rm g} \quad . \tag{4.8}$$

A similar expression can be written for the total radiative net heating rate of the gas, which is calculated according to Chapter 3 as function of the various particle densities, which depend on density and temperature, the radiation field and the velocity gradient

$$Q_{\rm rad} \;=\; Q_{\rm rad}\Big(\rho, T_{\rm g}, J_\nu, \Big\langle\tfrac{dv}{dl}\Big\rangle\Big) \quad . \tag{4.9}$$

Equations (4.7) to (4.9) define the thermodynamic system which is examined in the following parts of this work.

Together with the two external parameters J_ν and $\left\langle\frac{dv}{dl}\right\rangle$, any suitable set of two independent state variables is sufficient to determine the thermodynamic state and hence all gas properties. Equations (4.7) to (4.9) are formulated in terms of $(\rho, T_{\rm g})$, but other useful choices can be e. g. (p,ρ), $(p, T_{\rm g})$ or (p, h), depending on the problem.

Table 4.1: Molecular data for the determination of the internal energy.

molecule	$D^0_{\rm mol}$ [eV] $^{(1)}$	$\omega_{\rm mol}$ [1/cm] and (degeneracy) $^{(2)}$	$f_{\rm rot}$
H_2	4.48	4158.5(1)	2
CO	11.11	2143.2(1)	2
CH	3.46	2732.8(1)	2
C_2H	12.07	1920.0(1), 640.0(2), 3220.0(1)	2
C_2H_2	16.78	3373.7(1), 1973.8(1), 3281.9(1), 611.6(2), 729.3(2)	2
CH_4	16.99	2916.5(1), 1534.0(2), 3018.7(3), 1306.0(3)	3
C_2	6.15	1828.0(1)	2
C_3	13.70	1224.5(1), 63.1(2), 2040.0(1)	2
C_4	19.49	350.0(1), 450.0(1), 1088.0(1), 1103.0(1), 1431.0(1), 1568.0(1)	3
C_5	26.78	112.0(2), 222.0(2), 648.0(2), 863.0(1), 1632.0(1), 2220.0(1), 2344.0(1)	2
C_7	38.70	73.0(2), 157.0(2), 240.0(2), 598.0(2), 631.0(1), 710.0(2), 1206.0(1), 1745.0(1), 2132.0(1), 2281.0(1), 2376.0(1)	2
C_{10}	59.30	184.0(2), 253.0(2), 419.0(1), 497.0(2), 555.0(2), 568.0(2), 577.0(1), 661.0(1), 690.0(2), 946.0(1), 1118.0(2), 1522.0(2), 1971.0(2), 2013.0(2)	3
N_2	9.90	2330.0(1)	2
CN	7.72	2042.4(1)	2
C_2N	13.90	1924.0(1), 324.0(2), 1050.8(1)	2
C_2N_2	21.32	2330.0(1), 846.0(1), 2158.0(1), 503.0(2), 234.0(2)	2
HCN	13.09	2096.3(1), 713.5(2), 3311.5(1)	2
SiC_2	13.05	1742.0(1), 837.0(1), 186.0(1)	3
Si_2C	11.10	670.0(1), 275.0(2), 1600.0(1)	2
SiC	4.58	983.0(1)	2
SiO	8.23	1229.6(1)	2
SiS	6.38	744.5(1)	2
CS	7.35	1272.2(1)	2

(1): The total dissociation potential energy can be determined from the JANAF tables (Chase et al. 1985) according to $D^0_{\rm mol} = \Delta_f H^0({\rm mol}) - \sum_{\rm El} s^{\rm El}_{\rm mol} \Delta_f H^0({\rm El})$ at 0K. For the larger carbon molecules C_7 and C_{10}, the dissociation potentials are taken from ab initio quantum mechanical calculations ("scaled binding energies" from Raghavachari & Binkley 1987).

(2): Values for diatomic molecules are taken from Huber & Herzberg (1979) according to $\omega = \omega_e - 2\omega_e x_e$. Values for polyatomic molecules from Chase et al. (1985). Values for C4, C5, C7 and C10 from Raghavachari & Binkley (1987). The reader may verify the relation $f_{\rm vib} = 3N-5$ / $3N-6$ for linear and non–linear molecules, respectively.

In practice, such dependencies are coded by numerical inversion. One computer routine carries out the determination of thermodynamic state of the gas as stated above, yielding the values of all state variables as function of (ρ, T_{g}). If e. g. a formulation in (p, h) is needed, another computer routine finds the corresponding values for ρ and T_{g} which yield (p, h) by Newton–Raphson iteration.

Chapter 5

Thermal Bifurcations in the Circumstellar Envelopes of RCB Stars

As a first application of the thermodynamic description developed in this work, the topology of the radiative equilibrium solutions is investigated.

Radiative equilibrium (RE) is defined as the equality of radiative gains and losses. Supposing that other heating and cooling processes are negligible (as heat conduction and heating by magneto-acoustic waves or cosmic rays), RE is the main criterion for the thermal stability of gases under astrophysical conditions[1]. Since any long–term physically realized solution must be thermally stable, the condition of RE provides the basic equation for the determination of the gas temperature in the case of static conditions.

However, as shown in this chapter, the condition of RE may not be unique, but can have two or more stable temperature solutions. These multiple solutions are commonly called "thermal bifurcations". Thermal bifurcations are well–known to occur in the outer solar atmosphere (Ayres 1981; Muchmore & Ulmschneider 1985; Muchmore 1986), in late type stars (Kneer 1983) and in the interstellar medium (e. g. Biermann et al. 1972).

This chapter investigates the circumstellar envelopes of RCB stars. Here, the question of whether or not low–temperature solutions already exist at small radial distances to the star is of special scientific interest. The occurrence of such solutions might be related to the formation of dust in these envelopes, which causes the spectacular RCB–type decline events (cf. Sect. 1.3 and Appendix A).

The main intention of this chapter is to demonstrate that thermal bifurcations, in principle, can lead to different, coexisting phases of the gas in pressure equilibrium. The temperatures of these phases can easily differ by several thousands of degrees. The phenomenon of thermal bifurcations is expected to occur frequently in all partially molecular gases.

---

[1] A secondary criterion for thermal stability is that the gas must offer resistance against compression along a RE–trajectory, $\left.\frac{dp}{d\rho}\right|_{\rm RE} > 0$. Otherwise, the gas is unstable against collapsing

5.1 The Model

5.1.1 Definition of the Radiative Equilibrium Gas Temperature

In the following the gas temperatures where radiative heating and cooling balance each other are determined. The RE gas temperatures $T_{\rm g}^{\rm RE}$ are calculated for given values of the gas pressure p, the radiation field J_ν and the mean local velocity gradient $\left\langle \frac{dv}{dl} \right\rangle$ according to

$$Q_{\rm rad}\Big(p, T_{\rm g}^{\rm RE}, J_\nu, \left\langle \tfrac{dv}{dl} \right\rangle\Big) \;=\; 0 \quad . \tag{5.1}$$

Equation (5.1) is an implicit definition of the RE gas temperature, which may of course be non–unique. For stability one has to require that the derivative of $Q_{\rm rad}$ with respect to temperature is smaller than zero. Otherwise, a small enhancement in temperature $\delta T_{\rm g}$ will increase net heating, that is the gas element will absorb even more radiation and will heat up further.

$$\left.\frac{\partial Q_{\rm rad}}{\partial T_{\rm g}}\right|_{T_{\rm g}=T_{\rm g}^{\rm RE}} \quad \begin{cases} < 0 & \Leftrightarrow \quad \text{stable RE} \\ > 0 & \Leftrightarrow \quad \text{unstable RE} \end{cases} \tag{5.2}$$

The bifurcation points, where solutions appear or disappear, satisfy Eq. (5.1) and have zero first derivatives. They only exist for certain values of the other parameters, e. g. for special radiation fields.

5.1.2 Element Abundances

The element abundances of the prototype star R Coronae Borealis are considered, adopting the values from Cottrell & Lambert (1982)[2]. RCBs are chemically peculiar stars, showing strong hydrogen deficiency and considerable carbon enrichment (cf. Appendix A). Mg and Ne are assumed to have the solar abundances given by Allen (1973). Figure 5.1 summarizes the choice of the element abundances in this work for all models with regard to RCB stars.

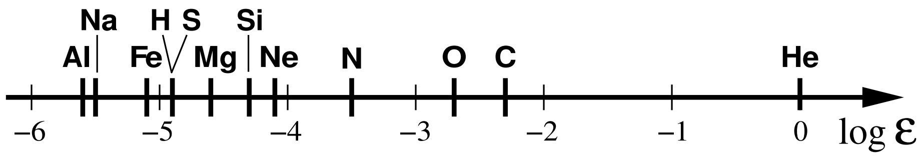

Figure 5.1: Assumed element abundances of R Coronae Borealis

[2]Other RCB stars show considerable, individual deviations from these abundances, especially for H:He and C:N:O (Lambert & Rao 1994).

5.1.3 Approximation of the Radiation Field

The radiation field is an important ingredient for the model, entering into both the determination of the particle densities and the calculation of the radiative heating and cooling rates. In this chapter, a two–parameter approximation of the radiation field is used. The radiation field is fitted by a radially diluted black body field of the effective temperature $T_{\rm eff}$ of the central star

$$J_\nu(r) = \frac{1}{2}\left(1 - \sqrt{1 - R_*^2/r^2}\right) B_\nu(T_{\rm eff}) \quad . \tag{5.3}$$

Absorption between the outer edge of the photosphere and the location of interest are neglected, i. e. the CSE is assumed to be optically thin. $T_{\rm eff}$ is set to be 7000 K, which is a representative value for this class of stars (cf. Appendix A). The approximation reasonably fits the stellar spectrum in the optical and IR region with a maximum deviation of a factor ~ 1.5, but leads to somewhat too high intensities for $\lambda < 300$ nm (Asplund et al. 1997), which is a consequence of the large UV optical depths in the stellar atmosphere. Furthermore, the stellar photosphere is assumed to be the dominant source for radiation at all wavelengths — chromospheric emissions, continuous UV–emissions from shocked gas layers in the circumstellar envelope and also IR–emissions from extended circumstellar dust–shells (cf. Appendix A) are ignored. Such effects would enhance the mean intensities in the UV and IR spectral regions, respectively, as compared to Eq. (5.3).

5.2 Results

Before studying the structure of the RE–solutions, some of the microphysical results of the RCB applications are stated first. In the following, the typical features for the ionization and the chemistry of the gas are summarized and the role of the various heating/cooling processes is discussed. Regarding the abundances (cf. Fig. 5.1), the results can differ a lot from those of a hydrogen–rich gas with nearly solar abundances as encountered in the interstellar medium or for example in the atmospheres of AGB–stars.

5.2.1 Degree of Ionization

Fractional ionization usually turns out to be large, irrespective of the gas temperature. This is a consequence of the large rates of photoionization according to the assumed radiation field with its strong UV intensities. The most abundant element helium, however, is mostly neutral unless the gas temperature is larger than ~ 30000 K, where the rates of collisional ionization come into play. Consequently, the degree of ionization equals almost 1 for $T_{\rm g} > 30000$ K and is approximately given by the C/He–ratio at lower gas temperatures. At very low temperatures $T_{\rm g} < 1200$ K, carbon is mainly present in the form of molecules and the electrons are provided by other elements, mainly Si and Mg. According to the somewhat poor fit of the UV part of the stellar spectrum, these results are still preliminary[3].

The character of the results changes for very large densities ($n_{<\mathrm{He}>} \gtrsim 10^{14}\,\mathrm{cm}^{-3}$ or $\rho \gtrsim 10^{-9}\,\mathrm{g\,cm}^{-3}$ or $p \gtrsim 100\,\mathrm{dyn\,cm}^{-2}$). For such densities, as present in the atmospheric layers of the star, the state of the gas is close to LTE due to the large efficiency of the various collisional processes, especially the three–body recombination rates. Consequently, the degree of ionization smoothly reaches the results of Saha–ionization with increasing densities.

5.2.2 Chemistry

Molecules become abundant in the gas phase approximately below a dividing line in the gas temperature / density–plane reaching from $T_\mathrm{g} \approx 4000\,\mathrm{K}$ at $n_{<\mathrm{He}>} = 10^{14}\,\mathrm{cm}^{-3}$ to $T_\mathrm{g} \approx 1500\,\mathrm{K}$ at $n_{<\mathrm{He}>} = 10^5\,\mathrm{cm}^{-3}$. With decreasing temperature, the first molecules to occur are CO and N_2.

Table 5.1: Abundant molecules in the circumstellar envelopes of RCB stars $^{(1)}$

Elements	most abundant molecules $^{(2)}$	abundant molecules $^{(3)}$
pure C	C_2, C_3, C_4, C_5, C_7, C_{10}(monocyclic ring), ...	—
C/N	N_2, CN, C_2N, C_2N_2	NCN, C_4N_2
O	CO	NO, O_2, CO_2, C_2O
Si/S	SiC_2, Si_2C, SiC, SiO, SiS, CS	SiN, Si_2, Si_3, Si_2N, SO, SN, S_2
H	C_2H, HCN, H_2, C_2H_2	CH, OH, HN, HS, SiH, CH_4, C_2H_4
Mg	— (atomic)	MgO, MgN, MgS, MgH
Fe	— (atomic)	FeO

$^{(1)}$: resulting from equilibrium chemistry based on the element abundances given in Fig. 5.1 for the range $n_{<\mathrm{He}>} = 10^6 \ldots 10^{12}\,\mathrm{cm}^{-3}$ and $T_\mathrm{g} = 800 \ldots 5000\,\mathrm{K}$

$^{(2)}$: molecules with $n_\mathrm{mol}/n_{<\mathrm{C}>} > 10^{-6}$ somewhere in the $(n_{<\mathrm{He}>}, T_\mathrm{g})$–plane

$^{(3)}$: molecules with $\max\limits_{\mathrm{El}} \{n_\mathrm{mol}/n_{<\mathrm{El}>}\} > 10^{-10}$, where El includes all elements the molecule is composed of.

Table 5.1 reviews the more abundant molecules for the hydrogen–deficient and carbon–rich element composition considered here. The chemistry is divided into the following subgroups. The most abundant group contains the pure carbon molecules with small chains, which are all radicals, and monocyclic rings. With decreasing gas temperature the concentrations of the more complex carbon molecules increase. See Goeres & Sedlmayr (1992) for more detailed information concerning the carbon chemistry. Oxygen is mostly blocked by the formation of CO and consequently all other molecules containing oxygen are not abundant. Especially H_2O is practically

[3] A substantial improvement of the model may be achieved by using a detailed model spectrum for RCB stars in future investigations.

absent from the gas phase. The next group are compounds formed out of nitrogen and carbon. The most important nitrogen molecule, however, is N_2. Furthermore, there are several abundant silicon, sulphur and hydrogen bearing molecules, all formed out of these elements and the abundant and unblocked elements C and N (except for SiO). Iron and magnesium bearing molecules are unimportant.

5.2.3 Radiative Heating and Cooling Rates

The question of important contributors to the heating and cooling of such special gas has to be investigated carefully. No preceding studies are available for this case. Table 5.2 summarizes the results of this work concerning the role of the various radiative processes for a typical choice of the parameters $T_{\rm eff}$, r/R_* and $\left\langle \frac{dv}{dl} \right\rangle$. The absolute value of the total radiative heating/cooling rate (as given in the first line of each panel in Table 5.2) increases with increasing gas temperature by many orders of magnitude and moderately decreases with decreasing density. The importance of the individual heating and cooling processes strongly depends on temperature and density. Usually one special radiative process dominates in a certain temperature / density regime. All basic radiative processes may cause heating or cooling and change the sign at different temperatures, which depend on the relation between J_ν and the source function at the characteristic wavelength of the process (cf. Fig. 3.5). Together with the strongly varying concentration of both the carriers of the heating/cooling rates and the collision partners (especially the electron density) a very complex picture appears, which shows the following features:

- Free–free heating/cooling is important for large densities ($n_{<{\rm He}>} \gtrsim 10^{12}\,{\rm cm}^{-3}$).
- Bound–free transitions, mainly of He and C, provide the most important heating/cooling process at large densities ($n_{<{\rm He}>} \gtrsim 10^{11}\,{\rm cm}^{-3}$), where all the bound–bound type transitions are optically thick.
- The heating/cooling rates of line transitions cover the whole temperature/density–plane and are generally important. They dominate the heating and cooling of the gas for not too large densities ($n_{<{\rm He}>} \lesssim 10^{11}\,{\rm cm}^{-3}$) and not too low temperatures. The most important contributors are He^+, C^+, N^+, S^+ and Fe^+, because of the high fractional ionization in the model (cf. Sect. 5.2.1).
- As soon as polar molecules become abundant in the gas phase, their large number of allowed transitions (vibrational and rotational) dominates the radiative heating and cooling of the gas. This happens below the dividing line described in Sect. 5.2.2. CO plays the overwhelming role concerning the heating and cooling of the gas by molecules, since it is the most abundant polar molecule by approximately two orders of magnitude. Further important molecules are CS and SiS. For larger densities ($n_{<{\rm He}>} \gtrsim 10^{10}\,{\rm cm}^{-3}$) the vibrational transitions are important, whereas for smaller densities the pure rotational transitions are more significant.

Table 5.2: Important heating/cooling processes for RCB abundances as function of temperature $T_{\rm g}$ and density $n_{<\rm He>}{}^{(1),(2)}$. Parameters are chosen as $T_{\rm eff}=7000\,$K, $r=2\,R_*$ and $\left\langle\frac{dv}{dl}\right\rangle=10\,{\rm km\,s^{-1}/R_*}^{(3)}$.

	$10^{14}\,{\rm cm^{-3}}$	$10^{12}\,{\rm cm^{-3}}$	$10^{10}\,{\rm cm^{-3}}$	$10^{8}\,{\rm cm^{-3}}$	$10^{6}\,{\rm cm^{-3}}$
50000 K	−1.0(14) −He-bf −ff −C-bf	−1.0(12) −He-bf −ff −C-bf	−1.2(11) −HeII −HeI −He-bf	−3.3(9) −CII −HeII −HeI	−4.3(7) −CII −HeII −HeI
20000 K	−5.3(10) −He-bf −C-bf −O-bf	−5.7(8) −He-bf −C-bf −O-bf	−8.1(8) −CII −HeI −SiII	−1.7(7) −CII −HeI −SiII	−3.5(5) −CII −OII −NII
10000 K	−1.2(8) −C-bf −ff −O-bf	−4.8(6) −CII −C-bf −SiII	−2.3(7) −CII −SiII −NII	−4.7(5) −CII −NII −SII	−2.6(4) −CII −NII −OII
6000 K	−1.9(6) −ff +C-bf +O-bf	−2.0(5) −ff +C-bf +O-bf	−3.2(5) −CII −NII −SiII	−1.7(4) −NII −CII −SII	−2.7(3) −NII −OII −FeII
3000 K	+2.1(7) +C-bf −ff +Si-bf	−4.6(5) −CO-vib +C-bf −ff	+1.8(5) +CII +C-bf +O-bf	+4.9(3) +CII +NII +SII	+4.7(2) +SII +NII −FeII
1500 K	+7.3(4) +Si-bf +Mg-bf +Fe-bf	−6.2(4) −CS-vib −CO-vib +SiII	+5.6(4) +CII +C-bf +SiII	−7.2(3) −CO-rot +CII +SII	−5.1(3) −CO-rot +SII +NII
800 K	+1.8(4) +Mg-bf +Fe-bf +Na-bf	+2.6(4) +CO-vib +SiS-vib +SiII	+4.9(2) +CO-vib +SiS-vib −CO-rot	−1.5(3) −CO-rot +FeII −HCN-rot	−1.0(3) −CO-rot +FeII +He-bf
400 K	+2.7(4) +Mg-bf +Fe-bf +Na-bf	+1.1(4) +SiS-vib +CO-vib +SiII	+7.6(2) +SiS-vib +SiII +FeII	+4.0(2) +FeII +CO-rot +SiII	+2.6(2) +CO-rot +FeII +SiII

Each panel of the table has two entries:

(1) The first line is the resulting total net radiative heating rate per mass of the gas $Q_{\rm rad}/\rho\,[{\rm erg\,s^{-1}\,g^{-1}}]$, where $X(Y)$ means $X\cdot 10^{Y}$.

(2) A list of the three most efficient heating/cooling processes is stated below in order of decreasing absolute net rates: − = cooling, + = heating, I = lines of neutral atom, II = lines of ionized atom, ff = free–free, bf = bound–free, vib = vibrational, rot = rotational transitions.

(3) $R_* = 73\,R_\odot$ is assumed in this context.

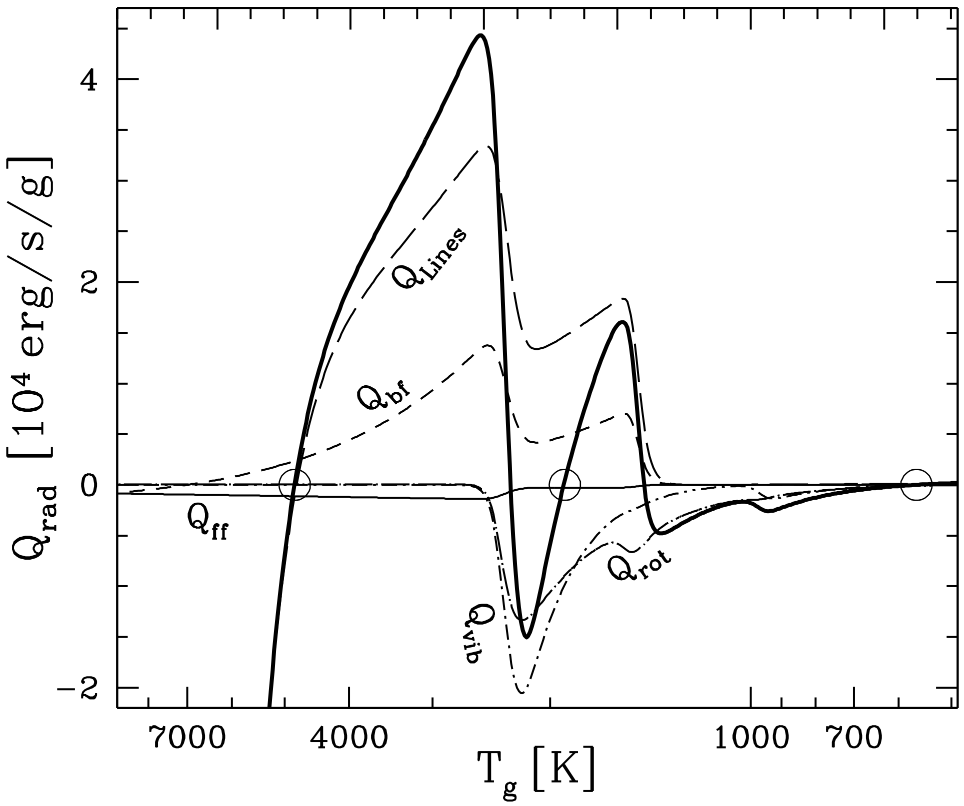

Figure 5.2: Heating/cooling rates as function of the gas temperature for $p = 10^{-3}\,\mathrm{dyn\,cm^{-2}}$ ($n_{<\mathrm{He}>} \approx 10^9 \ldots 2 \cdot 10^{10}\,\mathrm{cm^{-3}}$), $T_{\rm eff} = 7000\,$K, $r = 3R_*$ and $\left\langle\frac{dv}{dl}\right\rangle = 10\,\mathrm{km\,s^{-1}}/R_*$. The thick full line shows the total net heating rate. The other dashed and dotted lines depict the free-free rate $Q_{\rm ff}$, the total bound–free rate $Q_{\rm bf}$ (all atoms/ions), the total line heating/cooling rate $Q_{\rm Lines}$ (all atoms and ions), the total vibrational rate $Q_{\rm vib}$ (all molecules) and the total rotational rate $Q_{\rm rot}$ (all molecules). The circles denote stable radiative equilibrium temperature solutions.

5.2.4 Radiative Equilibrium Temperature Solutions

The solutions of the radiative equilibrium problem are related to the changes of sign of the total net radiative heating function $Q_{\rm rad}$ as a function of the gas temperature. I will briefly explore the reasons for these changes of sign in the following.

The heating/cooling rates as functions of the gas temperature are shown in Fig. 5.2 for a sample choice of the parameters. The sums of the rates of all kinds of processes (free-free, bound-free, lines, vibrational and rotational transitions) are depicted. For sufficiently high temperatures, all radiative processes cause net cooling. Considering the direction to lower gas temperatures, the different processes subsequently change the sign at different temperatures. For the parameters chosen in Fig. 5.2, one finds: bound–free $\sim 7000\,$K, spectral lines $\sim 4800\,$K, free-free $\sim 615\,$K, vibrational $\sim$575 K and rotational $\sim$200 K. Finally, for sufficiently low temperatures, all radiative processes cause net heating.

Thus, there always exists at least one stable solution for the radiative equilibrium problem. Considering the direction to low temperatures, the first solution to occur is henceforth called the "high–temperature solution". For the high temperatures in Fig. 5.2, the line transitions provide the dominant heating/cooling process. Consequently, the high–temperature solution ($\sim$4830 K) is usually close to the temperature, where the total line heating/cooling rate $Q_{\rm Lines}$ changes its sign.

> *The high–temperature solution refers to a predominantly molecule–free, partially ionized gas. The temperature is fixed by the change of sign of $Q_{\rm Lines}$ for small and $Q_{\rm bf}$ for large densities, respectively.*

The change of sign of $Q_{\rm Lines}$ is caused by the temperature–dependent competing processes of line absorption followed by collisional de-excitation, and collisional excitation followed by line emission. The change of sign of $Q_{\rm bf}$ is caused by the competing processes of photoionization followed by collisional (three–body) recombination, and collisional ionization followed by radiative recombination[4]. If molecule formation was not possible in the gas phase, the high–temperature solution would be the only solution and the radiative equilibrium problem would be unique.

However, once the gas has reached a sufficiently low temperature, molecules become abundant. Their large number of allowed vibrational and rotational transitions, located in the IR and microwave spectral region, enters into competition with the other atomic transitions which substantially increases the efficiency of the interaction between the gas and the radiation field at long wavelengths. Thereby, the appearance of molecules causes reinforced cooling for the present because of the comparable faintness of the central star at these wavelengths, as sketched in Fig. 3.5. Much lower temperatures are required to cause a change of sign of the molecular heating/cooling functions.

> *The additional temperature solutions are caused by the presence of molecules. Two types of stable solutions are found. The medium–temperature solutions result from an equilibrium between atomic heating and molecular cooling. The low–temperature solutions are caused by a change of sign of the dominant molecular heating/cooling function.*

For example in Fig. 5.2, one finds a second stable solution at $\sim$ 1900 K, where the radiative heating by lines and bound–free transitions is balanced by vibrational cooling. At about the third stable solution ($\sim$565 K) the vibrational heating/cooling function changes its sign. Additional unstable solutions exist at $\sim$ 2290 K and $\sim$ 1440 K.

[4]Strictly speaking, even $Q_{\rm bf}$ and $Q_{\rm Lines}$ may change the sign more than once, because of the superposition of the numerous transitions.

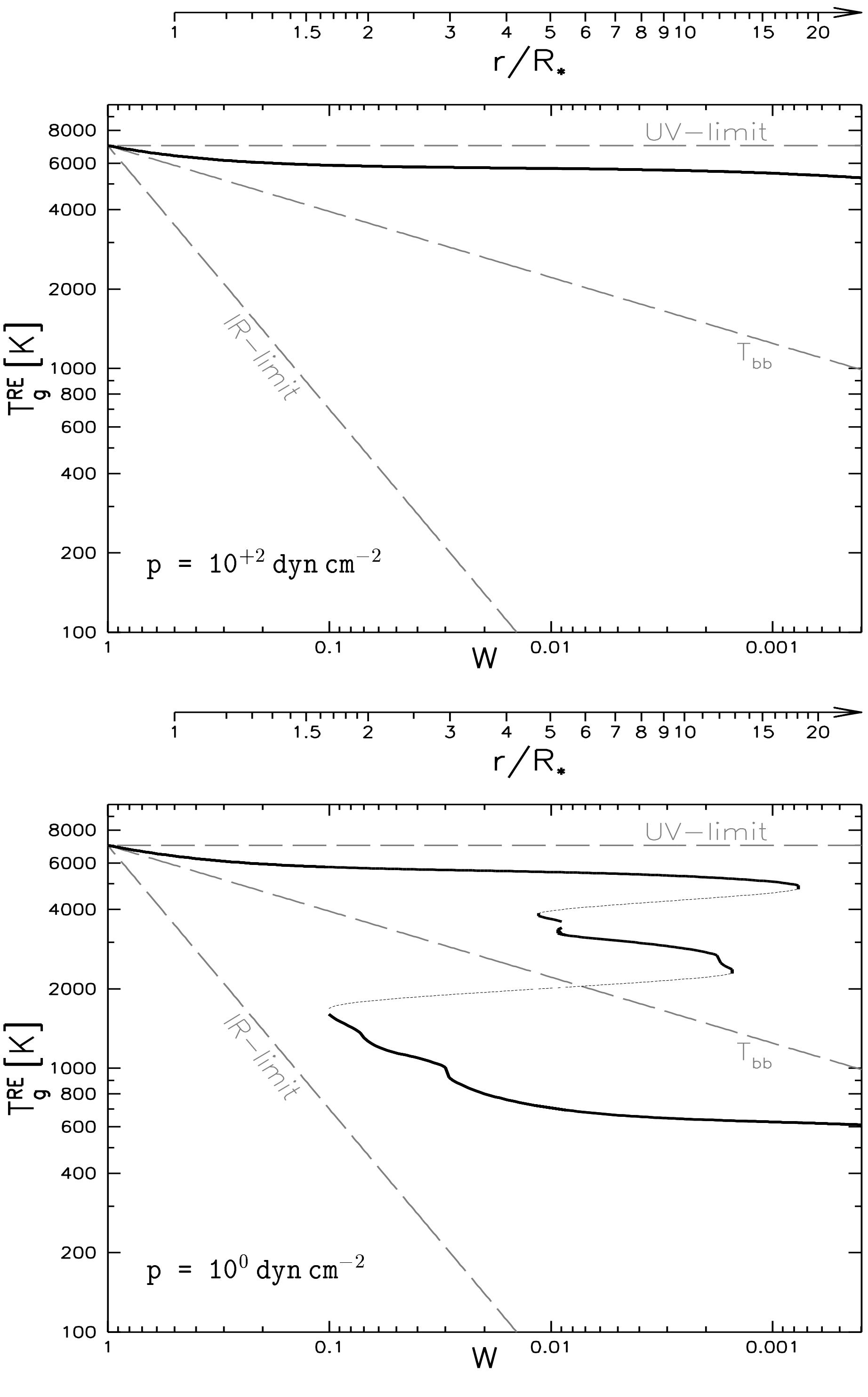

Figure 5.3: Thermal bifurcations in RCB envelopes for $p = 10^2\,\mathrm{dyn\,cm^{-2}}$ (upper panel, $n_{<\mathrm{He}>} \approx 10^{14} \ldots 5 \cdot 10^{15}\,\mathrm{cm^{-3}}$) and $10^0\,\mathrm{dyn\,cm^{-2}}$ (lower panel, $n_{<\mathrm{He}>} \approx 10^{12} \ldots 5 \cdot 10^{13}\,\mathrm{cm^{-3}}$). The radiative equilibrium temperature solutions $T_{\mathrm{g}}^{\mathrm{RE}}$ are shown versus dilution factor W in a Planck–type radiation field with $T_{\mathrm{eff}} = 7000\,\mathrm{K}$ and for $\langle\frac{dv}{dl}\rangle = 10\,\mathrm{km\,s^{-1}}/R_*$. Full and dotted black lines indicate stable and unstable solutions, respectively. The radius axis belongs to the optical thin limit (pure radial dilution) according to Eq. (1.7). The UV– and IR-limit and the black body temperature T_{bb} are the same as shown and explained in Fig. 1.1.

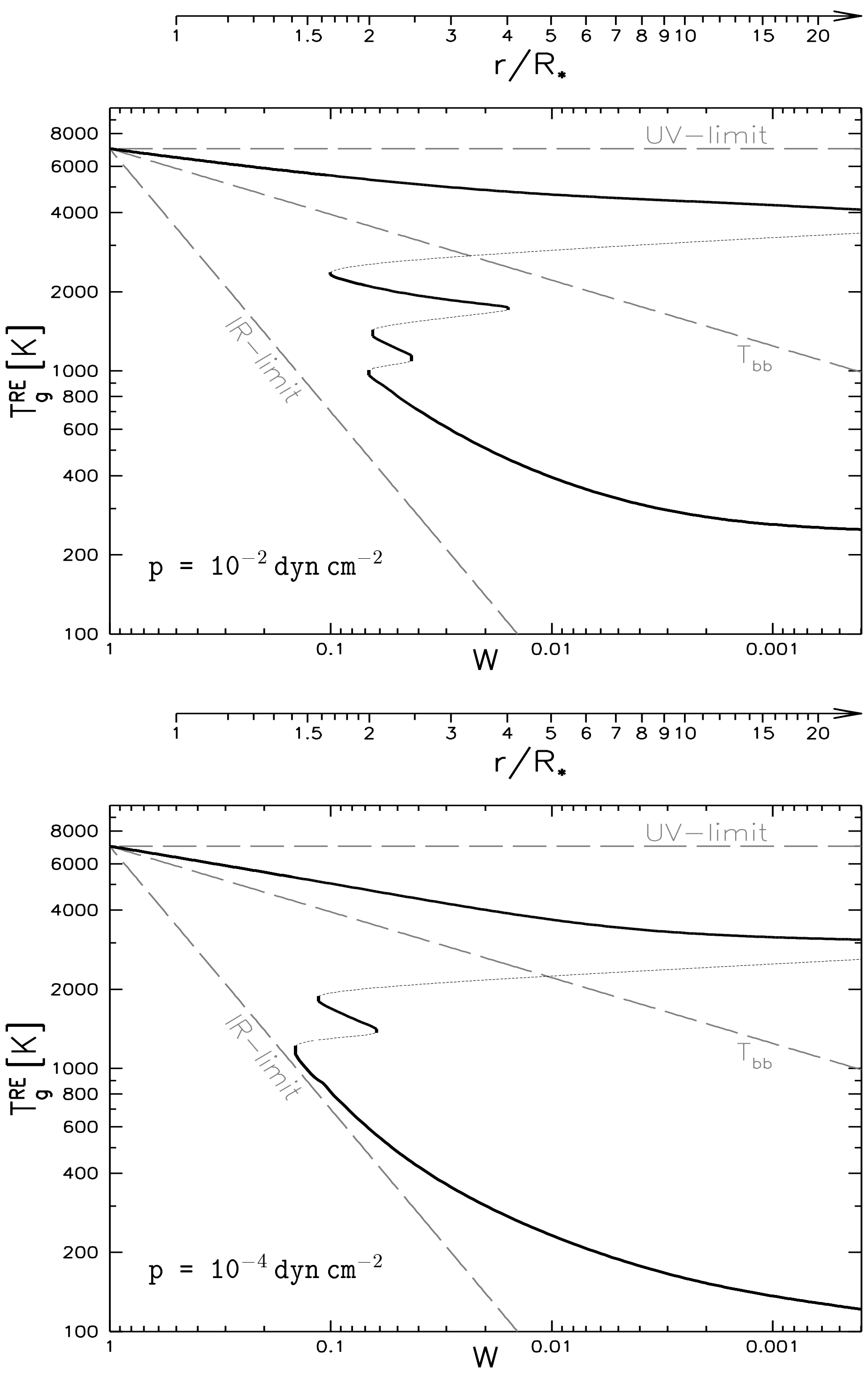

Figure 5.4: Same as Fig. 5.3, but for $p = 10^{-2}\,\mathrm{dyn\,cm^{-2}}$ (upper panel, $n_{<\mathrm{He}>} \approx 10^{10} \ldots 5{\cdot}10^{11}\,\mathrm{cm^{-3}}$) and $10^{-4}\,\mathrm{dyn\,cm^{-2}}$ (lower panel, $n_{<\mathrm{He}>} \approx 10^{8} \ldots 5{\cdot}10^{9}\,\mathrm{cm^{-3}}$).

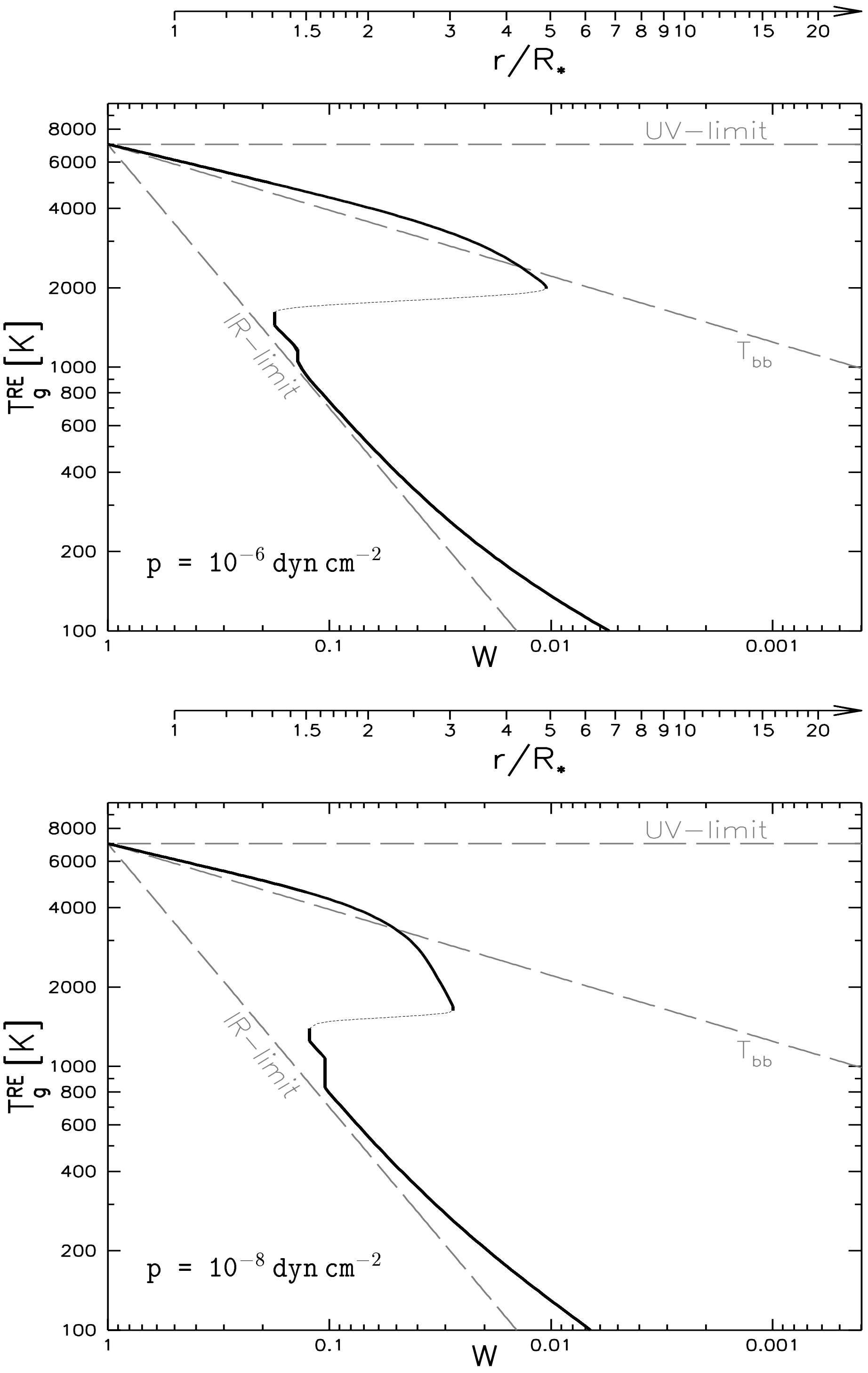

Figure 5.5: Same as Fig. 5.3, but for $p = 10^{-6}\,\mathrm{dyn\,cm^{-2}}$ (upper panel, $n_{<\mathrm{He}>} \approx 10^6 \ldots 5{\cdot}10^7\,\mathrm{cm^{-3}}$) and $10^{-8}\,\mathrm{dyn\,cm^{-2}}$ (lower panel, $n_{<\mathrm{He}>} \approx 10^4 \ldots 5{\cdot}10^5\,\mathrm{cm^{-3}}$).

The general topology of the radiative equilibrium solutions is depicted in the Figs. 5.3 to 5.5. The temperature solutions are shown as function of the dilution factor W. This factor is related to a distinct radial distance in the case of pure geometric dilution according to Eq. (1.7), but its meaning is more general. W characterizes the departure from an equilibrium and, hence, is an appropriate variable to study the structure of the bifurcations. $W=1$ together with RE implies complete thermodynamic equilibrium (TE) according to the concept of this work: In the case where $W=1$ the radiation field is a non–diluted Planck–field $J_\nu = B_\nu(T_{\rm rad})$ and the only solution of RE is given by $T_{\rm g}^{\rm RE} = T_{\rm rad}$. Every (collisional or photo-) process is directly balanced by its corresponding reverse process, which characterizes TE. Since all reverse processes are included by means of detailed balance considerations (cf. Chapter 3), this work accurately describes this behavior.

All calculated RE temperature solutions are located between the IR–limit ($T_{\rm IR} = W T_{\rm eff}$) and the UV–limit ($T_{\rm UV} = T_{\rm eff}$), nicely confirming the simple results of Sect. 1.2 where LTE and a δ–type gas absorption coefficient have been considered.

Thermal bifurcations are found to occur under the following conditions:

1) A high–temperature stable solution must be possible, i. e. a radiative equilibrium state of the gas mainly consisting of atoms and ions[5].
2) $W \lesssim 0.1$ ($r \gtrsim 1.5\,R_*$) is required to make possible a molecule–rich, low–temperature solution as motivated by the IR–limit.
3) $p \lesssim 1\,{\rm dyn\,cm^{-2}}$ ($n_{<{\rm He}>} \lesssim 10^{13}{\rm cm^{-3}}$) is required to limit the influence of the bound–free heating/cooling rates compared to the molecular heating/cooling rates. For too large densities, $Q_{\rm bf}$ dominates the heating and cooling even for low temperatures (cf. Table 5.2) and, consequently, molecule formation does not produce additional solutions.

Under these conditions, the gas is *always* found to be at least bi–stable. Up to 4 simultaneous temperature solutions may exist, depending on the pressure and the dilution factor. The stable temperature solutions (e. g. $\sim$5220 K, $\sim$2000 K, $\sim$1220 K *and* $\sim$ 810 K for $p = 10^{-2}\,{\rm dyn\,cm^{-2}}$ and $W = 0.05$) can differ by several thousands of degrees, usually yielding one high–temperature, atomic solution and one or more low–temperature, molecular solutions.

Another result of the model is that the RE gas temperatures are density–dependent, which can be seen by comparison of the Figs. 5.3 to 5.5. The general tendency is that a thin gas tends to be cooler than a dense gas, considering the same branch of solution. This is caused by the increasing importance of spectral lines and rotational transitions compared to bound–free and vibrational transitions for decreasing density, respectively. The former transitions have longer characteristic wavelengths compared to the latter, yielding lower RE temperatures according to Fig. 1.1.

[5] A violation of this criterion occurs at small pressures $p \lesssim 10^{-6}\,{\rm dyn\,cm^{-2}}$ and large dilutions $W \lesssim 0.01$ in Fig. 5.5. In this case the "high"–temperature solution drops below $\sim$2000 K, where it enters into the molecular regime and disappears. Only one low–temperature solution remains in this case.

5.3 Discussion

The circumstellar envelopes of RCB stars show a multi–stable character. Cool gas phases, mainly consisting of molecules, can principally coexist besides hot phases, mainly consisting of atoms and ions. Both phases are in radiative equilibrium and in pressure balance with each other.

The multi–stable character of the gas causes a kind of "cooling trap". Once the gas has reached a sufficiently low temperature, molecules are formed which cause reinforced radiative cooling[6]. The gas then cools down to much lower temperatures, until the heating and cooling by molecules alone produces another solution of the radiative equilibrium problem and stabilizes the low temperature.

Thermal bifurcations are found to occur in a large range of examined parameters, concerning both the radial distance to the star and the gas pressure. These findings indicate that the occurrence of thermal bifurcations is not restricted to the CSEs of RCB stars, but is a common phenomenon in partially molecular gases. However, the thermal bifurcations are expected to occur mainly in the CSEs of warm stars with $T_{\rm eff} \gtrsim 4500\,$K, where the atomic, high–temperature solution still exists (cf. criterion 1 of the item list on the previous page).

Concerning the CSEs of cool stars (as C– and M–stars on the AGB), the radiative equilibrium gas temperatures are expected to be much lower than the black–body temperatures. The gas in these circumstellar envelopes is molecule–rich. Consequently, the solutions of the radiative equilibrium problem should be similar to the low–temperature solutions discussed above. However, these envelopes are dust–enshrouded and hence optically thick. The approximation of the radiation field used in this chapter is not appropriate for this case and the results can be different.

Nevertheless, the consequences of the multi–stable character of the gas reach far, as F. Kneer (1983) wrote in view of this instability: "I conclude that RE stellar atmospheres with $T_{\rm eff} = 5800\,$K may not exist, *in principle*". I would not go that far, but consider for example a gas element which slowly moves outwards in a CSE with a temperature structure similar to that depicted in Fig. 5.5. The motion of the element shall be slow, so that RE remains valid. The gas element mainly consists of atoms and ions as long as the high–temperature solution is realized. The gas temperature slowly decreases with increasing radial distance down to about $\sim 2000\,$K, until suddenly, at about $4\,R_*$ in Fig. 5.5, a certain amount of molecules has been formed, just sufficient to destabilize the radiative equilibrium. The gas then quickly cools down towards the second, low–temperature solution at $\sim 200\,$K. The final chemical composition and the amount of dust formed in the gas element will crucially depend on the relation between the chemical and the cooling time scale during this transition. In the end, the chemistry freezes out and dust formation becomes impossible again. If this scenario proves to be true it would change our general theoretical view of the chemistry and the dust formation processes in stellar

[6] *How* such a sufficiently low temperature can be reached, is left open for the present.

envelopes quite dramatically. Other topics related to the multi–stable character of the gas could be inhomogeneities, cloud formation or a hysteresis–like behavior of the gas in the CSEs of pulsating stars.

The results of this chapter refer to the assumption of static RE. Chapter 6 will calculate radiative cooling time scales, which give an impression on the applicability of RE under dynamic conditions. For example, the low–temperature solutions can easily be destabilized by adiabatic heating/cooling rates, which diminishes the meaning of the low–temperature results of this chapter to some extent.

In contrast to the general finding, that thermal bifurcations should occur principally, a reliable determination of the gas temperature is difficult. In the static case it really depends on the details of (i) the chemistry, (ii) the heating/cooling functions and (iii) the radiation field. Each radiative process which is additionally taken into account may change the results for $T_{\rm g}^{\rm RE}$ substantially. This is fundamentally different from the results of Chapter 7, as will be discussed therein.

Chapter 6

Radiative Cooling Time Scales in the Circumstellar Envelopes of C–Stars

The second application of the thermodynamic methods developed in this work investigates the relaxation towards radiative equilibrium. A gas element in non–RE is considered. The element, being hotter or cooler than in RE, will consequently radiate away excess internal energy (radiative cooling) or gain radiative energy by net absorption (radiative heating), respectively. The key quantity which describes the efficiency of this relaxation is the time scale for radiative cooling or heating, which is defined below.

The character of the thermal behavior of the gas under dynamical conditions can be discussed by comparing this time scale (henceforth called the "radiative cooling time scale") with the other hydrodynamic or chemical time scales involved in the considered process. If the radiative cooling time scale is shorter than the others, the gas quasi instantaneously relaxes towards RE and, consequently, the condition of RE can be used to determine the gas temperature. If it is comparable or larger than the others, the temperature of the gas depends on the history of the process and must be calculated time–dependently.

> *In the following, the applicability of RE for the determination of the gas temperature under dynamic conditions is investigated.*

Concerning the chemistry and the dust formation in the CSEs of pulsating stars, the character of the thermal relaxation of the gas in response to propagating shock waves is of special importance. The pulsation in the interior of the star produces waves, which steepen up to shock waves in the atmosphere and propagate into the CSE (e. g. Bowen 1988, Fleischer et al. 1992). Thus, the gas elements in the envelopes of pulsating stars are hit by shock waves time and time again. The shocks dissipate mechanical energy and heat up the gas to considerably high temperatures. The gas must be able to radiate away this excess internal energy before the next shock hits the element. Otherwise, it will never become sufficiently cool to allow for complex chemical and dust formation processes.

Following this consideration, one would expect the stellar pulsation to hinder dust formation. In fact, from observations, just the opposite conclusions can be drawn. Many of the dust–forming objects are known to be pulsating stars. Moreover, a strong correlation between the occurrence of an IR excess (indicating dust formation) and a light variability (indicating stellar pulsation) can be observed for late type stars (Jura 1986), i. e. *stellar pulsation favors dust formation*. Therefore, an efficient relaxation of the shock–heated gas in circumstellar envelopes seems to be confirmed by observations.

This chapter considers the CSEs of pulsating C–stars. It picks up the controversial question of whether the shocks in these CSEs behave predominantly "isothermally" or "adiabatically" (more informations about this controversy can be found in Sect. 1.4). A clarification of this question is an important step towards the principal understanding of dust formation in the CSEs of pulsating stars.

6.1 The Model

6.1.1 Definition of the Radiative Cooling Time Scale

An arbitrary physical quantity y shall be considered. The time evolution of y is assumed to be given by the first order ordinary differential equation

$$\frac{dy}{dt} = f(y) \quad . \tag{6.1}$$

The equilibrium values of the physical quantity $\mathring{y}$ are implicitly defined by $f(\mathring{y}) = 0$. First order Taylor expansion of Eq. (6.1) in time yields $y(t+\Delta t) = y(t) + \Delta t \cdot f(y)$. If y is to relax toward equilibrium, i. e. $y(t+\Delta t) \equiv \mathring{y}$, the first order estimate of the time required for the relaxation is

$$\Delta t = \frac{\mathring{y} - y}{f(y)} \quad . \tag{6.2}$$

The radiative cooling time scale is defined analogously, considering pure radiative heating/cooling according to $\frac{de}{dt} = \widehat{Q}_{\rm rad}$ with $\widehat{Q}_{\rm rad} = Q_{\rm rad}/\rho$

$$\tau_{\rm cool}\left(\rho, T_{\rm g}, J_\nu, \left\langle\frac{dv}{dl}\right\rangle\right) = \frac{e\left(\rho, T_{\rm g}^{\rm RE}, J_\nu, \left\langle\frac{dv}{dl}\right\rangle\right) - e\left(\rho, T_{\rm g}, J_\nu, \left\langle\frac{dv}{dl}\right\rangle\right)}{\widehat{Q}_{\rm rad}\left(\rho, T_{\rm g}, J_\nu, \left\langle\frac{dv}{dl}\right\rangle\right)} \quad . \tag{6.3}$$

$T_{\rm g}^{\rm RE}$ is one RE temperature solution as defined in Chapter 5. Apart from the problem of RE multi–stability, $T_{\rm g}^{\rm RE}$ and thereby $\tau_{\rm cool}$ are completely determined by the thermodynamic quantities ρ and $T_{\rm g}$, the continuous background radiation field J_ν and the local velocity gradient $\left\langle\frac{dv}{dl}\right\rangle$. In the following, the aim is to calculate $\tau_{\rm cool}$ for the entire density– and temperature–range encountered in the shocked envelopes of pulsating C–stars.

6.1.2 Element Abundances

The element composition of C–stars is assumed to be solar except for carbon. The solar abundances are adopted from Lambert & Rao (1994) and references therein. The abundance of He is assumed to be $\epsilon_{\rm He}/\epsilon_{\rm H} = 0.1$ and the abundance of Mg is taken from Allen (1973). Carbon is assumed to be overabundant with respect to oxygen by $\epsilon_{\rm C}/\epsilon_{\rm O} = 1.7$, which according to Frantsman & Eglitis (1988) is a representative value for C–stars.

6.1.3 Approximation of the Radiation Field

For the applications with regard to C–stars the mean back–ground intensities are assumed to be given by an non–diluted Planck field ($W = 1$), that is

$$J_\nu \;=\; B_\nu(T_{\rm rad}) \quad . \tag{6.4}$$

This is done for three reasons. First, the CSEs of C–stars are supposed to be dust enshrouded and hence not optically thin. Eq. (6.4) represents the limiting case of an optically thick CSE. Second, the assumption considerably simplifies the evaluation of the cooling time scale as defined above. According to Eq. (6.4) there is always exactly one (trivial) RE temperature solution given by $T_{\rm g}^{\rm RE} = T_{\rm rad}$. Thereby, $\tau_{\rm cool}$ is well–defined according to Eq. (6.3). Third, the calculations are performed in order to determine $\tau_{\rm cool}$ and not to find the specific temperature solutions of RE. The latter of course requires more detailed knowledge about J_ν. The parameter $T_{\rm rad}$ is assumed to vary between 0 and 3000 K for C–star envelopes, considering 3000 K as a representative value for the effective temperatures of these stars. Even for the extreme cases $J_\nu = 0$ and $J_\nu = B_\nu(3000\,{\rm K})$, the results for the cooling time scales are remarkably similar (cf. Sect. 6.2.4). Therefore, the choice of the radiation field is not crucial for the determination of $\tau_{\rm cool}$. Chromospheric emissions and continuous emissions from shocked gas layers in the CSE are again ignored.

6.1.4 Local Velocity Gradient

Regarding the typical saw–tooth–like velocity structures in model calculations for the shocked envelopes of cool pulsating stars (e. g. Fig. 1 of Winters et al. 1994), the mean velocity gradient $\left\langle\frac{dv}{dl}\right\rangle$, as defined by Eq. (3.14), has more or less a certain characteristic value of the order of v_∞/R_* varying by about one order of magnitude throughout the whole considered circumstellar shell (except for the very thin shock fronts). Therefore, this parameter is fixed and set to $\left\langle\frac{dv}{dl}\right\rangle = 20\,{\rm km\,s^{-1}}/500\,R_\odot$. The influence of this parameter is small (cf. Sect. 6.2.5).

6.2 Results

Before discussing the results for the radiative cooling time scales, some of the microphysical results shall be stated first: the composition of the gas (degree of ionization and chemistry), the internal energy and the role of the different radiative processes.

6.2.1 Composition of the Gas

The composition of the gas is roughly depicted in Fig. 6.1. The upper panel of the figure shows contour lines of the concentrations of H_2 and e^- in the temperature / density–plane, indicating whether the gas is predominantly molecular, atomic or ionized. The two extreme cases $J_\nu = 0$ and $J_\nu = B_\nu(3000\,\mathrm{K})$ are considered on the left and right hand side of Fig. 6.1, respectively.

The resulting electron density is very important for the calculation of the radiative heating/cooling rates. It has a decisive influence on the bound–free rates and, as collision partner, also on the bound–bound collision rates. The degree of ionization of the gas is found to strongly depend on the radiation field.

In the case $T_{\rm rad} = 0$, fractional ionization is solely caused by collisional ionization, which is mainly balanced by radiative recombination. Since the rates of the both processes linearly depend on $n_{\rm e}$ (cf. Eq. 3.60 and 3.61), the density–dependence cancels out and the contour lines are horizontal lines on the left hand side of Fig. 6.1. The deviations from straight lines at high temperatures are caused by collisional excitation from excited states of hydrogen. For large densities a two–step collisional process $\mathrm{H} + \mathrm{e}^- \rightarrow \mathrm{H}^* + \mathrm{e}^-$ and $\mathrm{H}^* + \mathrm{e}^- \rightarrow \mathrm{H}^+ + 2\,\mathrm{e}^-$ turns out to be more efficient than a direct collisional excitation $\mathrm{H} + \mathrm{e}^- \rightarrow \mathrm{H}^+ + 2\,\mathrm{e}^-$ (cf. Sect. 3.2.2). Fractional ionization is found to be negligible ($<10^{-5}$) for $T_{\rm g} \lesssim 5000\,\mathrm{K}$ in the case $J_\nu = 0$.

For $T_{\rm rad} = 3000\,\mathrm{K}$ (right hand side) photoionization of metal atoms with low ionization potentials (Si, Mg, Fe, Na) additionally produces free electrons and is more important than collisional ionization for $T_{\rm g} \lesssim 5000\,\mathrm{K}$. Since the photoionization rates are density–independent, but the radiative recombination rates do depend on the density, the contour lines are approximately vertical lines for $T_{\rm g} \lesssim 5000\,\mathrm{K}$ on the right hand side of Fig. 6.1. A degree of ionization as large as 10^{-3} to 10^{-5} is retained for low temperatures, depending on the density[1]. Thus, fractional ionization is found to be much larger than in LTE at low temperatures for this radiation field.

The three–body recombination rates are found to be negligible compared to the radiative recombination rates in the entire temperature / density–plane under investigation. Consequently, LTE (Saha)–ionization is never achieved. For example, the gas remains predominantly neutral for the radiation fields under examination unless the temperature is as large as $\gtrsim 10000\,\mathrm{K}$. Only for very large densities, ($n_{\rm <He>} \gtrsim 10^{16}\mathrm{cm}^{-3}$) the calculated fractional ionization of the gas approaches LTE.

[1] Such degree of ionization is expected to cause considerable effects with regard to grain charge and grain drift, for example.

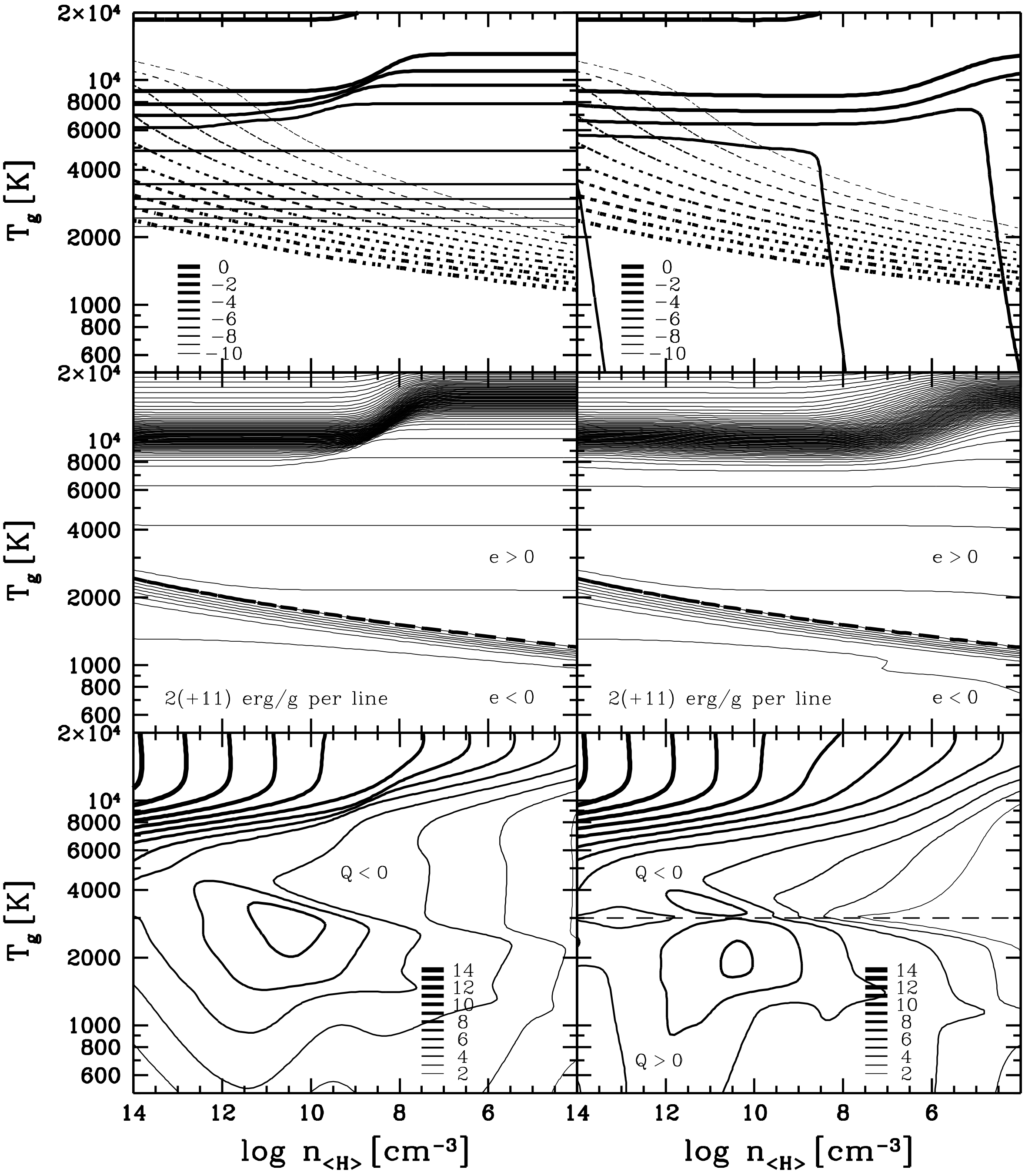

Figure 6.1: The composition, the internal energy and the net heating function of the gas as function of temperature and density. The **upper diagrams** are contour plots of the H_2–concentration $\log(n_{H_2}/n_{<H>})$ (dotted lines) and the electron concentration $\log(n_e/n_{<H>})$ (full lines). The **middle diagrams** show the total internal energy of the gas e on a linear scale ranging from about $-1.4(12)$ to $+1.3(13)$ erg/g. The zero–line is additionally shown as a dashed line and the sign of e is indicated. The **lower diagrams** show the total net heating function of the gas $\log|Q_{\rm rad}/\rho|$ [$\rm erg\,g^{-1}\,s^{-1}$]. On the right hand side, $Q_{\rm rad}$ is positive below and negative above the dashed $T_{\rm g}=3000\,$K–line. The **left column** considers the case $J_\nu=0$, whereas the **right column** considers the case $J_\nu=B_\nu(3000\,{\rm K})$. All calculation are made for $\left\langle\frac{dv}{dl}\right\rangle=20\,{\rm km\,s^{-1}}\,/\,500\,R_\odot$.

The chemical composition of the gas is calculated by assuming chemical equilibrium with respect to the neutral atom densities in this work (cf. Chapter 4). Consequently, the concentrations of the molecules are found to be very similar compared to the results of previous works using chemical equilibrium. The results of the application of chemical equilibrium to C–stars envelopes have thoroughly been described elsewhere (e. g. Gail & Sedlmayr 1988). Some modifications are caused by the somewhat different neutral atom densities due to the upper results concerning the ionization which yield somewhat different molecule concentrations (e. g. less silicon bearing molecules if Si is strongly ionized as in the case $T_{\rm rad} = 3000\,{\rm K}$). However, these modifications are small. The H_2–concentration, for example, is depicted by the dotted contour lines in the upper panel of Fig. 6.1.

6.2.2 Internal Energy

The determination of the internal energy of the gas is an important ingredient for the calculation of the cooling time scale. Moreover, it is essential for any time–dependent treatment of thermodynamics, for example in hydrodynamic models. It provides the basic link from the energy content, which is modified by radiative heating and cooling, to the temperature of the gas.

The middle diagrams of Fig. 6.1 depict contour lines of e in the temperature / density–plane. The internal energy differs a lot from that of an ideal gas ($e = fkT/(2\mu)$). Three different regimes can be distinguished which refer to the predominantly molecular, atomic and ionized state of the gas. The regimes are divided by considerable energy barriers in between. In oder to overcome such a barrier (to perform a phase transition), a considerable amount of energy is to be added or to be removed from the gas while the temperature only changes gradually. Within one phase, the internal energy approximately depends linearly on the temperature, close to the behavior of an ideal gas. The internal energy always increases monotonically with temperature.

All components of the internal energy (cf. Eq. 2.2), except for the electronic excitation energy, are found to significantly contribute to the total internal energy of the gas, at least in a particular region of temperature and density. $E_{\rm ion}$ is important for high temperatures where it reaches about $4 \times E_{\rm trans}$ at $20000\,{\rm K}$. $E_{\rm diss}$ dominates the internal energy at low temperatures, about $-59 \times E_{\rm trans}$ at $500\,{\rm K}$ (the internal energy is negative in the molecular regime). $E_{\rm rot}$ is about $0.57 \times E_{\rm trans}$ as soon as H_2 is more abundant than H. The contribution of $E_{\rm vib}$ depends on $T_{\rm rad}$, indicating that the population of the vibrational states of the molecules is strongly affected by the radiation field. Its maximum contribution is found to be $0.07 \times E_{\rm trans}$ for $T_{\rm rad} = 0$ and $1.2 \times E_{\rm trans}$ for $T_{\rm rad} = 3000\,{\rm K}$. $E_{\rm el}$ is found to be negligible ($< 3 \cdot 10^{-4} \times E_{\rm trans}$).

The internal energy of the gas is not completely determined by temperature and density. The dependence on the radiation field is significant. The ionic potential energy $E_{\rm ion}$ and the vibrational excitation energy of molecules $E_{\rm vib}$ are mainly responsible for these dependences. The dependence of e on the velocity gradient is principally also present, but negligible.

6.2.3 The Radiative Cooling Time Scale and the Role of the Various Heating and Cooling Processes

The radiative cooling time scales as function of ρ and T_g are depicted in Fig. 6.2 (for $T_\mathrm{rad}=0$) and in Fig. 6.4 (for $T_\mathrm{rad}=3000\,\mathrm{K}$). The dashed arrows will be discussed later (in Sect. 6.2.7) and are not of interest for the present. For completeness, the net radiative heating function $\widehat{Q}_\mathrm{rad}$ is additionally shown in the lower panel of Fig. 6.1.

Typical values for τ_cool are found to range from $\sim 10^{-2}\,\mathrm{s}$ for a hot and dense gas to $\sim$10 years for a warm and thin gas. The cooling time scale strongly depends on both the gas temperature and the gas density. The temperature–dependence is found to comprise 9 orders of magnitude at large and 3 orders of magnitude at small densities, considering gas temperatures of 500 … 20000 K. The density–dependence is also strong, 8 orders of magnitude at high and 3 orders of magnitude at lower temperatures, considering densities of $10^4 \ldots 10^{14}\mathrm{cm}^{-3}$.

These dependences result from a superposition of the different heating and cooling functions, which are affected by the varying particle concentrations, by minimum gas temperatures required for the efficient excitation of the upper states, by non–LTE effects and by radiative trapping. In general, a dense gas heats and cools more efficiently than a thin gas. However, a simple approach like $Q_\mathrm{rad} \propto \rho^2$ fails to provide a reasonable fit to the results. There are even cases, where a dense gas heats and cools less efficiently than a thin gas. This occurs for $T_\mathrm{g} \lesssim 4000\,\mathrm{K}$ and $n_{<\mathrm{H}>} \gtrsim 10^{11}\mathrm{cm}^{-3}$. In this region, all important radiative heating and cooling rates are of bound–bound transition type and the total rate is strongly reduced by the large optical depths in the lines. The heating/cooling efficiency is no more a question of the strength but of the *number* of lines taken into account. Therefore, the results are uncertain in this region. For sufficiently low gas temperatures ($T_\mathrm{g} \lesssim 1500\,\mathrm{K}$), low continuous radiation fields and high densities, the heating and cooling of the gas is possibly controlled mostly by the presence of dust grains (e. g. via thermal accommodation), since dust formation can take place efficiently in this region.

The most effective heating/cooling processes are stated in the Figs. 6.3 and 6.5. The following picture appears:

- For high temperatures ($T_\mathrm{g} > 6000 \ldots 10000\,\mathrm{K}$), hydrogen cooling dominates. For small densities cooling by Lyα and Hα is efficient, whereas for large densities bound–free cooling of hydrogen turns out to be more important due to the large optical depth in the hydrogen lines. Free–free cooling is also important for high temperatures and large densities.

- For intermediate temperatures, there is a zone of considerable smaller heating/cooling rates, i. e. larger cooling time scales. In this zone, the temperature is already too low in order to excite the H–atoms, but still too high for considerable molecule concentrations. The remaining radiative processes are lines of neutral and singly ionized metal atoms: CI, OI, SiI, FeI, FeII and also SI, CII and OII. At very large densities ($n_{<\mathrm{H}>} > 10^{11} \ldots 10^{12}\,\mathrm{cm}^{-3}$), bound–free transitions of H^- dominate the radiative heating and cooling.

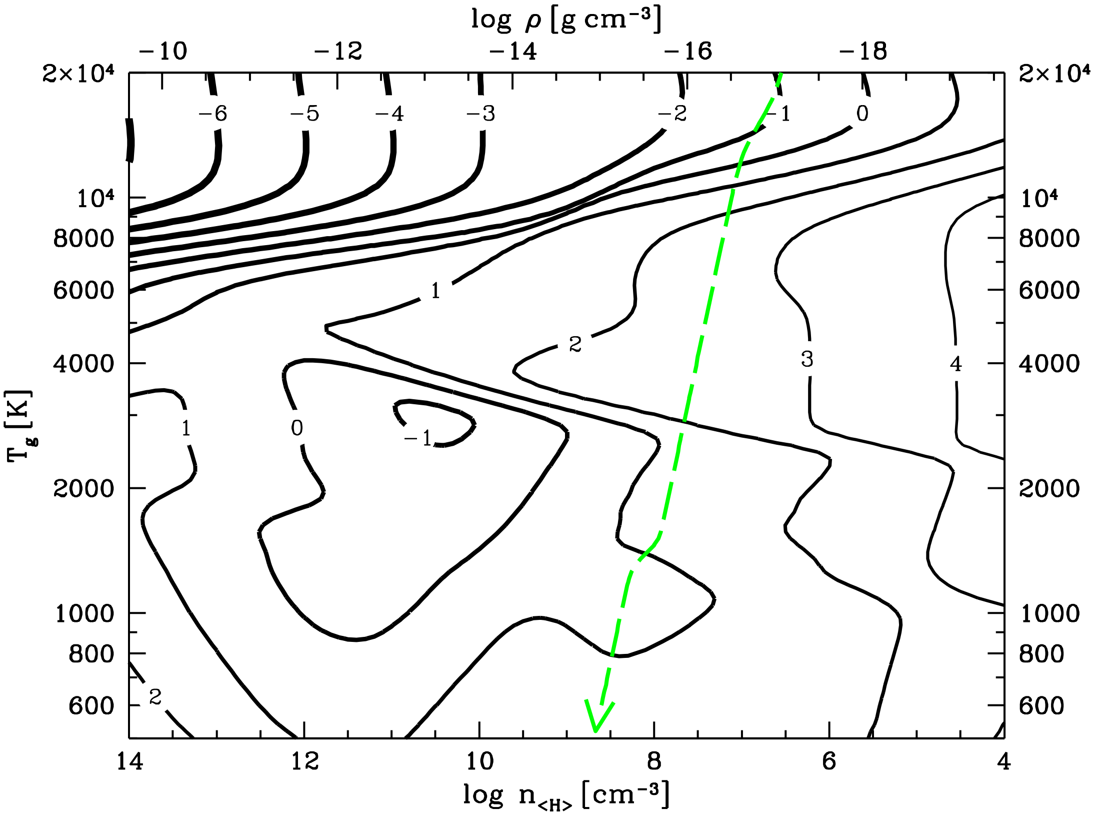

Figure 6.2: Contour lines of the radiative cooling time scales (full lines). The digits on the curves label log $\tau_{\rm cool}$ [days]. The dashed arrow indicates the critical (isobar) cooling track with a maximum radiative cooling time scale of one year on the track. Parameters: $T_{\rm rad} = 0$ and $\left\langle \frac{dv}{dl} \right\rangle = 20\,{\rm km\,s^{-1}}/500\,R_\odot$.

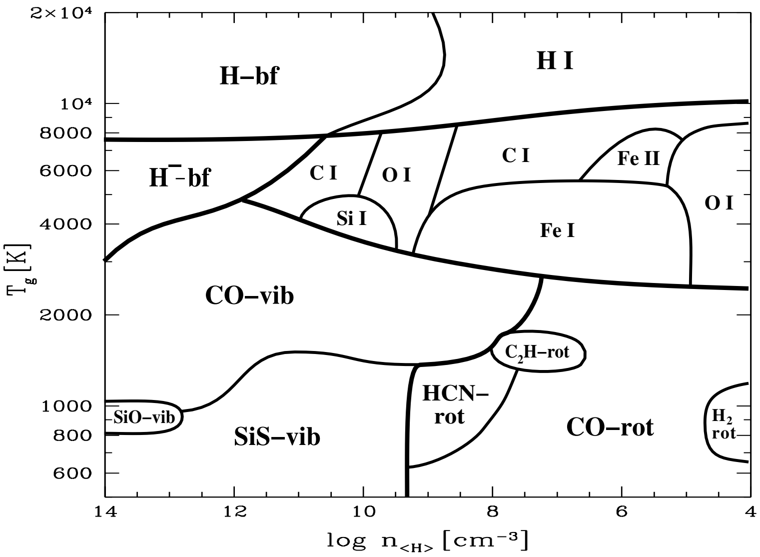

Figure 6.3: Most efficient cooling process referring to Fig. 6.2 (schematically, rot = rotational, vib = vibrational, I = lines of neutral atom, II = lines of ionized atom, bf = bound–free).

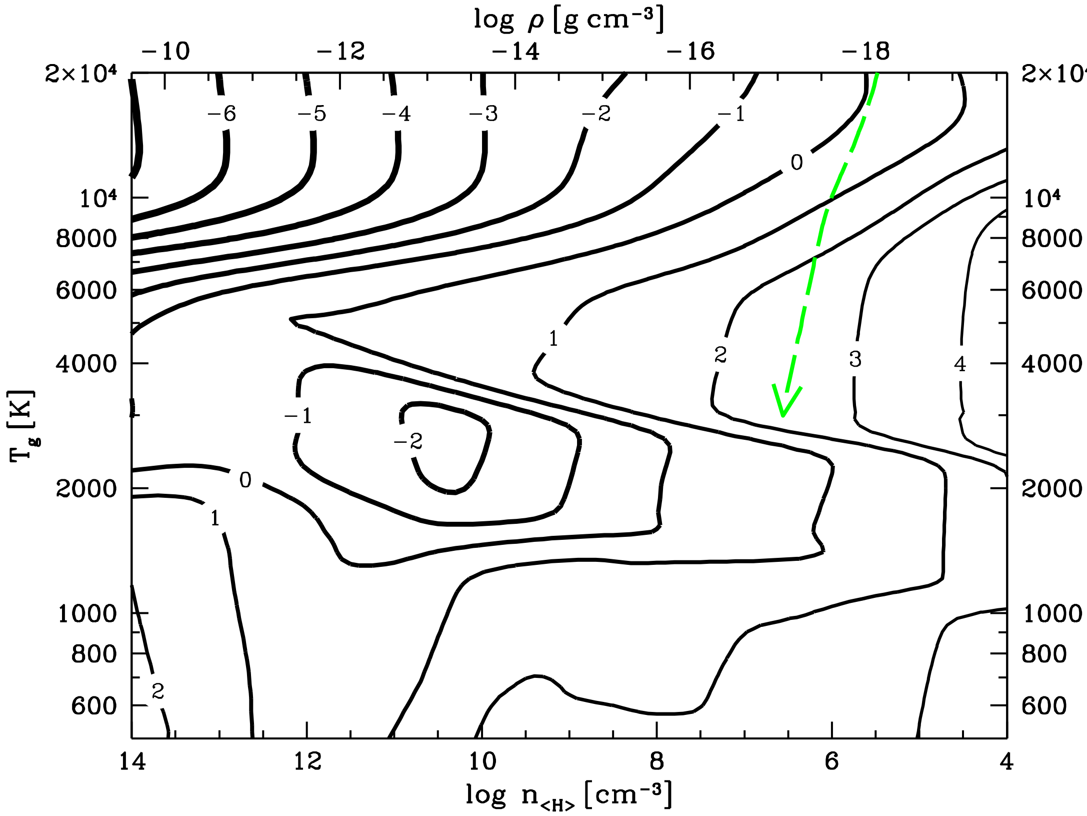

Figure 6.4: Contour lines of log $\tau_{\rm cool}$ [days] as in Fig. 6.2, but for $T_{\rm rad} = 3000\,$K. The critical cooling track ends at $T_{\rm g} = T_{\rm rad}$, where radiative equilibrium is re-established. Note that the cooling time scale remains positive and steady, although the net radiative heating function $Q_{\rm rad}$ changes its sign at $T_{\rm g} = 3000\,$K.

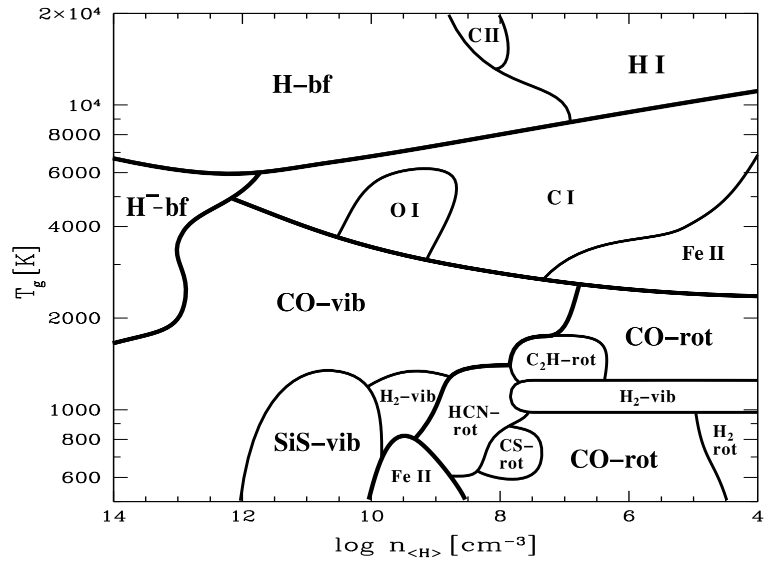

Figure 6.5: Most efficient heating/cooling process referring to Fig. 6.4.

- For low temperatures ($T_{\rm g} < 2000 \ldots 4000\,$K, as soon as CO is abundant), polar molecules dominate the radiative heating and cooling. Vibrational and rotational transitions of CO, SiS, HCN, C_2H, CS, H_2 and also of SiO and CN are important. For small densities rotational heating/cooling dominates, whereas for large densities the vibrational heating/cooling is more important, as expected from the larger critical densities for the thermal population of the vibrational states (cf. Sect. 3.1).

6.2.4 Dependence on the Radiation Field

The cooling time scale as function of J_ν is expected to vary between the values shown in the Figs. 6.2 and 6.4, supposed that $0 \le J_\nu \le B_\nu(3000\,{\rm K})$ for C–star envelopes. The radiative cooling time scale is found to be only marginally affected by the choice of the radiation field. The maximum deviation between the extremes $T_{\rm rad} = 0$ and $T_{\rm rad} = 3000\,$K is found to be 2.4 dex, which occurs in the region controlled by H^- at large densities and warm temperatures. However, the usual deviation is much smaller. The standard deviation is found to be 0.6 dex. This is a surprising result. For example, at $T_{\rm g} < 3000\,$K in Fig. 6.4, the radiative processes change from cooling to heating. One would expect the processes responsible for heating to have a different efficiency than those responsible for cooling. But this turns out to be wrong. The efficiency of radiative *heating and cooling* is an inherent feature of the gas, mainly controlled by temperature and density.

6.2.5 Dependence on the Velocity Gradient

The calculations have been repeated with the one tenth and ten times the usually assumed value of $20\,{\rm km\,s^{-1}}/500\,R_\odot$. Significant differences are only found for $T_{\rm g} \lesssim 4000\,$K and $n_{\rm <H>} \gtrsim 10^{11}{\rm cm^{-3}}$, where the evaluation of $Q_{\rm rad}$ has to be taken with care anyway as stated in Sect. 6.2.3. $Q_{\rm rad}$ never varies more than linearly with $\left\langle \frac{dv}{dl} \right\rangle$. For smaller densities or higher temperatures the dependence is much smaller.

6.2.6 Comparison to Analytical Heating/Cooling Functions

In the following, the results of this work are compared to previous analytical approaches to determine the radiative heating and cooling rates in circumstellar envelopes. As pointed out in Sect. 1.4, these approaches lead to considerable differences in the hydrodynamic model calculations concerning for example the resulting temperature structures.

6.2.6.1 Bowen's Heating/Cooling Function

The following analytic expression of the net radiative heating rate has been proposed by Bowen (1988):

$$\widehat{Q}_{\rm rad} = \frac{3k}{2\mu} \frac{\rho}{C'} \left(T_{\rm rad} - T_{\rm g}\right) \tag{6.5}$$

Bowen strictly assumes $Q_{\rm rad} \propto \rho^2$ throughout the circumstellar envelope. The heating/cooling processes which behave in such a way are limited by the collisional energy transfer as in the limiting case of small densities (cf. Sect. 3.1.1.3). Consequently, one might call Eq. (6.5) the strict non–LTE heating/cooling rate. A temperature–independent cooling time scale is furthermore assumed. The parameter C', reflecting the radiative cooling time scale, is chosen to be $10^{-5}\,{\rm g\,s\,cm^{-3}}$. For higher temperatures cooling by emission in Lyα is additionally taken into account. This H–cooling rate is calculated as described by Bowen (1988), although several assumptions are involved here, which with regard to this work seem to be questionable, as for example the assumption of a constant (density–independent) escape probability for Lyα.

6.2.6.2 LTE Heating/Cooling Function

Starting from the exact expression $\widehat{Q}_{\rm rad} = 4\pi\int\widehat{\kappa}_\nu J_\nu d\nu - 4\pi\int\widehat{\varepsilon}_\nu d\nu$, where $\widehat{\kappa}_\nu$ is the true absorption cross section per mass and $\widehat{\varepsilon}_\nu$ is the spectral emissivity per mass of the gas, the following expression for the net radiative heating rate can be obtained by means of the assumption of LTE $\widehat{\varepsilon}_\nu = \widehat{\kappa}_\nu B_\nu(T_{\rm g})$:

$$\widehat{Q}_{\rm rad} = 4\sigma\Big(\widehat{\kappa}_J(\rho, T_{\rm g})\,T_{\rm rad}^4 - \widehat{\kappa}_B(\rho, T_{\rm g})\,T_{\rm g}^4\Big) \tag{6.6}$$

$\widehat{\kappa}_J(\rho, T_{\rm g})$ is the intensity–mean and $\widehat{\kappa}_B(\rho, T_{\rm g})$ the Planck–mean absorption cross section per mass of the gas. σ is the Stefan Boltzmann constant. This analytical form of the net radiative heating rate has been used by Feuchtinger et al. (1993), assuming a constant grey gas absorption cross section. As far as $\widehat{\kappa}$ is density–independent, $Q_{\rm rad} \propto \rho$ results. Using Eq. (6.6) means to assume that all radiative processes refer to collisionally populated levels of the considered atoms and molecules, which in general requires very large densities (cf. Chapter 3). Furthermore, if one uses κ's which have been calculated by opacity sampling methods with respect to spectral lines (for example the numerous lines of molecules), the included lines are assumed to be optically thin[2]. Due to the lack of Planck–mean opacities, Rosseland mean opacities are used in the following for both opacities in Eq. (6.6). The Rosseland mean opacities $\widehat{\kappa}_{\rm R}(\rho, T_{\rm g})$ are interpolated from tables provided by Scholz (Scholz & Tsuji 1984).

6.2.6.3 Results of the Comparison

The resulting radiative cooling time scales according to Bowen's and according to the LTE heating/cooling function are depicted in the Figs. 6.6 and 6.7, respectively.

[2] In fact, these two assumptions contradict each other.

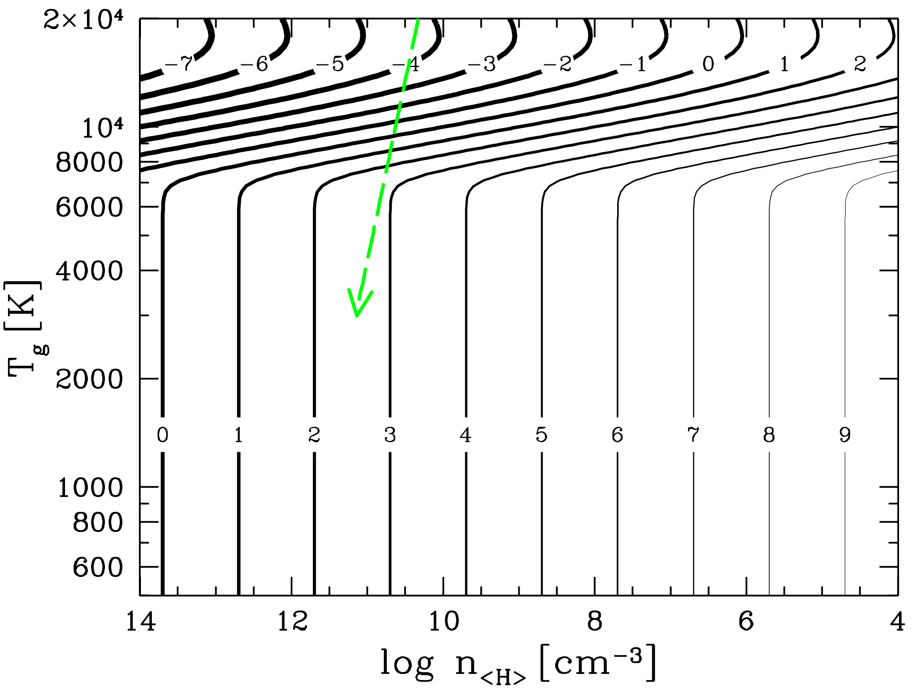

Figure 6.6: log $\tau_{\rm cool}$ [days] calculated from the analytical heating/cooling function proposed by Bowen (1988). $T_{\rm rad} = 3000\,{\rm K}$ is considered.

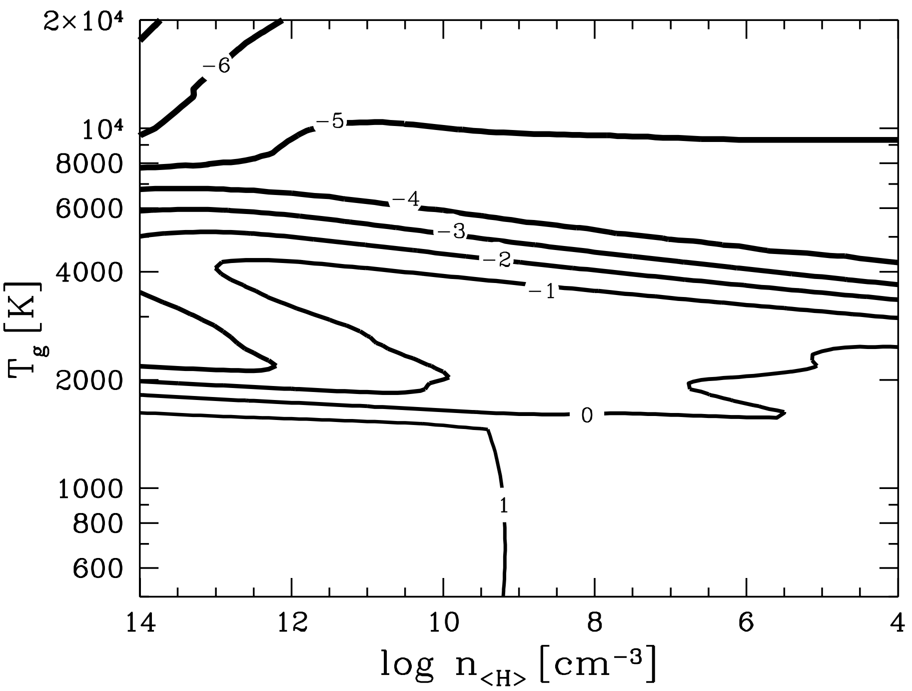

Figure 6.7: log $\tau_{\rm cool}$ [days] as in the upper figure, but calculated from the LTE–heating/cooling function. No critical cooling track exists here, since the radiative cooling time scale is always (much) shorter than one year.

In this context, $e = 3kT_g/(2\mu)$ with $\mu = 1.27$ amu is assumed for both approaches under discussion. These results can be compared to Fig. 6.4.

Neither the cooling time scales derived from Bowen's nor from the LTE rate show much agreement with the results obtained in this work. Bowen's heating/cooling function yields a strong density dependence ($\tau_{cool} \propto \rho^{-1}$, vertical contour lines), whereas the LTE heating/cooling function yields more or less density–independent cooling time scales (roughly horizontal contour lines). Compared to the heating/cooling rates calculated in this work, Bowen's rate usually gives much smaller values (up to a factor of 10^{-6} in the low–density, low–temperature regime), whereas the LTE rate usually gives much larger values (up to a factor of 10^{6} in the low–density, high–temperature regime). The best that can be said is that the cooling time scales calculated in this work usually lie between the values derived from the two analytical formulae.

Some rough agreements are found, nevertheless. For high temperatures ($T_g \gtrsim 8000$ K) Bowen's rate gives about the same slope and order of magnitude compared to the results of this work. As Bowen's rate to some extent treats hydrogen cooling more detailed, and since hydrogen cooling is dominant at high temperatures according to this work, this agreement was to be expected. The LTE rate produces a similar temperature–dependence as found in this work: very effective heating and cooling for high temperatures, an intermediate minimum for the predominantly atomic phase at warm temperatures and a re–increase of the heating/cooling efficiency in the molecular regime at low temperatures. Best agreement with the LTE cooling time scale is found on the left hand side of the diagrams at large densities (yielding similar cooling time scales within about 2 orders of magnitude). However, detailed agreement is not achieved, not even for these large densities. This disagreement might be caused by missing radiative processes in this work. However, more probably, it is because

i) Rosseland means of κ_ν have been used instead of Planck means,
ii) according to this work, the gas is still far from being in LTE at $n_{<\mathrm{H}>} = 10^{14}\,\mathrm{cm}^{-3}$ (especially with regard to the degree of ionization, cf. Fig. 3.9), and
iii) the LTE heating/cooling function neglects optical depths in the lines.

In summary, both analytical heating/cooling functions yield poor agreement with the results of this work. Bowen's rate seems to underestimate and the LTE rate seems to overestimate the heating/cooling efficiency by orders of magnitude. This stresses the necessity to use more detailed model calculations for the radiative heating and cooling. The proposed analytical functions are insufficient to describe the radiative heating and cooling in the circumstellar envelopes of cool stars.

6.2.7 The Transition from Isothermal to Adiabatic Shocks

The calculated radiative cooling time scales of this work allow for a quantitative discussion of the character of the thermal relaxation behind propagating shock waves in the circumstellar envelopes of pulsating stars.

A gas element being hit by a strong shock wave of velocity v_s is almost instantaneously heated up to high temperatures ($\approx 11500\,\mathrm{K}\cdot[v_s/20\,\mathrm{km\,s^{-1}}]^2$ for an ideal gas consisting of $\mathrm{H}+10\%\,\mathrm{He}$). After the passage of the shock, the gas radiates away the excess internal energy dissipated by the shock, i. e. it relaxes to RE, *in principle*.

However, considering the more or less periodically shocked envelopes of pulsating stars, only a limited time for this relaxation is available, before the next shock wave hits the element. This time is given by about one stellar pulsational period P. Furthermore, the propagating shock waves initiate a considerable compression and re-expansion of the gas accompanied by considerable adiabatic heating/cooling. The time scale of these processes is also given by P. Thus, the relation between the radiative cooling time scale $\tau_{\rm cool}$ and the stellar pulsational period P determines the character of the thermal behavior of the gas in the CSEs of pulsating stars.

$$\begin{array}{rcl} \tau_{\rm cool} \ll P & \Leftrightarrow & \text{isothermal shocks} \\ \tau_{\rm cool} \gtrsim P & \Leftrightarrow & \text{adiabatic shocks} \end{array} \tag{6.7}$$

If $\tau_{\rm cool}$ is much smaller than P, the gas quickly relaxes to RE behind the shocks. The adiabatic heating/cooling rates are meaningless. RE is established in the overwhelming parts of the circumstellar envelope, except for some thin temperature peaks at the location of the shock fronts (cf. Fig. 1.3). Apart from these peaks, the temperature structure of the CSE can be calculated by assuming RE.

If, however, $\tau_{\rm cool}$ exceeds P, a "chromospheric" situation results. The gas cannot radiate away the energy dissipated by one shock within one pulsational period. Consequently, the gas subsequently heats up due to the shocks (cf. Fig. 1.4), roughly cooling adiabatically in the meantime. The temperature structure must be calculated time–dependently.

In analogy to the situation in stationary shocks (e. g. Neufeld & Hollenbach 1994), an isobar cooling track in the temperature / density–plane is considered in the following. The total cooling time along such a track is roughly given by the maximum radiative cooling time scale $\tau_{\rm cool}$ on the track. The isobar cooling track with $\tau_{\rm cool} \leq 1\,\mathrm{yr}$ on the track (henceforth called the "critical cooling track") is depicted in Fig. 6.2, Fig. 6.4 and also in Fig. 6.6 as dashed grey arrow, considering one year as a typical period of pulsating C–stars. The deviations from a straight line are caused by changes of the mean particle mass due to phase transitions (cf. Fig. 6.1). The critical cooling track is an estimate for the dividing line between the shocks of predominantly isothermal and predominantly adiabatic character. Gas elements which are shocked to the left of the critical cooling tracks can reestablish RE before the next shock arrives — those which are shocked to the right of the critical cooling track will be hit by the next shock before RE can be achieved.

According to the results of this work, a transition of the character of the shock waves is to be expected to occur around post–shock densities of $10^6 \ldots 10^8\,\mathrm{cm}^{-3}$, changing from predominantly isothermal to predominantly adiabatic with decreasing density. Around $T_\mathrm{g} \approx 5000\,\mathrm{K}$ the cooling gas element spends most of its total cooling time. The cooling time scale in this temperature region is found to vary by $4-5$ orders of magnitude for the entire range of considered densities, which is 10 orders of magnitude. Therefore, a sharp transition is not expected to occur, rather a gradual change over a broad range of densities. For example, if $\tau_\mathrm{cool} < 0.01P$ was demanded for isothermal shocks, densities as large as $10^{10} \ldots 10^{12}\,\mathrm{cm}^{-3}$ would be required. A final answer to these questions can only be obtained by means of time–dependent hydrodynamic model calculations.

According to Bowen's rate, the transition from isothermal to adiabatic shocks already occurs at $\sim 10^{11}\,\mathrm{cm}^{-3}$. The LTE rate predicts the shocks to be close to the isothermal limiting case for all densities. This explains the differences between the model calculations of Bowen (1988) and Feuchtinger et al. (1993) concerning the resulting temperature structures.

6.3 Discussion

The results of this chapter strongly suggest to include time–dependent thermodynamics in the model calculations for cool stellar envelopes, especially in the case of pulsating stars. The basis for the thermodynamic description is a realistic calculation of the relevant heating and cooling rates. Simple analytical expressions previously used are not sufficient in this context.

A time scale discussion can be performed in order to clarify whether or not the condition of radiative equilibrium (RE) can be used to determine the gas temperature. By comparing the radiative cooling time scale τ_cool, as depicted in the Figs. 6.2 and 6.4, with the other time scales controlling the physical process under consideration, it can be decided whether the temperatures may be calculated from radiative transfer calculations (assuming RE), or whether, for instance, a simple adiabatic cooling law is more appropriate.

The general tendency of the results obtained in this work is that the condition of RE can only partly be used in order to determine the temperature of the gas. For the large densities close to the star the radiative cooling time scales are found to be of the order of days, so that RE is probably established and a temperature determination on the basis of RE is justified. However, in general, time–dependent effects as adiabatic cooling can throughout be important. The lower the density to be considered, the more questionable the determination of the temperature on the basis of RE becomes. For instance, at $n_{<\mathrm{H}>} \approx 10^7\,\mathrm{cm}^{-3}$ in the warm atomic phase, the radiative cooling time scale approaches the order of one year, already close to the expansion time scale in stationary wind models for C–stars (e. g. Krüger et al. 1994).

Concerning the shocked envelopes of pulsating stars, the thermodynamics should be treated time–dependently and if only for the existence of the shock waves. Additionally, apart from the locations of the shock fronts, strong deviations from RE are expected to occur roughly at densities $n_{<\mathrm{H}>} \lesssim 10^{8}\,\mathrm{cm}^{-3}$, connected with the gradual transition of the character of the shocks, changing from approximately isothermal to approximately adiabatic.

Time–dependent thermodynamic effects can cause substantial changes in the temperature structures of cool stellar envelopes. How far the chemical and the dust formation processes are affected is to be investigated. The proper inclusion of the heating and cooling rates calculated in this work into the time–dependent hydrodynamic model calculations can be achieved by tabulating Q_{rad} and the internal energy e as functions of ρ, T_{g} and further parameters characterizing the local continuous radiation field and the local mean velocity gradient. According to the strong temperature–dependence of the chemical and the nucleation processes, pronounced effects are conceivable[3]. Another topic which might be related to the results of this work is the formation of chromospheres.

[3]The following chapter will demonstrate what severe consequences a time–dependent thermodynamic modeling may have with regard to dust formation.

Chapter 7

Shock–Induced Condensation around RCB Stars

The third and last application in this work studies a distinct time–dependent thermodynamic process. The most complex level included in the work is achieved: time–dependent non–LTE (in the steady state approximation) and non–RE.

The circumstellar envelopes of pulsating RCB stars are considered. A thermodynamic description for fixed fluid elements which are periodically hit by shock waves is developed. As the shocks compress the gas, it re–expands in the meantime which causes considerable adiabatic cooling. The internal energy balance, the temperature of the gas and the possibility for effective carbon nucleation to occur in such fluid elements are investigated. Special attention is paid to the minimum radial distance required for such nucleation. The calculations provide a hypothesis for the physical cause of the spectacular RCB decline events which are supposed to be caused by dust formation close to these relatively hot stars. The astronomical background and the scientific meaning of these studies are further described in Sect. 1.3 and in Appendix A.

7.1 The Model: A Fixed, Periodically Shocked Fluid Element in a Constant Radiation Field

A chosen fluid element in the circumstellar envelope of a pulsating star is time and time again hit by propagating shock waves caused by the stellar pulsation. The shocks accelerate, heat, chemically alter and compress the gas (Bowen 1988, Fleischer et al. 1992, Feuchtinger et al. 1993). Between the shocks, the fluid element follows a roughly ballistic trajectory, while cooling, chemically relaxing and re–expanding (Gillet & Lafon 1983, Bowen 1988).

Thus, the CSEs of pulsating stars are astrophysical sites where a complex interplay of different physical processes takes place: hydrodynamics, thermodynamics, chemistry and dust formations. A complete modeling of these processes occurring in circumstellar shock waves is a very challenging work which goes far beyond the scope of this thesis. Instead, the model calculations presented in this chapter study the thermodynamic consequences of the hydrodynamic situation of periodically shocked gas. A simple gas–box description suitable for the thermodynamic investigations is developed for this situation which, according to observations, is apparently common among the dust–forming objects (Jura 1986).

The circumstellar envelope is assumed to oscillate in a periodic manner[1]. Furthermore, mass loss is neglected. Mass loss leads to an additional outward movement accompanied by additional expansion, which causes additional adiabatic cooling. Therefore, the neglection of mass loss systematically underestimates the effect discussed in this chapter, which is the temporal supercooling of the gas below its RE–temperature during the phases of re–expansion. According to these assumptions, the fluid element exactly returns to its starting point (cf. Fig. 7.1) and all hydrodynamic and thermodynamic quantities vary periodically in time with the pulsation period of the star. We will concentrate on this most simple case, which is considered as being typical for the envelopes of pulsating stars.

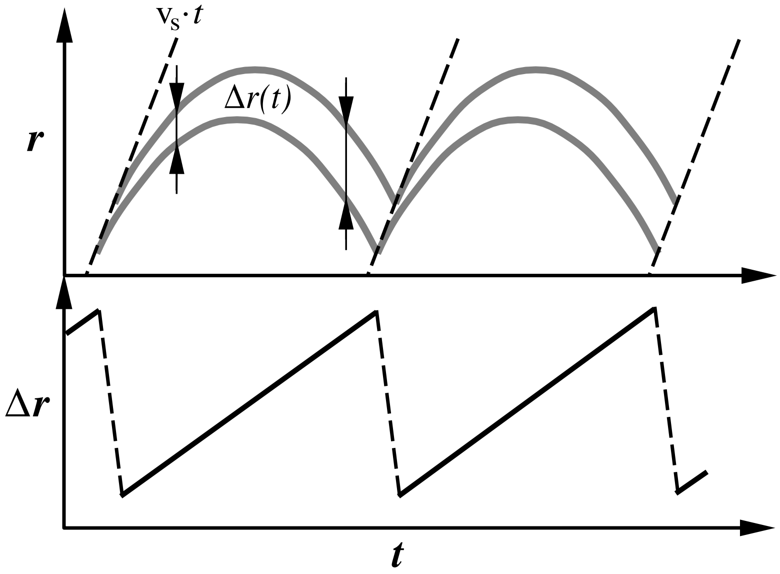

Figure 7.1: Lagrangian trajectories (schematically, upper panel) and distance between two neighboring fluid elements (lower panel) in the shock–levitated circumstellar envelope of a pulsating star without mass loss. v_s is the shock velocity in the laboratory frame. On average, the acceleration by shocks is balanced by gravitational deceleration. The re–expansion of the gas between the shocks is caused by the phase–shift of the ballistic trajectories according to the gravitation of the star.

The periodic situation as sketched in Fig. 7.1 can be divided into two phases: the shock transition and the re–expansion of the gas. Both processes are examined in the following in order find an appropriate prescription of the periodic boundary conditions, which the gas elements are exposed to.

[1]Fleischer et al. (1995) have pointed out that a multi-periodic or even chaotic oscillation of the envelope is possible even if the stellar pulsation is perfectly periodic.

7.1.1 Shock Transitions

The shock transitions are treated by applying the Rankine–Hugoniot relations (e. g. Landau–Lifschitz 1959). The shock front is considered as infinitesimally thin and the actual transition process as instantaneous. The jump conditions for a plane–parallel perpendicular shock ($\vec{v}\perp$ to the front) are given by the equations of the conservation of mass, momentum and energy in a comoving frame of the shock front. Negligible magnetic fields and vanishing contributions of the radiative flux are assumed:

$$\begin{aligned} \rho_1\, v_1 &= \rho_2\, v_2 \\ p_1 + \rho_1\, v_1^2 &= p_2 + \rho_2\, v_2^2 \\ \frac{1}{2}\, v_1^2 + h_1 &= \frac{1}{2}\, v_2^2 + h_2 \end{aligned} \tag{7.1}$$

Equations (7.1) relate the hydrodynamic and thermodynamic properties of the upstream flow (index 1, "pre–shock") to those of the downstream flow (index 2, "post–shock"). $h = e + p/\rho$ is the enthalpy and e the internal energy per mass of the gas. Together with the equation of state (cf. Chapter 4) the post–shock quantities can be calculated from the pre–shock thermodynamic state and the shock velocity v_1. Strictly speaking, the so–defined post–shock state refers to a definite time after the passage of the shock wave, when the gas has just relaxed to its steady state, so that the equation of state is applicable again. This time is assumed to be small compared to pulsation period P and the radiative cooling time scale.

Due to the non–trivial equation of state involved, the actual solution of the system of equations (7.1) requires an iteration. The following simple iteration scheme is applied which is found to converge reliably:

1) Start with a compression ratio of four ($v_2 = v_1/4$).
2) Put $h_2 = h_1 + (v_1^2 - v_2^2)/2$ and $p_2 = p_1 + \rho_1 v_1 (v_1 - v_2)$.
3) Calculate the post–shock density according to the equation of state in the form $\rho_2 = \rho_2\Big(p_2, h_2, J_\nu, \Big\langle\frac{dv}{dl}\Big\rangle\Big)$.
4) Define $\delta = |1 - (\rho_2 v_2)/(\rho_1 v_1)\,|$.
5) Perform one iteration step by $v_2 \to 0.1\, v_2 + 0.9\, v_1 \rho_1/\rho_2$.
6) Go back to step 2 unless $\delta < 10^{-8}$.

The radiation field J_ν, the velocity gradient $\Big\langle\frac{dv}{dl}\Big\rangle$ and the element abundances ϵ_i are additional parameters for the calculation of the equation of state (cf. Chapter 4). These parameters are set to fixed values during the calculations and are assumed to be equal on both sides of the front (cf. Sect. 7.1.6).

The calculated compression ratios ρ_2/ρ_1 for strong shocks ($v_1 \gg$ pre–shock sound speed) are found to be larger than the maximum value of 4 for an ideal gas. Typical values range from 5 to 9, depending on the shock velocity. This effect is caused by the dissociation and ionization potential energy terms in the equation of state. According to the theoretical description outlined, the gas is completely dissociated and partially ionized by strong shocks. Since the dissipated shock energy is partly consumed in order to break the chemical bonds and to ionize the atoms, the post–shock gas temperatures are found to be lower compared to an ideal gas. Typical values are 20000 K to 70000 K for shock velocities $20\,\mathrm{km\,s^{-1}}$ to $50\,\mathrm{km\,s^{-1}}$. The post–shock temperatures are higher compared to a hydrogen–rich gas because of the more massive hydrogen–deficient gas.

7.1.2 Re–Expansion Phases

Between the shocks, the change of the internal energy of the gas is calculated via the first law of thermodynamics (cf. Sect. 7.1.3). In order to find an appropriate description of the re–expansion process, a suitable state variable is chosen, whose explicit time–dependence can be prescribed. Of course, this is an approximate procedure. A consistent physical description would include time–dependent hydrodynamics and cannot by limited to single fluid element considerations. The following approach is adapted to the experience of hydrodynamic model calculations.

$$p^{-1/\gamma}(t) = p_2^{-1/\gamma} + \left(p_1^{-1/\gamma} - p_2^{-1/\gamma}\right) \frac{t \text{ MOD } P}{P} \qquad (7.2)$$

p_1 is the pre–shock and p_2 the post–shock gas pressure (cf. Eq. 7.1), MOD the modulo function and γ the adiabatic index of the gas, which is assumed to be 5/3 in this context. The main idea of this approach is to assume that the gas pressure monotonically decreases between the shocks with a power–law in time. The approach is motivated as follows:

(i) In the limiting (adiabatic) case of negligible radiative heating/cooling, where $pV^\gamma = const$, the volume varies like a saw–tooth function in time

$$V(t) = V_{\min} + (V_1 - V_{\min}) \frac{t \text{ MOD } P}{P} \quad . \qquad (7.3)$$

V_1 is the pre–shock volume and $V_{\min}$ the minimum volume of a fixed fluid element during one periodic cycle. $V_{\min}$ equals the post–shock volume V_2 in the adiabatic case. Equation (7.3) provides a good fit to the volume variations found in time–dependent hydrodynamic model calculations (e. g. Bowen 1988, see his Fig. 4). It is readily obtained if the gas actually behaves purely ballistic as sketched in Fig. 7.1. In this case, the Lagrangian trajectories $r(t)$ are second–order polynomials and the distance between two neighboring fluid elements Δr varies like a saw–tooth functions in time. Supposed that the amplitude of radial motion is small compared to the absolute radial distance, the enclosed volume $V \propto r^2 \Delta r$ is proportional to Δr and, therefore, also a saw–tooth function. In general, taking into account radiative heating and cooling, the calculated volume variation does not differ much from Eq. (7.3) as demonstrated in Fig. 7.3. The main difference is that in this case $V_{\min}$ is smaller than V_2, which will become more clear in the next paragraph.

(ii) According to Eq. (7.2) the gas pressure varies on a time scale of P. Hence, fast radiative cooling with $\tau_{\rm cool} \ll P$ automatically proceeds isobaricly. Consequently, the fluid element compresses by fast cooling, which especially occurs shortly after the passage of a shock wave, where the gas is hot and cools very efficiently. This matches well with the results of stationary shock models (e. g. Hollenbach & McKee 1979 and 1989, Neufeld & Hollenbach 1994), where the initial shock compression of about a factor 4 is followed by a subsequent post–shock compression, which amounts up to a factor 100. The reason for this behavior is that the flow is subsonic behind the front, so that pressure balance can establish. The cited calculations show that $p = const$ is valid within 25% accuracy in the whole post–shock region in the case of a stationary flow. Therefore, again considering the periodic shocks, $V_{\rm min}$ in general does not coincide with V_2, but is substantially smaller due to subsequent post–shock compression by radiative cooling[2]. The post–shock cooling usually proceeds so fast, that Eq. (7.3) is still a good approximation of the resulting overall volume variation.

(iii) According to the assumption that the pressure variation is monotonically decreasing between the shocks, the amplitude of pressure variation is given by the jump conditions Eq. (7.1). There is no need to introduce additional free parameters in order to describe the amplitude of the cyclic variations caused by the shocks. Especially $V_{\rm min}$ is a result of the calculations. If the volume was chosen to be prescribed, one free parameter, that is $V_{\rm min}$, would be additionally required.

The results are not much affected by the assumed slope of the pressure time–dependence. Additional calculations have been carried out with different values for γ and also calculations where the volume was chosen to be prescribed (using Eq. (7.3) with $V_{\rm min}$ as additional free parameter). The results are very similar — only the existence of a periodical perturbation of the fluid element and its amplitude (characterized by the shock velocity) are apparently important.

7.1.3 Thermodynamics

The time evolution of the internal energy e of the considered fluid element during the re–expansion phases is straightforwardly calculated via the first law of thermodynamics

$$\frac{de}{dt} = -\,p\,\frac{dV}{dt} + \widehat{Q}_{\rm rad} \quad . \tag{7.4}$$

Since the gas pressure is chosen to be prescribed, it is more convenient to consider the specific enthalpy $h = e + p/\rho$ and to solve instead

$$\frac{dh}{dt} = +\,V\,\frac{dp}{dt} + \widehat{Q}_{\rm rad} \quad . \tag{7.5}$$

Equation (7.5) is solved by implicit numerical integration with adaptive step size control. The key for this calculation is the determination of the state of the gas and

[2]Consequently, the trajectories are in fact not purely ballistic. In the hot post–shock regions the pressure gradient provides a non–negligible hydrodynamic force.

the net radiative heating/cooling rate as function of p, h, J_ν and $\left\langle\frac{dv}{dl}\right\rangle$ which yields V and $Q_{\rm rad}$ at every instant of time, so that Eq. (7.5) becomes an ordinary differential equation. The gas temperature $T_{\rm g}$ as function of time is an implicit result of these calculations.

7.1.4 The Modeling Procedure

A schematic description of the thermodynamic processes and the modeling procedure is sketched in Fig. 7.2. A fluid element in the CSE of a pulsating (RCB) star is considered. In phase 1 the element is hit by a propagating shock wave, where it is heated and compressed ($\rightarrow V_2$). During phase 2 it cools down and further compresses due to fast, approximately isobaric radiative cooling ($\rightarrow V_{\rm min}$). According to the periodicity in these envelopes, the gas element finally re-expands during the rest of each periodical cycle in phase 3 ($\rightarrow V_1$). These three phases repeat periodically.

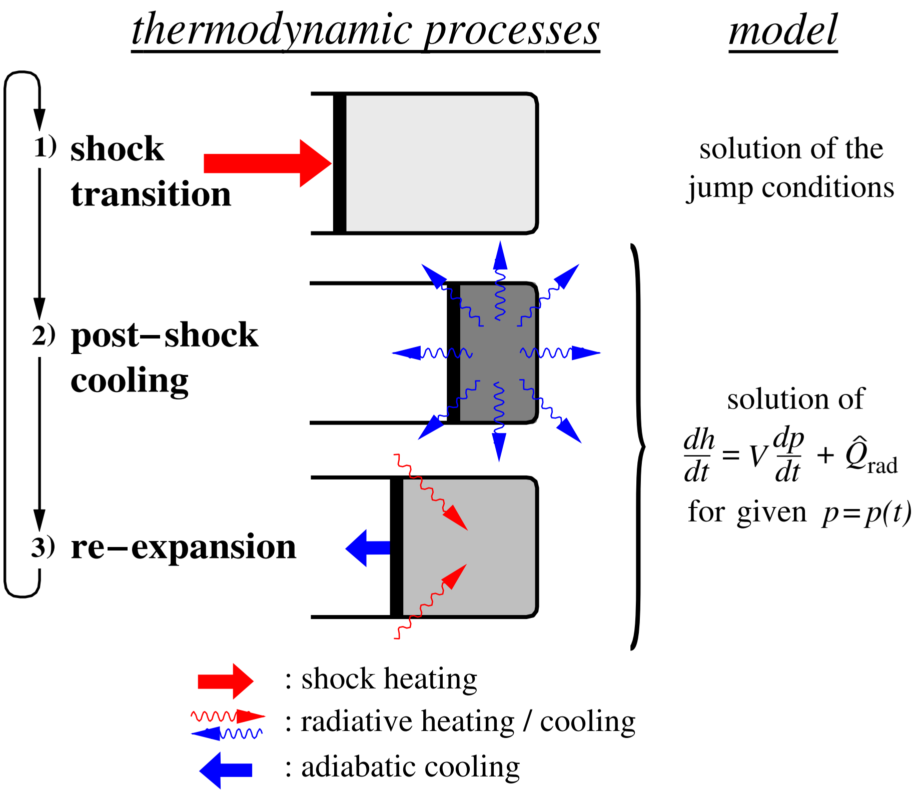

Figure 7.2: The three periodically repeating phases of *shock transition*, *post–shock cooling* and *re–expansion* for a fluid element in the circumstellar envelope of a pulsating star. Wiggled arrows indicate net radiative cooling (in phase 2) or heating (in phase 3). The theoretical description of the processes is outlined on the right hand side

The model simulates these processes by solving the shock jump conditions at the instants of time where the shock waves hit the gas element $t \in \{0, 1P, 2P, \ldots\}$ and by calculating the first law of thermodynamics in the meantime. The calculations are continued until the variations of the thermodynamic quantities in the gas element become periodically. Usually 3 to 25 periods are required in order to achieve periodicity. In detail, the calculations proceed as follows:

1) Choose a fixed radiation field J_ν, a fixed velocity gradient $\left\langle \frac{dv}{dl} \right\rangle$, a fixed shock velocity v_1 and at fixed pre–shock gas pressure p_1. Start with an arbitrary initial enthalpy h_1.
2) At every full period, solve the jump conditions Eq. (7.1) for the post–shock state (p_2, h_2).
3) Consider the time variation of the gas pressure during the forthcoming period as explicitly given according to Eq. (7.2) and calculate the enthalpy according to Eq. (7.5), yielding (p_1, h_1') at the end of this period.
4) Go back to step 2, unless all variations have become periodic.

7.1.5 Overview of Introduced Parameters

The final (periodic) results of the model depend on the following parameters:

- Two parameters for the description of the background continuous radiation field ($T_{\rm eff}$ and r/R_*, cf. Eq. 5.3).
- Two parameters for the strength and the frequency of the propagating shock waves (v_1 and P).
- Parameters for the composition and the overall density of the considered gas element (ϵ_i and p_1).
- Two additional parameters whose effects on the results are small, that is the local mean velocity gradient $\left\langle \frac{dv}{dl} \right\rangle$ and the power index γ for the explicit pressure time–dependence during re–expansion (cf. Eq. 7.2).

7.1.6 Examined Range of Parameters

$\mathbf{T}_{\rm eff}$ and $\mathbf{r/R_*}$: The effective temperature of the central RCB star is assumed to be 7000 K throughout this chapter, which apparently is a representative value for this class of stars (Lambert & Rao 1994). The variation of the radial position of the fluid element (as sketched in Fig. 7.1) is assumed to be small compared to R_*, so that r/R_*, for simplicity, is fixed. Thereby, the mean intensity J_ν is assumed to be constant during the calculations. In contrast, a significant radial motion of the fluid element would imply an additional time–dependence of J_ν, which is regarded as further complication of the model of minor importance. Radial distances of $1.5-5\,R_*$ are considered.

P: The pulsation period is assumed to be 44 days, which is the value suggested by Fernie et al. (1972) for R CrB. Since other RCB stars show very similar values for P (cf. Appendix A) this parameter is also fixed for the calculations.

$\mathbf{v_1}$**:** The shock velocity is uncertain, may be different for different RCB stars and will furthermore depend on the considered radial distance. Time–dependent models for the circumstellar envelopes of long–period variables (Bowen 1988, Fleischer et al. 1992, Winters et al. 1994, Feuchtinger et al. 1993) indicate that the shocks begin to develop somewhere below the photosphere, where the velocity variation is usually a few $\mathrm{km\,s^{-1}}$. The shocks considerably steepen up according to the exponential density gradient in the outer atmosphere and soon reach shock velocities of $\sim 30\,\mathrm{km\,s^{-1}}$ (the shock velocity can approximately be identified with the amplitude of velocity jumps occurring in these models). At larger radial distances, the density gradient becomes smaller and the shock velocity usually tends to decrease again, leading to $\sim 10\,\mathrm{km\,s^{-1}}$ or even almost zero, depending on the model. It is unclear, whether these results can be adopted to RCB stars. Large photospheric velocity variations of $\pm\,20\,\mathrm{km^{-1}}$ (implying shock velocities of $40\,\mathrm{km\,s^{-1}}$) have been observed for RY Sgr, which is the strongest known pulsating RCB star (cf. Appendix A). These measurements refer to the line formation region, i. e. to the photosphere of the star. Considerably stronger shocks can be expected in the CSE[3]. However, RY Sgr is an exceptional case. Other RCB stars show radial velocity variations of about ± 5 to $\pm 10\,\mathrm{km\,s^{-1}}$, but no line splitting which is an indicator for shock activity in the photosphere (Appendix A). Shock activity in the CSE is probably not directly detectable, at least not at maximum light (apart from the decline events), when the star is too bright. Therefore, the questions of the existence of shock waves in the CSEs of RCB stars and their velocities cannot be decided by observations yet. This work presupposes the presence of shock waves in RCB star envelopes, since (i) RCB stars show considerable radial velocity variations at the photosphere and (ii) even small amplitude waves are known to steepen up to considerable shock waves in the CSE from theory. Shock velocities of $20-50\,\mathrm{km\,s^{-1}}$ are considered.

$\epsilon_\mathbf{i}$**:** The elemental abundances of the prototype star R CrB are adopted from Cottrell & Lambert (1982), cf. Fig. 5.1.

$\mathbf{p_1}$**:** The pre–shock pressure of the fluid elements is varied independently of r/R_*. Although the mean gas pressure can be expected to monotonically decrease with increasing radial distance, the actual density structure of the circumstellar envelopes

[3] The following theoretical consideration points to larger shock velocities in RCB star envelopes compared to AGB star envelopes. For shock–levitated CSEs as sketched in Fig. 7.1, $v_1 \approx g_{\rm eff} P$ is a good approximation. $g_{\rm eff}$ is the gravitational deceleration corrected for radiative acceleration. The gravitational force at the photosphere of an RCB star is about 30 times larger than that of an AGB star (roughly assuming equal stellar masses and luminosities) and the pulsation period about a factor of 10 smaller, yielding about 3 times larger shock velocities compared to AGB stars. If $10\,\mathrm{km\,s^{-1}}$ is considered as a typical value for AGB stars, values of about $30\,\mathrm{km\,s^{-1}}$ are deduced for the envelopes of RCB stars.

of RCB stars is not known. Pre–shock gas pressures of $10^{-7} - 10^{+1}\,\mathrm{dyn\,cm^{-2}}$ are considered.

The mean local velocity gradient is no crucial parameter to the model and is assumed to be given by $\left\langle \frac{dv}{dl} \right\rangle = v_1/R_*$. The stellar radius is assumed to be $R_* = 73\,R_\odot$ in this context (Fernie 1982). The power index for the prescription of the time–dependence of the gas pressure is set to $\gamma = 5/3$.

7.2 Results

7.2.1 Cyclic Variations in the Periodically Shocked Fluid Elements

An example of the results for the cyclic variations of the thermodynamic state variables in fixed, periodically shocked, circumstellar fluid elements is depicted in Fig. 7.3. The first 3 periods after periodicity has been achieved are plotted on a linear time scale. The post–shock gas temperature is found to be $\sim 24000\,\mathrm{K}$ in the considered case, which is out of the depicted range. During the first $\sim 1.5\%$ of the period (~ 16 hours) the gas efficiently cools down to $\sim 10000\,\mathrm{K}$, which causes further compression. The shock compression factor is ~ 6.2 and the post–shock compression factor is ~ 2.0. An attempt to depict the difference between the shock and the post–shock compression is made in the middle panel, but on this linear scale the total (shock + post–shock) compression phase appears like a single, almost instantaneous process. The gas approximately re–expands adiabatically after this compression. A saw–tooth like behavior of the volume results. The temperature reaches T_g^RE after about 10% of the period and is clearly below T_g^RE afterwards. Here and in the remainder of this chapter T_g^RE denotes the first stable "high–temperature" solution of radiative equilibrium as defined in Chapter 5. T_g^RE is density–dependent and hence not constant.

In fact, the value of T_g^RE is practically meaningless for the gas in the depicted case of $p_1 = 1.6 \cdot 10^{-5}\,\mathrm{dyn\,cm^{-2}}$, which corresponds to a density variation of $n_{<\mathrm{He}>} = 6 \cdot 10^7 \ldots 7 \cdot 10^8\,\mathrm{cm^{-3}}$. The time–dependent temperature of the gas is essentially determined by the shock transition and the efficiency of the radiative cooling at high–temperatures during the post–shock cooling phase. These two phases determine the start temperature and the total (de–)compression factor for the forthcoming phase of re–expansion which proceeds approximately adiabatically. RE is never realized and cannot be used to determine the temperature of the gas.

Further details are shown in Fig. 7.4, where the same setting of the parameters is investigated except for a larger shock velocity of $50\,\mathrm{km\,s^{-1}}$. In this case, the post–shock temperature is found to be $\sim 64000\,\mathrm{K}$ and the shock and post–shock compression factors are ~ 8.4 and ~ 11, respectively. All radiative processes cause net cooling behind the shock and since the cooling time scale is as short as initially $\sim 100\,\mathrm{s}$, the fluid element very quickly cools down due to radiative losses. Within the first $\sim 0.3\%$ of the period (~ 3 hours), the temperature drops to $\sim 8000\,\mathrm{K}$.

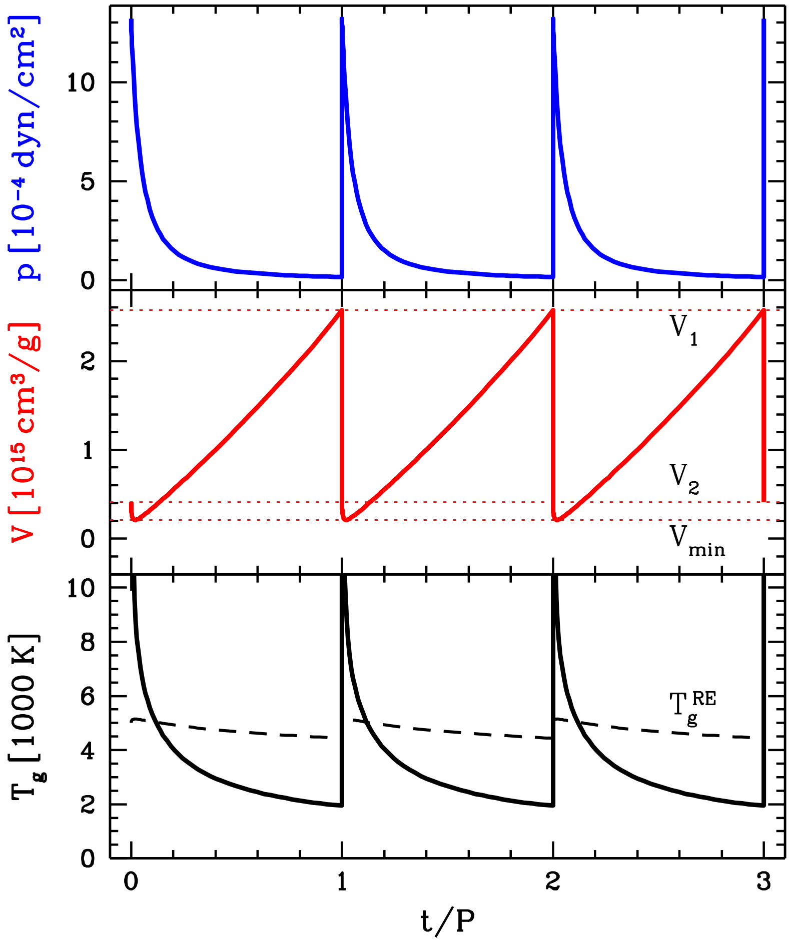

Figure 7.3: Time variations in a fixed, periodically shocked, circumstellar fluid element of an RCB star. The gas pressure (assumed, upper panel) and the specific volume and the gas temperature (calculated, middle and lower panel) is plotted for distance $r = 2R_*$, shock velocity $v_1 = 20\,\mathrm{km\,s^{-1}}$ and pre–shock pressure $p_1 = 1.6 \cdot 10^{-5}\,\mathrm{dyn\,cm^{-2}}$. The dotted lines in the middle panel indicate the pre–shock, post–shock and minimum volume. The dashed line in the lower panel depicts the radiative equilibrium gas temperature.

During this phase, which is plotted on a logarithmic time scale in Fig. 7.4, the fluid element compresses as can be seen from the increasing density in the upper panel. The temperature reaches $T_{\rm g}^{\rm RE}$ after $\sim 1\%$ of the period (~ 10 hours). During the remaining time of the period, the fluid element re-expands by a total factor of ~ 92. This re-expansion causes intense adiabatic cooling as indicated by the cooling rate $Q_{\rm adb} = V dp/dt$ in Fig. 7.4, which is the concurring rate for dh/dt in Eq. (7.5). Consequently, the gas temperature decreases below $T_{\rm g}^{\rm RE}$ and the total net radiative heating function $Q_{\rm rad}$ changes its sign (note the twofold logarithmic y–axis in the lower panel of Fig. 7.4).

The decisive point for the thermal behavior of this fluid element is reached now. The point is related to the first intermediate maximum of $Q_{\rm rad}(T_{\rm g})$ depicted in Fig. 5.2 at a temperature of ~ 3000 K. The question is whether or not the adiabatic cooling of the gas is sufficient in order to overcome this maximum. If the answer is no, the adiabatic cooling of the gas is compensated by net radiative heating, the cooling of the gas is stopped and the re–expansion proceeds more or less isothermally (with $T_{\rm g} \lesssim T_{\rm g}^{\rm RE}$). If the answer is yes, the adiabatic rate dominates during the remaining time of the period (at lower gas temperatures $|Q_{\rm rad}|$ is usually smaller compared to the first maximum), and the re-expansion approximately proceeds adiabatically.

> *The character of the re–expansion process, being either isothermal or adiabatic, is decided by the efficiency of the radiative heating in the predominantly neutral, atomic phase of the gas (caused by line and bound–free transitions) prior to molecule formation*[4].

In the figure, the adiabatic cooling exceeds the net radiative heating rate ($|Q_{\rm adb}| > |\widehat{Q}_{\rm rad}|$) and, thus, the cooling of the gas continues. Subsequently, the gas becomes cool enough in order to allow for considerable molecule formation. While so far the line heating/cooling rate has been dominating, now the vibrational and rotational heating/cooling functions enter into competition, and soon become more important than $Q_{\rm Lines}$. Since the molecular rates cause net radiative cooling for the present, $Q_{\rm rad}$ again changes its sign and the adiabatic cooling of the gas is finally even supported by net radiative cooling. However, $Q_{\rm adb}$ remains the most important rate during the re–expansion, which is plotted on a linear scale in Fig. 7.4. Consequently, the re–expansion which takes about 99% of the period approximately is an adiabatic process.

Thus, the gas temperature is lower than in radiative equilibrium almost all the time. The gas temperature finally reaches a minimum value of 780 K and is below 1500 K for about 60% of the period at densities $n_{<\rm He>} = 4 \cdot 10^8 ... \ 1.5 \cdot 10^8\,{\rm cm}^{-3}$. These are thermodynamic conditions favorable for effective carbon nucleation, as will be discussed in the Sect. 7.2.4.

[4]This statement refers to cases where the gas first of all is capable to quickly radiate away the excess internal energy dissipated by a shock, cf. Sect. 7.2.2.

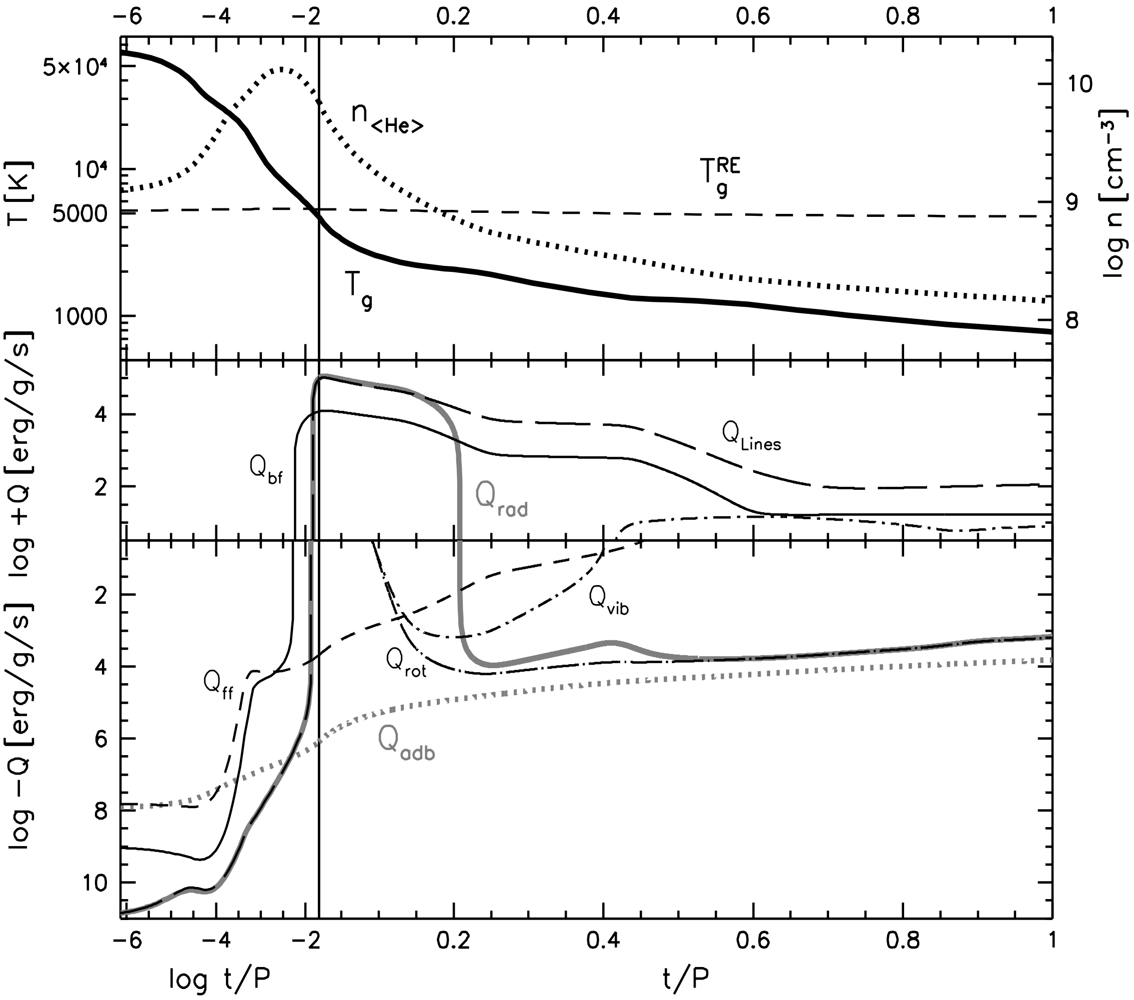

Figure 7.4: Details of the time variations in a fixed, periodically shocked, circumstellar fluid element of an RCB star. The x–axis is broken in this plot. The first $\sim 2\%$ of the period are depicted on a logarithmic scale, whereas the other $\sim 98\%$ are plotted linearly. The **upper panel** shows the gas temperature (full line), the RE temperature (dashed line) and the total helium particle density (dotted line). The **middle** and **lower panel** depict the heating and cooling rates, respectively. The thick full line shows the total net radiative rate and the other thin dotted and dashed lines depict partial rates, theses are the net free–free, bound–free, atomic line, vibrational and rotational rates. The latter rates are the sums of the radiative gains/losses caused by the indicated transition type (i. e. all bound–free transitions, all vibrational transitions etc.). The adiabatic cooling rate is depicted by the thick dotted line. Parameters: $r = 2R_*$, $v_1 = 50\,\mathrm{km\,s^{-1}}$ and $p_1 = 1.6 \cdot 10^{-5}\,\mathrm{dyn\,cm^{-2}}$.

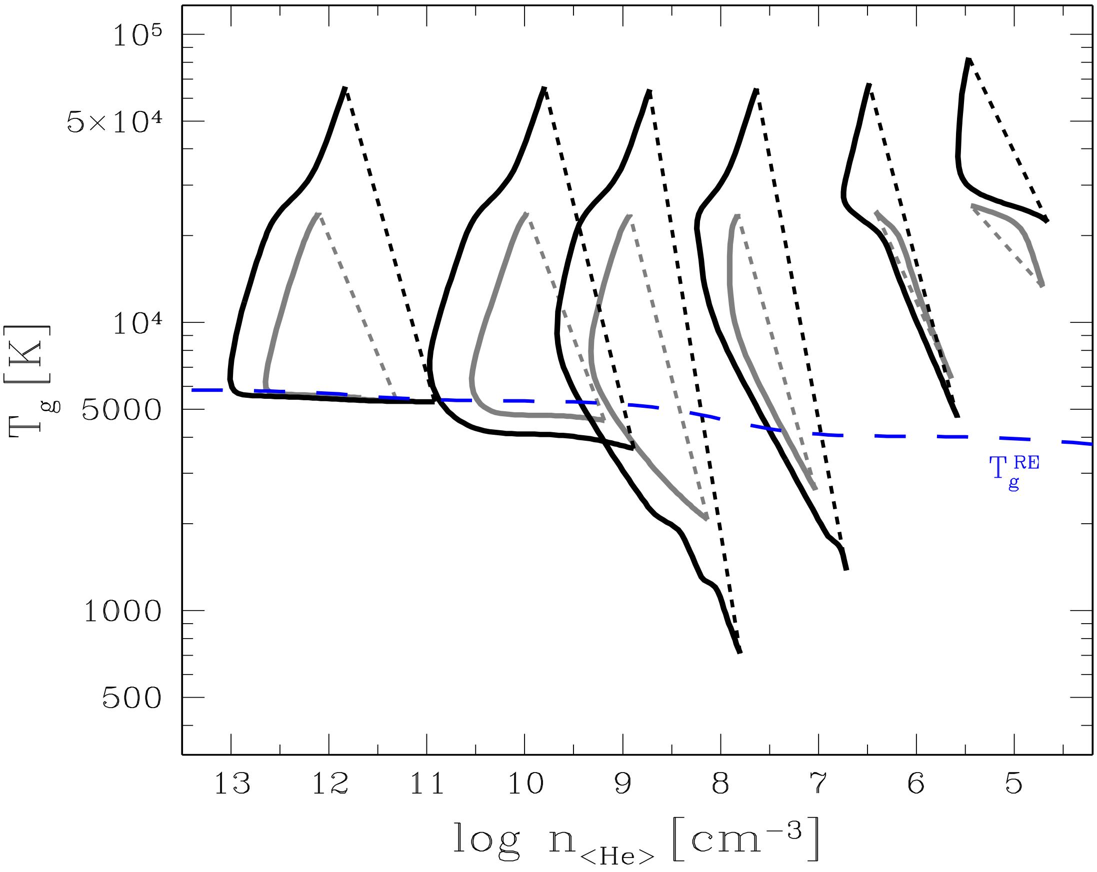

Figure 7.5: Cyclic variations of density and temperature in periodically shocked fluid elements at $r = 2R_*$. The elements differ by different values of the pre–shock gas pressure. The gray and black cycles depict the results for shock velocities $v_1 = 20\,\mathrm{km\,s^{-1}}$ and $v_1 = 50\,\mathrm{km\,s^{-1}}$, respectively. The short dashed lines indicate the shock transitions. The long dashed line shows the radiative equilibrium gas temperature.

7.2.2 Dependence on Density

The results discussed so far have been calculated for a particular pre–shock gas pressure p_1, which fixes the mean density of the gas during the periodic variations. Since the efficiency of the radiative heating/cooling is strongly affected by the density (cf. Chapter 6), the thermal behavior of the gas in response to the periodic shocks is quite different for other densities. This density–dependence is depicted in Fig. 7.5, where the periodically repeating thermodynamic processes appear as counterclockwise cycles.

Concerning very large densities, the three phases sketched in Fig. 7.2 are well separated and an almost triangular cycle results (see l.h.s. of the figure). Beginning with the post–shock state (upper corner), the gas element reaches RE (left corner) within $\sim 1\%$ of the period due to efficient, approximately isobaric radiative cooling. The slight departure from a straight line on this cooling track is related to the recombination of He, where the mean gas particle weight changes by a factor of 2. Since the coupling to RE is strong at these densities, the adiabatic cooling rates are negligible compared to the radiative rates in the subsequent phase of re–expansion. Therefore, the gas temperature stays close to $T_{\rm g}^{\rm RE}$ during this process leading to the right corner. Finally, the fluid element is shocked and jumps to the upper corner again, etc. The triangular cycles are typical results for the limiting case of isothermal shocks. For about 99% of the period, the element is close to RE. Therefore, the condition of RE can be used to determine the gas temperature during the overwhelming part of the period. However, this procedure is only feasible for large densities. Roughly speaking, RE is a reliable criterion for temperature determination for densities $n_{<\rm He>} \gtrsim 10^{11}{\rm cm}^{-3}$.

On the other extreme, considering the case of very small densities, the excess internal energy dissipated by one shock cannot be radiated away during one period and, consequently, the gas never approaches RE. On the contrary, a corona–like situation results, where the gas is heated up to extremely high temperatures due to the energy dissipation of waves. For example, in the cycle on the r.h.s. for $v_1 = 50\,{\rm km\,s^{-1}}$, the gas is predominantly ionized and always hotter than 20000 K. This behavior is typical for the limiting case of adiabatic shocks. The resulting periodic tracks (see r.h.s. of Fig. 7.5) consist of shock transition, He recombination and adiabatic re–expansion. Once the gas has recombined, its cooling time scale becomes much larger than the period.

Concerning an intermediate range of densities, the radiative energy exchange is efficient enough in order to cause a fast relaxation of the gas towards RE after the shocks, but is not too efficient in order to be maintain balance with the adiabatic cooling rates during the phases of re–expansion. In this case the fluid element cools down far below $T_{\rm g}^{\rm RE}$ as discussed in Sect. 7.2.1. The small kinks on the almost adiabatic tracks at the lower part of Fig. 7.5 are caused by molecule formation (mainly CO and C_3), where the further cooling of the gas is delayed by the liberation of molecule dissociation energy.

> *A supercooling of the gas occurs within a distinct density–interval caused by a two–step process of radiative cooling at high temperatures followed by adiabatic cooling at low temperatures.*

The density–dependence depicted in Fig. 7.5 is a natural consequence of the density–dependent cooling/heating efficiency of the gas. Regarding the broad spectrum of densities encountered in CSEs, it seems inevitable that somewhere in the envelope of a pulsating star the density is just appropriate for this effect.

7.2.3 Dependence on Shock Velocity

Larger shock velocities v_1 produce higher maximum temperatures behind the shocks, but do also allow for lower minimum temperatures. At first sight, this dependence might be surprising, but it is actually straightforward. The total compression ratios are larger for strong shocks, implying larger adiabatic cooling rates during the phases of re–expansion. The shock velocity can be regarded as a measure for the amplitude of the perturbation, causing both up– and downward deviations from RE.

7.2.4 Preconditions for Carbon Nucleation

In the following, the possibility of effective carbon nucleation to take place in these periodically shocked fluid elements is investigated[5]. Considering the densities encountered in circumstellar envelopes, the size of the critical cluster usually is as small as 10 atoms. Therefore, the chemical reactions involved in the formation process of such seeds are assumed to be controlled by the gas temperature rather than the RE temperature of macroscopic dust particles (the "dust temperature"). According to

[5]The formation of macroscopic dust grains is not discussed in this work. According to the assumed radiation field, macroscopic grains (strictly speaking, graphite grains in the small particle limit of Mie theory) definitely evaporate at the small radial distances under investigation, because their internal temperatures are much too high (Fadeyev 1988). In contrast, large molecules might be stable provided that their optical and UV absorption properties are comparable smaller.

Apparently, the formation of dust close to the star must be accompanied by some kind of shielding. Absorption by the dust itself is a promising candidate in order to block off the radiation field and to cause a local reduction of the dust temperature. The phase transition from gas to dust can easily increase the absorption coefficient of the gas/dust mixture by a factor of 10^5. Therefore, once a *dust cloud* has formed, the radiation flows around the optically thick region and new dust particles may condense and grow in the shadow of this cloud, whereas the grains at the inner edge of the cloud towards the stars will evaporate. A quasi stable situation might be conceivable where the dust cloud survives the strong radiation field via self–shielding in a dynamical sense.

In contrast, the formation of a spherical *dust shell* seems to be absolutely impossible close to the star. Spherical dust formation in a distinct radial layer causes an increase of the dust temperatures in the layers within the shell via back–warming and has almost no effect on the dust temperature in the outer layers, because the radiation flux is not blocked, but just transmitted.

Thus, an instability caused by dust formation possibly exists which favors dust cloud formation rather than dust shell formation in cases where the gas is sufficiently dense and cool for nucleation but a strong radiation field hinders the seed particles to grow further.

Difficult questions are raised by these considerations, which may be important not only for the dust formation in RCB stars but for any harsh radiation field environments, e. g. in Wolf–Rayet star envelopes. In order to clarify these questions, at least 2D model calculations are required, which must include radiative transfer and time–dependent dust formation/destruction — a very challenging problem which goes far beyond the scope of this work. Therefore, I will concentrate on the first necessary step concerning the transition from the gas phase to dust particles, which is the formation of seed particles and leave aside the problem of the thermal stability of macroscopic dust grains. Dust formation close to the star in any case must proceed via this first step.

this assumption, the supersaturation ratio S is calculated as

$$S = \frac{n_{\rm C} k T_{\rm g}}{p_{\rm sat}(T_{\rm g})} \quad , \tag{7.6}$$

where $n_{\rm C}$ is the particle density of neutral carbon atoms in the gas phase and $p_{\rm sat}$ is the vapor pressure of carbon atoms over the bulk material (graphite) at gas temperature. A necessary condition for carbon nucleation to take place is $S > 1$. Figure 7.6 shows this condition and gives an overview of all results concerning the periodically shocked fluid elements at $r = 2R_*$. The minimum gas temperature occurring in one periodic cycle is depicted as a function of the mean helium particle density during the cycle which is defined as

$$\overline{n}_{<{\rm He}>} = \frac{1}{P} \int_0^P n_{<{\rm He}>} \, dt \quad . \tag{7.7}$$

Figure 7.6 demonstrates that the conditions appropriate for effective carbon nucleation are temporarily present in the periodically shocked fluid elements, concerning a distinct density–interval bracketed by $n_{<{\rm He}>} = 10^{7.3}{\rm cm}^{-3}$ and $10^{9.3}{\rm cm}^{-3}$. In contrast, dust formation is thermodynamically impossible at $r = 2R_*$, if the temperature of the gas is given by $T_{\rm g}^{\rm RE}$, which is the high–temperature solution of radiative equilibrium (cf. Chapter 5).

The nucleation rate J_*, which is the number of seed particles forming per volume and per second, is calculated by applying classical nucleation theory (Gail et al. 1984). The nucleation rates are plotted as contour lines in Fig. 7.6. Considering the interesting density–interval, nucleation rates of $J_*/n_{<{\rm He}>} = 10^{-13.5} \ldots 10^{-15.5}\,{\rm s}^{-1}$ occur, which are large values compared to those experienced from time–dependent models for the envelopes of long–period variables (Fleischer et al. 1992), indicating that efficient carbon nucleation may take place.

The total growth time for a seed particle to reach a macroscopic size, say $0.01\,\mu$m, can be estimated by considering the three dimensional growth by accretion, taking into account all thermally impinging carbon bearing species (except for the amount of carbon locked in CO). The dust temperature is assumed to be sufficiently low so that dust growth is possible (cf. footnote 5):

$$\tau_{\rm gr}^{\rm tot} = \frac{0.01\,\mu{\rm m}}{V_0\,(n_{<{\rm C}>} - n_{<{\rm O}>})\,v_{\rm th}\,\alpha} \tag{7.8}$$

$V_0 = 4/3\pi a_0^3$ is the monomer volume ($a_0 = 1.28 \cdot 10^{-8}$cm for graphite, Gail et al. 1984), $v_{th} = \sqrt{kT_{\rm g}/(2\pi m_{\rm C})}$ the thermal velocity (which is a bit smaller if molecules are considered) and α the sticking probability. Assuming $\alpha = 1$, a lower limit is calculated for the actual total growth time.

In order to cause a RCB decline event, the total growth time in the dust forming region should not exceed the time scale of the initial drop of the light–curve, which is of the order of a few weeks (Feast 1986). In any case, the total growth time must

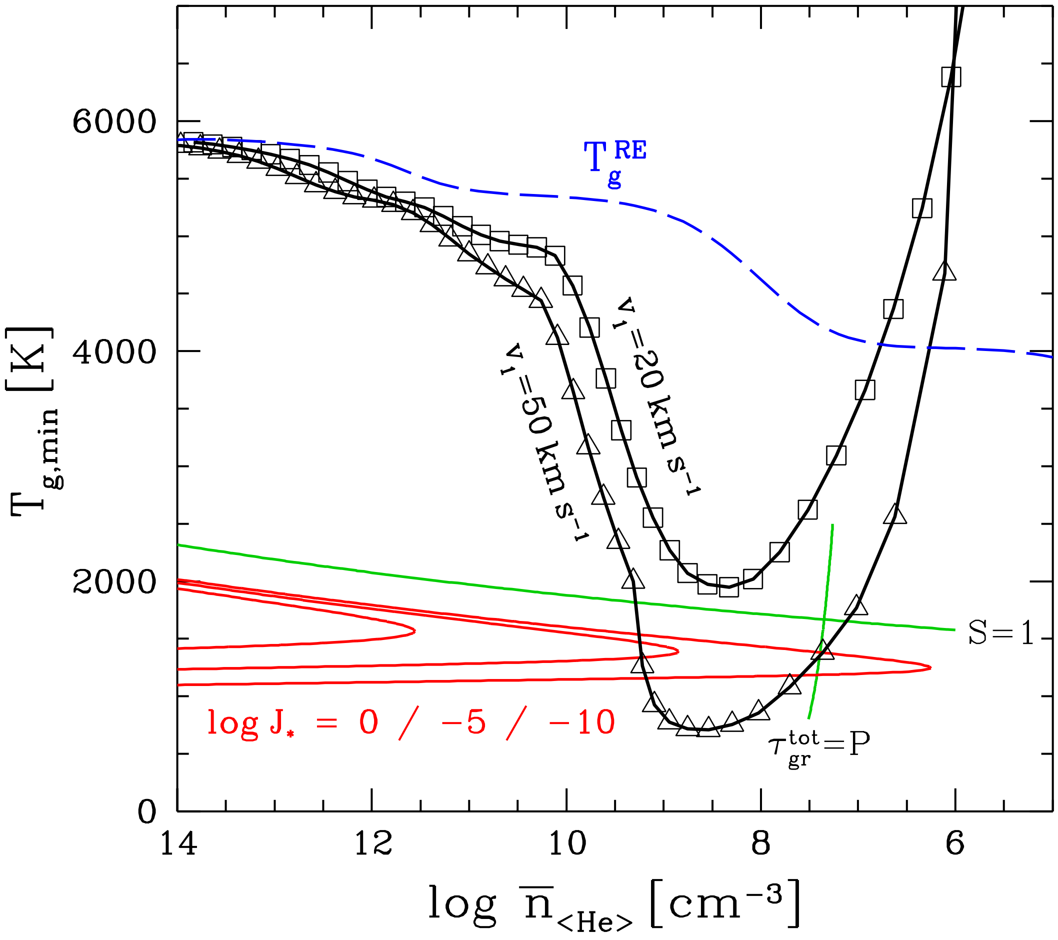

Figure 7.6: Minimum gas temperatures and the possibility of carbon nucleation to occur at a radial distance of $r = 2R_*$. The **full lines and points** depict the minimum temperatures occurring in one periodic cycle as function of the mean gas density during the cycle for two different shock velocities as indicated. The **dashed line** is the radiative equilibrium gas temperature. The lower part of the figure sketches the **condensation regime**, i.e. the region of favorable thermodynamic conditions for carbon nucleation. Only below the $S = 1$–limit, the gas is supersaturated with respect to graphite. Contour lines of the logarithm of the classical nucleation rate J_* [$cm^{-3}\,s^{-1}$] are plotted. On the right edge, the growth time for a seed particle to reach the macroscopic size of 0.01μm exceeds one pulsation period.

not exceed the pulsation period of the star. This condition is additionally shown in Fig. 7.6, constituting an absolute lower limit for the density in the dust forming region, which can be responsible for an RCB decline event. As depicted in Fig. 7.6, this condition is just fulfilled within the density–interval, where the supercooling of the gas occurs.

7.2.5 Dependence on Radial Distance

The predictions of the model concerning the minimum radial distance required for efficient carbon nucleation are of special interest. Previous modeling of dust formation in the CSEs of RCB stars has suffered from the necessity to consider rather large radial distances in order to obtain sufficiently low temperatures, whereas observations tell us that dust formation probably occurs much closer to the star (cf. Sect. 1.3 and Appendix A).

The dependence of the results of this model on the parameter r/R_* is depicted in Table 7.1, where the minimum of the $T_{\rm g,min}$– curve (cf. Fig. 7.6) is stated in the first row and the interval of mean helium particle densities with $T_{\rm g,min}(\overline{n}_{<\rm He>}) < 1500\,\rm K$ is stated in the second row.

Table 7.1: Results as function of radial distance and shock velocity.

	$v_1 = 20\,\rm km\,s^{-1}$	$v_1 = 50\,\rm km\,s^{-1}$
$r = 1.5R_*$	2200 K –	1060 K $(0.2\,...\,6.5)\cdot 10^8\rm cm^{-3}$
$r = 2.0R_*$	1950 K –	710 K $(0.2\,...\,18)\cdot 10^8\rm cm^{-3}$
$r = 3.0R_*$	1300 K $(3.7\,...\,13)\cdot 10^8\rm cm^{-3}$	500 K $(0.2\,...\,69)\cdot 10^8\rm cm^{-3}$
$r = 5.0R_*$	950 K $(2.3\,...\,77)\cdot 10^8\rm cm^{-3}$	200 K $(0.2\,...\,650)\cdot 10^8\rm cm^{-3}$

The general tendency of the results is as expected: the larger the radial distance to the star, the easier low temperatures appropriate for carbon nucleation are achievable. However, in the examined case of time–dependent non–RE, this dependence is much less distinctive than experienced from RE. A change of the shock velocity, for example, can easily cause very different conditions. Considering the $20\,\rm km\,s^{-1}$ shocks, gas temperatures lower than 1500 K are produced for $r \gtrsim 3R_*$, whereas concerning the $50\,\rm km\,s^{-1}$ shocks, even lower gas temperatures occur for all considered radial distances.

Compared to the influence of r/R_*, the density–dependence is very selective. The temporal supercooling of the gas behind shock waves is only possible within a special, narrow density–interval. The deeper the temperature–minimum, the wider this interval, centered around a few $10^8\rm cm^{-3}$ in all considered cases. The particular density–range is in good agreement with the estimates presented by Goeres (1992) for the density of the dust forming regions in the envelopes of RCB stars.

Therefore, the influence of r/R_* on the results is less pronounced than the influence of v_1 and $\overline{n}_{<\mathrm{He}>}$. The predicted values for the condensation distance are hence not very distinct. The essential outcome of this model it that shock waves are principally capable to produce low temperatures appropriate for carbon nucleation at radial distances as small as $1.5 - 3\,R_*$. Strictly speaking, this statement refers to the investigated case of periodic shocks. However, since the basic processes of shock heating and compression followed by re–expansion is supposed to be an inevitable, straightforward consequence of circumstellar shock waves, I conclude:

> *Favorable thermodynamic conditions for carbon nucleation occur, whenever a sufficiently strong shock wave encounters those parts of the circumstellar envelope, where the gas density is just appropriate for the two–step cooling process described in Sect. 7.2.2.*

7.3 Discussion

The thermodynamic behavior of periodically shocked fluid elements in the CSEs of pulsating RCB stars has been investigated. The complex interplay between shock–heating, radiative heating and cooling and adiabatic cooling has been examined. Large time–variations of the thermodynamic conditions in fixed fluid elements are found to occur in this situation, comprising $1 - 2$ orders of magnitudes for both the gas density and the gas temperature, depending on the shock velocity.

The calculations provide a hypothesis for the physical cause of the onset of dust formation close to a pulsating RCB star, connected with the question of the trigger of the RCB–type decline events. As a consequence of the presence of shock waves, the gas is usually not in RE. In the time–dependent non–RE situation, favorable conditions for carbon nucleation are found to be temporarily present close to the star, despite of the high effective temperatures of the RCB stars. The following two basic conditions are required in order to allow for effective condensation close to the star. The gas density must be bracketed by about $10^8 - 10^9\mathrm{cm}^{-3}$ and the shock velocity must be larger than about $20\,\mathrm{km\,s}^{-1}$. The results can be generalized to arbitrary shock waves, no matter how the shock was created.

In the following I will briefly summarize the advantages of this model on the one hand, and the main points of criticism on the other hand. For comparison, an overview of previously published models can be found in Appendix A. A short discussion of the possible links to observations completes this chapter.

7.3.1 Advantages of the Model

1) The obvious attraction of the model is that dust formation close to the star is explained from physics. The model predicts that temperatures as low as

1000 K can be present at radial distances as small as $2\,R_*$. According to the calculations, these conditions last for more than half of the period which in fact means favorable conditions for carbon nucleation.

2) The condensation distances are found to be as small as $1.5 - 3\,R_*$, in agreement with the values inferred from observations (e. g. Clayton et al. 1992, cf. Sect. 1.3). In contrast, none of the published models can explain this fundamental feature of the dust formation in RCB envelopes in a quantitative way.

3) The narrow density–interval necessary for the two–step cooling process causing the low temperatures agrees with previous estimates of the density in the nucleation zone of RCB stars (Goeres 1992). This agreement is not self–evident. The density–dependence of the model is caused by a completely different physical property of the gas, which is the radiative heating/cooling efficiency. This efficiency decreases with decreasing gas density due to increasing non–LTE effects.

4) The dependency of the model on the effective temperature of the star is small. Preliminary test calculations with $T_{\rm eff} = 5000 - 9000$ K yield similar results as depicted above. Even for $T_{\rm eff} = 9000$ K, gas temperatures below 1000 K occur at $1.5\,R_*$ for a shock velocity of $50\,{\rm km\,s^{-1}}$. This insensibility of the model with respect to $T_{\rm eff}$ apparently agrees with observations, since the RCB phenomenon is reported for a variety of stars comprising effective temperatures of 4000 – 20000 K. In contrast, all other proposed physical models exhibit a pronounced $T_{\rm eff}$–dependence.

7.3.2 Criticism

1) Shock activity in the photosphere of RCB stars is only confirmed for one exceptional object, which is RY Sgr. Other RCB stars show considerable radial velocity variations, but no shock activity in the photosphere as inferred from absorption line splitting (cf. Appendix A). Therefore, the presence of shock waves in RCB envelopes is generally doubted.

Comments: The basic problem of the above argument is that the observations refer to the photosphere of the star, whereas informations about the conditions in the circumstellar envelope are required. A direct observation of circumstellar shock waves is very difficult, due to contrast effects with regard to the bright star. A chance to observe circumstellar properties may be present during the early phases of the decline events. At the present state of observations, no precise informations about circumstellar shock activity have been deduced, at least one cannot rule out the possibility that shock waves are in fact present in all RCB stars envelopes. From theory, even small amplitude (subsonic) waves in the photosphere of the star are known to be capable to steepen up to considerably strong shock waves in the CSE, depending on the photospheric density gradient. Just in those cases, where the initial radial pulsation is small, the density gradient turns out to be large, which amplifies the waves.

2) RCB stars show similar decline events with respect to decline frequency, time scales and decline amplitude, regardless of their special pulsation properties (e. g. the radial velocity amplitudes). Therefore, a causal connection between pulsation and dust formation seems suspect.

Comments: This is the most serious objection to the proposed model. Of course, the comments on the upper point may be repeated, but in fact this criticism is more substantial. In any case, the pulsation of the star should be responsible for the circumstellar shock waves, so that some correlations are expected. From observations, the often claimed correlation between the begin of a decline and the pulsation phase of the star (cf. Appendix A) would contradict the above argument, but observational evidence is poor concerning this correlation (cf. Appendix A).

3) The model at first sight seems to suggest dust shell formation rather than dust cloud formation, as far as a spherically symmetric pulsation of the star is considered. Dust shell formation, however, can be ruled out from observations (cf. Appendix A). Feast (1997) argues that the proposed instability which might be responsible for a "fragmentation" of the forming dust shell into dust clouds (cf. footnote 5) is not very convincing, at least cannot explain why always only a very few — probably just one — dust cloud per pulsation period survives the dust–destroying radiation field.

Comments: This is certainly a weak point of the model. However, the model in fact does not make any predictions of what happens after the onset of nucleation. It only intends to show how the onset of nucleation is possible near to the star, which in any case must be the starting point of the decline events. Once the gas becomes optically thick due to dust formation, the basic assumption of optical thinness breaks down and the radiation field must be calculated by means of the solution of a (non–local) radiative transfer. It is principally not possible to model the formation of a cloud without taking into account the important physical interactions in a more–dimensional way. All models published so far suffer from this inconsistency. A trivial way out is the prescription of a non–spherical situation prior to dust formation. One could, for example, consider a superposition of non–spherical shock waves due to non–radial pulsations, or one could prescribe the existence of inhomogeneities. In both cases, the conditions for dust formation are different in neighboring fluid elements, which might lead to the formation of dust clouds. The presented thermodynamic methods are of course applicable to such prescribed situations. However, in my personal opinion, such assumptions do not really explain anything. What is necessary is the modeling of the physical process of cloud formation from a previously homogeneous situation, no matter whether this process takes place prior to dust formation, or whether the cause of cloud formation is related to the process of dust formation itself. The problem of the survival of the dust close to the star is serious and is not restricted to the proposed model.

7.3.3 Interpretations of Observations with Regard to the Model

1) If the RCB decline events are in fact caused by shock–induced condensation, similar initial thermodynamic conditions of the gas would be present in the nucleation zone at the beginning of all declines, concerning for instance the gas density. This could to some extent explain the principal similarity of the light–

curves concerning light amplitudes and time scales involved, irrespective of the wide range of stellar properties of RCB stars such as effective temperature, element abundances and pulsation properties. The model suggests that the decline events are caused by a distinct physical process of the gas independent and apart from the star.

2) According to the model, a forming dust cloud in the line of sight would always be located *behind a shock wave*, whose hot post–shock region might be responsible for some "chromospheric" line emissions as observed during the early declines. If then the entire complex of shock wave and dust cloud moves farther out, the shock encounters less and less dense parts of the circumstellar envelope, probably causing a fading of the line emissions as the decline progresses. Additionally, the observed blue–shift of the emission lines of typically $10\,\mathrm{km\,s^{-1}}$ agrees with the proposed scenario, because the shock propagates *outwards*, leaving the post–shock gas with an outward directed velocity of about $v_1/2$. The shock–induced emission lines are expected to be sharp and unpolarized, in agreement with observations, because the gas emits undisturbed in front of the dust. Therefore, the model seems to generally agree with the spectral properties and the time–evolution of the observed narrow emissions lines, if interpreted as shock activity rather than as activity from a static chromosphere.

3) The proposed mechanism constitutes a causal connection between shock waves and dust formation in circumstellar envelopes, which might naturally explain the observed correlation between the begin of a decline and the pulsation phase of the star at maximum light (e. g. Lawson et al. 1992), supposed that the small range of the gas densities necessary for this mechanism is solely present at a particular radial distance to the star, and supposed that the shocks always take a particular time to reach this distance.

In summary, the proposed model provides a solution to the central problem how dust condensation may occur close to the star, but is certainly not capable to provide a complete explanation of the puzzle of the RCB decline events so far. More complex model calculations are required in order to achieve this aim. The present model yields about the right conditions for dust formation as inferred from theory and from observations: temperatures, densities, radial distances and time scales. It apparently bridges a gap between the theory of dust formation on the one hand, and the observations of RCB stars on the other hand (cf. Sect. 1.3), which is manifested by the controversy about the condensation distances. Therefore, it seems promising to include the developed thermodynamic methods into more complex calculations as a kind of starting point.

Other results, which are worth to be mentioned, are as follows. The low–temperature solutions of RE found in Chapter 5 are never found to be realized or to have any effect on the results in the periodically shocked situation. Once the adiabatic cooling rates are sufficiently strong in order to destabilize the high–temperature solution, they are definitely stronger than the remaining heating/cooling rates around the low–temperature solutions. Similarly, the details of the chemistry, the radiative heating and cooling rates and the spectral peculiarities of the background radiation field do not cause principal changes in the cyclic thermodynamic processes. What happens, for example, if another important heating/cooling rate is included, is that the density–interval appropriate for the two–step cooling process shifts a bit. Hence, in contrast to the results of the thermal bifurcations discussed in Chapter 5, the results of this chapter have a much more general meaning.

In principle, the effect discussed in this work is expected to occur in all circumstellar envelopes of pulsating stars — not only in RCB envelopes. The influence of the stellar parameters must be further investigated. Especially the dependences on the effective temperature, the pulsation properties of the star and the elemental abundances (e. g. the H deficiency) might provide an explanation for the fact, that the RCB phenomenon is restricted to a special class of objects. Time–dependent hydrodynamic model calculations are required in order to allow for a more realistic modeling of the circumstellar envelopes of RCB stars. Higher dimensional calculations including radiative transfer and a time–dependent treatment of the dust complex would be required in order to model the formation and destruction of macroscopic dust grains close to the star, closely related to the self–shielding in dust clouds.

Chapter 8

Conclusions

The thermal state of diluted gases being subject to stellar radiation fields has been investigated. Radiative heating and cooling rates have been calculated considering the typical (p, T)–range and the radiation fields present in the circumstellar envelopes (CSEs) of cool and warm stars.

These studies intend to lay the foundations for theoretical methods to determine the temperature of gases under static as well as dynamic conditions. As an important ingredient, such methods must be part of any fundamental modeling of CSEs, especially with regard to the simulation of the chemical and dust formation processes, which are known to be strongly temperature–dependent.

The results of this work show that a non–LTE treatment of the atoms and molecules is essential in order to calculate the efficiency of the radiative heating and cooling processes in CSEs. The possibility to include the calculated heating and cooling rates into more complex calculations (e. g. time–dependent hydrodynamic models) is also regarded as essential. A proper coupling, however, can be achieved only if the basic assumptions are compatible. Therefore, a compromise method has been proposed where the state of the gas is calculated by means of the assumption of a *steady state*. On one hand, this method accounts for non–LTE ionization, non–LTE population of the excited electronic, vibrational and rotational states and optical depths effects of spectral lines in Sobolev approximation. On the other hand, all macroscopic properties of the gas do not depend on history and can be calculated as function of local, instantaneous physical quantities, which are available in such models.

Thus, a thermodynamic description has been developed, where the state of the gas is determined by two independent state variables, e. g. ρ and $T_{\rm g}$ (as usual in LTE), plus two external parameters which are the radiation field J_ν and the local mean velocity gradient $\left\langle\frac{dv}{dl}\right\rangle$. The method goes one step beyond LTE, but does not represent a full time–dependent non–LTE approach. It includes LTE as a limiting case, which occurs at large densities. The latter is achieved by strictly including all reverse processes by means of detailed balance considerations.

Three applications of this method have been presented:

First, the topology of the solutions of radiative equilibrium (RE) has been examined, considering the CSEs of R Coronae Borealis (RCB) stars. The results show that the condition of RE, i. e. the equality of radiative gains and losses, can have two or more stable temperature solutions. Two different types of solutions have been identified: high–temperature, predominantly atomic states and low–temperature, predominantly molecular states. The molecule–rich states are found to be substantially cooler than a black body in RE. This result is straightforward, inferred from the large sensitivity of the molecules in the infrared spectral region. It is expected that this result is valid in cool stellar envelopes as well, possibly with important consequences for the chemistry and the dust formation in these envelopes. Concerning the CSEs of warm stars with $T_{\rm eff} \gtrsim 4500\,K$, the high–temperature, atomic solutions additionally come into play which means that in principle a spatial coexistence of high–temperature and low–temperature gas phases is conceivable, both in RE and in pressure balance with each other ("thermal bifurcations").

Second, the time scales of radiative relaxation processes towards RE have been studied for the case of C–stars envelopes. Comparison to the other time scales involved in the process to be modeled yields a criterion for the applicability of the methods of temperature determination which are based on RE. If the radiative cooling time scale is much shorter than the others, the character of the thermodynamic process is approximately isothermal and the temperature can be calculated by means of RE. In the opposite case the gas behaves more or less adiabatically. The thermal relaxation of the gas behind circumstellar shock waves has been discussed accordingly. The gas density has been identified to be the key quantity which decides upon the character of such relaxation. With deceasing density, increasing non–LTE effects lead to a decrease of the efficiency of the radiative heating and cooling processes. Consequently, a gradual change of the nature of the shocks is expected to occur around $10^8\,\mathrm{cm}^{-3}$, changing from predominantly isothermal to predominantly adiabatic. These results strongly suggest to include time–dependent methods for temperature determination into the models of the envelopes of pulsating stars.

Third, a model for periodically shocked fluid elements has been developed, applicable to shock–levitated atmospheres of pulsating stars. Large time–variations of the thermodynamic conditions are found to occur in such fluid elements, comprising $1-2$ orders of magnitudes in the state variables, dependent on the shock velocity. With regard to RCB stars, the following effect has come to light. In certain cases after the heating and compression by a shock wave, the gas first radiates away the excess internal energy dissipated by a shock wave and then re–expands adiabatically. This two–step cooling process can produce temperatures substantially lower than in RE within a distinct density interval. Temperatures as low as 1000 K are found to temporarily occur for shock velocities $20-50\,\mathrm{km\,s^{-1}}$ at radial distances as small as $1.5-3\,R_*$, despite of the high effective temperatures of these stars. Such conditions are favorable for carbon nucleation. Thus, the present work states the hypothesis that the onset of dust condensation close to the star is caused by shock waves, which might trigger the spectacular RCB–type decline events.

In conclusion, basic studies of the thermodynamic behavior of gases in circumstellar envelopes have been undertaken, providing new insights and new ideas on the processes leading to dust formation.

Appendix A

Current Status of RCB Research

This appendix intends to give a brief overview on the current status of RCB research, providing an important background for the investigations in Chapter 5 and 7. Since this class of stars shows so many interesting aspects in various fields, only the topics which provide clues on the dust formation and the decline events are summarized. The reader can find further informations in the diploma thesis of S. Friedrich (1995) and in the recent reviews of Lambert & Rao (1994) and Clayton (1996).

A.1 General Observations

Classification: The class of RCB stars today comprises 32 known objects in our Galaxy (Lambert & Rao 1994). This number varies as a consequence of recent observations and the classification of some objects is still under discussion (Clayton 1996). A certain verification requires at least the successful observation of one decline event, which is quite a difficult observational task. Therefore, the true number of RCB stars is undoubtfully much larger, probably between 200 and 1000 in the Galaxy (Lawson et al. 1990). For example, the third brightest RCB star on the sky, V854 Cen, was not discovered before 1986[1]. The main criterion for classification is the occurrence of the RCB–type decline events (cf. A.2: Light Curves). Additional criteria are a carbon overabundance (C/He = 0.01 to 0.1) and a clear but strongly varying hydrogen deficiency among the objects of ($\log \mathrm{H/He} = -0.3$ to -7.2), and also the occurrence of small–scale visual brightness variations. RCB stars are single stars of typical spectral type F–G Ib with absolute brightnesses $M_V = -4$ to -5 (Feast 1979), suggesting luminosities of about $L_* \approx 10^4 L_\odot$. The stellar masses can be determined by pulsational models, yielding $0.8 - 0.9\,M_\odot$ (Weiß 1987). The effective temperatures typically are $T_{\rm eff} = (7000 \pm 1000)$ K (Lambert & Rao 1994). However, also extreme values from about 4000 K for WX CrA and S Aps up to about 20000 K for DY Cen and V348 Sgr occur. Compared to this large spread of effective temperatures, the decline events of the individual RCB stars show a remarkable similarity in their decline light curves, e. g. the decline amplitudes and time scales involved. Therefore, a unique physical mechanism seems to be responsible for all the events (involving dust formation), which is apparently not very sensitive to the effective temperature of the star.

[1] This is because this object is in decline most of the time.

Pulsations: Besides the decline events, all thoroughly observed RCB stars show more or less periodical visual brightness variations with amplitudes ranging from ± 0.1 to ± 0.4 mag for periods of typically 40 days (Feast 1990; Lawson et al. 1992; Lawson & Kilkenny 1996). For a considerable number of RCB stars, radial velocity variations have additionally been deduced from the Doppler–shift of photospheric absorption lines, yielding about ± 5 to $\pm 10\,\mathrm{km\,s^{-1}}$ and about $\pm 20\,\mathrm{km\,s^{-1}}$ for the exceptional case of RY Sgr. The variations of velocity and brightness usually occur in phase, suggesting the RCB stars to be *irregular radial pulsators* (Lawson et al. 1990). There are several clues that the pulsations have a direct feedback on the dynamics and the chemistry of the outer atmospheres of these stars. The most extreme pulsator RY Sgr shows phase–correlated line–splitting, which is interpreted as the propagation of a shock wave through the atmosphere of the star (Lawson 1986, Lawson et al. 1991). Furthermore, besides some permanent emission lines probably of chromospheric character (e. g. CII $\lambda 1335$Å), there occur phase–correlated emission features in the UV, which might be caused by shock heating. The equivalent widths of electronic absorption bands of C_2 (Swan) and CN (violet), associated with the outer atmosphere, show a clear correlation with the pulsational phase of the star in case of R CrB (Clayton et al. 1995).

Mass Loss: The question of whether or not the RCB stars — besides the occasional mass loss events due to dust cloud formation — undergo an underlying permanent mass loss, is under controversial discussion. The narrow emission lines seen during the declines (cf. A.2: Spectroscopy) are blue–shifted by typically $10\,\mathrm{km\,s^{-1}}$, which according to Feast (1990, 1996) suggests a permanent radiation–driven mass loss. However, these effects can hardly be distinguished from the dust and gas clouds, which apparently are present out of the line of sight at any time near the star (cf. A.1: Dust Shells). For the theoretical understanding of the dust formation in RCB envelopes, a clarification of this question would be decisively important. In a massive stellar wind, which is not driven by the dust itself, the dust formation might be a secondary process and could occur rather distant from the star. In contrast, if there is no massive wind, the densities are too low and dust cannot form at large distances. Estimates for the mean mass loss rates inferred from the sum of dust cloud formation events range from $10^{-6}\,\mathrm{M_\odot\,yr^{-1}}$ (Feast 1986) to $10^{-7}\,\mathrm{M_\odot\,yr^{-1}}$ (Clayton et al. 1992).

Dust Shells: The infrared photometry of RCB stars show a clear excess at about $2-25\,\mu$m, irrespective whether the star is in decline or not. The excess can be fitted by blackbody–curves of characteristic temperatures 600–900 K (Kilkenny & Whittet 1984). This thermal emission is obviously caused by the total amount of dust in the vicinity of the star, which has been formed during the former decline events or out of the line of sight[2,3]. The mean radial distances of these "dust shells" are estimated

[2]This interpretation is strongly supported from the observation of the very first declines of FG Sge (Jurcsik 1996), showing a more or less permanent IR excess after those declines, but no excess before.

[3]Since these dust clouds have proven to be optically thin in late decline, it would actually be more appropriate to fit the excess by $(1/\lambda)\,B_\lambda(T)$.

to be 10–90 stellar radii (Walker 1985). Recently, Feast et al. (1997) published extensive long–term infrared photometry data for 12 RCB stars and concluded that there is evidence for a spread in dust temperatures in each RCB shell, where the hottest components are always limited by about 1500 K[4]. Feast (1997) argues that the mean dust temperature is increasing, if the L–flux, representing the total dust mass, increases. This is an argument in favor of the formation of hot dust close to the star. Since the limiting value of 1500 K is constant for all RCB stars observed, the condensation temperature of carbon possibly is the controlling factor in all RCB envelopes. Furthermore, another excess in the far IR (60–100 μm) can be observed for several objects (e. g. R CrB and SU Tau), which points to distant, fossil dust and gas shells, probably connected with the former evolution of the star. According to Gillett et al. (1986), the linear size of the shell of R CrB is about 18 arc min ($\sim$8 pc)[5].

Stellar Evolution: The popularity of the RCB stars is also caused by their mysterious origin. Since the RCB stars are so rare, they must be either a manifestation of a peculiar side path of stellar evolution, or a common, but rapidly evolving stage. Two major evolutionary scenarios have been worked out during the last 15 years (Iben 1983, Schönberner 1986, Renzini 1990), indicating that the RCB stars are in fact a topic of recent research on stellar evolution. The merging of two white dwarfs (Double Degenerate (DD) scenario) and the re–birth of an post–AGB star as a consequence of a last thermal pulse (Final helium shell Flash (FF) scenario). These models make different predictions about the surface elemental composition, the lifetimes of RCB stars and their spatial distribution in the Galaxy. However, agreement with observations is still rather poor. Last but not least, the very fast evolution of FG Sge (Kipper 1996, Jurcsik 1993) across the HR–diagram during the last century suggests that the birth of a new RCB star has actually been observed.

A.2 Observations During the Decline Events

Light Curves: The individual light curves of the spectacular decline events are quite different in appearance concerning both the different events and the different stars. Nevertheless, their eye–catching shape is so typical that they essentially define this class of objects. The light curves of the RCB stars start with a sudden drop in the visual brightness of typically 3−6 mag within a few weeks, whereas the recovery from deep declines usually takes months or years. Between the initial decrease and the final recovery phase there usually is a phase of low–level chaotic light variation, lasting between zero and several years (Goeres & Sedlmayr 1992). Multiple minima, superimposing each other, are often observed, suggesting multiple dust formation events.

Color Variations: The decline events of RCB stars are accompanied by complex color variations. The initial decrease in light always appears slightly reddened. The

[4]In good agreement with the carbon condensation temperature, cf. A.3: Goeres & Sedlmayr

[5]As huge as the angular size of the moon.

light then may become bluish (a "blue" decline according to Cottrell et al. 1990) or remains reddened (a "red" decline). As the decline progresses, a strong reddening occurs, until the light finally increases again and the star slowly reaches its usual brightness and color. These variations result in typical loops in the $V/(B-V)$ –diagram (Alexander et al. 1972, Cottrell et al. 1990). The final light increase apparently proceeds on a unique line for all RCB stars with slope +5 in the V/(B−V)–diagram, which is an unusually large value compared to interstellar reddening (Cottrell 1996), providing clues on the nature of the dust. The cause of the bluing in early decline has been proposed to be an additional, radial extended, hotter light source than the star itself (Pugach 1991, Clayton et al. 1992), emitting at 3900 − 5700 Å mainly in form of line emission (Asplund 1995). This "chromosphere" initially is not, or is at least much less, eclipsed by the dust cloud. The difference between red and blue declines may be caused by different cloud geometries during the declines. Varying cloud radii during the initial formation and/or varying distances from the line of sight might produce red or blue declines.

IR Observations: The light variations in the infrared regions during the declines have smaller amplitudes compared to the optical region. As a rule, the amplitudes decrease with increasing wavelength and vanishes at about the L–band ($\lambda = 3.6\mu$m), where the light is already dominated by thermal dust emission (e. g. Feast et al. 1997). No anti–correlation between the optical and IR brightness has been found, which would be expected if the dust was present in a spherical symmetric fashion. This is the main observational argument for dust cloud formation rather than dust shell formation (Forrest et al. 1972). Furthermore, the dust mass produced in one decline apparently is small compared to the total mass of the dust present in the vicinity of the star.

Extinction of the Dust Particles: The possibility to observe the RCB stars twice, uncovered and covered by dust, allows for a direct determination of the extinction curve of the material responsible for the decline events. The results clearly indicate the carbonaceous character of the dust material ($\kappa_\nu \propto 1/\lambda$). However, the position of the well–known graphite "bump" at 2200 Å is shifted to 2400−2500 Å in case of RCB stars (e. g. Hecht et al. 1984). The general shape of the extinction curve as well as the special appearance of this feature is discussed in various publications concerning the nature of the dust grains in RCB envelopes (e. g. Holm et al. 1987, Maron 1989, Wright 1989, Drilling & Schönberner 1989, Hecht 1991, Jeffery 1995, Zubko 1996). Many interpretations are possible. Unusual size distributions, no hydrogen at the surface or unusual lattice or microscopic structures ("glassy" carbon, "onion–like" structures, amorphous carbon cores covered by graphite mantles, fullerenes). The only clear unique tendency in these papers seems to be the unusual small radii of the dust particles, typically 50 Å to maximum values of about 600 Å.

Spectroscopy: So far, only two decline events of RCB stars have been completely monitored as function of time by optical spectroscopy: The 1967 decline of RY Sgr (Alexander et al. 1972) and the 1988 decline of R CrB (Cottrell et al. 1990). However, fragmentary spectral data is available for several events of the three brightest

RCB stars R CrB, RY Sgr and V854 Cen, covering certain phases of the declines (e. g. Lambert et al. 1990, Lawson et al. 1992, Clayton et al. 1992, Rao & Lambert 1993, Asplund 1995). The spectra indicate a special time evolution. Until the beginning of a decline, no spectral changes have been reported so far (Cottrell et al. 1990, Lawson 1992)[6]. As the intensity of the photospheric (absorption line) spectrum decreases, a rich "chromospheric" emission line spectrum comes to light. Alexander et al. (1972) distinguish between three components, named E1, E2 and BL. Most of the emission line belong to the class of narrow ($\sim 50\,\mathrm{km\,s^{-1}}$) E1–lines of high excitation energy ($\sim 8\,\mathrm{eV}$) of neutral or singly ionized metal atoms, which are blue-shifted by typically $10\,\mathrm{km\,s^{-1}}$ and disappear after some weeks. A smaller number of narrow E2–emission lines of low excitation energies ($\sim 3\,\mathrm{eV}$), mainly multipletts of Sc II and Ti II remain visible for $50-150$ days. As the decline progresses, the optical spectrum mainly consists of five broad ($100-200\,\mathrm{km\,s^{-1}}$), unshifted BL–emission lines: Ca II H&K, Na I D and a line at 3888 Å, probably He I (Feast 1975). Finally the photospheric absorption line spectrum re–appears and soon dominates the light from the remaining emission lines. The physical nature of the emission lines is usually described by "chromospheric", although they do not look like the chromospheric emissions of any other stars (Clayton 1996).

The BL–lines usually show a multi–component structure. Different emission and absorption components can be observed, especially blue–shifted features with typical velocities of $200\,\mathrm{km\,s^{-1}}$ towards the observer. These components are supposed to originate from the gas dragged along with the dust clouds being accelerated by radiation pressure. Hence, these velocities can be associated with the velocities of the dust clouds.

Polarization: The light during the declines generally is strongly polarized (Serkowski & Kruszewski 1969, Coyne & Shawl 1973, Standford et al. 1988, Efimov 1990). In the continuum, degrees of polarization up to 14%, especially in the blue spectral region, have been reported. In contrast, the emission lines remain more or less unpolarized (Whitney et al. 1992). The physical effect causing the polarization is mainly the scattering of light at the surfaces of dust grains[7]. Therefore, these observations allow for important conclusions. First, the dust is distributed non–spherically and second, the dust cloud causing the decline does not eclipse the regions responsible for the line emissions, at least much less than the photosphere. Consequently, the dust seems to form *below* the line emission regions, suggesting dust formation occurs rather close to the photosphere.

Further Observations: Several observational clues can be found which point to a causal connection between the pulsations and the decline events. For at least two objects (RY Sgr and V854 Cen) there is some evidence for the onset of the declines to occur at particular pulsational phases of the star (e. g. Lawson et al. 1992). Furthermore, the multiple drops of the light curve in the beginning of the decline

---

[6] To catch a star just before a decline, however, needs a very lucky moment, since no predictions can be made.

[7] Possibly at the surfaces of other distant dust clouds out of the line of sight.

events seem to occur at time intervals corresponding to the period of the star (Feast 1996). According to Jurcsik (1996), the decline–activity, i. e. the inverse of the mean time between the declines, is increasing with increasing hydrogen abundance. Finally, long–time variations of the decline–activity have been reported, acting on time scales of a few thousand years (Menzies 1986, Feast 1990). According to the personal opinion of the author, the observations reviewed in this last paragraph are less striking than those outlined before, still leaving enough room for interpretation.

A.3 Models

Compared to the number and the quality of observations, only a few theoretical approaches to model the RCB decline events have been carried out so far. The modest activity of the theoreticians is possibly caused by the complexity of the processes and the somewhat troublesome geometry involved. These obstacles prevent simple theoretical approaches and solutions. A consistent, physical description of the problem obviously must contain (i) a detailed calculation of thermodynamics, chemistry and dust formation, (ii) a solution of radiative transfer and (iii) a modeling of the hydrodynamics for the dust–enriched gas. Due to the cloudy geometry all these investigations have to be worked out *in more than one spatial dimension*.

None of the published models — including this work — satisfy these requirements. Presently, there are on one hand a few theoretical works which focus on certain key problems of the declines, e. g. on the trigger for the sudden onset of dust formation. On the other hand, several empirical models prescribe the existence, the geometry and the movement of the dust in front of the star, calculate the observable consequences and argue in favor or against certain scenarios.

A.3.1 Historical Models

Loreta (1934) and O'Keefe (1939): Loreta (1934) assumes that dust formation occasionally occurs in a massive, spherical stellar outflow, which causes the declines. O'Keefe (1939) agrees with Loreta's hypothesis, but proposes that the dust forms in ejected blobs of gas, similar to solar protuberances. The solid matter proposed to condense is believed to be "principally carbon". Both models assume that dust formation takes place rather distant from the star, where the temperature is low enough to allow for the phase transition. Based on some fundamental thermodynamic considerations, O'Keefe derives condensation temperatures of 1360 K, densities $\sim 10^7\,\mathrm{cm}^{-3}$ and distances of about 8 stellar radii. Reviewing these early statements, which up to date provide the basic idea for the explanation of the RCB declines, the progress since then has apparently been rather slow.

A.3.2 Model Calculations

Wdowiak (1975): Giant convection cells are proposed to be present at the surfaces of RCB stars. Scaling the observations of the granulation and the super–granulation of the sun to giant star dimensions, Wdowiak argues for considerably lower temperatures over certain restricted areas of the star. Following his ideas, this favors dust formation over these areas, followed by dust cloud ejection. Feast (1996) took over this picture and argued that even the semi–regular visual light variations might be caused by this effect rather than by stellar pulsation. Problems remain as even a few thousand degrees less may not be sufficient for dust formation in the photosphere, especially for hot RCB stars, as Wdowiak stated himself. His argument is only qualitatively, as no calculations of the super–granulation have been carried out and the formation of dust has not been calculated.

Fadeyev (1983 – 1988): Y. Fadeyev was the first who applied classical nucleation theory, based on the bulk material data for graphite, to the circumstellar envelopes of RCB stars[8]. In his latest most advanced work (Fadeyev 1988), the temperature is prescribed as $T = T(r)$, and a radially expanding fluid element is followed starting at the sonic point with a given initial velocity. According to the assumptions of an optically thin radiation field, grey gas opacities, radiative equilibrium in the gas and including the greenhouse effect for amorphous carbon, dust formation is possible outside of about $20\,R_*$. Strong correlations with the effective temperature of the star and its (prescribed) mass loss rate are found. The acceleration time scale of the gas due to radiation pressure on dust grains yields about 150 days. In his earlier works, a temporal enhancement of the gas density caused by propagating shock waves are also considered. The model principally has difficulties to explain (i) the dust formation in RCB stars of different effective temperatures, (ii) the pre–existence of a massive stellar wind and (iii) the occurrence of high velocity features soon after the beginning of a decline.

Goeres & Sedlmayr (1992): Goeres (1992) and Goeres & Sedlmayr (1992) have thoroughly investigated the carbon chemistry and the nucleation under the prevailing conditions in RCB envelopes. The chemistry is dominated by a mixture of pure carbon molecules in an inert helium gas, similarly to recent laboratory experiments concerning the formation of "bucky balls" (C60). However, the main chemical pathway to the formation of soot particles involves small carbon chains, monocyclic rings and larger dehydrogenized, curved, but not closed polyaromatic carbon molecules (PACs). Fullerenes are proposed to form as minor by–products of this pathway. Gas temperatures roughly below 1500 K are inevitably necessary for carbon nucleation. The main growth species is the abundant C_3 radical. Molecule drift is proposed to trigger the further growth to larger molecules. The declines are caused by density enhancements due to superimposing shock waves which originate from non–radial pulsations. The descending and the ascending branches of the light curve are explained by hydrostatic dust growth and radial dilution at a constant outflow velocity, respectively. The gas temperature is prescribed as in the model of Fadeyev, causing the same principal problems as above.

Asplund & Gustafsson (1996): Gustafsson & Asplund (1996) have worked out detailed atmosphere calculations for hydrogen deficient stars (static, planeparal-

[8]... and published his results.

lel, LTE), using accurately calculated, line–blanketed absorption coefficients, which yield good agreement with the observed spectra. According to these models, the surfaces of the stars are below the so–defined Eddington limit ($\Gamma = g_{\rm rad}/g_{\rm grav} = 1$). However, radiative instabilities are present in the deeper photospheric layers at the helium ionization zone (at $\tau_{\rm Ross} \approx 10$). In these layers, the radiative acceleration exceeds the gravitational deceleration $\Gamma > 1$ which, according to their models, is balanced by pressure inversions. Asplund & Gustafsson (1996) recognize that such layers are unstable against compression and outward acceleration of gas blobs. As they put forward themselves, the reason for a decline event is proposed to be the acceleration of such a gas blob in the deep photosphere of the star, followed by a supersonic injection through the atmosphere, radiative cooling and dust formation. Thus, the cause of the RCB declines might be found in the radial atmospheric structure of the star itself. The model seems to be promising, but so far the investigations are restricted to hydrostatic considerations. Hydrodynamical models for the process of blob injection have not been performed. Dust formation has not been calculated. The model does not explain the reason for dust formation close to the star, it only provides the necessary density conditions.

A.3.3 Empirical Models

Humphreys & Ney (1974): A secondary cool star with an optically thick dust envelope causes the decline events. Such binary models have principal problems to explain the asymmetry and the true randomness of the light curves. Furthermore, no observational evidence for binary RCB stars have been reported so far.

Wing et al. **(1972) and Grinin (1988):** Orbiting dust clouds from time to time obscure the star — the problems are the same as above. Moreover, the dust clouds should be driven away from the star due to radiation pressure rather than doing Kepler orbits.

Pugach (1984 – 1994): Pugach and co–workers have developed a comprehensive model for the dust cloud evolution which causes the declines. Over the years, the approach has varied a bit, but the main idea remains the expansion of a dust cloud of constant mass at a fixed location in front of the star. Radiative transfer calculations for the different colors have been performed for the following geometry. A massive, initially infinitesimal small, spherical dust cloud with a Gaussian density profile homologously expands ($v = r/t$) at a fixed place with a certain offset from the line of sight in front of the star. The model introduces three parameters: the total dust mass, the offset from the line of sight and the intensity of scattered or additionally emitted radiation, which is not affected by the dust cloud but depends on wavelength. Pugach showed with his work, that the shape of the light curve, and the color variations, can be reproduced by this scenario. No hydrodynamical movement of the cloud is needed, no dust formation must be considered. It can all be explained by pure geometry. Estimates for the total dust cloud masses yield values of $5 - 500 \cdot 10^{20}$g (Pugach & Koval'chuk 1994). The shortcoming of this model is of course that it does not really explain anything. The existence of the dust cloud is prescribed and the reason for the homologous cloud expansion remains mysterious.

Efimov (1990): Spontaneous changes of the absorption properties of a pre–existing dust shell cause the declines, e. g. via spontaneous alignment of non–spherical dust particles. The model can to some extent describe the shape of the light curve and the color variations, but a reason for the spontaneous changes as well as the existence of such special dust is not provided.

Further Models: Many further comments and estimates are stated in the literature, e. g. Feast (1986, 1996, 1997), Alexander et al. (1972), Forrest et al. (1971, 1972). However, these publications mainly present observations and discuss the results in view of some ad–hoc assumed scenarios. Therefore, they do not appear as extra "models" in this Appendix. Nevertheless, important conclusions can be drawn from these considerations. The standard model in these publications clearly is the formation of dust clouds near to the star, followed by radial expansion and dilution. From the IR observations of R CrB, Forrest et al. (1972) concluded that the dust cloud causing the 1972 decline only covered about 3% of the solid angle (corresponding to a semi cone angle of about 20°). According to Feast (1986), the angular sizes of the dust clouds and the decline activities of RCB stars are in agreement with the formation of one dust cloud per pulsational period.

References

ALEXANDER, J. B., ANDREWS, P. J., CATCHPOLE, R. M., FEAST, M. W., LLOYD EVANS, T., MENZIES, J. W., WISSE, P. N. J., WISSE, M. (1972). A spectroscopic and photometric study of the pulsating R Coronae Borealis type variable RY Sagittarii. *MNRAS* **158**, 305–360.

ALLAIN, T. (1996). *Photodestruction and growth of interstellar polycyclic aromatic hydrocarbons.* Dissertation, Technische Universität Berlin, FRG.

ALLEN, C. W. (1973). *Astrophysical Quantities.* London: The Athlone Press.

ASPLUND, M. (1995). Spectroscopy of RY Sgr during the 1993 minimum. *A&A* **294**, 763–772.

ASPLUND, M., GUSTAFSSON, B. (1996). Are the declines of R Coronae Borealis stars caused by super-Eddington luminosities? In C. S. Jeffery und U. Heber (Hrsg.), *Hydrogen-Deficient Stars*, pp. 39–42. ASP Conf. Ser. 96.

ASPLUND, M., GUSTAFSSON, B., KISELMAN, D., ERIKSSON, K. (1997). Line-blanketed model atmospheres for R Cornonae Borealis stars and hydrogen-deficient carbon stars. *A&A* **318**(2), 521–534.

AYRES, T. R. (1981). Thermal bifurcation in the solar outer atmosphere. *ApJ* **244**, 1064–1071.

BECK, H. K. B. (1993). *Ionization, Chemistry and Dust Formation in the Outflows of Classical Novae and Red Giants.* Dissertation, Technische Universität, Berlin, FRG.

BECK, H. K. B., GAIL, H.-P., HENKEL, R., SEDLMAYR, E. (1992). Chemistry in circumstellar shells. I. Chromospheric radiation fields and dust formation in optically thin shells of M-giants. *A&A* **265**, 626–642.

BIERMANN, P., KIPPENHAHN, R., TSCHARNUTER, W., YORKE, H. (1972). Phase Transition in the Interstellar Medium. *A&A* **19**, 113–122.

BOWEN, G. H. (1988). Dynamical modelling of long-period variable star atmospheres. *ApJ* **329**, 299–317.

BURKE, J. R., HOLLENBACH, D. J. (1983). The Gas–Grain Interaction in the Interstellar Medium: Thermal Accommodation and Trapping. *ApJ* **265**, 223–234.

CHASE JR., M. W., DAVIES, C. A., DOWNEY JR., J. R., FRURIP, D. J., MCDONALD, R. A., SYVERUD, A. N. (1985). JANAF Thermochemical Tables. In *J. Phys. Chem. Ref. Dat., Vol.14 Suppl.1.* National Bureau of Standards.

Cherchneff, I., Barker, J. R., Tielens, A. G. G. M. (1992). Polycyclic Aromatic Hydrocarbon formation in carbon-rich stellar envelopes. *ApJ* **401**, 269–287.

Chin, G., Weaver, H. A. (1984). Vibrational and rotational excitation of CO in comets: nonequilibrium calculations. *ApJ* **285**, 858–869.

Clayton, G. C. (1996). The R Coronae Borealis Stars. *PASP* **108**, 225–1996.

Clayton, G. C., Whitney, B. A., Meade, M. R., Babler, B., Bjorkman, K. S., Nordsieck, K. H. (1995). Long-term spectroscopic and polarimetric monitoring of R Coronae Borealis near maximum light. *PASP* **107**, 416–426.

Clayton, G. C., Whitney, B. A., Stanford, S. A., Drilling, J. S. (1992). Observations of R Coronae Borealis stars in decline: Empirical arguments for dust formation near the stellar surface. *ApJ* **397**, 652–663.

Cottrell, P. L. (1996). R Coronae Borealis stars: current status of the observational data. In C. S. Jeffery und U. Heber (Hrsg.), *Hydrogen-Deficient Stars*, pp. 13–25. ASP Conf. Ser. 96.

Cottrell, P. L., Lambert, D. L. (1982). The chemical composition of R Coronae Borealis and XX Camelopardalis. *ApJ* **261**, 595–611.

Cottrell, P. L., Lawson, W. A., Buchhorn, M. (1990). The 1988 decline of R Coronae Borealis. *MNRAS* **244**, 149–167.

Coyne, G. V., Shawl, S. J. (1973). Polarimetry of R Coronae Borealis at visual light minimum. *ApJ* **186**, 961–966.

Drilling, J. S., Schoenberner, D. (1989). On the nature of newly formed dust around the hydrogen-deficient star V348 Sagittarii. *ApJ* **343**, L45–L48.

Efimov, Y. S. (1990). R CrB in the brightness minimum of 1988/1989. *SvA* **34**, 247–254.

Elitzur, M. (1983). On vibrational excitation of interstellar molecules. *ApJ* **266**, 609–613.

Fadeyev, Y. A. (1983). Graphite grain formation in the atmospheres of R Coronae Borealis stars. *Ap&SS* **95**, 357–368.

Fadeyev, Y. A. (1986). Theory of dust formation in R Coronae Borealis stars. In K. Hunger et al. (Hrsg.), *Hydrogen Deficient Stars and Related Objects*, Dordrecht, pp. 441–451. D. Reidel Pub. Comp.

Fadeyev, Y. A. (1988). Carbon dust formation in R Coronae Borealis stars. *MNRAS* **233**, 65–78.

Feast, M. W. (1975). The R Coronae Borealis type variables. In V. Sherwood et al. (Hrsg.), *Vaiable Stars and Stellar Evolution*, pp. 129. IAU Symp. 67.

Feast, M. W. (1979). . In F. M. Bateson et al. (Hrsg.), *Changing Trends in Variable Star Reseach*, pp. 246. IAU Coll. 46.

Feast, M. W. (1986). The RCrB stars and their circumstellar material. In K. Hunger et al. (Hrsg.), *Hydrogen Deficient Stars and Related Objects*, Dordrecht, pp. 151–161. D. Reidel Pub. Comp.

Feast, M. W. (1990). The periodicities of R Coronae Borealis stars and their shells. *ASP Conf. Ser.* **11**, 538–548.

Feast, M. W. (1996a). Some general problems concerning RCB stars. In C. S. Jeffery und U. Heber (Hrsg.), *Hydrogen-Deficient Stars*, pp. 3–11. ASP Conf. Ser. 96.

Feast, M. W. (1996b). The pulsation, temperatures and metallicities of Mira and semiregular variables in different stellar systems. *MNRAS* **278**, 11–21.

Feast, M. W. (1997). The R Coronae Borealis stars – II. Further inferences from the infrared data. *MNRAS* **285**(2), 339–357.

Feast, M. W., Cartner, B. S., Roberts, G., Catchpole, R. M. (1997). The R Coronae Borealis stars – I. Infrared photometry and long-term variations. *MNRAS* **285**(2), 317–338.

Fernie, J. D. (1982). R Coronae Borealis near maximum light. *PASP* **94**, 172–176.

Fernie, J. D., Sherwood, V., DuPuy, D. L. (1972). A photometric study of selected R Coronae Borealis variables. *ApJ* **172**, 383–390.

Feuchtinger, M. U., Dorfi, E. A., Höfner, S. (1993). Radiation hydrodynamics in atmospheres of long–period variables. *A&A* **273**, 513–523.

Fleischer, A. J., Gauger, A., Sedlmayr, E. (1991). Generation of shocks by radiation pressure on newly formed circumstellar dust. *A&A* **242**, L1–L4.

Fleischer, A. J., Gauger, A., Sedlmayr, E. (1992). Circumstellar Dust shells around Long-period Variables. I. Dynamical models of C-stars including dust formation, growth and evaporation. *A&A* **266**, 321–339.

Fleischer, A. J., Gauger, A., Sedlmayr, E. (1995). Circumstellar Dust shells around Long-period Variables. III. Instability due to an exterior κ–mechanism caused by dust formation. *A&A* **297**, 543–555.

Forrest, W. J., Gillett, F. C., Stein, W. A. (1971). Variability of radiation from circumstellar grains surrounding R Coronae Borealis. *ApJ* **170**, L29–L31.

Forrest, W. J., Gillett, F. C., Stein, W. A. (1972). Infrared measurements of R Coronae Borealis through its 1972 marche june minimum. *ApJ* **178**, L129–L132.

Fox, M. W., Wood, R. P. (1985). Shock waves in Mira variables. II. Theoretical models. *ApJ* **297**, 455–475.

Frantsman, Y. L., Eglitis, I. E. (1988). The C / O – ratio in N stars: observations and theory. *SvA* **14**, L109 – L111.

FRIEDRICH, S. (1995). Die Physik der R CrB-Sterne: Phänomenologie und ihre Konsequenzen für die Modellierung. Diplomarbeit, Technische Universität, Berlin, FRG.

GAIL, H.-P., SEDLMAYR, E. (1986). The primary condensation process for dust around late M-type stars. *A&A* **166**, 225–236.

GAIL, H.-P., SEDLMAYR, E. (1988). Dust formation in stellar winds. IV. Heteromolecular carbon grain formation and growth. *A&A* **206**, 153–168.

GILLET, D.; LAFON, J.-P. J., DAVID, P. (1989). Radiative shocks in atomic and molecular stellar atmospheres. III. The shock wave velocity problem in Mira stars. *A&A* **220**, 185–196.

GILLETT, F. C., BACKMAN, D. E., BEICHMAN, C., NEUGEBAUER, G. (1986). IRAS observations of R Coronae Borealis - detection and study of a fossil shell. *ApJ* **310**, 842–852.

GOERES, A. (1992). *Staubbildung in den Hüllen von Kohlenstoffsternen: R Coronae Borealis*. Dissertation, Techn. Univ. Berlin, Berlin.

GOERES, A. (1996). Chemistry and Thermodynamics of the Nucleation in R CrB star shells. In C. S. Jeffery und U. Heber (Hrsg.), *Hydrogen-Deficient Stars*, pp. 69–81. ASP Conf. Ser. 96.

GOERES, A., SEDLMAYR, E. (1992). The envelopes of R Coronae Borealis stars. I. A physical model of the decline events due to dust formation. *A&A* **265**, 216–236.

GOLDREICH, P., SCOVILLE, N. (1976). OH-IR Stars. I. Physical properties of circumstellar envelopes. *ApJ* **205**, 144–154.

GRININ, V. P. (1988). On the blue emission visible during deep minima of young irregular variables. *SvA Lett.* **14**, 27–28.

GUSTAFSSON, B., ASPLUND, M. (1996). Model atmospheres for cool hydrogen-deficient carbon stars. In C. S. Jeffery und U. Heber (Hrsg.), *Hydrogen–Deficient Stars*, pp. 27–38. ASP Conf. Ser. 96.

HECHT, J. H. (1991). The nature of dust around R Coronae Borealis stars: isolated amorphous carbon or graphite fractals? *ApJ* **367**, 635–640.

HECHT, J. H., HOLM, A. V., DONN, B., WU, C.-C. (1984). The dust around R Coronae Borealis type stars. *ApJ* **280**, 228–234.

HELLWEGE, K.-H. (1982). *Landolt-Börnstein: Numerical data and functional relationships in science and technology*, Band II/14 of *new series*. Berlin: Springer-Verlag.

HOLLENBACH, D., MCKEE, F. (1979). Molecule formation and infrared emission in fast interstellar shocks. I. Physical processes. *ApJS* **41**, 555–592.

HOLLENBACH, D., MCKEE, F. (1989). Molecule formation and infrared emission in fast interstellar shocks. III. Results for J shocks in molecular clouds. *ApJ* **342**, 306–336.

Holm, A. V., Wu, C.-C., Hecht, J., Donn, B. (1987). The fading of R Coronae Borealis. *PASP* **99**, 497–508.

Huber, K. P., Herzberg, G. (1979). *Molecular Spectra and Molecular Structure*, Band IV. Constants of Diatomic Molecules. Van Nostrand Reinhold Company.

Humphreys, R. M., Ney, E. P. (1974). Infrared Stars in binary systems. *ApJ* **190**, 339–347.

Iben, I. J., Kaler, J. B., Truran, J. W., Rezini, A. (1983). On the evolution of those nuclei of planetary nebulae that experience a final helium shell flash. *ApJ* **264**, 605–612.

Jeffery, C. S. (1995). The ultraviolet properties of cool material ejected by hydrogen-deficient stars. *A&A* **299**, 135–143.

Jørgensen, U. G. (Hrsg.) (1994). *IAU Colloquium 146: Molecules in the Stellar Environment*, Berlin. Springer Verlag.

Jura, M. (1986). The Role of dust in mass loss from late-type stars. *Irish astr. J.* **17**, 322–330.

Jurcsik, J. (1996). On the Inter-fades Periods of R CrB Type Variables. In C. S. Jeffery und U. Heber (Hrsg.), *Hydrogen-Deficient Stars*, pp. 96. ASP Conf. Ser. 96.

Kilkenny, D., Whittet, D. C. B. (1984). Infrared photometry and broadband flux distributions of southern R Coronae Borealis stars. *MNRAS* **208**, 25–33.

Kneer, F. (1983). A possible explanation of the Wilson-Bappu relation and the chromosheric temperature rise in late-type stars. *ApJ* **128**, 311–317.

Krüger, D., Gauger, A., Sedlmayr, E. (1994). Two–fluid models for stationary dust–driven winds. I. Momentum and energy balance. *A&A* **290**, 573–589.

Lambert, D. L., Kameswara Rao, N. (1994). The R Coronae Borealis Stars – A Few Mere Facts. *JA&A* **15**, 47–67.

Lambert, D. L., Rao, N. K., Giridhar, S. (1990). High resolution spectroscopy of R Coronae Borealis during the 1988 – 1989 minimum. *JA&A* **11**, 475–490.

Lawson, W. A. (1986). RY Sgr: pulsation related phenomenon. In K. Hunger et al. (Hrsg.), *Hydrogen Deficient Stars and Related Objects*, Dordrecht, pp. 211–215. D. Reidel Pub. Comp.

Lawson, W. A. (1992). Spectroscopy of the R Coronae Borealis star V854 Cen through a decline onset. *MNRAS* **258**, 33–36.

Lawson, W. A., Cottrell, P. L., Clark, M. (1991). Radial velocity variations of the R Coronae Borealis star RY Sgr. *MNRAS* **251**, 687–692.

Lawson, W. A., Cottrell, P. L., Gilmore, A. C., Kilmartin, P. M. (1992). Predicting mass loss events in R Coronae Borealis: declines of V854 Cen. *MNRAS* **256**, 339–348.

Lawson, W. A., Cottrell, P. L., Kilmartin, P. M., Gilmore, A. C. (1990). The photometric characteristics of cool hydrogen-deficient carbon stars. *MNRAS* **247**, 91–117.

Lawson, W. A., Kilkenny, D. (1996). The observational characterization of hydrogen-deficient carbon stars as pulsating stars. In C. S. Jeffery und U. Heber (Hrsg.), *Hydrogen-Deficient Stars*, pp. 349–360. ASP Conf. Ser. 96.

Lepp, S., Shull, M. (1983). The Kinetic Theory of H_2 Dissociation. *ApJ* **270**, 578–582.

Loreta, E. (1934). Nota sulle stelle variabili R Coronidi. *Astron. Nachr.* **254**, 151.

Luttermoser, D. G., Johnson, H. R. (1992). Ionization and excitation in cool giant stars, I. Hydrogen and helium. *ApJ* **388**, 579–594.

Luttermoser, D. G., Johnson, H. R., Avrett, E. H., Loeser, R. (1989). Chromospheric structure of cool carbon stars. *ApJ* **345**, 543–553.

Maron, N. (1989). Properties of the circumstellar grains in R Coronae Borealis. *Ap&SS* **161**, 201–207.

Mendoza, C. (1983). Compilation of transition probabilities, electron excitation rate coefficients and photoionization cross sections. In D. R. Flower (Hrsg.), *Planetry Nebulae*, Dordrecht, pp. 154–172. D. Reidel Publishing Company.

Menzies, J. W. (1986). RY Sgr: Can the time of the next minimum be predicted? In K. Hunger et al. (Hrsg.), *Hydrogen Deficient Stars and Related Objects*, Dordrecht, pp. 207–210. D. Reidel Pub. Comp.

Mihalas, D. (1978). *Stellar Atmospheres* (2^{nd} ed.). San Francisco: W. H. Freeman and Company.

Mihalas, D., Weibel Mihalas, B. (1984). *Foundations of Radiation Hydrodynamics*. Oxford University Press.

Millikan, R. C., White, D. R. (1964). Systematics of vibrational relaxation. *J. Chem. Phys.* **39**(4), 3209–3213.

Muchmore, D. (1986). Non-unique solutions to the stellar atmosphere problem. *A&A* **155**, 172–174.

Muchmore, D., Ulmschneider, P. (1985). Effects of CO molecules on the outer solar atmosphere: a time–dependent approach. *ApJ* **142**, 393–400.

Neufeld, D. A., Hollenbach, D. J. (1994). Dense molecular shocks and accretion onto protostellar disks. *ApJ* **428**, 170–185.

Neufeld, D. A., Kaufman, M. J. (1993). Radiative cooling of warm molecular gas. *ApJ* **418**, 263–272.

NUTH, A. N., DONN, B. (1981). Vibrational disequilibrium in low pressure clouds. *ApJ* **247**, 925–935.

O'KEEFE, J. A. (1939). Remarks on Loreta's Hypothesis concerning R Coronae Borealis. *ApJ* **90**, 294–300.

PIGOTT, E. (1797). . *Philos. Trans. R. Soc. London* **1**, 133.

PUGACH, A. F. (1977). On the connection between pulsations of RY Sgr and the total light declines. *Inform. Bull. Variable Stars* **1277**(IAU Commun. 27), 1–3.

PUGACH, A. F. (1984). A model of the R Coronae Borealis phenomenon. *SvA* **28**, 288–292.

PUGACH, A. F. (1990). Interpretation of photometric observations of R Coronae Borealis. Light curves. *SvA* **34**, 646–649.

PUGACH, A. F. (1991). Interpretation of photometric observations of R Coronae Borealis. Color features. *SvA* **35**, 61–65.

PUGACH, A. F. (1992). Interpretation of photometric observations of R Coronae Borealis. A noncentral eclipse by an inhomogeneous cloud. *SvA* **36**, 612–618.

PUGACH, A. F., KOVAL'CHUK, G. U. (1994). Interpretation of R Coronae Borealis Photometric Obervations: The Synthetic Light Curve. *Astronomy Reports* **38**, 219–224.

PUGACH, A. F., SKARZHEVSKII, V. O. (1993). Interpretation of photometric observations of R Coronae Borealis. Approximation tables. *Astronomy Reports* **37**, 169–175.

PULS, J., HUMMER, D. J. (1988). The Sobolev approximation for the line force and line source function in a spherically–symmetrical stellar wind with continuum opacity. *A&A* **191**, 87–98.

RAGHAVACHARI, K., BINKLEY, J. S. (1987). Structure, stability and fragmentation of small carbon clusters. *J. Chem. Phys.* **87**(4), 2191–2197.

RAO, N. K., LAMBERT, D. L. (1993). High resolution spectroscopy of the R Coronae Borealis star, V854 Centauri, during a deep minimum. *AJ* **105**, 1915–1926.

RENZINI, A. (1990). Evolutionary scenarios for R CrB stars. *ASP Conf. Ser.* **11**, 549–556.

SCHMETEKOPF, A. L., FEHSENFELD, F. C., FERGUSON, E. E. (1967). Laboratory measurement of the rate constant for $H^- + H \rightarrow H_2 + e$. *ApJ* **148**, L155–L156.

SCHMUTZLER, E. (1987). *Zum thermischen Zustand dünner Plasmen unter dem Einfluß beliebiger Photonenspektren*. Dissertation, Universität Bonn, Bonn, FRG.

Scholz, M., Tsuji, T. (1984). The effects of spherical extension upon the photospheric structure and spectrum of red giants: comparison of M and C stars. *A&A* **130**, 11–18.

Schönberner, D. (1986). Evolutionary status and origin of extremely hydrogen-deficient stars. In K. Hunger et al. (Hrsg.), *Hydrogen Deficient Stars and Related Objects*, Dordrecht, pp. 471–480. D. Reidel Pub. Com.

Serkowski, K., Kruszewski, A. (1969). Changes in polarization of the R CrB star RY Sgr. *ApJ* **155**, L15.

Spizer, L. (1978). *Physical Processes in the Interstellar Medium.* New–York: J. Wiley & Sons.

Stanford, S. A., CLayton, G. C., Meade, M. R., Nordsieck, K. H. ans Whitney, B. A., Murison, M. A., Nook, M. A., Anderson, C. M. (1988). R Coronae Borealis dust ejections: A preferred plane? *ApJ* **325**, L9–L12.

Stilley, J. L., Callaway, J. (1970). Free-free absorption coefficient of the negative hydrogen ion. *ApJ* **160**, 245–260.

Turner, J., Kirby-Docken, K., Dalgarno, A. (1977). The Quadrupole Vibration–Rotation Transition Probabilities of Molecular Hydrogen. *ApJS* **35**, 281–292.

Unsöld, A. (1968). *Physik der Sternatmosphären* (2. Auflage ed.). Berlin, Heidelberg: Springer.

Walker, H. J. (1985). IRAS photometry of dust shells around hydrogen-deficient stars. *A&A* **152**, 58–62.

Wdowiak, T. J. (1975). Coarse photospheric convection and the ejection of dust by R Coronae Borealis. *ApJ* **198**, L139–L140.

Whitney, B. A., Balm, S. B., Clayton, G. C. (1993). Dust formation in RCB stars. In D. Sasselov (Hrsg.), *Luminous High Latitude Stars*, pp. 115–122. ASP Conf. Ser. No. 45.

Whitney, B. A., Clayton, G. C., Schulte-Ladbeck, R. E., Meade, M. R. (1992). Spectropolarimetry of V854 Centauri at minimum light: Clues to the geometry of the dust and emission-line region. *AJ* **103**, 1652–1657.

Wing, R. F., Baumert, J. H., Strom, S. E., Strom, K. M. (1972). Infrared photometrie of R CrB during its recent decline. *PASP* **84**, 646–647.

Winters, J. M. (1994). *Internal structure and optical appearance of circumstellar dust shells around cool carbon giants.* Dissertation, Technische Universität, Berlin, FRG.

Winters, J. M., Fleischer, A. J., Gauger, A., Sedlmayr, E. (1994). Circumstellar Dust shells around Long-period Variables. II. Theoretical lightcurves of C–stars. *A&A* **290**, 623–633.

Wishart, A. W. (1979). The bound–free photo-detachment cross-section of H^-. *MNRAS* **187**, 59p–60p.

WOITKE, P. (1992). Staubbildung in der Supernova 1987 A. Diplomarbeit, Technische Universität, Berlin, FRG.

WOOD, P. R. (1979). Pulsation and mass loss in Mira variables. *ApJ* **227**, 220–231.

WRIGHT, E. L. (1989). Fractal dust grains around R Coronae Borealis stars. *ApJ* **346**, L89–L91.

ZUBKO, V. G. (1996). On the interpretation of the extinction curves of RCB stars. *MNRAS* **in press**, .

// Meinen *Dank* ...

... möchte ich zunächst Herrn Prof. Dr. Sedlmayr aussprechen. Von seiner unverwechelbaren Art zu denken habe ich und werde ich hoffentlich auch noch in Zukunft viel lernen. Ich danke ihm für die Freiheit, die er mir auf meinem wissenschaftlichen Weg einräumte, und das Vertrauen, das er mir trotz zwischenzeitlicher Differenzen schenkte. Er war es, der es mir durch unbürokratische Maßnahmen ermöglichte, an das Institut für Astonomie und Astrophysik zurückzukehren und hier meine Dissertation zu beenden.

Weiterhin danke ich Herrn Priv. Doz. Dr. Kaufmann für die Erstellung des Zweitgutachtens sowie Herrn Prof. Dr. Zimmermann, der sich bereit erklärt hat, den Prüfungsvorsitz zu übernehmen.

Für die Toleranz, die Hilfbereitschaft und die fruchtbaren Diskussionen bei der Erstellung der Arbeit möchte ich allen Mitgliedern des Institutes danken, insbesondere bedanke ich mich bei Holger Beck, Christiane Helling, Jan Martin Winters und bei Peter Cottrell, die mir bei der Korrektur der Arbeit und der Erledigung der Prüfungsformalitäten tatkräftig zur Seite gestanden haben. Weiterhin danke ich Uwe Bolick, der durch seine größtenteils unentgeltliche Arbeit an den Rechnern des Institutes diese Arbeit erst möglich machte.

Daniel Krüger hat ganz wesentlich bei der naturwissenschaftlichen Konzeption dieser Arbeit mitgewirkt. Die Grundidee erwuchs aus seiner Diplomarbeit, auf die wiederum Andreas Gauger Einfluß hatte. Ich möchte mich bei Dir, Daniel, für die zahlreichen Diskussionen und Deine Korrekturen besonders bedanken — vielleicht kann ich mich dafür bald revanchieren ...

Achim Goeres danke ich von Herzen für die Beratung nicht nur in fachlichen Fragen. Neben einer Art innerer Seelenverwandschaft fühle ich bei ihm stets das aufrichtige Bestreben, meine Arbeit oder vielmehr meine Person zu unterstützen. Ich werde nie vergessen, wie er auf der internationalen Tagung in Bamberg (1995) seinen eingeladenen Vortrag dafür hergab, um meinen darauf folgenden Kurzvortrag einzuleiten.

Mein innigster Dank gehört jedoch Dietrich Ewert, von dessen Hartnäckigkeit, schier unendlicher Energie und liebevoller Zielstrebigkeit ich noch viel lernen werde. In einer Zeit, als ich mit der Astrophysik innerlich fast schon abgeschlossen hatte, hat er mich *täglich* ermuntert, meine Arbeit fortzusetzen.

Lebenslauf

Peter Woitke

Persönliche Daten

Alter: 32 Jahre
Geburtsort: Berlin–Spandau
Familienstand: ledig
Anschrift: Schwendyweg 6, 13587 Berlin

Schule und Studium

Sept. 1971 – Juli 1977	Astrid–Lindgren–Grundschule in Berlin–Staaken
Sept. 1977 – Dez. 1983	Freiherr–vom–Stein–Gymnasium in Berlin–Spandau
Apr. 1984 – Okt. 1992	Studium der Physik an der Technischen Universität Berlin Thema der Diplomarbeit: „Staubbildung in der Supernova 1987A“, Abschluß als Diplom–Physiker

Studienbegleitende Tätigkeiten:

Jan. 1984 – März. 1984	Industriepraktikum bei der Firma Siemens
Apr. 1987 – Feb. 1989	Kurse und Praktika in Bionik und Evolutionsstrategie
Apr. 1989 – März. 1992	Tutor im physikalischen Grundpraktikum (Projektlabor)

Beruflicher Werdegang

ab Nov. 1992	Tätigkeit als wissenschaftlicher Mitarbeiter am Institut für Astronomie und Astrophysik der TU Berlin bei Prof. Dr. E. Sedlmayr mit den Aufgabenbereichen: Betreuung von Seminarvorträgen und Diplomarbeiten Arbeit und Mitarbeit an wissenschaftlichen Publikationen Teilnahme an internationalen Tagungen (z.B. St. Louis, 1994)
Okt. 1996 – Jan. 1997	Tätigkeit als Netzwerk–Administrator und Informatiker bei der Firma BBJ Servis gGmbH

Besondere Kenntnisse

Sprachen:	Englisch (sicher in Wort und Schrift), Französisch (Schulkenntnisse)
EDV:	diverse Erfahrungen mit PCs, work stations und Großrechnern unter DOS, Windows und UNIX. Computersprachen: C, C++, Fortran, GFA–Basic, Pascal und Assembler. Erfahrungen mit PC–Netzwerken unter Novel 3.12, Datenbank–Programmen (Paradox 5.0) sowie mit Standardsoftware–Produkten wie MS-Word und Excel.
Sport:	Tätigkeit als Trainer von Herren- und Damenmannschaften im Volleyball

Berlin, den 31. Juni 1997